Study of Graphitization in Carbon Steel Weldments for Remaining Life Assessment

A Dissertation Presented for the
Doctor of Philosophy
Degree
The University of Tennessee, Knoxville

Maneel Bharadwaj
December 2016

Copyright © 2016

All rights reserved.

Acknowledgements

The author sincerely acknowledges his major professor Dr. Carl D. Lundin for his invaluable guidance, encouragement and his advices throughout this project and graduate studies. The author also appreciates Professors Dr. Carl J. McHargue, Dr. Hahn Choo and Dr. Steven J. Zinkle for agreeing to be in his doctoral dissertation committee and providing some invaluable research advices for this project.

The author would like to extend his sincere appreciation to Dr. Martin Prager, Director of Materials Properties Council (MPC) for providing funding and technical expertise with this project. The author appreciates the generous help his fellow Materials Joining Group (MJG) team members, Dr. Josh Burgess, Mr. John Bohling, Mr. Will Hoskins, Mrs. Rebecca Agle, and Gabriela Apolonio. Special thanks to Professor Danie Hattingh and his team at Nelson Mandela Metropolitan University, South Africa for assistance with friction repair welding. Appreciation to Mr. Doug Fielden and MSE machine shop staffs for their help with sample preparation. Last but not least, sincere thanks to my family and friends for their continued support and encouragement throughout my graduate school studies.

Abstract

Carbon steels and low-alloy steels are often used in various stages of the refining process in petrochemical industries and power plants where they are susceptible to graphitization after prolonged exposure at temperatures of 800°F (427°C) or above. Graphitization is a result of solid-state phase transformation of metastable iron carbide to form iron and graphite structure. The formation of graphite results in the loss of tensile strength, ductility, and creep strength, which may result in untimely catastrophic failure of the component. The current study focused on developing a further understanding of graphitization on ex-service welded carbon steel components, which were removed from service after 17 years at 800°F (427°C). The materials received were examined using metallography, hardness, creep-testing, bend tests, Gleeble thermal simulation, Cryo-cracking, and heat-treatment for further fundamental studies of graphitization. In the materials examined, graphitization was primarily observed in a narrow band just outside of the visible HAZ which corresponds to a weld thermal cycle just below the lower-critical transformation temperature (Ac_1). A hypothesis to support for the increased amount of graphitization observed in the base metal just outside of the HAZ was proposed. The materials examined also exhibited increased amount of graphitization with the increase of

aluminum content. A hypothesis to support this increase in graphitization with aluminum content based on thermodynamic principles was also proposed in this study. Creep studies using accelerated stress and temperature conditions were performed to evaluate the remaining service life of the graphitized components. An accelerated heat-treatment studies were performed to obtain the time-temperature behavior of graphite nucleation and growth. A potential in situ inspections studies using both non-destructive (ultrasonic inspection) and destructive methods (core extraction) were studied. In situ studies showed possible viable approach towards the inspection of graphitized carbon steel components for run, repair or replace decisions. Repair welding performed on core extraction sites using friction hydro tapered pillar processing (FTHPP), showed viable approach.

Executive Summary

Carbon steels and low-alloy steels are often used in various stages of the refining process in petrochemical industries and power plants due to the balance of strength and economy. The carbon and low-alloy steel components are susceptible to graphitization after prolonged exposure at temperatures of 800°F (427°C) or above. Graphitization occurs when cementite from steel transforms to form iron and graphite, to acquire thermodynamically equilibrium state. The formation of graphite results in the loss of tensile strength, ductility, and creep strength, which may result in untimely catastrophic failure of the component. This study focused on developing a further understanding of graphitization morphology to obtain further fundamental understanding with regards to graphitization. Several service-exposed welded carbon steel components, which were removed after 17 years of service at steam temperature of 800°F (427°C), were a subject of this study. This program was undertaken to assist power plants and industry partners who has welded carbon steel components operating in graphitization susceptible temperatures and are concerned about the remaining life and continued serviceability of their components at these temperatures. Thus, an effort to assist industry with remaining life assessment and possible in situ examination was carried out for fitness-for-service evaluation

to assist in making run, repair and retire decisions. The presence, extent and morphological features of graphitization was studied using metallographic examination and cryo-cracking. Quantitative metallography using both ASTM E562 manual point count method and automated image analysis technique was used for volume fraction quantification.

In the materials examined, graphitization was primarily observed in a narrow band just outside of the optically visible heat-affected zone (HAZ) corresponding to weld thermal cycles with peak temperatures just below the lower critical transformation temperature (Ac_1) during welding. A hypothesis to support the increased amount of graphitization in the base metal just outside of the optically visible HAZ is proposed in this investigation. Random/isolated graphite nodules were observed in the base metal remote from the heat-affected zone (HAZ). The maximum extent of graphitization was only about 1-2 volume percent in the most graphitized region (in a thru-wall quantification). With regards to graphitization, there is a historical significance that if steels are de-oxidized with aluminum/silicon they tend to graphitize quickly. The material studied in this investigation exhibited positive correlation with regards to aluminum content, i.e. tendency to graphitize increased with an increase of aluminum content. A hypothesis to support the influence of aluminum on

carbide stability and carbon solubility to result in an increase amount of graphitization was proposed in this investigation.

Creep studies using accelerated stress (4.4 ksi-10 ksi) and temperature (850-950°F) conditions were performed to evaluate remaining service life of graphitized components. Graphitized cross-welded creep specimens were tested up to an equivalent time of 100 years at a typical operating temperatures of 800°F (427°C). No noticeable change in creep performance was observed at 1-2 volume % of graphitization damage. Steady-state creep rates for various temperature/stress combinations was obtained for graphitized components. An accelerated heat-treatment studies were also performed to obtain time-temperature behavior on nucleation and growth of graphite nodules. A potential in situ examination using core sample (~8 mm diameter, ¾ of the component wall) extraction was performed to evaluate the presence and extent of graphite nodules. The metallurgical examination was performed on extracted cores, which represented the overall metallurgical characteristics of the entire through-wall sample. The core extraction sites were repair welded using friction tapered hydro pillar processing (FTHPP). The repair-welds were also examined to understand the service performance at elevated temperatures using metallography (microstructural examination), hardness (mechanical properties),

creep-testing (remaining service-performance), and heat-treatment studies (susceptibility for re-graphitization). The friction-weld heat-affected zone (HAZ) showed formation of complex eutectic micro constituents, consisting of Ledeburite and proeutectoid cementite in accordance to constitutional liquation. Formation of these complex microconstituents was a result of carbon diffusion from pre-existing graphite, which appeared as "carbon-dusting" microstructurally upon cooling. Nucleation of "new" graphite nodules (1-2 μm) was observed in these "dusted" regions of friction weld HAZ during after creep-testing and heat-treatment studies at temperature >900°F. However, creep performance or bend ductility was not influenced by the presence of these complex microconstituents or nucleation of "new" nodules in the HAZ.

Table of Contents

Chapter 1 - Introduction 1
Chapter 2 - Literature Review 8

2.1 Graphitization 8

2.2.1 Types of Graphitization 8

2.2 Thermodynamic Considerations for Graphitization 11
2.3 Historical Overview - Graphitization 20

2.3.1 Early Research 20
2.3.2 Effect of De-Oxidation Practice 27
2.3.3 Weld Related Graphitization 32

2.4 Factors Influencing Graphitization 41

2.4.1 Effect of Service Conditions 41
2.4.2 Effect of Alloying Elements 44
2.4.3 Effect of Prior Thermal Treatment 47
2.4.4 Effect of Welding Conditions 48
2.4.5 Effect of Stress, Cold-Working and Deformation 49
2.4.6 Effect of Grain-size 49

2.5 Kinetics of Graphitization 50
2.6 Graphitization Rehabilitation Program 53
2.7 Weldcore® Technology 55

Chapter 3 - Project Objective 67
Chapter 4 - Materials and Experimental 70

4.1 Metallurgical Characterization 72

4.1.1 Metallographic Examination 72
4.1.2 Cryo-cracking 74
4.1.3 Thermal Cycle Simulation of HAZ using Gleeble 74

4.2 In Situ Inspection for Graphitization 75

4.2.1 Ultrasonic Inspection 75
4.2.2 Weldcore® Technology 76

4.3 Mechanical Testing 77

4.3.1 ASME Section IX Bend Tests 77

4.3.2 Creep Testing 77
4.4 Heat Treatment Studies 78
Chapter 5 - Results and Discussion 82
5.1 Metallurgical Characterization 82
5.1.1 Metallographic Examination 82
5.1.2 Cryo-cracking 96
5.1.3 Effect of Aluminum on Graphitization 102
5.1.4 Weld Related Graphitization 111
5.2 In Situ Inspection for Graphitization 145
5.2.1 Ultrasonic Inspection 145
5.2.2 Weldcore® Technology 155
5.3 Mechanical Testing 177
5.3.1 ASME Section IX Bend Test 177
5.3.2 Creep Testing 178
5.4 Heat-Treatment Studies 189
Chapter 6 - Conclusions 202
6.1 General Conclusions: 202
6.2 In Situ Inspection Studies Conclusions: 205
6.3 Creep Studies Conclusions: 207
6.4 Effect of Aluminum on Graphitization 208
6.5 Weld Related Graphitization 209
List of References 211
Appendix 219
Appendix-A - Tables for Thermodynamic Calculations 220
Appendix B - Metallographic Examination 223
Appendix C - Creep Data 227
Appendix D – Relevant ASTM Standards 236
Vita 244

List of Tables

Table 1. Timeline of major graphitization failures. 26
Table 2. Reported threshold amount for aluminum content for occurrence of graphitization in carbon and C-Mo steels. 30
Table 3. Previous reported temperature ranges for the most graphitized region of the HAZ [2, 7, 11, 24, 56, 58-62]. 38
Table 4. Microstructures showing various degrees of graphitization in the HAZ of carbon steel [58]. 56
Table 5. Recommended rehabilitation example on a hypothetical installation of a carbon steel component by Thielsch [58] 57
Table 6. Sample designations of the materials studied in this study. 70
Table 7. Chemical composition (wt.%) of the base metals used in the current study. 73
Table 8. Table showing the effect of aluminum on graphitization in service-exposed (17 years at 800°F) carbon steel materials. An aluminum content of 0.005 wt.% found to be the threshold amount for occurrence of graphitization. 103
Table 9. Table showing the effect of aluminum on graphitization in C-½ Mo materials subjected to laboratory heat-treatment studies at 1000°F for 4000 hours. 103
Table 10. Steady creep rate (%/hr x 10^{-4}) for graphitized carbon steel samples tested at 10 ksi (68.9 MPa) stress as a function of temperature. 182
Table 11. Steady creep rate (%/hr x 10^{-4}) for graphitized carbon steel samples tested at a temperature of 900°F (482°C) as a function of stress. 182

List of Figures

Figure 1. Optical micrographs showing a typical microstructure in carbon steels (with no graphitization), white = ferrite, dark = pearlite, (Top) 100X, (Bottom) 500X, 2% Nital etch. 2
Figure 2. Optical micrographs showing examples of graphitization A) random/isolated graphitization, B) planar/chain graphitization in carbon steel (100X magnification), 2% Nital etch. 3
Figure 3. Rupture along the longitudinal seam weld as a result of chain graphitization[4, 5] 4
Figure 4. Graphitization related failure in a C-½ Mo super heater tube, A) Fissure oriented at 45° on the inside diameter surface, and B) Optical micrograph (29X) showing graphite nodule oriented at a similar orientation to the fissure shown in A, Nital etch [26]. 12
Figure 5. SEM micrographs showing example of A) lamellar pearlitic structure, and B) spherical cementite structure after spheroidization heat-treatment. 14
Figure 6. Standard free energy of formation of cementite (Fe_3C) from iron and graphite, $3Fe + C = Fe_3C$ [30]. 16
Figure 7. Standard free energy change for cementite decomposition to form iron (Fe) and graphite (C) [27, 29]. 18
Figure 8. Time-temperature plot for pearlite decomposition by mechanisms of spheroidization and graphitization in carbon and low-alloy steels [24]. .. 19
Figure 9. Graphitization in carbon steel during a 670°C for 170-hour heat-treatment in 1912[32] (Top) and Graphitization observed during a routine examination of a low-carbon steel tube from petroleum cracking unit (1935) (Bottom)[6]. 21
Figure 10. Intergranular graphitization at extremity of HAZ as shown by white arrows (Eyebrow Graphitization) in the base metal which led to the first major graphitization failure at Springdale Power Station in 1943[41]. 24

Figure 11. Example of planar/chain type "*weld related graphitization*" observed just outside of the optically visible HAZ in carbon steel after 17 years of service at 800°F (427°C). Dashed line indicates the transition between the end of the optically visible HAZ and the base metal, 2% Nital etch. Decarburization in the areas adjacent to graphite nodules is evident… 33
Figure 12. Schematic diagram showing the various regions of the HAZ corresponding to carbon steel with 0.15 wt.% C indicated on the Fe-Fe_3C equilibrium phase diagram [59]..... 35
Figure 13. Composite of optical micrographs (50X) and individual optical micrographs (100X) showing various regions of the HAZ of a 0.2 wt.% carbon steel, 2% Nital etch. 37
Figure 14. Carbon steel weldment showing evidence of a moderate level of graphitization just outside of the HAZ[64]. 40
Figure 15. Logarithm plot of diffusion coefficient versus reciprocal of absolute temperature (K) [65]. 43
Figure 16. Effect of de-oxidation practice on growth of graphite nodules as a function of temperature after 300 hours in 0.15 % carbon steel[16]. 46
Figure 17. Overall solid-state transformation kinetics[73]. 52
Figure 18. Isothermal time-temperature transformation curve for graphitization in a carbon steel (1 wt. % carbon). Times for 28.5% of carbon to transform to graphite [74]. 52
Figure 19. Photograph showing core retrieval tools [78] (Top) and sketch showing the cross-sectional view of the core retrieval process (Bottom). 59
Figure 20. Cross-sectional view showing a set-up for FTHPP welding (before) and after (right). Note that the diameter of the consumable tool machined is smaller than the bored hole. 62
Figure 21. Macrograph of a typical friction tapered hydro pillar processing (FTHPP) weld performed on X65 pipeline steel using 10 mm diameter stud, 3% Nital etch [81]. 63
Figure 22. Process parameters, Z-axis force and rotational speed as a function of time for friction tapered hydro pillar processing (FTHPP). 66

Figure 23. Creep testing plan to obtain steady state creep rate[89]. 80
Figure 24. Photograph of a typical cross weld jumbo sized creep specimen used in this study. 81
Figure 25. Cross-sectional macrograph of the circumferential weld -A (CW-A), 2% Nital etch..... 83
Figure 26. Optical panorama showing severe graphitization in the base metal region just outside of the optically visible HAZ (boxed region the macrograph) in CW-A, 2% Nital etch. 84
Figure 27. Optical micrographs showing, planar graphitization observed just outside of the visible HAZ on CW-A (A2 Base Metal), 2% Nital etch.. 85
Figure 28. Optical micrographs, showing evidence of random graphitization in the base metal remote from the HAZ on CW-A (A2 Base Metal), 2% Nital etch. 86
Figure 29. Macrograph of a circumferential weld, CW-B, 2% Nital etch..... 88
Figure 30. Optical micrographs, showing planar graphitization in the base metal just outside of the HAZ of CW-B, 2% Nital etch. 89
Figure 31. Optical micrographs showing random and isolated graphitization in the FGHAZ in CW-B, 2% Nital etch..... 90
Figure 32. Weld C - Circumferential weld macrograph, 2% Nital etch. 92
Figure 33. Optical micrographs showing planar graphitization, A) 100X, and B) 500X in CW-C (C2) base metal HAZ, 2% Nital etch. 93
Figure 34. Optical micrographs showing isolated graphitization, A) 100X, and B) 500X in C2 base metal, 2% Nital etch. 94
Figure 35. Cryo-cracking sample extraction location is shown by dashed lines. ~2 mm deep notch (shown by arrow) was placed perpendicular to the weld fusion line to propagate fracture along the desired location..... 97
Figure 36. Cryo-cracking fractograph showing various regions of the weldment: weld deposit, HAZ and the base metal. Note the presence of graphite observed even at low magnification fractograph. 97
Figure 37.Three dimensional schematic illustrating the presence of graphite in a cryo-cracked fracture surface along with the polished and etched

optical micrograph. White arrows indicate typical graphite nodules. Graphitization was primarily located just outside of the visible HAZ and random/isolated graphite nodules were observed in the base metal remote from the HAZ. 99
Figure 38. SEM cryo-cracked fractographs (A1, B1 = 1000X and A2, B2 = 5000X of the region just outside of the visible HAZ, showing agglomeration of graphite nodules. Higher magnification SEM fractographs are shown in Figure 39. 100
Figure 39. SEM cryo-cracked fractographs of graphite nodule exhibited rosette pattern (i.e. initiated at the center and grew in outward direction. EDS examination conformed graphite nodule..... 101
Figure 40. Effect of aluminum on graphitization of service-exposed carbon steel studied in the current project. An aluminum content of 0.005 wt.% found to be the threshold amount for occurrence of graphitization.... 104
Figure 41. SEM micrograph showing nucleation of graphite nodules along ferrite-cementite interface with in a pearlite colony (observed after 500-hours exposure at 1000°F). 106
Figure 42. SEM micrograph showing nucleation of graphite nodules along ferrite-cementite interface with in a pearlite colony (observed after 500-hours exposure at 1000°F). 107
Figure 43. Atom probe tomography measurements across ferrite-cementite lamella in a pearlite colony in a low carbon steel. (square box denote across cementite region)[90]. 108
Figure 44. Change in solubility of carbon in iron as a function of alloying elements [91]. 110
Figure 45. Composite (50X) and higher magnification (200X) optical micrographs showing various regions of the heat-affected zone (HAZ). Graphite nodules were primarily observed in the SCHAZ. Note: the microstructure (ferrite and pearlite) adjacent to the graphite nodules in the SCHAZ is optically identical to that of the unaffected base metal, 2% Nital etch. 112

Figure 46. Weld thermal cycles and the resulting microstructures of the various HAZ regions for a typical carbon steel (ASTM A516-70) experiencing a weld energy input 50 KJ/inch (1″ plate, no preheat). Thermal cycles for times 0-24 seconds shown in the inset plot illustrates the difference in heating/cooling rates for various HAZ regions..... 116
Figure 47. Dilatometry curve showing on-heating (Ac_1) and on-cooling (Ar_1) transformation temperatures for the heat-affected zone peak temperature cycle of 1425°F (774°C) and an energy input of 50 KJ/inch (1″ plate, no preheat). Note that the lower critical transformation temperature Ac_1 is 1384°F (751°C). 118
Figure 48. Weld thermal cycles for a peak temperature of 1425°F (774°C) and 1380°F (749°C). These temperatures were selected to simulate the microstructure above and just below the effective lower critical transformation temperature (Ac_1 =1384°F/751°C). Ac_1 position is indicated by the green line. Note that these thermal cycles are identical with regards to heating/cooling rates and the only difference is the peak temperature. 120
Figure 49. Dilatation curves for thermal cycles simulated at peak temperatures 1380°F and 1425°F. Note: No evidence of transformation was observed for a 1380°F peak temperature. 121
Figure 50. Comparative optical micrographs at 60X and 300X, A) Equilibrium microstructure B) Simulated to a peak temperature of 1380°F, and C) Simulated to a peak temperature of 1425°F. 123
Figure 51. Schematic of Fe- Fe_3C diagram re-drawn to show the solubility difference of carbon in alpha-ferrite as a function of temperature. This phase diagram is not drawn to scale to accentuate the alpha-ferrite region. 125
Figure 52. Schematic illustration of a typical microstructure in hypoeutectoid steel, consisting of microconstituents ferrite and pearlite. 130

Figure 53. Step I – Hypoeutectoid steel at ambient temperature (T_1) prior to welding. Schematic illustration of a typical hypoeutectoid steel microstructure with ferrite (white) and cementite (black). 131
Figure 54. Step II – Hypoeutectoid steel is heated rapidly (~160F°/sec) during welding from ambient temperature (T_1) to a temperature below the lower critical transformation temperature Ac_1 (T_2). 132
Figure 55. Step III – Hypoeutectoid steel is rapidly cooled (~75F°/sec) from a temperature below the lower critical transformation temperature Ac_1 (T_2) to ambient temperature (T_1) after welding. 133
Figure 56. Comparative SEM micrographs prior to simulation (equilibrium microstructure, left) and subsequent to the simulation of 1380°F (749°C) peak temperature. 134
Figure 57. Step IV – Welded hypoeutectoid steel component is heated from ambient temperature (T_1) to a typical service temperature (T_3) of ~800°F/427°C. 137
Figure 58. SEM micrographs showing evidence of graphitization at ferrite-cementite (Fe-Fe_3C) interface. Graphitization was observed after 500 hours of exposure at 1000°F (538°C). 138
Figure 59. SEM micrograph showing evidence of graphitization at ferrite-cementite (Fe-Fe_3C) interface. Graphitization was observed after 500 hours of exposure at 1000°F (538°C). 139
Figure 60. Iron-Aluminum (Fe-Al) binary phase diagram (left), Portion of (Fe-Al) phase diagram emphasizing the region showing the difference of solubility of aluminum between austenite and ferrite (right) [92]. 142
Figure 61. Iron-Silicon (Fe-Si) binary phase diagram (left), Portion of (Fe-Si) phase diagram emphasizing the region showing the difference of solubility of silicon between austenite and ferrite (right) [92]. 143
Figure 62. Optical micrographs (50X) from CW-A weldment showing the extent and orientation of graphitization on A1 and A2 base metals. 148

Figure 63. Ultrasonic examination of CW-B, B2 base metal. Red dashed box shows area used for ultrasonic scan. No indications were observed remote from the fusion line. 150
Figure 64. Ultrasonic examination of CW-B, B1 base metal. Red dashed box shows area used for ultrasonic scan. The major UT reflections were observed adjacent to the fusion line and the intensity decreases remote from the fusion line. 151
Figure 65. Ultrasonic examination of CW-A, A1 base metal. Red dashed box shows area used for ultrasonic scan. The major UT reflections were observed adjacent to the fusion line and the intensity decreases remote from the fusion line. 152
Figure 66. Ultrasonic examination of CW-A, A2 base metal. Red dashed box shows area used for ultrasonic scan. The major UT reflections were observed adjacent to the fusion line and the intensity decreases remote from the fusion line. 153
Figure 67. Core extraction procedure, a) Location showing the most graphitization susceptible region which was selected for core extraction to examine extent of graphitization in the component, and b) Dashed red boxes in the macrograph shows approximate core extraction location on CW-B circumferential weldment. 157
Figure 68. Metallographic examination of the core sample extracted from CW-B. 158
Figure 69. Photograph showing the extracted core and core extraction site prior to finishing for repair welding. 160
Figure 70. Photograph showing the completed FTHPP weld prior to sectioning the excess plug material. Red arrow shows flash formation of the consumable tool as a result of plastic deformation. 161
Figure 71. Cross-sectional view of the completed FTHPP weld showing the position of the consumable (Plug Material) with respect to the fusion line, 10% Nital etch. 162
Figure 72. Macrograph showing completed FTHPP weld, 10% Nital etch. 163

Figure 73. Cross-sectional macrograph showing the friction weld repaired plugs on the CW-A arc weld, 2% Nital etch. 165
Figure 74. Panorama of the FTHPP weld showing evidence of dusting around graphite nodules adjacent to the interface. 166
Figure 75. Diffusion of carbon from graphite nodule resulted carbon rich region in immediate vicinity which optically appear as carbon "dusting" in the friction weld HAZ. Graphite nodules remote from the weld deposit did not exhibit any evidence of "dusting" appearance, 2% Nital etch. 168
Figure 76. Diffusion of carbon from graphite nodule resulted carbon rich region in the immediate vicinity, which optically appear as carbon "dusting" in the friction weld HAZ. Graphite nodules remote from the interface did not exhibit "dusting" appearance, 2% Nital Etch. 169
Figure 77. Partial melting adjacent to graphite nodule in accordance to constitutional liquation, 2% Nital Etch. 170
Figure 78. SEM Micrographs of the boxed region from Figure 77, showing formation of pro-eutectoid cementite and pearlite (lamellar structure). 171
Figure 79. Diffusion of carbon from pre-existing graphite nodules resulting in dusted region, 2% Nital etch. 172
Figure 80. SEM Micrographs of the boxed region from Figure 79, showing formation of pro-eutectoid cementite (shown by red arrows) and pearlite (lamellar structure)..... 173
Figure 81. Hardness traverse (100 gf) across the dusted region (as shown in micrograph) showing peak hardness of 650 HV. Average hardness outside the dusted region = 200 HV. 174
Figure 82. Creep curve for CW-A circumferential weld. Creep testing conditions and steady sate creep rate provided in Table below. 180
Figure 83. Normalized creep curve to obtain steady-state creep rate for a typical operating temperature of 800°F for CW-A. Normalization was performed using Larson Miller Parameter, with constant of 15. 181

Figure 84. Steady creep rate for graphitized carbon steel samples tested at 10 ksi (68.9 MPa) stress as a function of temperature..... 184
Figure 85. Steady creep rate for CW-A as a function of temperature for different stresses..... 185
Figure 86. Photograph of a full-wall cross-weld creep specimen (CW-A-1), showing two friction weld repaired plugs on either side of the girth weld, RA = 1%, 2% Nital Etch. 187
Figure 87. Creep Curve (Top) for friction welded specimens from CW-A and normalized creep curves (bottom) for friction welded specimens at 800°F using LMP constant C= 15. 188
Figure 88. Comparative optical micrographs in service-exposed (17 years at 800°F) and additional heat-treatment studies (900°F/567 hours + 950°F/168 hours). Heat-treatment is equivalent to ~11 years at a typical service-temperature of 800°F. 190
Figure 89. SEM micrographs on CW-A, A) Prior pearlitic region adjacent to graphite nodule, B) Prior pearlitic region further away from graphite nodule. Micrographs show that prior pearlitic region is completely spheroidized. 192
Figure 90. SEM micrographs (50kx and 100kx) from location A in Figure 89. Note that the prior pearlitic region is completely spheroidized and carbon denuded. 193
Figure 91. Comparative SEM micrographs before and after creep tests (different time) in the "dusted" region in friction weld HAZ showing evidence of nucleation of "new" graphite nodules. 194
Figure 92. Comparative SEM micrographs (25 KX) after 0, 50, 100, and 250 hours of exposure at 1000°F (538°C). 197
Figure 93. SEM micrograph showing evidence of graphitization along the ferrite-cementite interface (~500 nm) at 200 KX, observed after 250 hours at 1000°F (538°C). 198
Figure 94. Comparative SEM micrographs (25 KX) after 500, 1000, 2000, and 3000 hours of exposure at 1000°F (538°C). 199

Figure 95. SEM micrograph showing graphitization along Fe-Fe3C interface and along pearlite-ferrite boundary. 200
Figure 96. Average graphite nodule diameter as a function of time. The nodule growth rate showed a typical Avrami type transformation, which exhibited initial incubation period, which followed a rapid growth stage and acquired an equilibrium state. 201

Nomenclature and Abbreviations

AW	As-Welded
AWS	American Welding Society
ASTM	American Society of Testing Materials
ASME	American Society of Mechanical Engineers
CS	Carbon Steel
C -½ Mo	Carbon – ½ Molybdenum
CGHAZ	Coarse-Grained Heat-Affected Zone
FHPP	Friction Hydro Pillar Processing
FTHPP	Friction Tapered Hydro Pillar Processing
FGHAZ	Fine-Grained Heat-Affected Zone
HAZ	Heat Affected Zone
ICHAZ	Intercritical Heat-Affected Zone
MJG	Materials Joining Group at the University of Tennessee
MPC	Materials Properties Council
MPa	Mega Pascal (10^6 Pa)
NDE	Non Destructive Examination
NMMU	Nelson Mandela Metropolitan University
OLM	Optical Light Microscopy
PWHT	Postweld Heat Treatment
ppm	parts per million
SCHAZ	Subcritical Heat-Affected Zone
SEM	Scanning Electron Microscope
SAW	Submerged Arc Welding
SMAW	Shielded Metal Arc Welding
UTK	University of Tennessee, Knoxville
WRC	Welding Research Council
Weldment	Weld Deposit, Base Metal, and Heat-Affected Zone

Chapter 1 - Introduction

Carbon and low-alloys steel components are used in various stages of petroleum refineries, petrochemical industries, and steam power plants which are operating in a temperature range of 600°F-1100°F (316°C-593°C). Carbon and low-alloy steels are susceptible to graphitization, which is a transformation of metastable iron carbide (Fe_3C) to graphite (C) when exposed to the temperatures of 800°F-1100°F (427°C-593°C) [1] as shown by Equation 1 below.

$$Fe_3C = 3Fe + C \text{ (graphite)} \qquad \text{Equation 1}$$

A typical microstructure of a carbon steel, consists of ferrite (white) and pearlite (dark) constituents, as shown in Figure 1 at 100X and 500X. The formation of graphite results in loss of tensile strength, ductility, creep rupture properties, and the reduces the overall structural integrity of the component which may eventually lead to untimely catastrophic failures. Graphitization occurs in two morphologies in steels: 1) isolated/random, and 2) planar/chain. Examples of each of these morpologies of graphitization morphologies in carbon steel are shown in Figure 2.

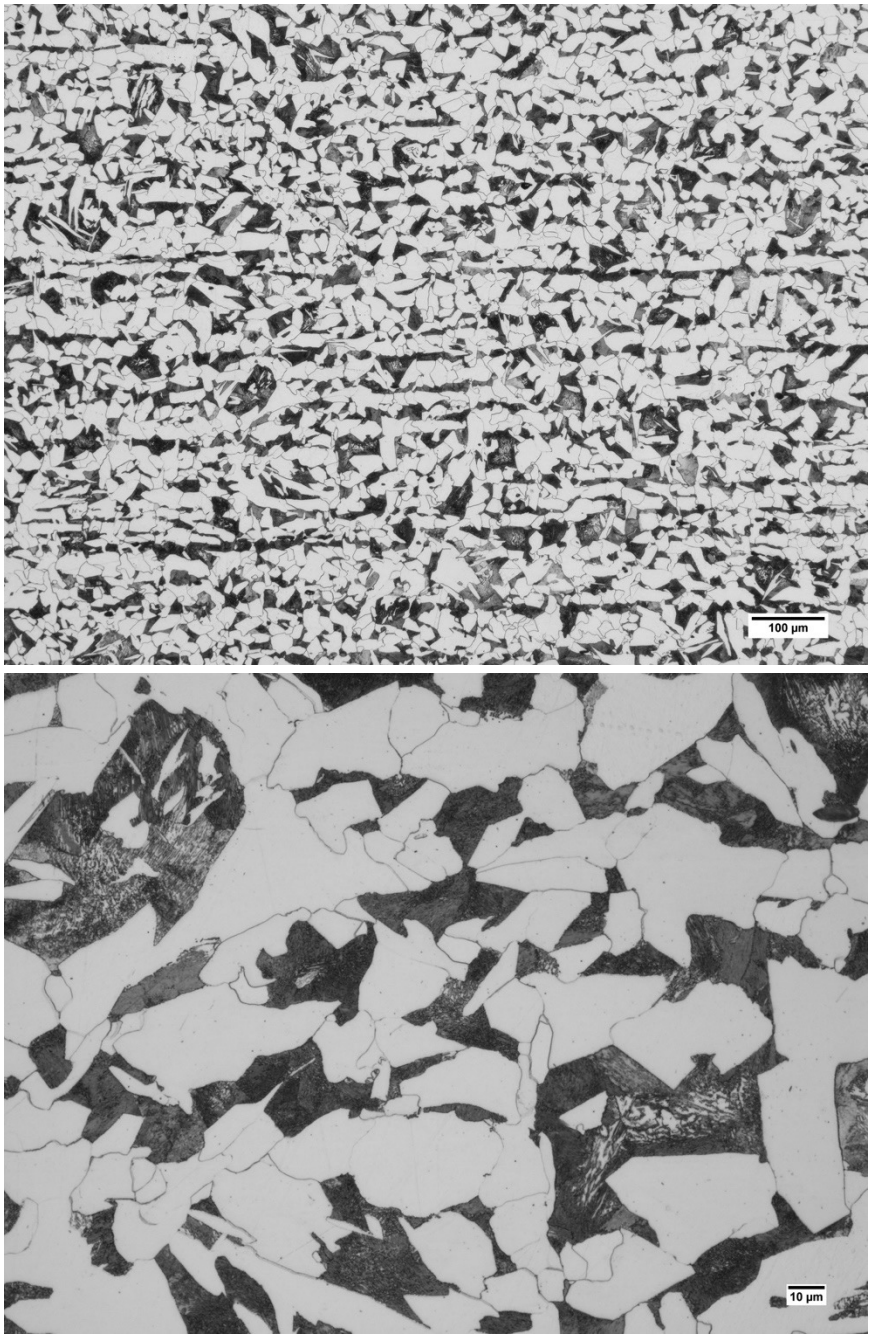


Figure 1. Optical micrographs showing a typical microstructure in carbon steels (with no graphitization), white = ferrite, dark = pearlite, (Top) 100X, (Bottom) 500X, 2% Nital etch.

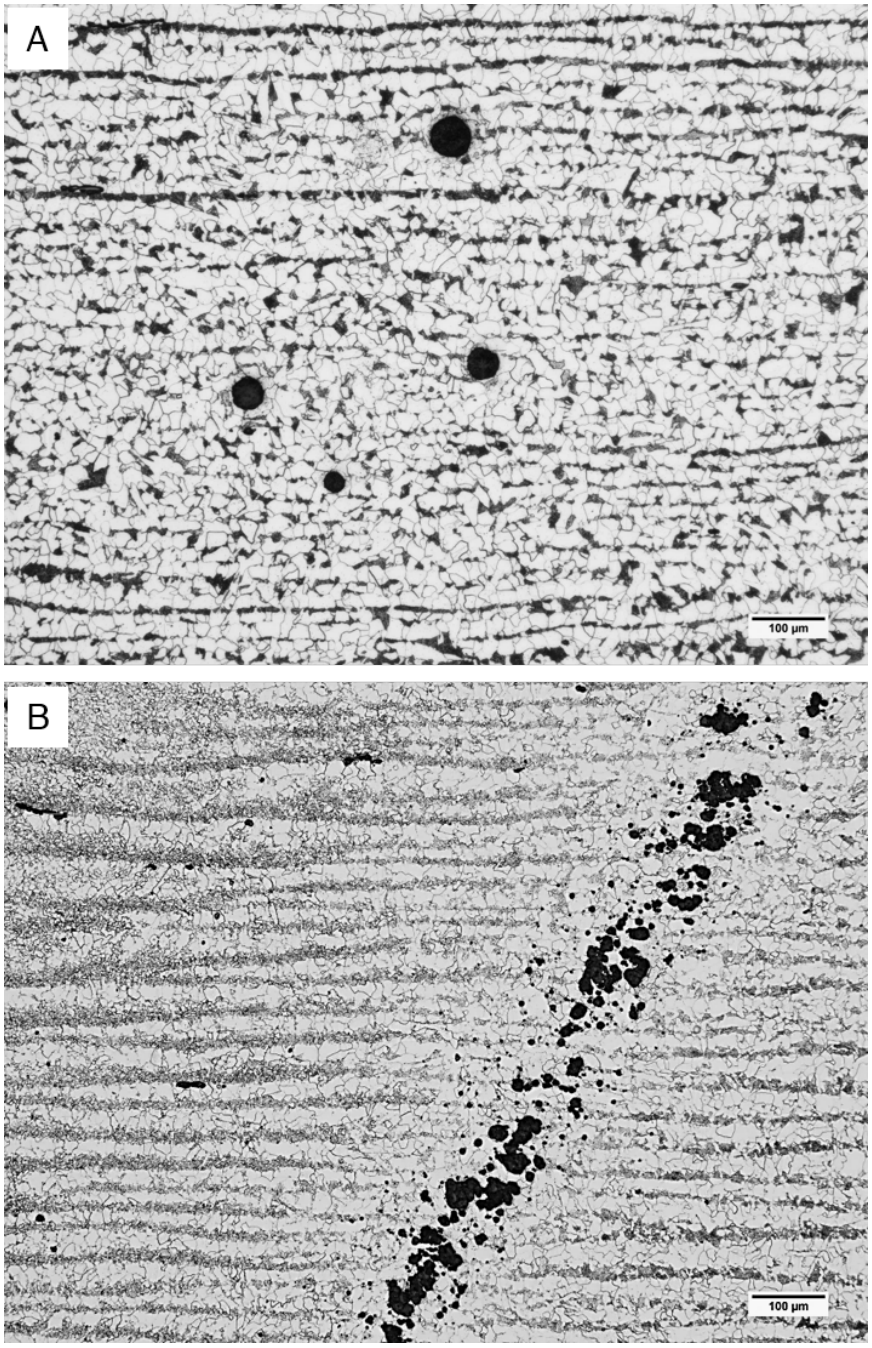


Figure 2. Optical micrographs showing examples of graphitization A) random/isolated graphitization, B) planar/chain graphitization in carbon steel (100X magnification), 2% Nital etch.

An isolated/random form of graphitization is not considered to be significant to the structural integrity of the component, however, graphitization when forms in planar/chain morphology have a considerable effect on the load bearing capability of the component. This form of graphitization tends to increases the potential for brittle fracture and also lowers the creep strength to result in catastrophic failures [2, 3]. Figure 3 shows an example of a rupture in a longitudinally seam welded boiler tube, resulting from chain-type graphitization along the heat-affected zone of a weld[4, 5].



Figure 3. Rupture along the longitudinal seam weld as a result of chain graphitization[4, 5].

Graphitization in carbon and low-alloy steels have been a long-standing problem and a significant amount of research has been performed over last 60-70 years to obtain a fundamental understanding of graphitization in carbon steels. The true kinetics of graphitization in steels is still not been clearly understood to date, as graphitization depends on various metallurgical factors (such as: chemical composition, prior thermal history, microstructure, welding, etc.) and service-conditions (such as: time, temperature and stress). Graphitization has resulted in periodic failures in power plants and refineries over last 60-70 years. Graphitization was first observed in steels in a thermal cracking unit of a refinery in 1935 during a routine inspection [6], but it only after the Springdale Power Station rupture in 1943, graphitization sparked interest amongst various researchers. The Springdale failure was observed in a C-½ Mo steel circumferential weld after 5-½ years of service at 935°F (502°C)[7]. Fracture was observed in the base metal region just outside of the heat-affected zone (HAZ) [7]. The Springdale failure instigated all the major power plants to evaluate their components proactively for the presence of graphitization[2, 7-18]. Two other failures due the graphitization were experienced at the Oak Ridge gaseous diffusion plant in 1957 which was operating for more than 100,000 hours at 935°F (502°C)[19]. These Oak Ridge failures were similar to the Springdale failure and

were also weld related. Planar type of graphitization was observed in a narrow band region just outside of the HAZ. The next reported graphitization related failure occurred at Pennelec's Williamsburg station in 1977, this incident resulted in 6 casualties [20]. The most recent failure related to graphitization in steel was observed in 2011 (C-½ Mo steel) and 2015 (carbon steel)[21, 22]. These failures with regards to graphitization has been recurring and has been a continued industry concern for last 50-60 years. Thus, a careful consideration of all the important metallurgical variables (microstructure, composition, welding thermal cycle, prior thermal cycle, stress, etc.) is required for a complete understanding of graphitization in carbon steels. Due to the potential for catastrophic failure, a quantitative/qualitative understanding of graphitization in relation to mechanical properties is required for remaining life estimation. This project was initiated to assist the industry partner, who has miles of carbon steel components operating in a graphitization susceptible temperature range and are concerned about remaining life. Apart from assisting the industry partner with remaining life assessment of the carbon steel components, fundamental understanding with regards to the occurrence of graphitization was acquired in this study.

The primary objective of this study is to examine service-exposed materials for the presence and the extent of graphitization to enhance earlier

understanding on the occurrence of graphitization. An enhanced metallographic examination using optical light microscopy (OLM) and scanning electron microscopy (SEM) was performed to study the presence, extent and morphology of graphitization. The understanding of the remaining life is important for the continued operation of the graphitized carbon steel component, thus, an accelerated creep testing was performed to obtain run, repair, and retire decisions. In the past, the extent of graphitization has primarily been analyzed on a purely qualitative basis [24], a quantitative metallurgical evaluation of the volume fraction graphite was performed to relate the influence of graphite on creep performance. An ultrasonic examination studies using state-of-the-art focused phased array and phased array techniques was performed for evaluation of in situ detection capabilities of graphitized components. Core extraction technique to evaluate the efficacy of graphitized components for further in service inspection was performed. The subsequent repair welding of the core extraction sites using friction tapered hydro pillar processing (FTHPP) was studied.

Chapter 2 - Literature Review

2.1 Graphitization

Graphitization is a formation of graphite in iron-carbon alloys which happens either during the solidification stage (liquid to solid) or during the elevated temperature service when thermodynamically metastable Fe_3C transforms to form iron (Fe) and graphite (c) based on Equation 2.

$$Fe_3C = 3Fe + C \text{ (graphite)} \qquad \text{Equation 2}$$

2.2.1 Types of Graphitization

Graphitization is generally observed in two modes in iron-carbon alloys: Primary graphitization and Secondary graphitization.

1. Primary Graphitization

Primary graphitization is a formation of graphite during solidification from liquid to solid resulting in a stable iron-graphite structure. This form of graphitization is observed in cast irons and based on the morphologies of the graphite observed upon solidification, they are distinguished into various types. Gray iron (flake graphite), ductile iron (spheroidal graphite), and compacted graphite iron (compacted vermicular graphite) (grey or ductile iron) are

examples of primary graphitization modes[25]. The current study only discuses secondary graphitization.

2. Secondary Graphitization

Secondary graphitization is a result of solid-state phase transformation of metastable iron-carbide (Fe_3C) to form stable iron graphite structure graphite after prolonged exposure at elevated temperatures (>800°F/427°C). This project is only deals with secondary graphitization in carbon steels and thus for simplicity throughout this document will be referred only as graphitization. Carbon steel components are typically used either in normalized or as-rolled condition in power plants. The microstructure in normalized or as-rolled condition typically consists of ferrite and pearlite (ferrite + cementite). Figure 1 shows an example of normalized carbon steel (ASTM A516-70) consisting of ferrite and pearlite (ferrite + cementite) microstructure. When these steels are exposed at elevated temperature for extended period of time, cementite (Fe_3C) decomposes to form ferrite and graphite (c). The major driving force for graphitization reaction ($Fe_3C \rightarrow 3Fe + C$) is metastable nature of cementite to acquire equilibrium state in the form of iron and graphite structure. Secondary graphitization is distinguished in two forms based on their morphological features: A) isolated/random and B) planar/chain.

A. Isolated/Random Graphitization

Graphitization of this form is observed randomly, and are isolated from other graphite nodules. Graphite when forms in an isolated and random manner are considered not significant to the structural integrity of the component. Figure 2A (100X) shows an example of the isolated/random type of graphitization. This form of graphitization is generally observed in the base metal remote from the weld deposit (away from HAZ).

B. Planar/Chain Graphitization

Graphite when segregates in cluster of nodules to form a continuous chain is called planar/chain type graphitization. The continuous formation of graphite results in a plane of weakness lowering yield and tensile strength of the material. This form of graphitization generally has a significant effect on the load bearing capability of a component and may result in catastrophic failures. Figure 2B shows a micrograph of a typical example of planar/chain type graphitization. Planar graphitization has been primarily associated with welds called weld HAZ planar graphitization or "eye-brow graphitization". This form of graphitization is considered one of the most catastrophic and is discussed in further detail in section 2.3.3.

Although planar/chain type of graphitization has been more common to the welds, there has been few instances when planar graphitization failures has been observed solely in base metals[4, 26, 27]. This form of graphitization is termed as non-weld related graphitization, and has been a common problem specially in boiler and super heater tubes. Figure 4 shows an example of an in-service failure of a super heater tube resulting from the base metal graphitization[27]. The graphite nodules are oriented 45° degrees to the longitudinal axis of the tube. This form of graphitization results by the formation of slip planes or a because of localized strain due to plastic deformation or bending stresses in service[26, 27].

2.2 Thermodynamic Considerations for Graphitization

The major driving force for graphitization reaction is the free energy (ΔG) differential between metastable cementite and graphite. The metastability nature of cementite has been thoroughly investigated by various researchers [28-31]. The standard free energy of formation ($\Delta G°$) of cementite from iron and graphite was determined by Chipman according to Equation 3[31], which is a function of enthalpy ($\Delta H°$) and entropy ($\Delta S°$). Chipman showed that Fe_3C is thermodynamically metastable compared to graphite at all temperatures.

$$\Delta G° = \Delta H° + \Delta S° \qquad \text{Equation 3}$$

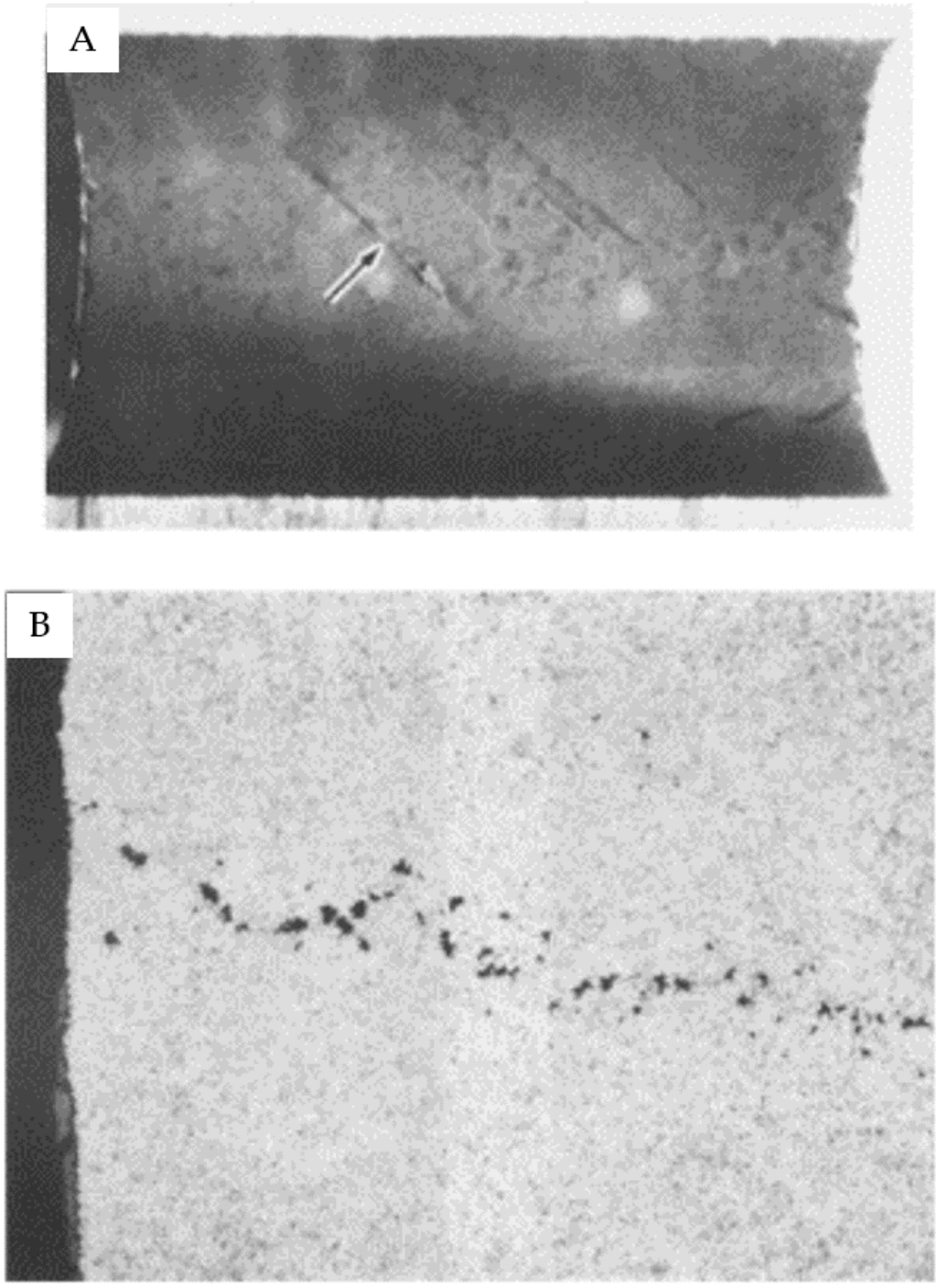


Figure 4. Graphitization related failure in a C-½ Mo super heater tube, A) Fissure oriented at 45° on the inside diameter surface, and B) Optical micrograph (29X) showing graphite nodule oriented at a similar orientation to the fissure shown in A, Nital etch [27].

Prior to discussing thermodynamics behind the driving force for graphitization reaction, it is a must to discuss pearlite decomposition reaction. Pearlite decomposition occurs by two known processes: graphitization or spheroidization, specially at temperatures these steels are operating (800-1100°F) in steam power plants. Spheroidization is a process in which lamellar pearlitic structure decomposes to form spherical cementite particle to reduce interfacial energy. The major driving force for spheroidization reaction is the large interfacial area per unit volume in a lamellar pearlitic structure at ferrite cementite interface. Figure 5 shows scanning electron microscopy (SEM) micrographs depicting example of lamellar pearlitic structure in a carbon steel before and after spheroidization reaction. Free energy at a ferrite-cementite interface is a function of interfacial energy per unit area and inter-lamellar spacing (λ), as shown in Equation 4 [32]. The spheroidization reaction also results in reduction of total free energy at the ferrite-cementite interface.

$$\Delta G = \frac{2}{\lambda} \Upsilon_s \qquad \text{Equation 4}$$

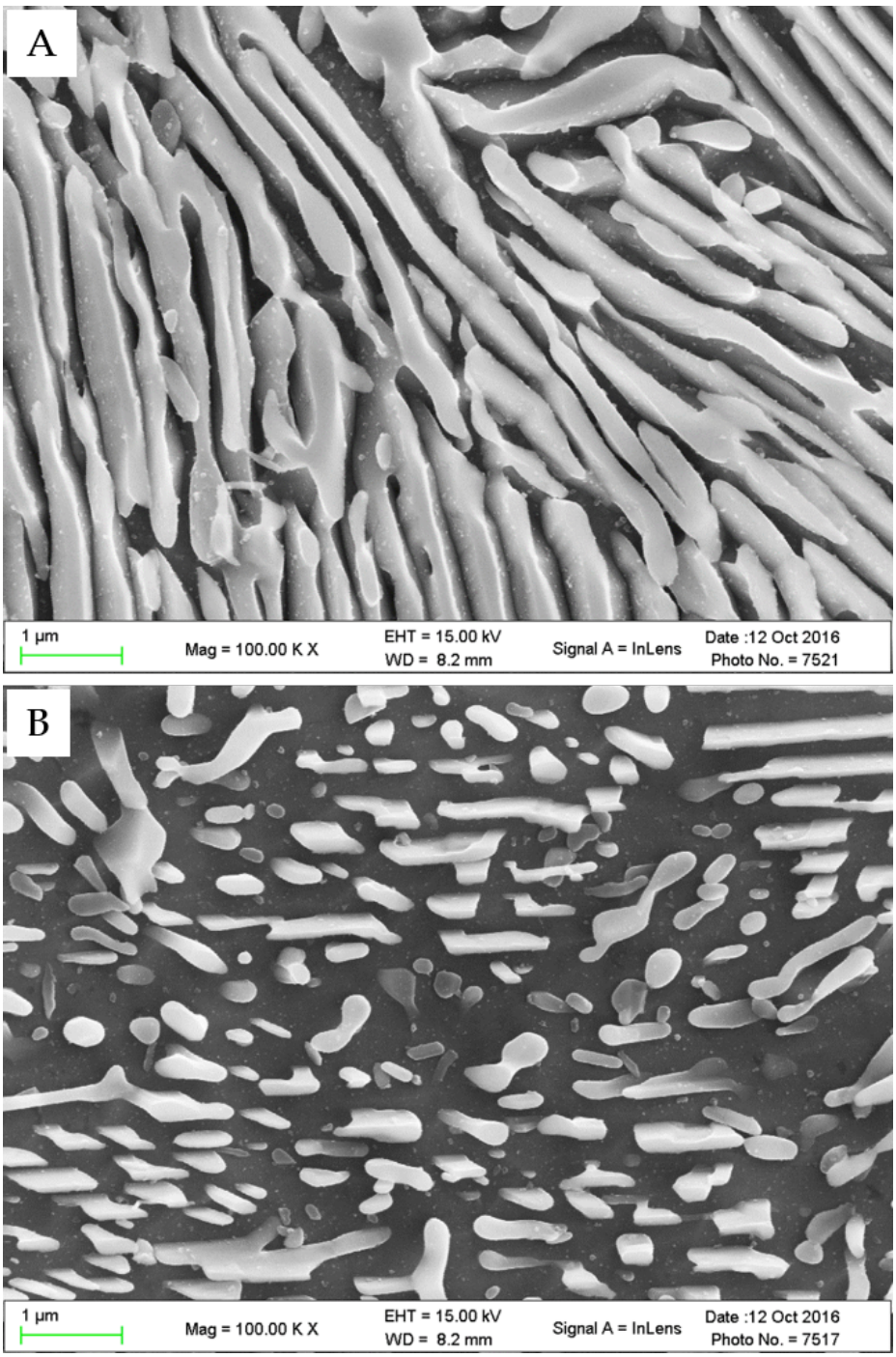


Figure 5. SEM micrographs showing example of A) lamellar pearlitic structure, and B) spherical cementite structure after spheroidization heat-treatment.

Graphitization is a solid-state phase transformation of metastable iron-carbide to form a stable iron graphite structure. Graphitization results in an alignment of graphite nodules to form a plane of embrittled region and thus is a more of a design concern than spheroidization. The formation of graphite results in a loss of tensile strength, ductility, and creep properties, which eventually may lead to premature failure of the component. The graphitization reaction is driven by the metastability nature of cementite. Figure 6 shows the standard free energy of formation of cementite (J/mole) as function of temperature. It shows cementite is metastable at all temperatures[31].

The free energy (G) of a system is given by enthalpy (H) and entropy (S), as shown in Equation 5.

$$G = H - TS \qquad \text{Equation 5}$$

If the thermal energy is provided to overcome the activation barrier, cementite prefers to acquire the stable iron and graphite structure. This results in graphitization. The driving force for the cementite decomposition to form graphite is provided by free energy difference between cementite and graphite.

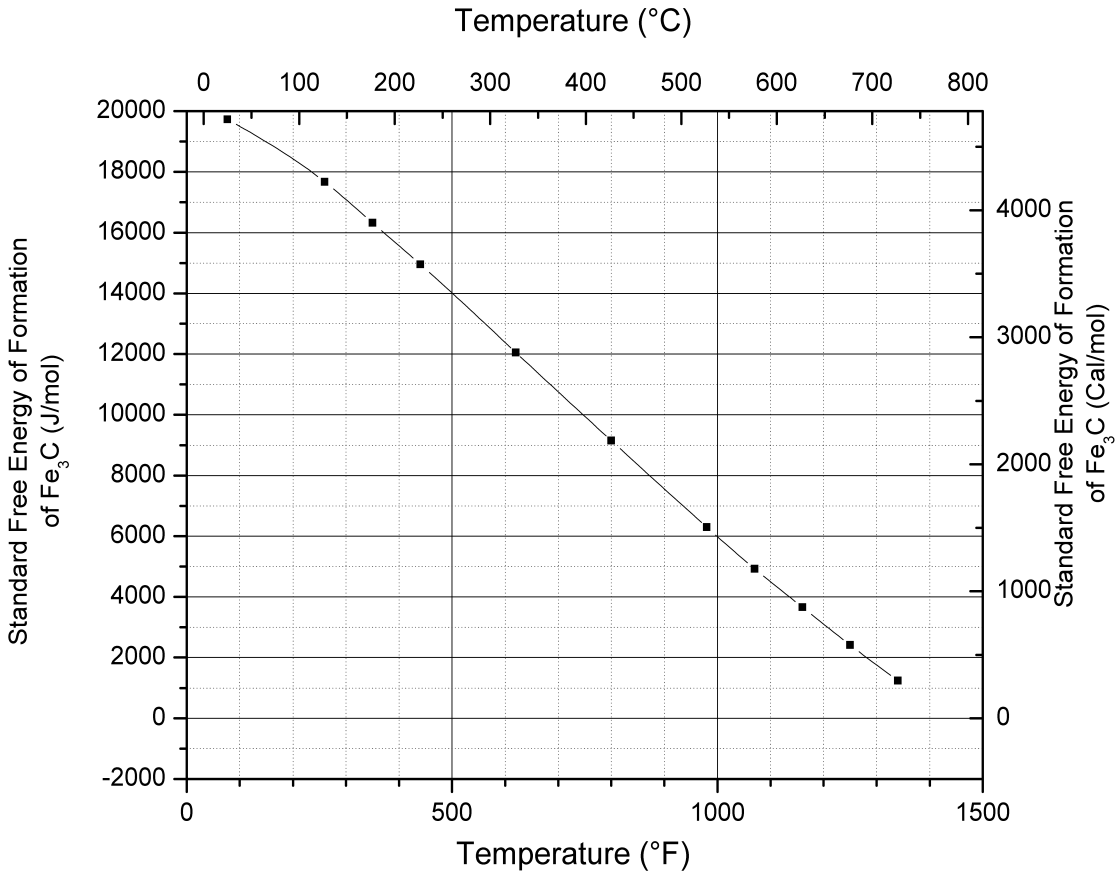


Figure 6. Standard free energy of formation of cementite (Fe_3C) from iron and graphite, $3Fe + C = Fe_3C$ [31].

The graphitization reaction is favorable if the overall free energy change is negative (see equations below).

$$Fe_3C \rightarrow 3Fe + C$$

$$\Delta G° = \Delta H° + \Delta S°$$

$$\Delta G_{(3Fe+C)} - \Delta G_{Fe_3C} < 0\ (Proceeds\ Forward)$$

Figure 7 shows the free energy change during the cementite decomposition reaction[28, 30]. The free energy differential during the cementite decomposition reaction increases with temperature and acquires a local minimum at temperature range from 800-1100°F. The components susceptible to graphitization are operating in this temperature range. Figure 8 shows a time-temperature plot of the pearlite decomposition for spheroidization or graphitization for carbon and low-alloy steels [25]. Graphitization is generally more prevalent at temperatures lower than 1050°F (566°C) and is most likely to spherodize at higher temperatures (above 1050°F or 566°C). At intermediate temperatures both spheroidization and graphitization occur simultaneously.

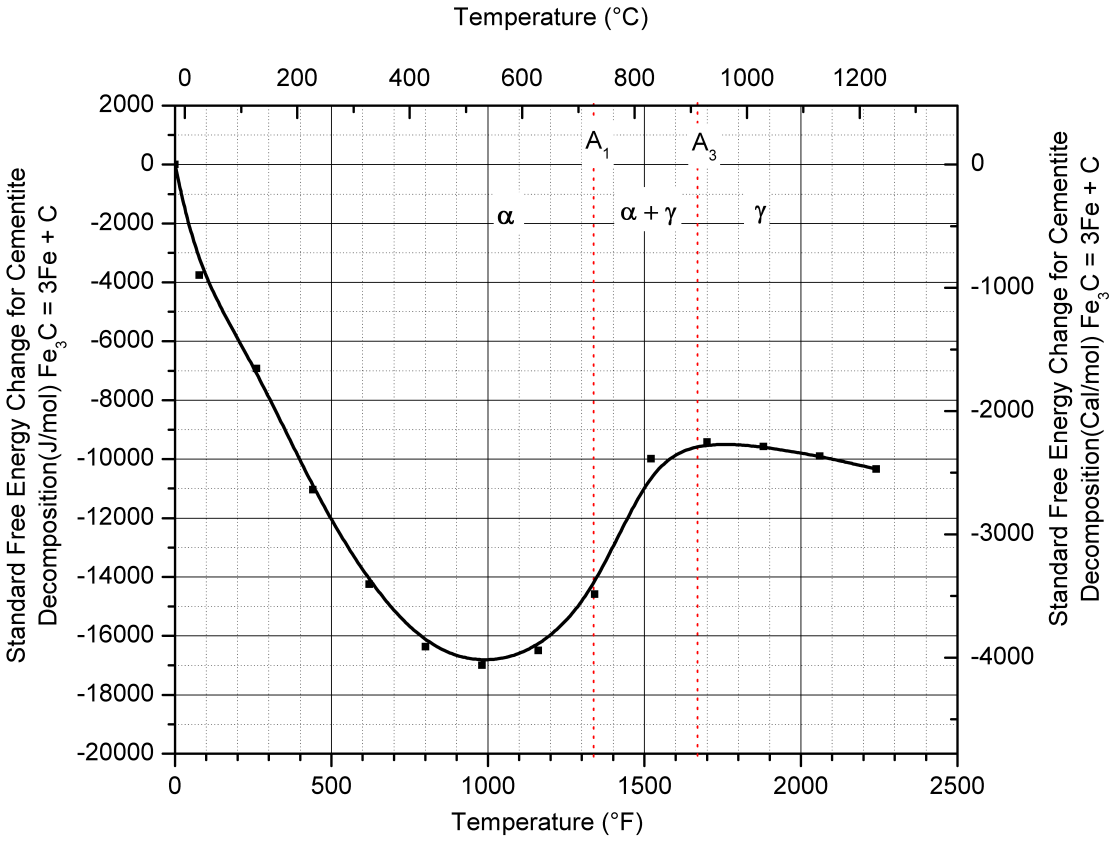


Figure 7. Standard free energy change for cementite decomposition to form iron (Fe) and graphite (C) [28, 30].

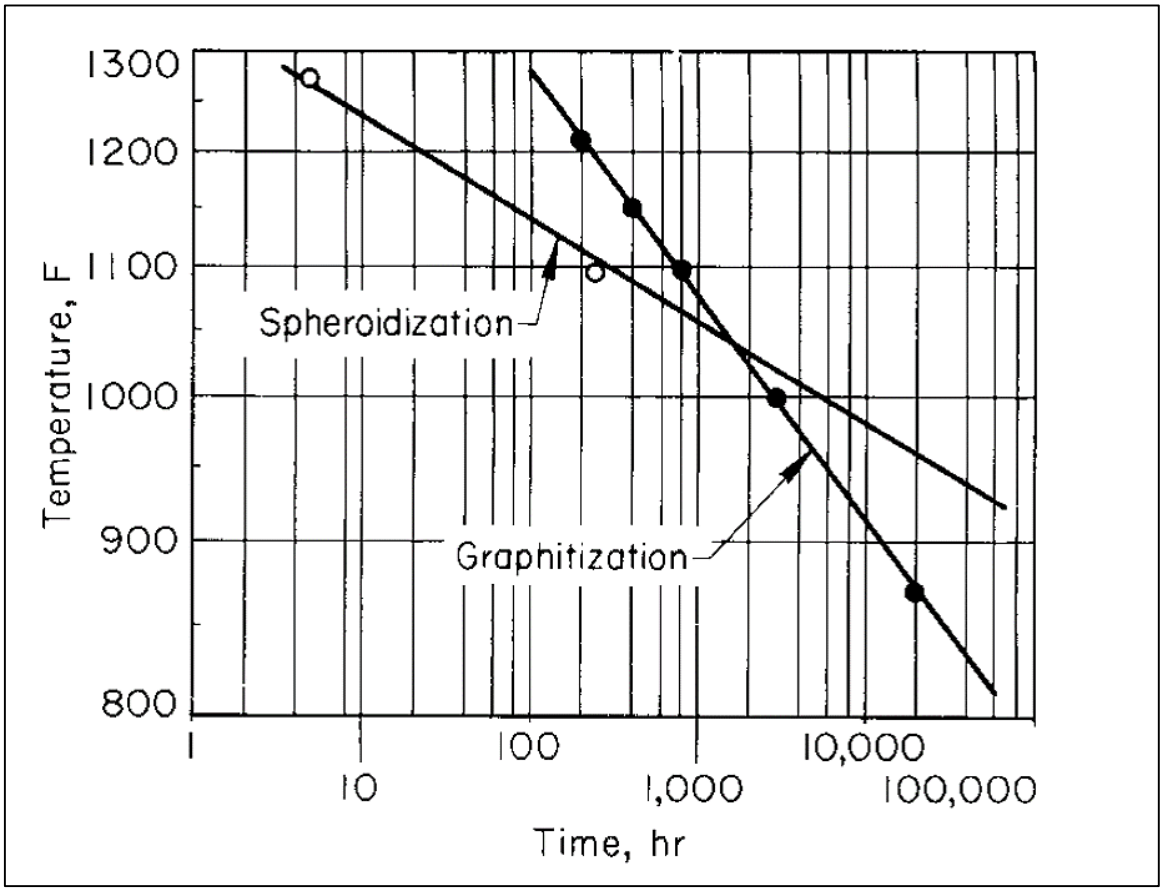


Figure 8. Time-temperature plot for pearlite decomposition by mechanisms of spheroidization and graphitization in carbon and low-alloy steels [25].

2.3 Historical Overview - Graphitization

2.3.1 Early Research

Graphitization related failures in carbon and low-alloy steels have been a long standing problem and a significant amount of research has been performed over last 60-70 years to understand the kinetics of graphitization in steels. The first evidence of graphitization dates to 1912 when Dr. A Sauveur observed graphitization in carbon steel (0.9 wt. % C) during his heat treatment studies (1238°F/670°C for 170 hours)[33, 34]. There were no other reported evidences of graphitization until 1935 when Kinzel observed graphitization during a routine examination of a carbon steel tube from petroleum cracking unit[6]. The carbon steel component (0.15 wt. % C, 0.49 wt.% Mn, 0.02 wt. % Si, 0.023 wt. % S, 0.015 wt.% P) was operating at 1202°F (650°C) for 3 years. Figure 9 shows optical micrographs reported by Sauveur (1912)[33] and Kinzel (1935)[6, 34]. Micrographs clearly show evidence of graphitization, with microstructures consisting of ferrite (white) and graphite (black). Wells in 1938 reported evidence of graphitization in high purity iron-carbon alloys during his investigation on the metastability nature of cementite[8].

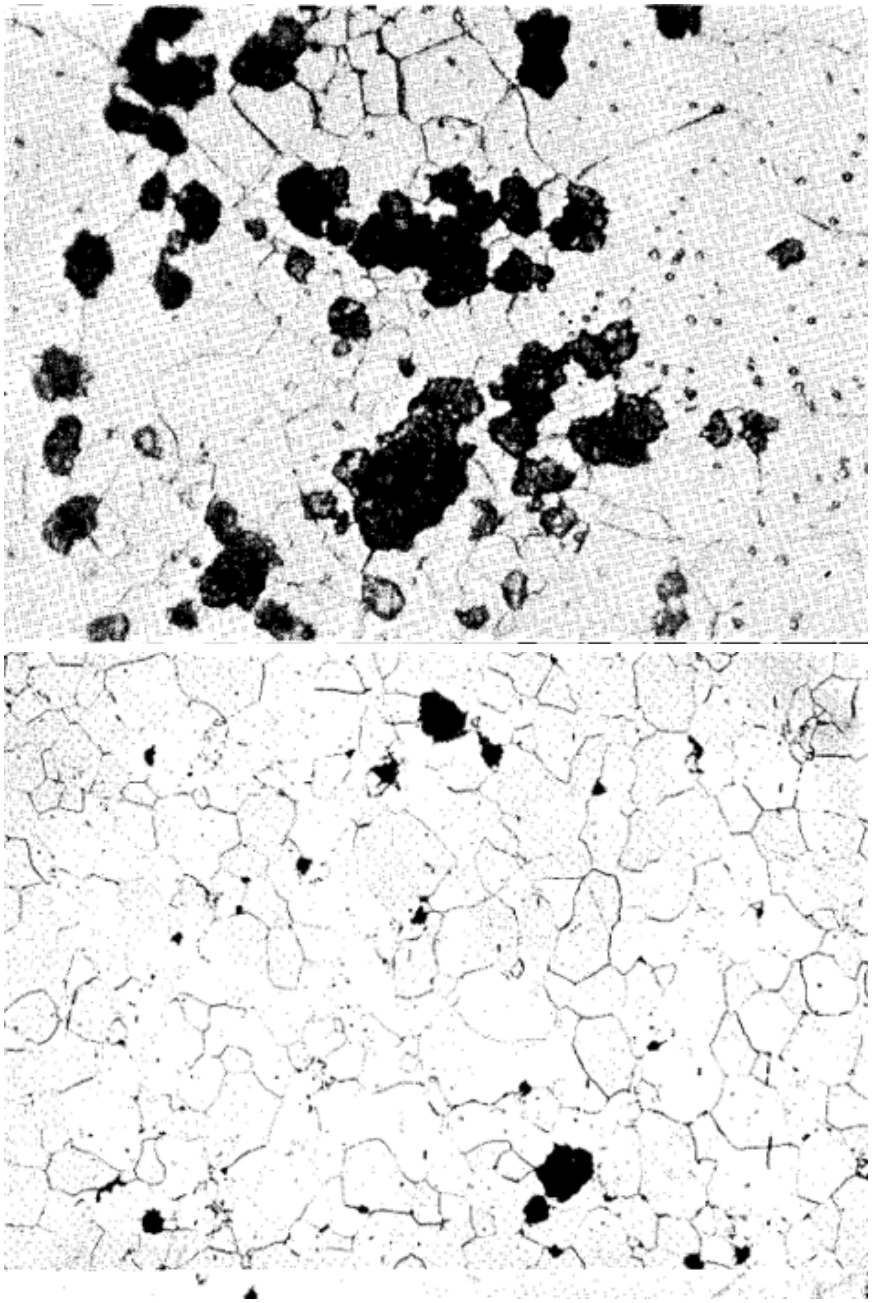


Figure 9. Graphitization in carbon steel during a 670°C for 170-hour heat-treatment in 1912[33] (Top) and Graphitization observed during a routine examination of a low-carbon steel tube from petroleum cracking unit (1935) (Bottom)[6].

Graphitization was not given a greater attention and was only an academic interest until 1943 Springdale Power Station failure. In 1943 Springdale Power Station failure at West Penn Power Company sparked interest on graphitization amongst various researchers. C-½ Mo welded pipe in the Springdale Power plant was operating for 5-½ years of service at a temperature 935°F (502°C) and pressure of 1250 psi (8.82 MPa)[7]. A continuous plane of graphite was observed in the base metal on the outer edge the heat-affected zone (HAZ) in Springdale failure during metallurgical examination result[7]. The failure was attributed to the poor steel making practice. After the Springdale failure, every power plant in US was concerned about the serviceability of their component which was operating in the similar temperature and stress range. In August 1943, Edison Electric Institute and Power Generation Company initiated a joint research program to further understand the fundamental causes of graphitization. Over 40 companies assisted in this study by providing samples for investigation of graphitization [2, 7-18]. Six progress report were published by Edison Electric Institute between [35-41] and the study concluded that the high aluminum de-oxidation practice promoted in the occurrence of graphitization. The carbon and carbon-moly steels which were made prior to 1939 were based

on ASTM standards A158, A206, and A280 "Specification for Seamless Ferritic Alloy Steel Pipe for High Temperature Application". These standards required de-oxidation with at least 750 ppm of aluminum (high aluminum grade) and 250 ppm of aluminum (low aluminum grade) in addition to silicon de-oxidation[35]. In June 1944, ASTM in conjunction with ASME initiated another joint research program to further investigate graphitization issues and the requirement of de-oxidation practice. In 1952, ASTM withdrew all the standards A158, A206, and A280 and were replaced by ASTM A335. The mandatory requirements for de-oxidation practice was removed in ASTM A335 and shall be in agreement between the manufacturer and the purchaser.

The graphitization failures with regards to graphitization have been recurring over 60-70 years and been a continued industry concern. Figure 10 shows a macrograph of the C-½ Mo welded pipe from the Springdale Power plant. Graphite nodules were observed in the base metal on the outer end of the HAZ, appeared like "eyebrow" when evaluated macroscopically [7]. White arrows in the macrograph indicate the presence of graphite nodule outside of the visible HAZ.

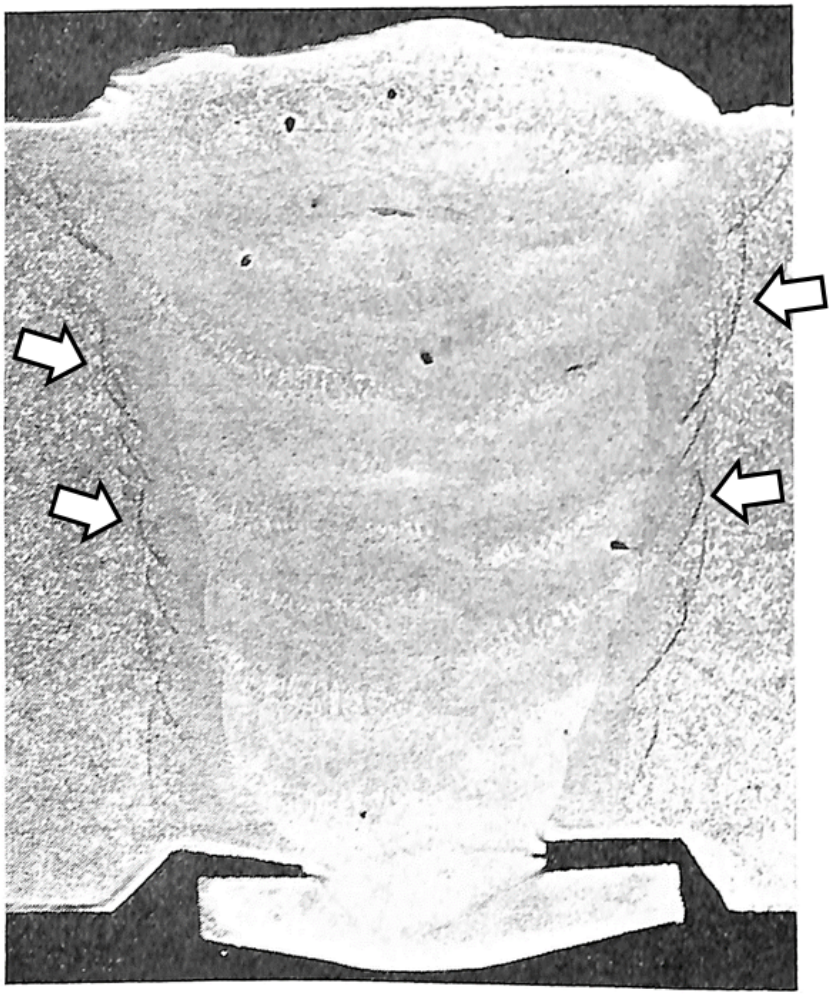


Figure 10. Intergranular graphitization at extremity of HAZ as shown by white arrows (Eyebrow Graphitization) in the base metal which led to the first major graphitization failure at Springdale Power Station in 1943[42].

Table 1 shows the timeline of some of the major graphitization related failures in carbon and carbon-moly steels. Three carbon steel (stainless steel clad) catalytic cracking units failed in 1951; 8-foot-long crack was found to have originated on the outer edge of the heat-affected zone (HAZ). Graphitization was not concluded to be the primary cause of failure but was believed that presence of graphite deteriorated stress-rupture properties [43]. Two other failures due the graphitization were experienced at the Oak Ridge gaseous diffusion plant in 1957 (more than 100,000 hours at 935°F/502°C). These Oak Ridge failures were similar to the Springdale PowerStation failure were also weld related [21]. Planar graphitization was observed in the narrow band region just outside of the HAZ. The next reported graphitization related failure occurred at Pennelec's Williamsburg station in 1977, this incident resulted in 6 casualties [20]. Graphitization in power plants and refineries was a big problem between 1950s-70s, but the move to the higher alloyed Cr-Mo steels has reduced graphitization problems in most of steels in recent times. One of the most recent occurrence with regards to graphitization in steel was in 2011 (C-½ Mo steel) and 2015 (carbon steel)[21, 22].

Table 1. Timeline of major graphitization failures.

Year	Remarks
1935	Carbon denudation and graphitization was observed in carbon-molybdenum steel of a thermal cracking refinery unit after 3 years in service around 900-1000°F [6].
1943	Springdale Power Station Ruptured failure after 5-1/2 years at 935°F, in the girth weld (just outside of the visible HAZ) – Considered the first major failure and all the power plants were proactive in examination for graphitization in their components after this failure [7].
1951	Three Reactors in Catalytic Refining Plant. Failure examination showed presence of graphite but the primary reason of failure was not attributed to graphitization, but the design failures.
1957	Oak Ridge gaseous diffusion plant, failure in the base metal just outside of HAZ, at operating temperature ~ 900°F after more than 100,000 hours (~11 years) in service. Two failures occurred in Sept 4th and 17th both as a result of graphitization [19, 44] .
1977	Pennelec's Williamsburg Station fracture (resulted in 6 death) [20].
2003	Fracture in an outlet pipe of steam generator of power station operating at 896°F, 100,000 hours (~11 years) in service in DIN 15Mo3 alloy steel [23].
2011	C-½ Mo Steel super heater inlet piping rupture after 275,000 hours (~31 years) in service at 830°F (3 other failures in the same plant between 1970 and 2011, but they were not investigated) [6].
2015	Carbon Steel (SA210-A1) Primary Super Heater Tube Fracture of a Boiler (950°F, 1.3 ksi, 96,000 hours in service). This was attributed to the use of wrong SA210-A1 material instead of SA209-T1 material [7].

2.3.2 Effect of De-Oxidation Practice

With regards to graphitization, there is a historical significance that when steels are operated in a certain temperature range, de-oxidation practice (primarily aluminum) has the most influence. However, there has been no profound explanation on why aluminum de-oxidized steels graphitize rather quickly but is only a hypothesis. This has influenced on how people perceive graphitization to date. Aluminum is the most discussed element with regards to graphitization in carbon steels, however its true influence on graphitization is not fully understood [9, 11, 12, 16-18, 45-51]. Aluminum is primarily added as a deoxidizing element along with silicon during the steelmaking process to minimize porosity because of their de-oxidation power and stability of oxides at steelmaking temperatures. Aluminum is generally added as a pure aluminum, because of its low melting point 1220°F (660°C), however silicon 2577°F (1414°C) is added as an eutectic of iron as ferrosilicon 2210°F (1210°C) to lower the melting point and improve fluidity during steelmaking [52, 53]. Apart from being a strong de-oxidizer, aluminum also improves strength of steel by refining grain size. Aluminum combines with nitrogen to form aluminum nitride (AlN) or oxygen to form aluminum oxide (Al_2O_3) to create nucleation sites for austenite grains [54].

$$4Al + 3O_2 = 2Al_2O_3, \Delta G° = -173{,}279 \text{ cal/mol } (-725 \text{ KJ/mol})$$

$$Si + O_2 = SiO_2, \Delta G° = -155{,}354 \text{ cal/mol } (-650 \text{ KJ/mol})$$

$$* \Delta G° \text{ at Typical Steelmaking Temperature}$$

After the 1943 Springdale failure resulting from graphitization[42], researchers from various power plants were proactive in evaluating existing components for the presence of graphitization. Examination of hundreds of samples led various investigators to believe that aluminum-killed steels were more susceptible to graphitization than non-aluminum-killed steels[2, 7-18]. The role of aluminum in the occurrence of graphitization was first investigated by Austin and Fetzer in 1945, who studied eighteen one-percent carbon steels and found that heat treatment in an oxidizing environment increased the tendency for graphitization[9, 45]. Oxygen from the environment can diffuse into the steel and reacts with aluminum in solution to form alumina, which act as nucleation sites for graphitization[9]. The theory on aluminum acting as nucleating agent and the tendency of graphitization increased with the soluble aluminum content rather than aluminum which is tied up as aluminum oxide was later espoused by various other investigators [11, 12, 46, 49, 50]. In addition, Kerr and Eberle examined over eighty service-exposed carbon and C-Mo materials and observed increased

amount of graphitization in aluminum de-oxidized steels[9, 40]. They proposed that graphite nucleated around oxides, nitrides, or sulfides of aluminum or other elements, although this was not experimentally determined[12, 46]. An irregular form (not spherical) of graphite nucleating from an aluminum nitride particle was observed by He. et al in a carbon steel with 0.38 wt.% C, 1.44 wt.% Al, and 1.82 wt.% Si, when examined using transmission electron microscopy (TEM) but nodular graphite did not show the presence of a nucleating agent [48]. Weaver[16] and Smith[55] compared the effect of de-oxidation practice (using different levels of aluminum and silicon) on graphitization and found aluminum-killed steels were more susceptible compared to silicon-killed. However, Wilder observed mixed behavior regarding the effect of aluminum de-oxidation practice for the occurrence of graphitization, graphitization was not observed in steels without any de-oxidation practice but found on some instances that aluminum de-oxidized steels highly resistant to graphitization[18]. Investigators have reported graphitization in steels with different levels of aluminum (see Table 2), and thus the actual threshold amount of aluminum which results in the occurrence of graphitization is controversial.

Table 2. Reported threshold amount for aluminum content for occurrence of graphitization in carbon and C-Mo steels.

Investigator(s)	**Materials**	**Threshold Amount of Aluminum for Occurrence of Graphitization**
Blumberg[7]	carbon steels	Graphitization when greater than 1000 ppm No graphitization when present less than 250 ppm
Austin/Fetzer[9]	carbon and C-Mo steels	Graphitization occurs when greater than 750 ppm No graphitization when present less than 250 ppm
Kerr/Eberle[13]	80 carbon and C-Mo steels	Steel susceptible to graphitization when Al-deoxidized None when less than 250 ppm
A. White[17]	carbon steel	500-750 ppm None when less than 250 ppm for CS and C-Mo
G.V. Smith[18]	carbon steel	500 pm
Smith/ MacMillan/Dulis[51]	carbon steel	None when less than 250 ppm for CS and C-Mo
J.G. Wilson (API Research) [56]	250 carbon and C-Mo steels	160 ppm

The observations on aluminum being a "graphitizer" have been based solely on empirical observations using metallography to determine the presence of graphite and chemical analysis for aluminum content. No clear observations of graphite nodules nucleating from aluminum oxide/nitride particles have been observed. Some of the early theories proposed by various investigators [9, 11, 12, 16-18, 45-51] with regards to the effect of aluminum on graphitization are:

1. Al_2O_3 or AlN act as heterogeneous nucleation sites for graphitization.

2. Aluminum present in ferrite solid-solution is more potent for graphitization than insoluble aluminum.

    a. Aluminum in solid-solution reacts with oxygen diffused from the service-environment to form Al_2O_3, which segregates to grain boundaries to act as nucleating agent for graphitization.

However, these conclusions have been primarily empirical and the theories on aluminum acting as a nucleating agent have not been experimentally supported.

2.3.3 Weld Related Graphitization

Apart from the influence of aluminum on the occurrence of graphitization, the other topic which have been thoroughly discussed with regards to graphitization is "*weld related graphitization*". This form of graphitization has been extensively discussed in the literature[2, 7, 9, 16, 19, 20, 44, 57]. Weld related graphitization is considered to be the most detrimental and the most frequently occurring form of graphitization. Most of the major failures attributed to graphitization are associated with weld related graphitization. In graphitization of this type, graphite nodules are aligned in a narrow band in the base metal immediately outside of the optically visible heat-affected zone (HAZ). The alignment of graphite nodules results in the formation of a "plane of an embrittlement" through which cracks may readily propagate [58]. Figure 11 shows a micrograph illustrating an example of weld related graphitization in carbon steel. Graphitization in Figure 11 was observed after 17 years of service at a steam temperature of 800°F(427°C). Note that the graphite nodules are aligned in a base metal region immediately outside of the optically visible HAZ. This region of the HAZ is called subcritical heat-affected zone (SCHAZ)

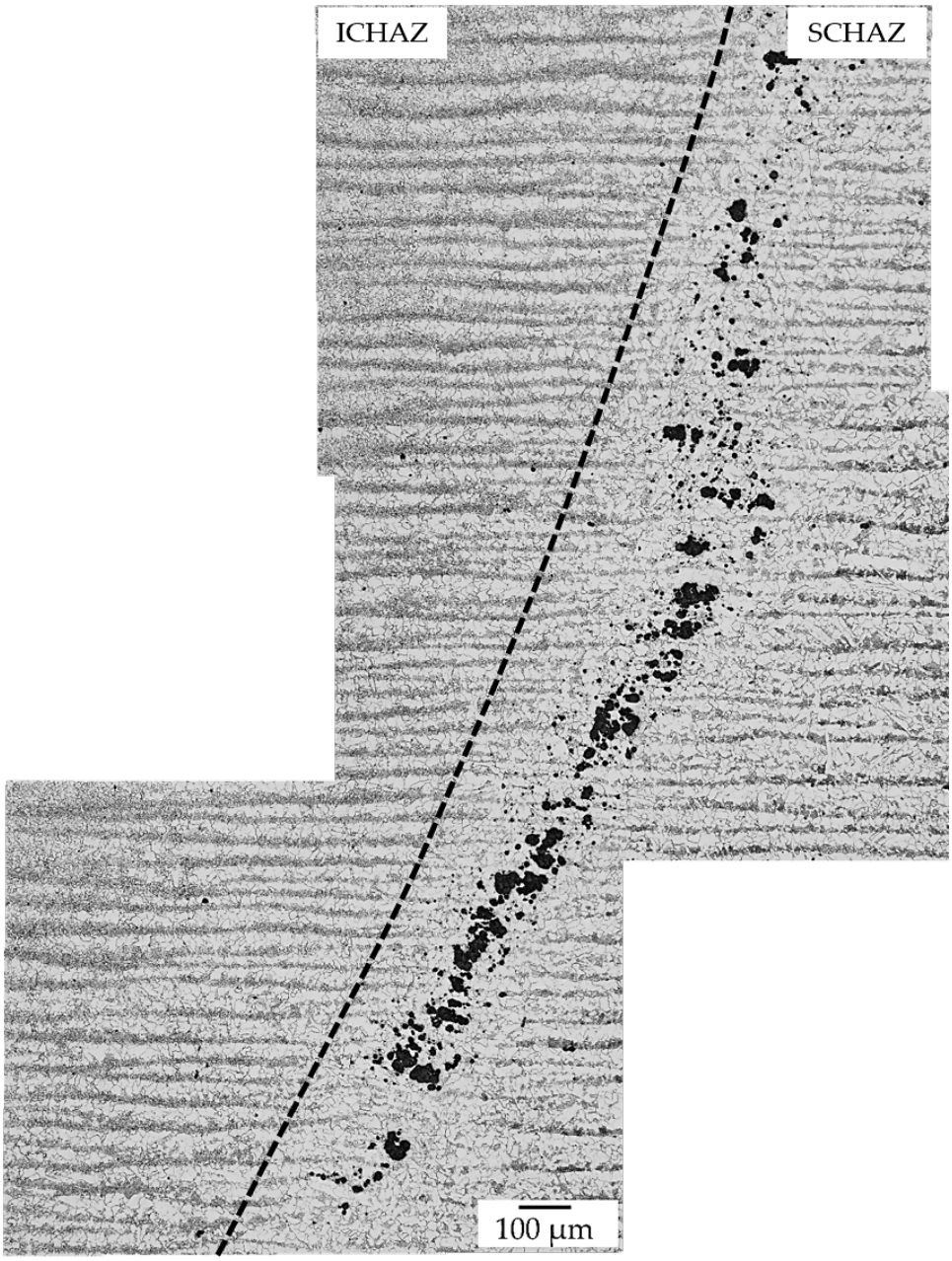


Figure 11. Example of planar/chain type *"weld related graphitization"* observed just outside of the optically visible HAZ in carbon steel after 17 years of service at 800°F (427°C). Dashed line indicates the transition between the end of the optically visible HAZ and the base metal, 2% Nital etch. Decarburization in the areas adjacent to graphite nodules is evident.

The SCHAZ does not exhibit any optically discernible microstructural difference when compared to the unaffected base metal region remote from the HAZ (apart from the presence of graphite). The occurrence of graphitization in the SCHAZ is associated to specific peak temperatures during weld thermal cycle. For a clear understanding of weld related graphitization, it is critical to review all pertinent thermal cycles experienced by different HAZ regions. The HAZ is the portion of the base metal which is not melted during welding, but exhibits microstructural changes due to the weld thermal cycle. Figure 12 schematically shows peak temperatures experienced by different HAZ regions, in conjunction with the iron-iron carbide (Fe- Fe_3C) metastable phase diagram [59]. Depending upon the peak temperature experienced during welding, the HAZ is divided into four principal regions: coarse-grained HAZ (CGHAZ), fine-grained HAZ (FGHAZ), intercritical HAZ (ICHAZ) and subcritical HAZ (SCHAZ).

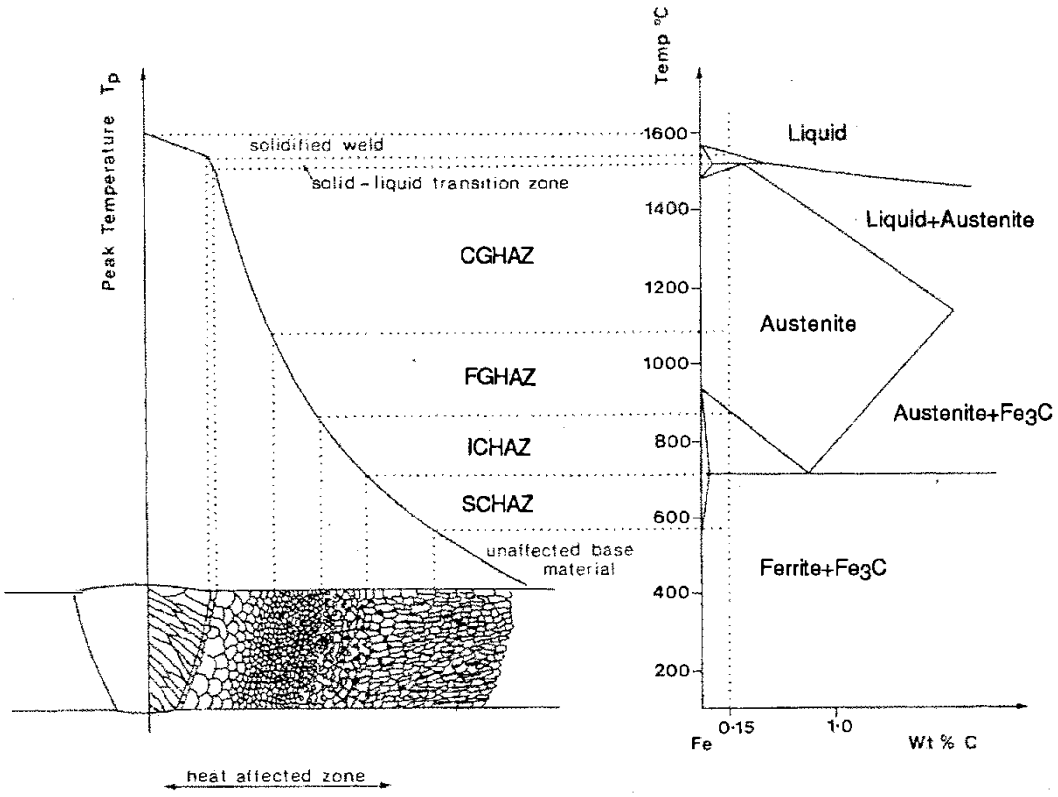


Figure 12. Schematic diagram showing the various regions of the HAZ corresponding to carbon steel with 0.15 wt.% C indicated on the Fe-Fe_3C equilibrium phase diagram [59].

These HAZ regions are typically defined by the following peak temperature ranges during welding.

CGHAZ	1100°C – Melting Point
FGHAZ	Ac_3 – 1100°C
ICHAZ	Ac_1 – Ac_3
SCHAZ	Below Ac_1

Ac_1 and Ac_3 correspond to the lower and upper critical transformation temperatures, respectively upon heating. The Ac_1 and Ac_3 transformation temperatures are higher than the equilibrium transformation temperatures (Ae_1 and Ae_3) because of the rapid heating rates during welding. Thus, the transformation temperatures shown in conjunction with the distribution of peak temperatures in Figure 12 are only for illustration purposes and are not exact for welding conditions (i.e. non-equilibrium heating/cooling). Figure 13 shows a composite of optical micrographs obtained at 50X showing various regions of the HAZ for a 0.2 wt.% carbon steel. Higher magnification optical micrographs at 100X of four pertinent regions of the HAZ are also shown in Figure 13.

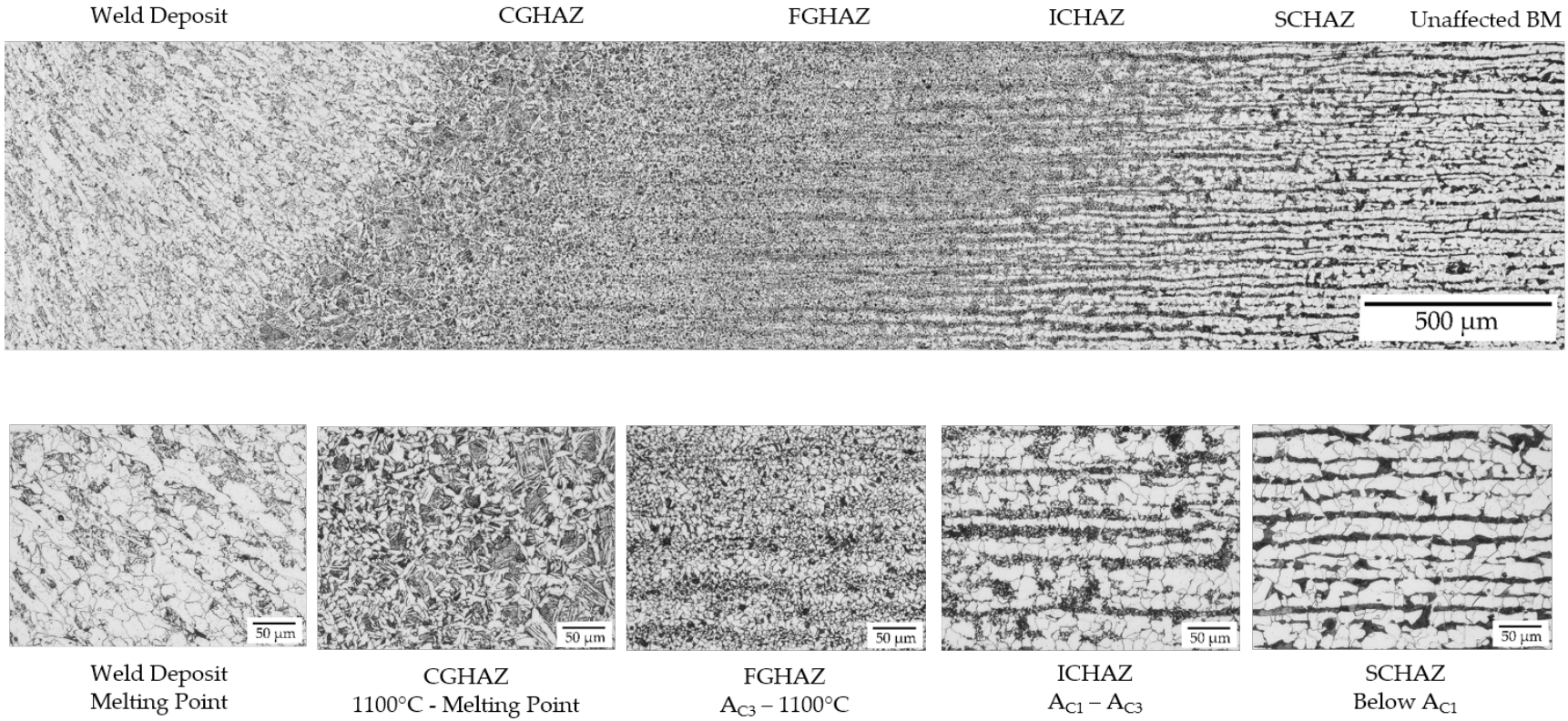


Figure 13. Composite of optical micrographs (50X) and individual optical micrographs (100X) showing various regions of the HAZ of a 0.2 wt.% carbon steel, 2% Nital etch.

The SCHAZ region, which readily graphitizes, exhibits no optically discernible microstructural difference compared to the base metal region remote from the HAZ, which is unaffected during welding. With regards to the peak temperature experienced by the SCHAZ, various researchers have espoused different opinions. Some of the researchers believe that the region most susceptible to graphitization (SCHAZ) is above the lower critical transformation temperature (Ac_1), however some investigators have proposed this region to be below the Ac_1 temperature [2, 4, 10, 26, 58, 60-64]. Table 3 shows some of the early opinions with regards to the peak temperatures of the most readily graphitized region associated with welding.

Table 3. Previous reported temperature ranges for the most graphitized region of the HAZ [2, 7, 11, 24, 56, 58-62].

Investigators	**Suggested Peak Temperature for Most Graphitized Region Related to Weld HAZ**
Emerson (1945) [10]	1350°F-1400°F
Eberle (1946) [60]	1300°F-1400°F
Thielsch (1954) [58]	1325°F-1425°F
Port (1989) [4, 26]	*Above the lower critical transformation temperature*
Foulds (2001, 2015) [61, 63, 64]	*Above the lower critical transformation temperature*

In a multi-pass weld, graphite nodules have also been observed to align in the base metal along the outer boundary of the weld HAZ through the entire cross sections which appear as an "eyebrow" macroscopically and optically. This type of graphitization has been termed as "eyebrow" graphitization. An illustration of this form of graphitization is shown in Figure 14[10]. The aligned nature of graphitization (eyebrow) results from a weld thermal cycle of constant temperature at that location. Some of the early investigators have suggested, in SCHAZ interstitial elements (especially carbon and nitrogen) diffuse during welding [57, 58, 62, 63]. When cooled these elements may result in the formation of unstable carbides and carbon enriched alpha solid-solution, which precipitate as graphite when exposed to elevated temperature [58, 59, 63, 64].

In the current investigation, a through approach to obtain mechanistic view of the weld related graphitization was performed. A hypothesis to support the increased amount of graphitization observed in the SCHAZ is proposed in this study from a fine-scale microstructure and compositional variation standpoint during welding. The peak temperature with regards to the most graphitized region of the HAZ was also investigated in the current study.

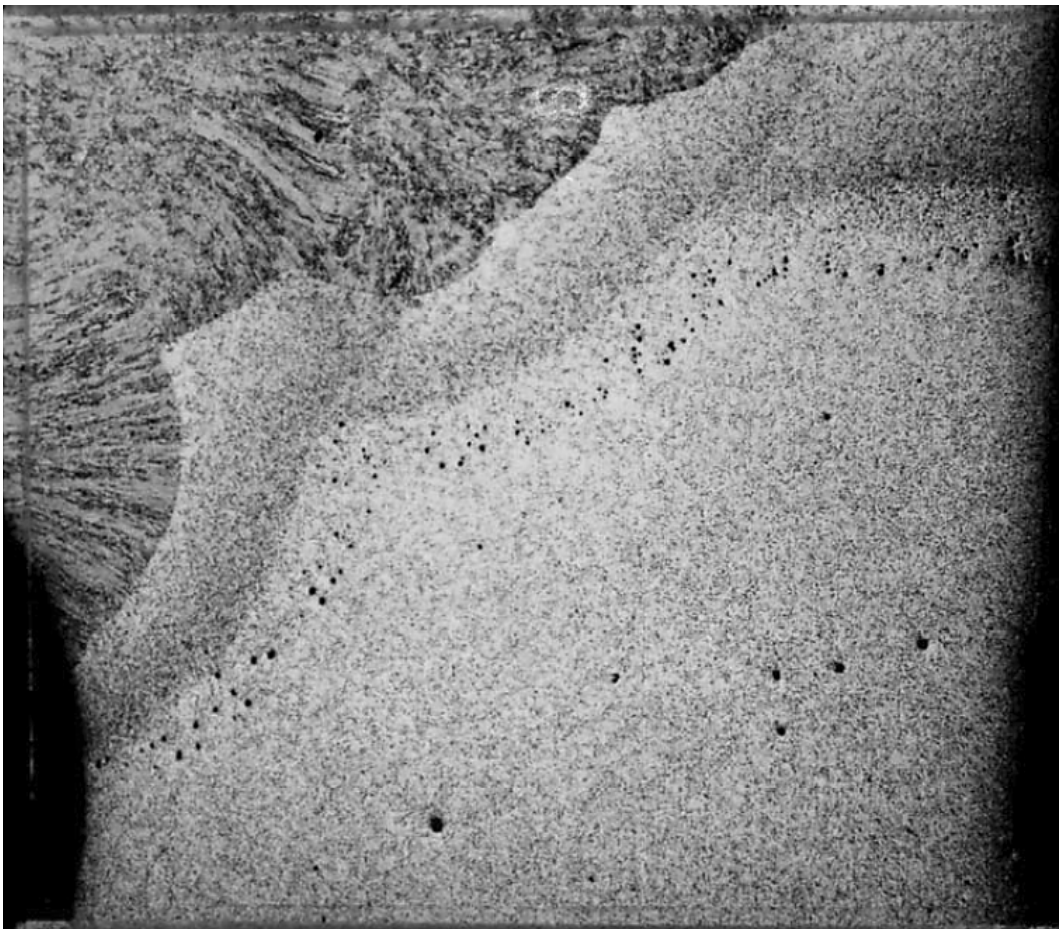


Figure 14. Carbon steel weldment showing evidence of a moderate level of graphitization just outside of the HAZ[64].

2.4 Factors Influencing Graphitization

The occurrence and degree of graphitization in steels is influenced by various metallurgical factors, such as temperature, stress, chemical composition, welding, etc. Certain steels have greater tendency to graphitize compared to the others under the same operating conditions. Thus, it is critical to consider each of these factors and discuss thoroughly their influence on graphitization:

2.4.1 Effect of Service Conditions

Graphitization in steels is a result of the phase transformation of metastable iron-carbide (Fe_3C) to form stable iron and graphite (C) structure during elevated temperature exposure. The solid-state transformation during graphitization is a diffusional process and the rate of transformation increases exponentially with an increase of temperature. Based on Arrhenius equation below, the reaction rate for a solid-state transformation is given by Equation 6.

$$\text{Reaction Rate} = C\, e^{-Q/RT} \qquad \text{Equation 6}$$

Where, C = Temperature Independent Constant

Q = Activation Energy

R = Universal Gas Constant

T = Absolute Temperature

The reaction rate for transformation is approximately doubled when temperature is increased by 10C° (18F°). Diffusivity of carbon in ferrite and austenite increases with an increase of temperature, as shown in Figure 15[65]. Tendency for steels to graphitize increases with an increase of temperature. Studies by Wilson showed that the rate of graphitization increased significantly when the temperature was greater than 1000°F (538°C). However, the location of graphitization was not influenced by the increase of temperature [56]. As discussed in the literature review section 2.2, the change in free energy for cementite decomposition to form iron and graphite (Figure 7) increases with the increase of temperature and reaches a local minimum at a temperature of 1050°F (566°C). The graphitization rate decreases when the temperature is higher than 1050°F (566°C) and the spheroidization rate increases (see Figure 8). Graphite does not nucleate when the temperature is above the lower critical transformation temperature (Ae_1), unless prior graphite nuclei is present [66].

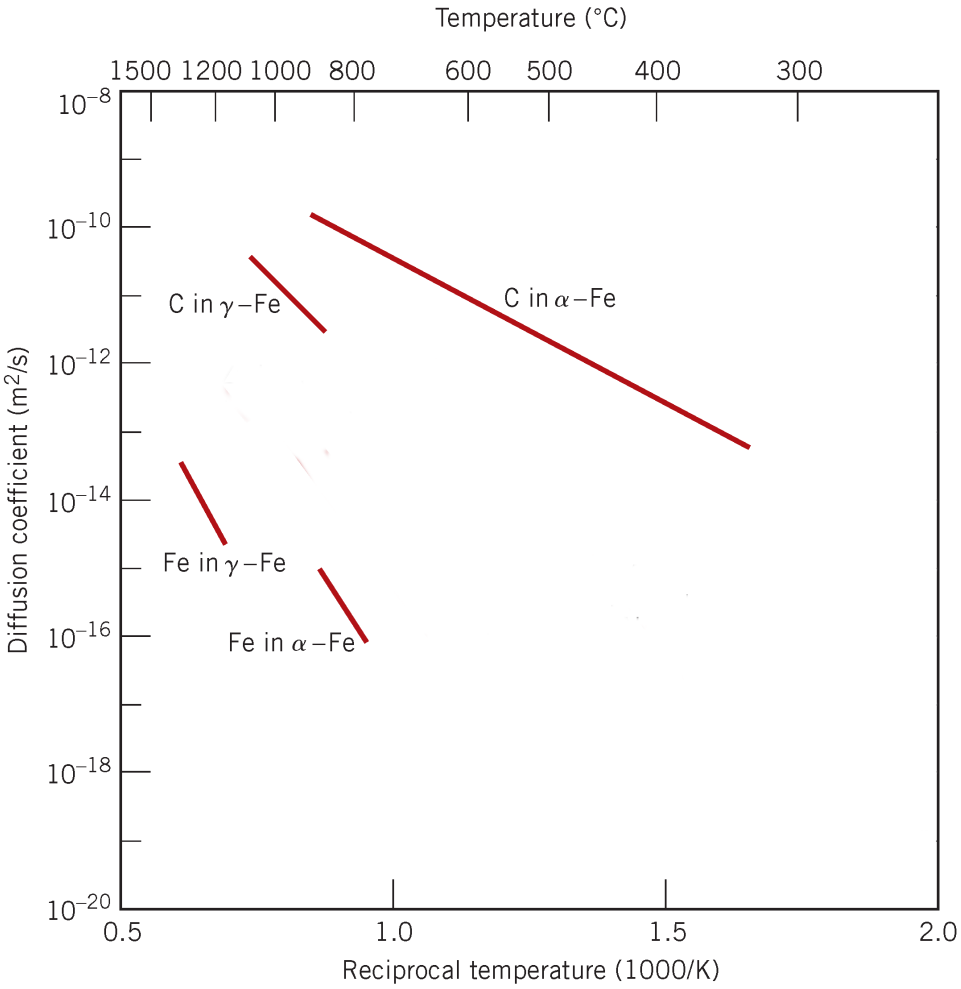


Figure 15. Logarithm plot of diffusion coefficient versus reciprocal of absolute temperature (K) [65].

2.4.2 Effect of Alloying Elements

Various studies have been performed to examine the effect of alloying elements on graphitization susceptibility of steels [1-23]. Influence of the major alloying elements on steels and their tendency to cause graphitization is discussed below:

Aluminum

Aluminum is probably the most discussed element with regards to graphitization in carbon steels and its influence with regards to graphitization in steel is already been discussed in section 2.4.2.

Silicon

Silicon, similarly to aluminum is also added in steels as a deoxidizing element. Silicon-killed steels were found to be less susceptible to graphitization than aluminum-killed steels by multiple researchers [12, 16, 67]. Weisberg in his study showed that the graphitization in silicon-killed steel was not segregated in heat-affected zone of the C-½ Mo steel [8]. Kerr and Eberle in their investigation did not observe any evidence of graphitization when steel was silicon-killed but observed when steel was aluminum killed [12]. Weaver in his investigation of

deoxidized steels reported silicon-killed steels appeared to graphitize slower than the aluminum-killed steel in a 0.15 wt. % C under the same operating conditions. This is shown in Figure 16 below.

Carbon

The tendency of steels to graphitize increases with an increase of carbon content[2, 11, 15, 68]. Carbon is primarily present as iron carbides (Fe_3C), in carbon and low-alloy steels, and is available in low concentration in ferrite. The solubility of carbon in alpha-ferrite is ~0.025 wt. % (see Fe-C phase diagram, Figure 12).

Molybdenum

Addition of molybdenum improves carbon stability by lowering the free energy of cementite thus reduces propensity for graphitization. Smith and Brambir, in their study of end-quenched carbon and carbon-molybdenum steel [2], were able to graphitize at the same time when both of these steels were under same conditions.

Chromium

Although present in relatively low level in carbon and carbon-molybdenum steel, chromium is believed to retard/prevent graphitization

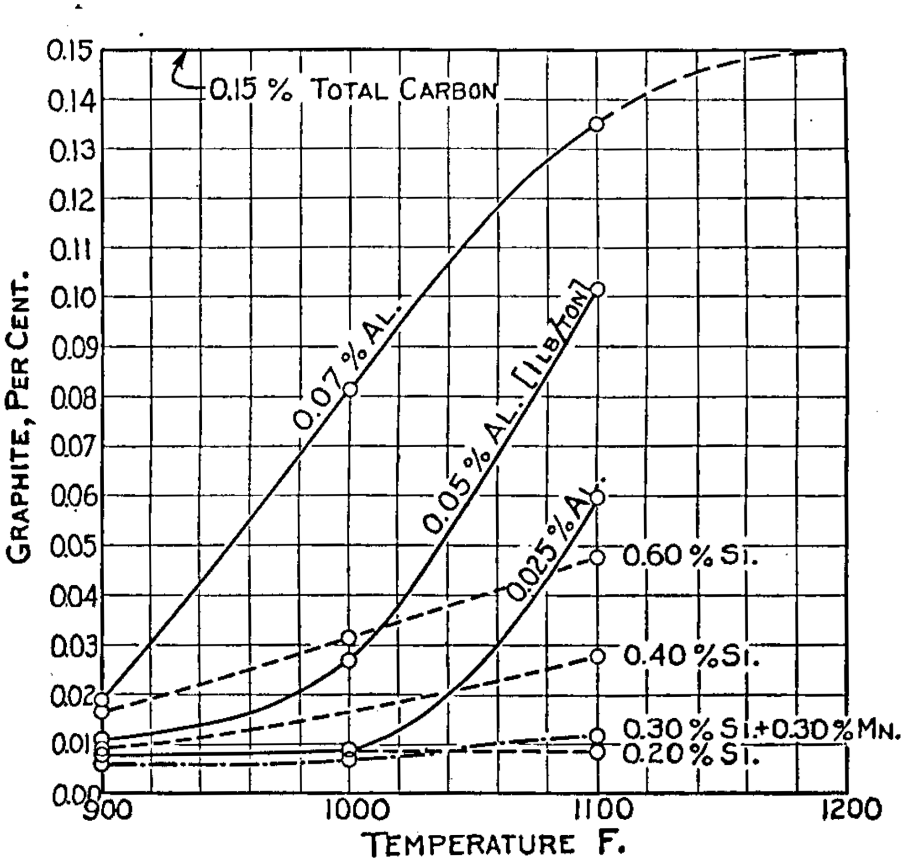


Figure 16. Effect of de-oxidation practice on growth of graphite nodules as a function of temperature after 300 hours in 0.15 % carbon steel[16].

susceptibility with improving carbide stability for elevated temperature service. Various investigations of chromium containing steels from 0.7 wt. % to 2 wt. %, showed no evidence of graphitization in examination of both laboratory and ex-service components [2, 67, 69, 70]. Graphitization was observed by few researchers when chromium content was 0.5 wt. % or lower [68, 71]. However, graphite was only observed in the steel with finer grain size when chromium content was 0.25 wt. % [71]. Thus, it was not conclusive whether the presence of graphitization was a result of lower chromium content or a de-oxidation practice [71].

2.4.3 Effect of Prior Thermal Treatment

Normalizing heat-treatment at relatively higher temperatures which result in an increase of austenite grain size showed the presence of chain type graphitization. When steel was normalized at a lower temperature which resulted in pearlitic microstructure caused formation of random and isolated graphite nodules [10, 72]. However, it was reported by Smith et. al. that when steels were normalized at higher temperature, its reduced to form graphitization was reduced [2, 60]. Slower cooling in C-½ Mo steels resulting in bainitic microstructure are more prone to graphitization than faster cooling, which resulted in

martensitic structure. However, it was found opposite for carbon steel, martensitic structure was found to be more susceptible to graphitization.

2.4.4 Effect of Welding Conditions

Welding perhaps has the most significant effect on the occurrence of graphitization. The region of the base metal heat-affected zone (HAZ) which is exposed to a peak temperature just below the lower critical transformation (Ac_1) has been found to be the most susceptible to graphitization. However, there has been a mixed-view with regards to the exact peak temperature of this region during welding. The localized graphitization susceptibility increased when the heat-input was increased (steeper temperature gradient)[9]. Postweld heat treatment (PWHT) reduced tendency for C-½ Mo steels to graphitize, 1300°F (704°C) for 4 hours was recommended for optimum performance[9]. Other studies also showed 1400°F (760°C) PWHT improved graphitization susceptibility[14, 37, 42, 70]. The materials under investigation in this study are carbon steels, which are generally not given a postweld heat-treatment subsequent to the weld (as it is not mandated by ASME boiler and pressure vessel code).

2.4.5 Effect of Stress, Cold-Working and Deformation

It has been reported in previous investigations that stress or plastic deformation accelerates graphitization. However, no conclusive evidence has been reported and this has not been confirmed in laboratory experiments. Hoyt's in his investigation reported that stress accelerates graphitization but the effect of stress was not attributed be the primary cause for graphitization in steels [11]. It was only attributed to increase the extent of graphitization.

2.4.6 Effect of Grain-size

The susceptibility of graphitization in steel increases with the finer-grain size, as a result of increased diffusion path during elevated temperature exposure. However, fine-grained heat-affected zone is generally not the most graphitization susceptible region of a weldment. Thus, the effect of fine grain on the occurrence/susceptibility of graphitization is only a secondary one. Aluminum, apart from acting as a deoxidizing agent, it is also used a grain-refiner. Aluminum reacts with oxygen or nitrogen to form aluminum oxide or aluminum nitride (Al_2O_3 or AlN), which segregate to grain boundaries and restricts the austenite grain-growth. The early investigation on effect of grain-size on graphitization has been fairly inconclusive. The investigators were

unsure if the increased amount of graphitization on fine-grained steel was a result of fine-grain size or the presence of Al_2O_3 or AlN, which acted as heterogeneous nucleation sites for graphite nodules [9, 60].

2.5 Kinetics of Graphitization

Graphitization is a result of solid-state transformation of metastable cementite (Fe_3C) to form an equilibrium iron and graphite structure as shown by equation below.

$$Fe_3C \rightarrow 3Fe + C$$

The overall transformation involves a sequential processes of dissolution of cementite, diffusion of carbon, formation of graphite nuclei, and graphite growth[66]. The overall kinetics of transformation can be divided into two stages: nucleation and growth. Graphite nodules nucleate on preferred nucleation sites such as grain boundaries, dislocation defects, or inclusion-matrix interfaces. The nucleation rate (N°) is driven by an availability of free carbon, carbon activity, and total number of nucleation sites. The ferrite-cementite interface was found to be an easy nucleation site for graphite nodules. Once graphite nuclei reach a critical size, nucleation stage is followed by nodule growth step. A critical nucleus size was reported to be 4.1 Å by Tkachenko [63].

After initial incubation stage, nucleation and growth stages occur simultaneously, i.e. new graphite nodule nucleates when previously nucleated nodules continue to grow. The growth occurs by long range atomic diffusion of carbon atoms primarily through grain boundaries and also through matrix to nuclei. Growth is a diffusion controlled process is influenced by temperature, by an Arrhenius type equation (shown below)[73]. C is temperature independent pre-exponential constant, Q is activation energy, and R is gas constant.

$$\dot{G} = C\, e^{-Q/RT}$$

The overall solid-state transformation including nucleation and growth stages is shown in Figure 17[73]. The growth rate which is primarily diffusion controlled increases exponentially with an increase of temperature. The reaction rate is approximately doubled when the temperature is increased by 10C° (18F°). The rate of nucleation and growth of graphite nodules was measured by Brown [74] using polished and etched specimens. Fraction transformed showed a typical Avrami-type sigmoidal (S-shaped) type curve equation (shown below). A typical transformation plot is shown in Figure 18 [74].

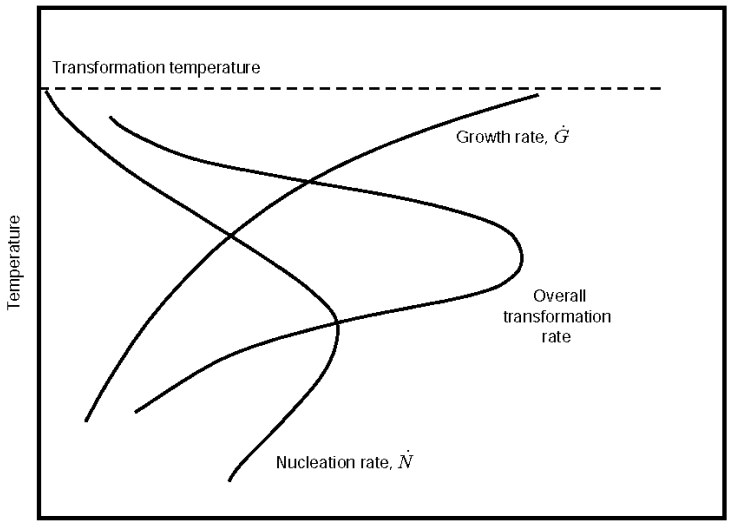


Figure 17. Overall solid-state transformation kinetics[73].

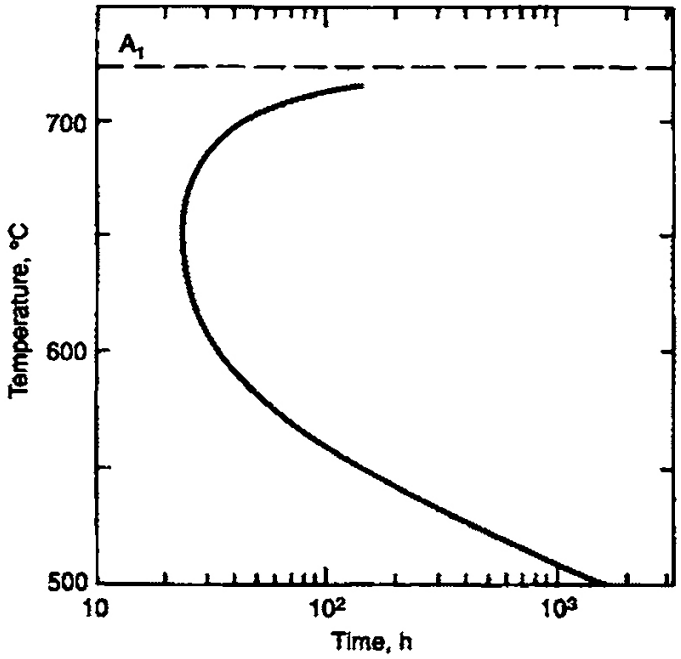


Figure 18. Isothermal time-temperature transformation curve for graphitization in a carbon steel (1 wt. % carbon). Times for 28.5% of carbon to transform to graphite [74].

2.6 Graphitization Rehabilitation Program

The complement replacement of a graphitized component is economically an unviable option. Thus, various rehabilitation programs has been studied on graphitized components by various researchers [19, 24, 58, 75]. The most commonly used rehabilitation methods employed were: 1) Re-austenitizing heat treatment, 2) Removal of graphitized region of the component followed by repair welding of the removal site using arc welding, and 3) Replacement of the graphitized component.

1. **Re-austenitizing Heat-Treatment (or Solution Treatment)**:

In this process, the graphitized region of the component is locally heated above the critical transformation temperature (Ac_3) is hold for an amount to time to allow graphite to go back to austenite solid-solution (γ_{ss}). Generally the graphitized region was heated to austenitizing temperature of 1700-1750°F (927-954°C) for 4 hours. This method was succesfuly employed by various investigators as it was cheaper and easier but was only considered to be a temporary cure [58, 75]. Oak Ridge steam lines graphitization was rehabilitated temporarily performing austenitization treatment at 1750°F (954°C) for 2 hours[19].

Re-austenitizing treatment left behind small voids in the previously graphitized region and which acted as nucleations sites for graphite when the components are placed back in service [58, 76]. Rehabilitated components in the Oak Ridge steam line which was replaced with 1-¼ Cr - ½ Mo [19]. Thielsch stated that this method did not improve ductility/toughness of the material but instead weakned the material [58].

2. **Removal of Graphitized Region**:

In this method, the graphitized region of the component is excavated out and the removal site was repair welded using welding process. This dissertation discusses friction hydro pillar processing (friction-welding), which has been used for repair welding of the excavated site. This is discussed in later in the Weldcore® section.

3. **Replacement of the Graphitized Component**:

In this method, the graphitized component is entirely removed and replaced by virgin material. Generally the replacement is performed using the higher alloyed material than previously used to minimize the re-occurance of graphite. The selection of the rebilitation program was determined by the

severety of graphtiization, estimated remaining life, and operating conditions. Thielsch based on the degree of graphitization (shown in Table 4) recommended rehabilitation senario for a hypothetical installation, as shown in Table 5.

2.7 Weldcore® Technology

The prediction of remaining life assessment is important for the continuation of the component in service in both power plants and petroleum refineries. The various in situ non-destructive (ultrasonic inspection or surface-replication) and destructive (boat samples) examination methods have been employed in past to predict extent of various service-related damage like creep, graphitization, HTHA, or cracking. However, the examination of samples using surface replica metallography assumes that the damage is uniform through the pipe/plate wall and, thus, may not be an exact representative of non-uniform through-wall damage. The metallurgical sample examination process by boat sample is difficult which requires repair welding of the boat sample extraction site which has been found challenging [77]. Thus, a Weldcore® technology; a combination of sample extraction followed by the friction hydro pillar processing (FHPP) repair.

Table 4. Microstructures showing various degrees of graphitization in the HAZ of carbon steel [58].

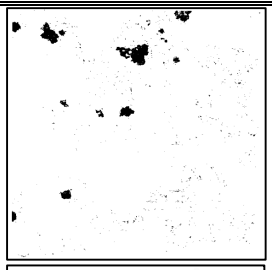
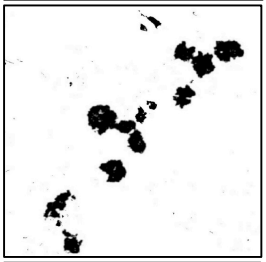
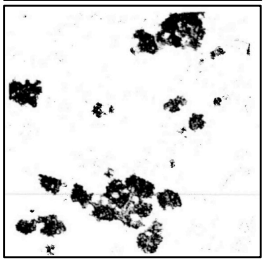
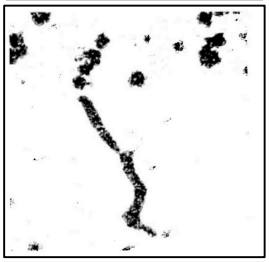
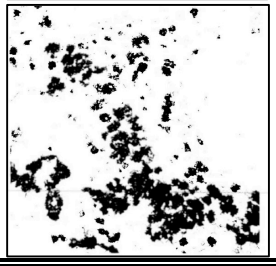
Extent of Graphitization	Micrograph (250X)
Mild	
Moderate	
Heavy	
Severe	
Extremely Severe	

Table 5. Recommended rehabilitation example on a hypothetical installation of a carbon steel component by Thielsch [58].

Operating Parameters	
Total Operation	100,000 hours
Expected Future Operation	150,000 hours
Operating Temperature/Pressure	890°-915°F and 970-980 psi.
Shut-downs	2 per year
Conditions for Severe Thermal Shock	Negligible
Exposure to Mechanical Vibrations	Negligible
Degree of Graphitization (See Table 4)	**Recommended Rehabilitation**
None	Take another weld-probe specimen after 20000 - 30000 hours of service.
Mild	Take another weld-probe specimen after 8000 - 10000 hours of service.
Moderate	Gouge out (partially) heat-affected zone and repair weld the extracted site.
Heavy	Gouge out (completely) heat-affected zone and repair weld the extracted site.
Severe	Replace respective piping or valve material at next scheduled shutdown and check affected materials for cracks.
Extremely Severe	Present condition of material extremely hazardous. Check for cracks, make immediate repairs and replace materials as soon as replacement sections can be obtained.

Notes: ASTM A206, 1000 ppm of aluminum, 1.3″ wall, 12-3/4″ OD

This technique was developed by Nelson Mandela Metropolitan University (NMMU) researchers and this technique allows extraction of larger sized samples consisting of majority of the component wall and is an efficient repair process [77, 78]. The Weldcore® technique has allowed more thorough investigation of in service components to make run, repair, or retire decisions.

The Weldcore® methodology utilizes two steps: 1) Core Sample Extraction for Metallurgical Characterization and 2) Repair Welding Process using FHPP.

Sample/Core Extraction

The first step of the core extraction is to identify the location of an interest for metallurgical examination and mechanical testing. A core sample (7-10 mm) in diameter is generally extracted for the area of interest. The length of the extracted core depends upon the wall-thickness of the component. The extracted core generally contains approximately 60% of the wall-thickness [79]. The core extraction process involves four stages, which requires four specially designed tools as shown in Figure 19 [78].

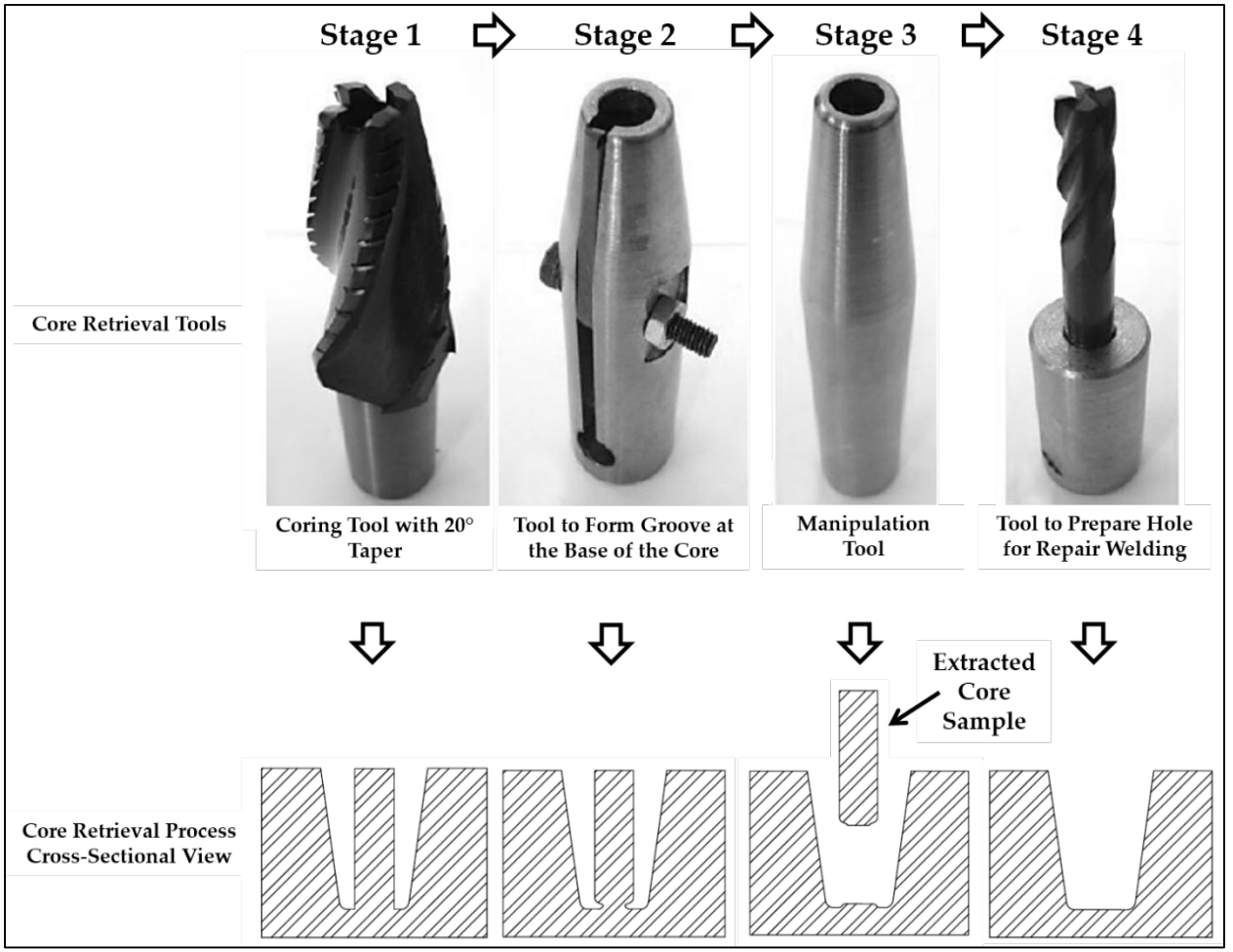


Figure 19. Photograph showing core retrieval tools [78] (Top) and sketch showing the cross-sectional view of the core retrieval process (Bottom).

Tool 1 is utilized for initial coring operation with 20 degrees taper. Tool 2 is a custom designed tool, which is inserted in the core to form a groove (undercut) at the bottom of the core. Tool 3 is utilized to perform manipulation and remove the core manually from the hole. Tool 4 is utilized to provide smooth finish to the hole for subsequent repair welding process. The cross-sectional view of each of the four stages of the core extraction process is shown in Figure 19 [78].

Repair Process

The core extraction site was subsequently repaired using friction tapered hydro pillar processing (FTHPP). FTHPP is one of the variant of friction welding process which utilizes the rotating motion of one component against another to produce a frictional heat to produce solid state bonding. FHPP was developed and patented by The British Welding Institute (TWI) in 1991 [80]. Since, the development of this method, various studies have been performed to understand and improve the characteristic of the finished weld and has been successfully employed by various researchers on various ferrous and non-ferrous alloys. This method is also called drill and fill method [80]. The FTHPP weld is produced by rotating a consumable tool concentrically inside a drilled hole while applying the

downward force to generate a frictional heat along the faying surface, which forms a solid-state bonding with the parent material [77-81]. The drilled hole can either be parallel or tapered to the consumable rod utilized to fill the hole. The FHPP process which utilizes a tapered hole is called friction tapered hydro pillar processing (FTHPP) [80, 82]. The tapered consumable tool used is smaller in diameter than the tapered hole in order to maintain the clearance between the tool during welding [78]. Figure 20 (left) shows the cross-sectional view of the typical tool overlaid on top of the tapered hole prior to repair welding. Figure 20 (right) shows the cross-sectional schematic after the FTHPP weld repair is completed. Figure 21 shows the macrograph of a typical FTHPP weld showing good bonding on a X65 pipeline steel [81]. Flash formation as a result of plastic flow of the base material when the upsetting force is applied is also clearly apparent. There are various important parameters critical to the quality of the finished weld (bonding, microstructure, and mechanical properties) relevant to the FTHPP process. Most important parameters are: spindle rotational speed (rpm), downward/axial force (N), and the forging force.

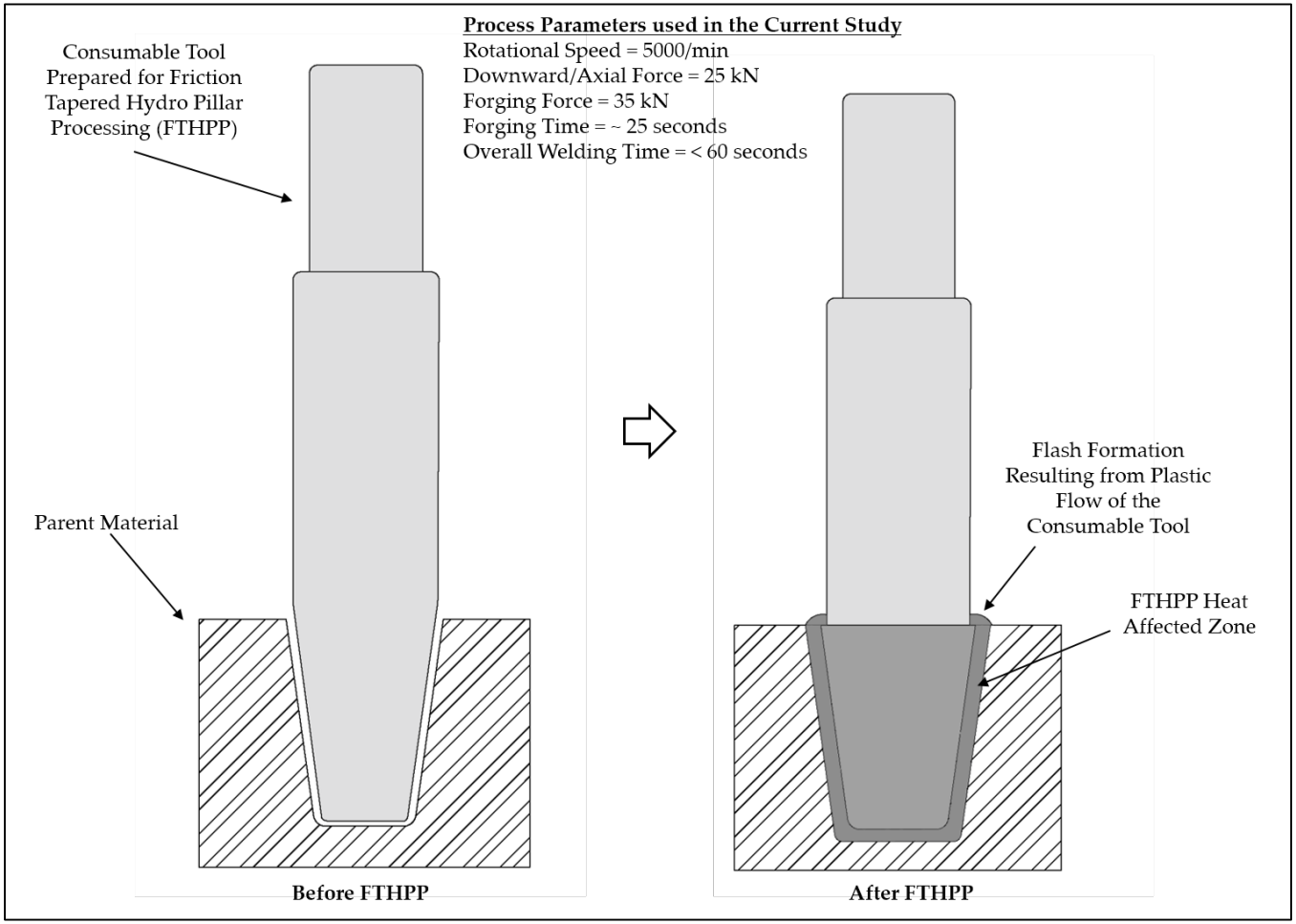


Figure 20. Cross-sectional view showing a set-up for FTHPP welding (before) and after (right). Note that the diameter of the consumable tool machined is smaller than the bored hole.

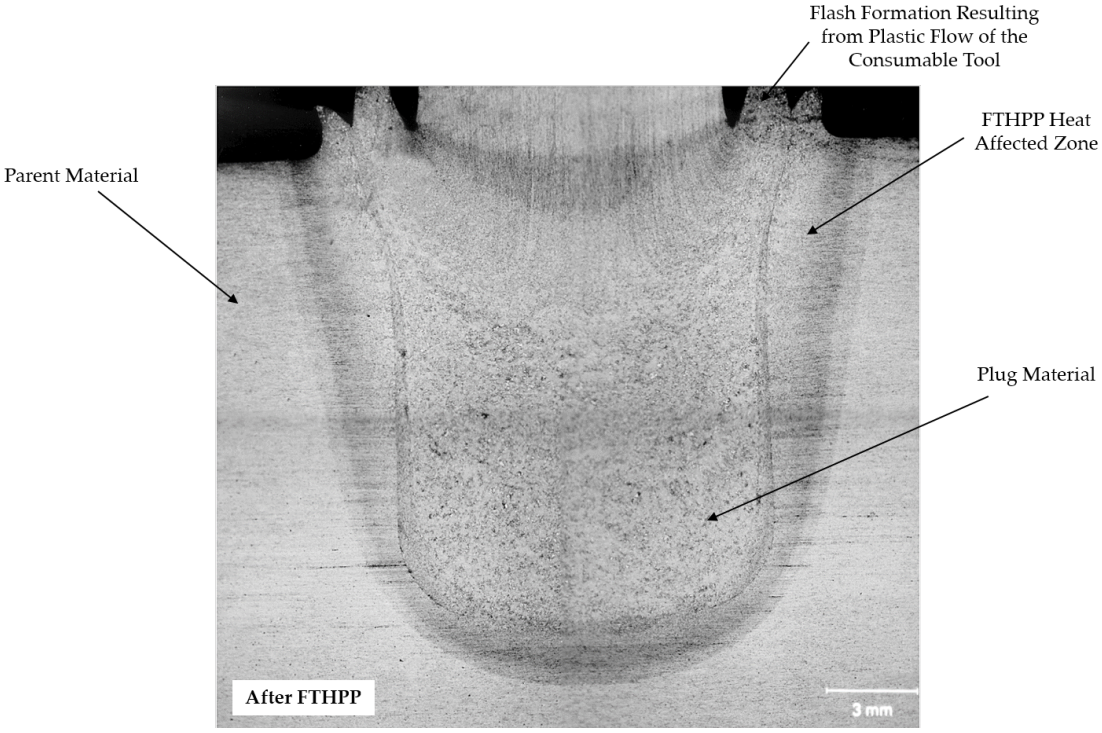


Figure 21. Macrograph of a typical friction tapered hydro pillar processing (FTHPP) weld performed on X65 pipeline steel using 10 mm diameter stud, 3% Nital etch [81].

An extensive research studies have been performed to optimize the FTHPP process parameters by various researchers[77, 80, 81, 83, 84]. In the current study, a rotational speed of 5000 rpm, axial force of 25 kN, forging force of 35 kN was used. Figure 22 shows the plot of the axial load and rotational speed as a function of time.

Although FTHPP is a rapid process and is completed within sixty seconds, the entire process is sub-divided into number of phases [81, 85]. During the first phase, the consumable tool is rotated which comes in contact to the faying surface when an axial load is applied. This phase is also called the "dry friction" phase. During this phase, temperature rapidly increases as a result of frictional-heat, which results in plasticization of the consumable tool along the contact surface. The plasticized layer is sheared off from the consumable tool, which is pushed up along the interface with continual application of constant axial load. Once the plasticized layer is spread across the interface, the rotating tool is stopped and the forging force is applied. The forging force is held constant for 20-30 seconds and then the load is removed. FTHPP weld is completed and the excess tool is cut off.

Friction Tapered Hydro Pillar Processing Weld Thermal Cycle

Similarly, to an arc welding, FTHPP introduces a complex thermal cycle (rapid heating and cooling) in the base metal adjacent to the interface. The FTHPP thermal cycle determines the final microstructure and thus the resulting mechanical properties. The region of the base metal which is thermally effected during welding is called heat-affected zone (HAZ), which consists of several regions, coarse-grained HAZ (CGHAZ), fine-grained HAZ (FGHAZ), intercritical HAZ (ICHAZ), and subcritical HAZ (SCHAZ). These regions are defined by the peak temperature experienced during the welding process. Figure 12 shows the schematic illustration of the positions of these various HAZ regions HAZ in the Fe- Fe_3C metastable phase diagram[59]. Various efforts have been performed to measure the actual thermal cycle of a FTHPP weld [81, 85, 86]. It is extremely challenging to measure exact thermal cycle at the interface as a result of difficulty of reading temperatures using thermocouples attached adjacent to the interface, whose position may be influenced by the plastic flow during the FTHPP process [81]. Hattingh recorded a peak temperature of 2016°F (1102°C) at the bottom of the tapered at a distance of 0.5 mm from the hole.

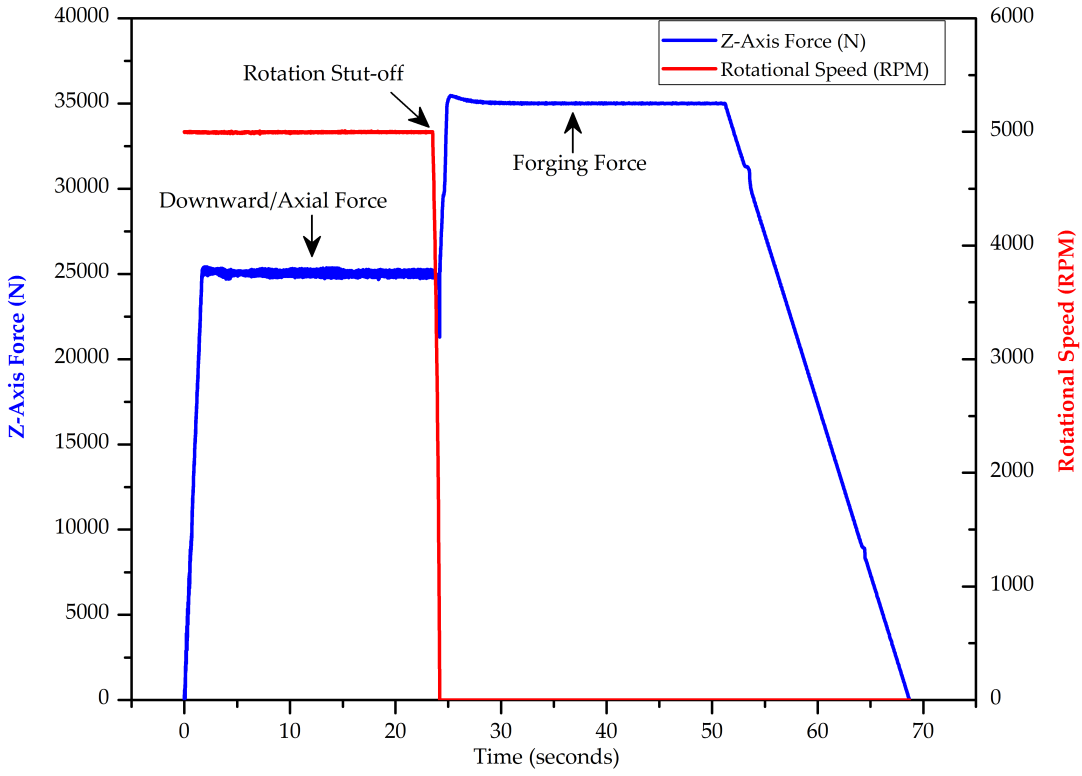


Figure 22. Process parameters, Z-axis force and rotational speed as a function of time for friction tapered hydro pillar processing (FTHPP).

Chapter 3 - Project Objective

The research proposed herein is intended to characterize microstructural examination of graphitized components with regards to creep performance and remaining life performance. The major goals of the project are:

1. To obtain more complete understanding on graphitization in steels (specially with regards to influence of aluminum and weld related graphitization) to assist power plants and refineries.
2. Build an important database to assist industry which consists of metallography and creep testing results which will be of assistance for making run, repair, or retire decisions on the components.
3. Study to examine efficacy of in situ examination methods for graphitized components.
4. Further understanding on time-temperature behavior of graphitization in carbon steel components.

To acquire above mentioned goals the investigation approaches used were as follows:

1. A microstructural examination to characterize the presence, type, morphology, and location of graphitization was performed. This was accomplished using optical light microscopy (OLM), scanning electron microscopy (SEM).
2. Cryo-cracking, which followed a subsequent SEM examination was used to study the morphological features of graphite growth.
3. The quantitative metallographic examination was performed to determine the extent of graphitization using both manual point count method and automated image analysis software. Manual point count method was performed utilizing ASTM E562 procedure and Image J software was used for automated method.
4. The mechanical properties of the materials of interest was examined using creep testing, ASME IX bend tests and hardness assessments.
5. Post creep-test metallographic examination was performed to evaluate the influence of creep-testing on microstructure.
6. Ultrasonic testing was performed with an assistance of Team Industrial Services to develop a protocol for in situ examination of graphitized components.

7. Core-extraction study was performed to evaluate efficacy for in service examination was performed with an assistance of Nelson Mandela Metropolitan University (NMMU). Subsequent repair welding of core extraction site was also studied using friction tapered hydro pillar processing (FTHPP).

8. The estimation on the increase of graphitization upon further aging and creep-testing were studied on the service-exposed and repair-welded materials.

9. The heat-treatment studies provided a further understanding on the time-temperature (nucleation and growth) on graphitization of carbon steel components. This was accomplished using a series of accelerated heat-treatment studies followed by periodic microstructural examination using OLM & SEM.

Chapter 4 - Materials and Experimental

In order to increase the understanding of graphitization in carbon and low-alloy steels; a detailed study was performed at the University of Tennessee, Knoxville. Six ex-service carbon steel weldments consisting of both circumferential (CW) or longitudinal seam welds (LSW) were received for further graphitization studies. These materials were removed after a 17 years of service at a steam temperature of 800°F (427°C) and a pressure of 629 psi (4.3 MPa). Table 6 shows the designations of the welds used in the current study. Typical wall-thickness of the materials studied were greater than ¾″ (19 mm).

Table 6. Sample designations of the materials studied in this study.

Sample ID	**Weld Type**	**Wall-Thickness (inches/mm)**
CW-A	CW between Base Metals A1 and A2	1-⅜″ (35 mm)
CW-B	CW between Base Metals B1 and B2	1-⅜″ (35 mm)
CW-C	CW between Base Metals C1 and C2	¾″ (19 mm)
LSW-A1	LSW – Base Metal A1	1-⅜″ (35 mm)
LSW-D	LSW – Base Metal D	1″ (25 mm)
LSW-E	LSW – Base Metal E	1″ (25 mm)
CW – Circumferential Weld, LSW – Longitudinal Seam Weld		

Metallographic examination using both optical light microscopy (OLM) and scanning electron microscopy (SEM) was performed to evaluate the presence, extent and morphology of graphitization. Cryo-cracking was performed to further examine the morphology of graphite growth. Creep testing was performed to examine the influence of graphitization in creep performance. Heat treatment studies were performed on the selected materials to further fundamental understanding of graphite nucleation/growth. Ultrasonic detection capabilities for graphitization using modern state-of-the-art techniques for in situ inspection with an assistance of level III NDE expert from Team Industrial Services was explored. Metallurgical characterization using core extraction followed by subsequent repair welding was also studied to evaluate the efficacy of in situ core extraction studies. Details on each of these procedures is explained later in this chapter.

The chemical composition of the all the base materials were acquired using a standard optical emission spectroscopy (OES). The chemical composition of base metals conforms to a typical carbon steel composition similar to that of ASTM A516 (pressure vessel plates, carbon steel for moderate and low temperature service, see Appendix D). Table 7 shows the chemical

composition of all the materials investigated in this study. The major alloying elements are carbon, manganese, and silicon.

4.1 Metallurgical Characterization

4.1.1 Metallographic Examination

Samples for the metallographic examination were extracted from the desired locations and orientation. Samples were prepared following a sequential order using 120, 400, 600, and 1200 grit diamond grinding disks, polished with 6 μm and then 3 μm diamond paste on a woven napless nylon cloth. Samples were finished to a 0.05 μm alumina finish in a micro-cloth. To ensure retention of graphite, grinding times must be minimized. Samples were etched using 2% Nital (nitric acid and ethanol). Samples were examined for the presence and location of graphite using both optical light microscopy (50X-1000X) and scanning electron microscopy (500X–100,000X). Energy dispersive spectroscopy (EDS) was performed for examination of graphite and other elements if associated with nucleation of graphite.

Table 7. Chemical composition (wt.%) of the base metals used in the current study.

Elements	CW-A1	CW-A2	CW-B1	CW-B2	LSW-D	LSW-E	CW-C1	CW-C2
C	**0.228**	**0.230**	**0.180**	**0.182**	**0.263**	**0.181**	**0.117**	**0.203**
Mn	0.82	0.83	0.82	0.81	0.82	0.82	0.96	0.63
P	0.015	0.017	0.015	0.022	0.014	0.014	0.02	0.015
S	0.013	0.008	0.013	0.01	0.008	0.011	0.022	0.016
Si	0.25	0.24	0.25	0.20	0.20	0.24	0.16	0.29
Cu	0.04	0.01	0.04	0.04	0.01	0.02	0.07	0.01
Ni	0.02	0.02	0.02	0.08	0.01	0.02	0.66	0.02
Cr	0.03	0.01	0.03	0.07	0.01	0.04	0.05	0.03
Mo	0.006	0.002	0.006	0.02	0.002	0.01	0.014	0.004
V	0.002	0.004	0.002	0.002	0.002	0.002	0.002	0.004
Nb	< 0.01	0.001	< 0.01	< 0.01	<0.01	<0.01	0.001	0.001
Ti	0.001	0.001	0.001	0.001	0.002	0.001	0.001	0.002
Co	0.005	0.005	0.005	0.004	0.004	0.004	0.008	0.003
Al	0.046	0.014	0.045	0.002	0.006	0.047	0.003	0.035
B	0.0001	0.0003	0.0001	0.0002	0.0004	0.0001	0.0002	0.0003
W	< 0.01	< 0.01	< 0.01	< 0.01	< 0.01	< 0.01	<0.01	<0.01
Sb	0.001	0.002	0.001	0.001	0.001	0.001	0.001	0.001
As	0.005	0.003	0.005	0.005	0.002	0.005	0.009	0.002
Sn	0.002	0.001	0.002	0.006	<0.001	0.002	0.008	0.002
Zr	< 0.001	< 0.001	0.001	< 0.001	<0.001	0.001	0.001	0.001
Pb	0.001	< 0.001	0.001	0.001	0.001	0.001	0.001	0.001
N	0.005	0.005	0.005	0.007	0.004	0.006	0.011	0.003
O	0.001	0.001	0.010	0.014	0.004	0.008	0.002	0.001

4.1.2 Cryo-cracking

The cryo-cracking technique was further used to study the presence and morphology of graphite. During cryo-cracking, a selected steel sample is cooled to a liquid nitrogen temperature of [-320°F (-196°C)] and a fracture is imposed at a desired location by using a rapid force. This technique preserves the preexisting surface features as no plastic deformation is produced during crack propagation and allows three-dimensional topographic observation. The cryo-cracked fracture surface was examined using SEM for presence and extent of graphitization. Energy dispersive spectroscopy (EDS) was performed for examination of graphite and if other elements associated with nucleation of graphite. Cryo-cracking was only performed on CW-A weldment based on the initial metallographic results.

4.1.3 Thermal Cycle Simulation of HAZ using Gleeble

The region of the base metal, which is thermally effected during welding, is called heat-affected zone (HAZ), which consists of several regions, coarse-grained HAZ (CGHAZ), fine-grained HAZ (FGHAZ), intercritical HAZ (ICHAZ), and subcritical HAZ (SCHAZ). These regions are defined by the peak temperature (thermal cycle) which result in specific microstructure experienced

during welding. Lower/upper critical transformation temperature (Ac_1, Ac_3) were determined using Gleeble dilatometry. Graphitization during various preliminary studies [2, 7, 12, 13, 15, 16, 51, 55, 57, 68, 70, 87] was observed primarily just outside of the visible HAZ (SCHAZ) and in a minimal extent in the CGHAZ and FGHAZ regions. Because of the relative importance to the occurrence of graphitization in the SCHAZ, thermal cycle simulation studies were performed to examine the microstructure of these regions using Gleeble 1500D. A thermal simulation parameters were performed using measured F(s,d) data for a 1″ plate with 50 KJ/inch energy input with no preheat [88]. These parameters are typical of the components under investigation in this study. Microstructural examination of the thermally simulated samples was performed using optical and scanning electron microscopy.

4.2 In Situ Inspection for Graphitization

4.2.1 Ultrasonic Inspection

The presence of graphitization in the materials under investigation was performed using the modern state-of-the-art ultrasonic inspection techniques, such as phased array, focused phased array. Ultrasonic inspection was performed with an assistance of level III NDE expert from Team Industrial Services. The major objective of NDE studies was to enhance the ultrasonic

inspection capabilities for detection of graphitized materials and to develop a protocol for inspection. Circumferential weldments (CW-A and CW-B) were selected for ultrasonic inspection studies. Post metallographic examination was performed to further enhance learning from the ultrasonic inspection.

4.2.2 Weldcore® Technology

In order to evaluate the extent of graphitization damage in situ condition, efficacy of core extraction methodology was performed using Weldcore® technology. Weldcore® technology involved core extraction for metallurgical characterization, which subsequently followed friction weld repair. Core extraction and repair welding was performed with an assistance of Nelson Mandela Metropolitan University (NMMU), South Africa.

Two carbon steel circumferential welds designated CW-A and CW-B were selected for core extraction and repair welding studies. These two weldments exhibited the most extensive graphitization compared to the other materials examined that were examined. CW-A consisted of base metals A1 and A2, and CW-B consisted of base metals B1 and B2. Graphitization was observed on both A1 and A2 base metals. CW-B showed graphitization only on the B1 base metal. Graphitization was not observed in any locations of B2 base metal. The maximum extent of graphitization (planar morphology) was observed in the base

metal just outside of the visible HAZ for both weldments at the location which was exposed just below the lower critical transformation temperature (Ac_1). The enhanced microstructural characterization was performed on the extracted cores and the repair welded components to understand the microstructure.

4.3 Mechanical Testing

4.3.1 ASME Section IX Bend Tests

An ASME Section IX root bend test (3/8″ × 1-1/2″ × 6″) was performed to examine if bend ductility of the component was influenced by the presence graphite. Bend test was performed on CW-A weldment only, which was based on the initial metallographic examination results (which is discussed later in the metallographic examination results). Metallographic examination showed maximum extent of graphitization just outside of the visible HAZ. Bend samples were centered just outside of the HAZ to examine the bend ductility along the outer edge of the HAZ. A face bend was performed on longitudinal samples.

4.3.2 Creep Testing

Creep testing was performed to obtain the steady state creep rates (%/hr) at various temperatures and stress combinations to establish potential remaining service life. In order to maximize the creep data acquisition; temperature and

stress was varied in a sample and the steady state creep rate can be determined at various temperature and stress combinations. Figure 23 shows a typical creep testing plan for a constant stress and a constant temperature combination. A jumbo sized specimens consisting majority of the pipe wall was used in this study. These jumbo samples provide a better representation of in-service stress conditions taking into account microstructural variation (weld deposit, base metal, HAZ). The use of jumbo type sample eliminates influence of oxidation (at elevated temperature properties) on creep rupture behavior. Figure 24 shows a typical example of the specimen which was used during this study. Metallographic evaluation (OLM and SEM) was conducted on the creep tested samples to establish a correlation between microstructural and creep behavior. A total of 30 specimens which included service-exposed and friction welded materials were tested in the current study. Creep testing was performed at Materials Technology Corporation (MTC), Ann Arbor, MI who is capable of performing these large cross-section specimens.

4.4 Heat Treatment Studies

To further understand the kinetics of graphitization, a long term heat-treatment studies were performed both service-exposed and friction repair-welded components. The primary goal of this study is to further understand

growth of pre-existing graphite nodules and also nucleation/growth of new nodules. The temperatures selected for the heat treatment studies are slightly higher (900-1000°F) than the typical operating temperatures (800°F) of these components to accelerate the reaction rate. Post metallographic examination of on the heat treated samples were performed using optical and scanning electron microscopy.

Three non-graphitized C-½ Mo steel materials (Sample #1 0.014 wt.% Al, Sample #2: 0.034 wt.% Al and Sample #3: 0.004 wt.% Al) with varying amount of aluminum content was subjected to heat-treatment studies. Heat-treatment was performed at 1000°F and the samples were sequentially examined after 50, 100, 250, 500, 1000, 2000, 3000, and 4000 hours for evaluation regarding the progression of nucleation and growth of graphite nodules.

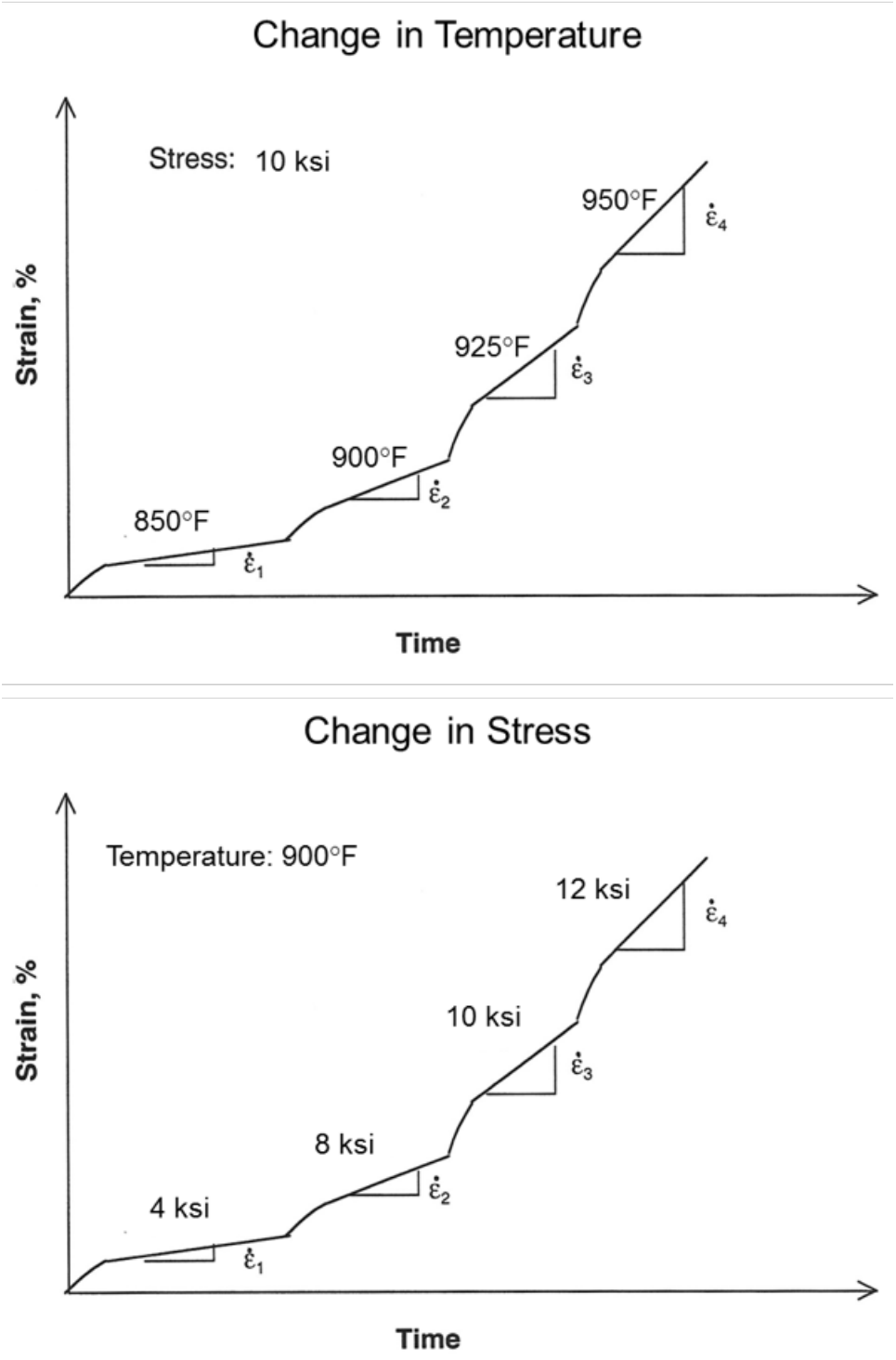


Figure 23. Creep testing plan to obtain steady state creep rate[89].

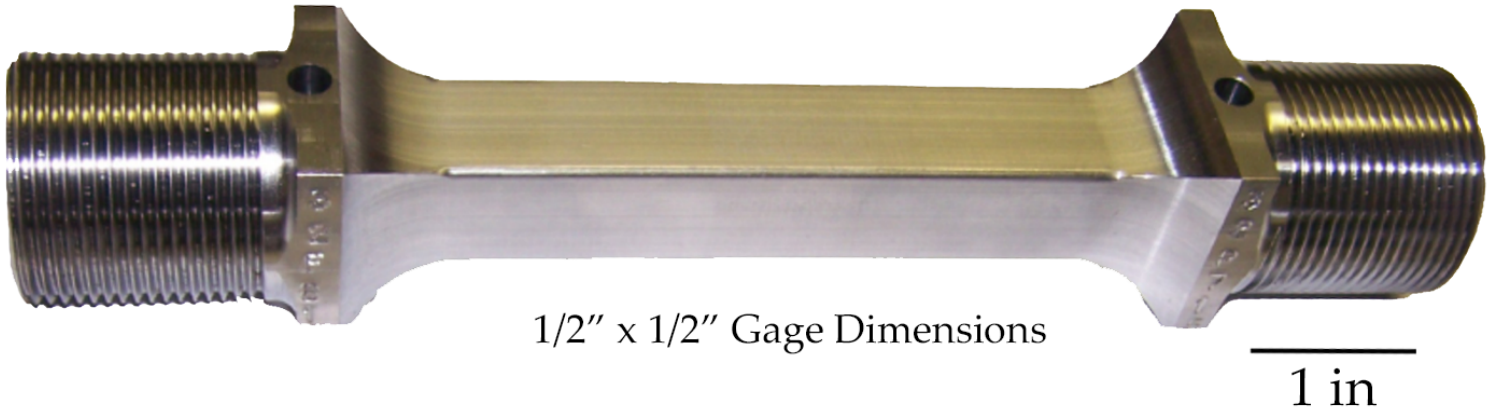


Figure 24. Photograph of a typical cross weld jumbo sized creep specimen used in this study.

Chapter 5 - Results and Discussion

5.1 Metallurgical Characterization

5.1.1 Metallographic Examination

Circumferential Weld (CW-A)

CW-A is a circumferential weld between two 36″ (914 mm) diameter long seam welded pipe sections A1 and A2. Cross-sectional specimens were extracted for metallurgical examination (macrograph shown in Figure 25). Graphitization was observed in both base metals A1 and A2 and the extent and morphology of graphitization did not vary with circumferential positions. The maximum extent of graphitization was observed just outside of the optically visible HAZ on both sides of the heat-affected zone. Figure 26 shows optical panorama depicting evidences of graphitization on both sides of the CW-A weldment. The higher magnification optical micrographs are shown in Figure 27. Graphitization in the base metal remote from the fusion line was random/isolated and was to a reduced extent compared to the base metal outside of HAZ (Figure 28). No graphitization was not observed in the weld deposit. Few evidences of graphitization were observed in the FGHAZ and the CGHAZ (see Appendix for additional optical micrographs).

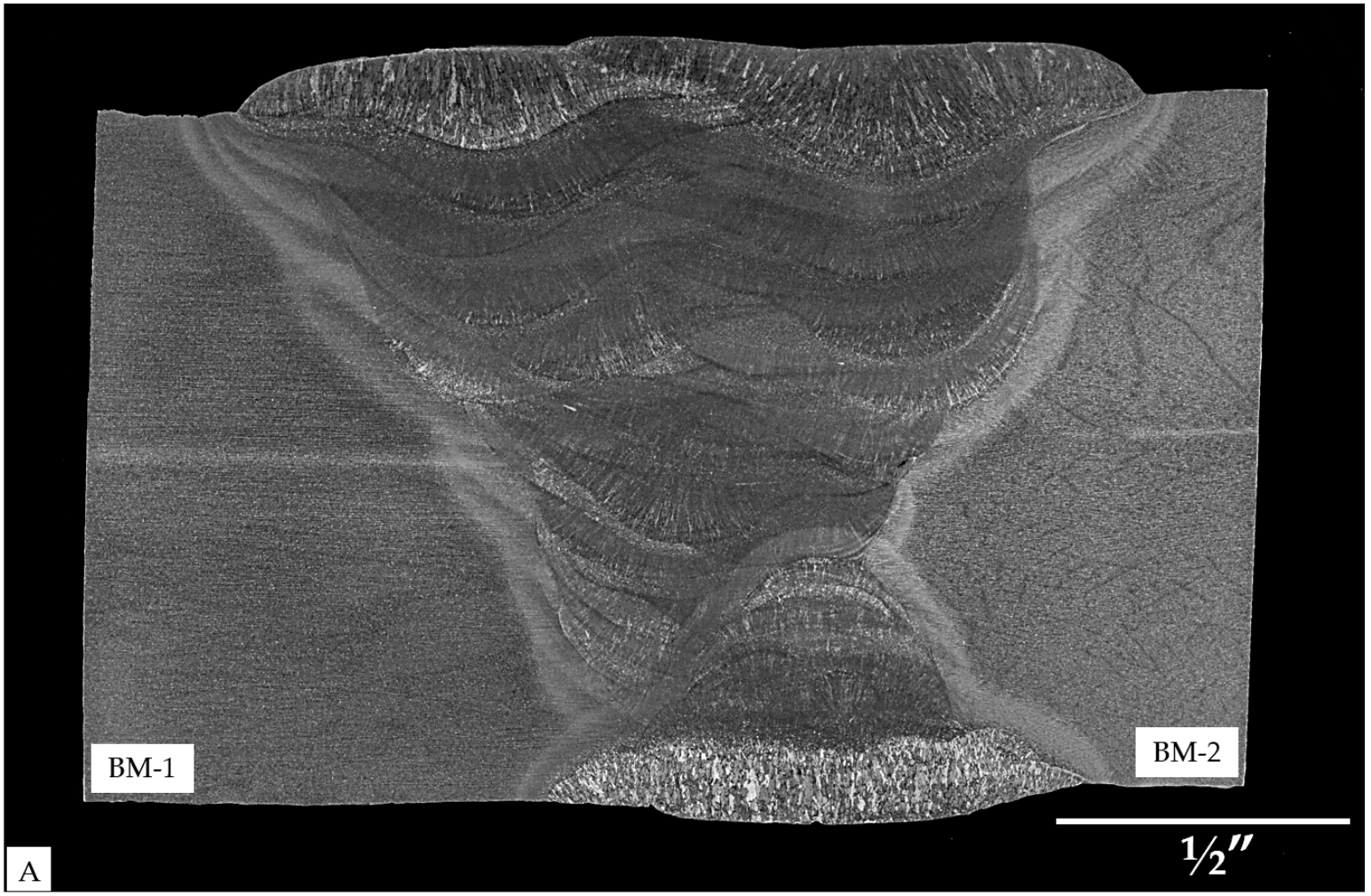


Figure 25. Cross-sectional macrograph of the circumferential weld -A (CW-A), 2% Nital etch.

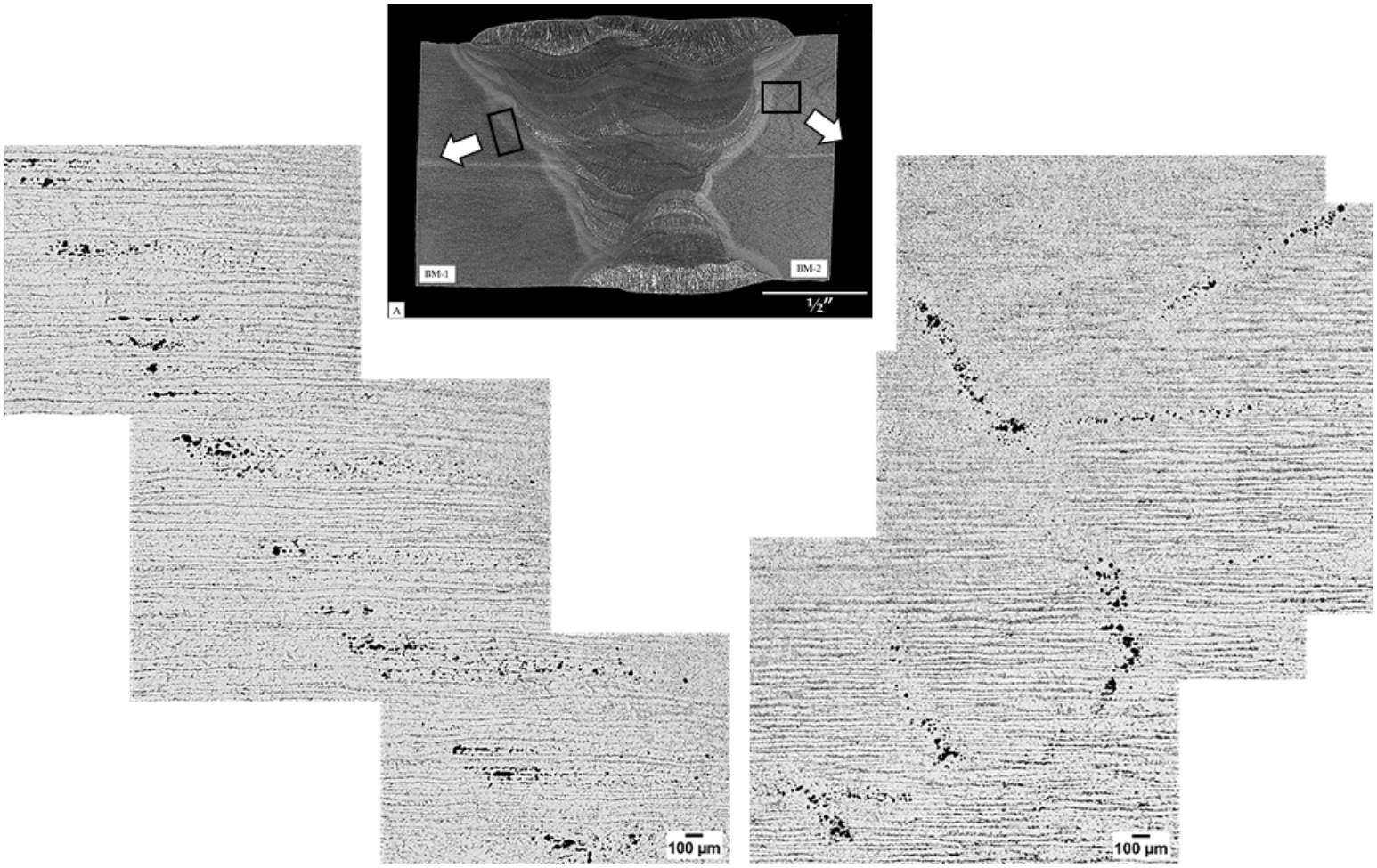


Figure 26. Optical panorama showing severe graphitization in the base metal region just outside of the optically visible HAZ (boxed region the macrograph) in CW-A, 2% Nital etch.

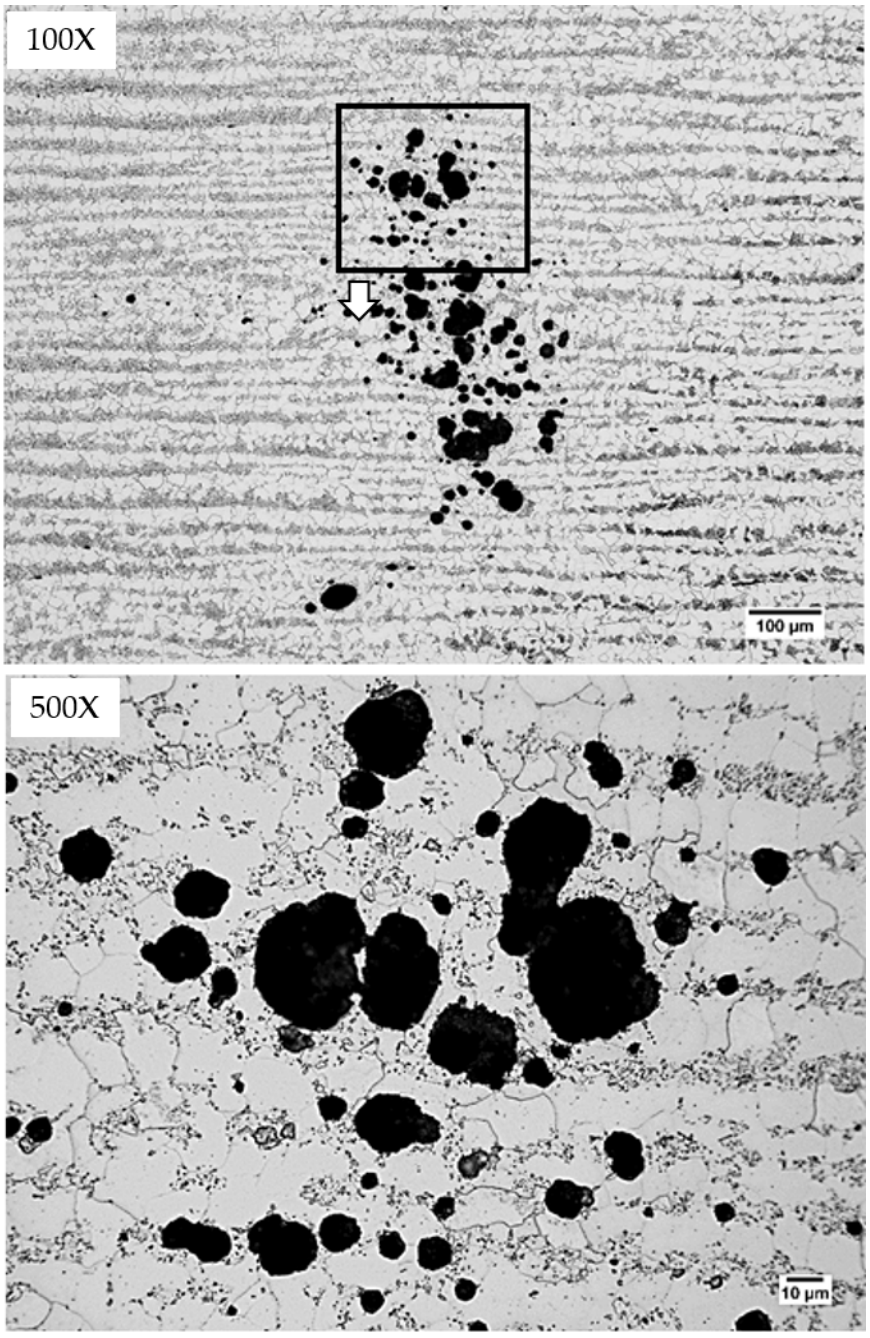


Figure 27. Optical micrographs showing, planar graphitization observed just outside of the visible HAZ on CW-A (A2 Base Metal), 2% Nital etch.

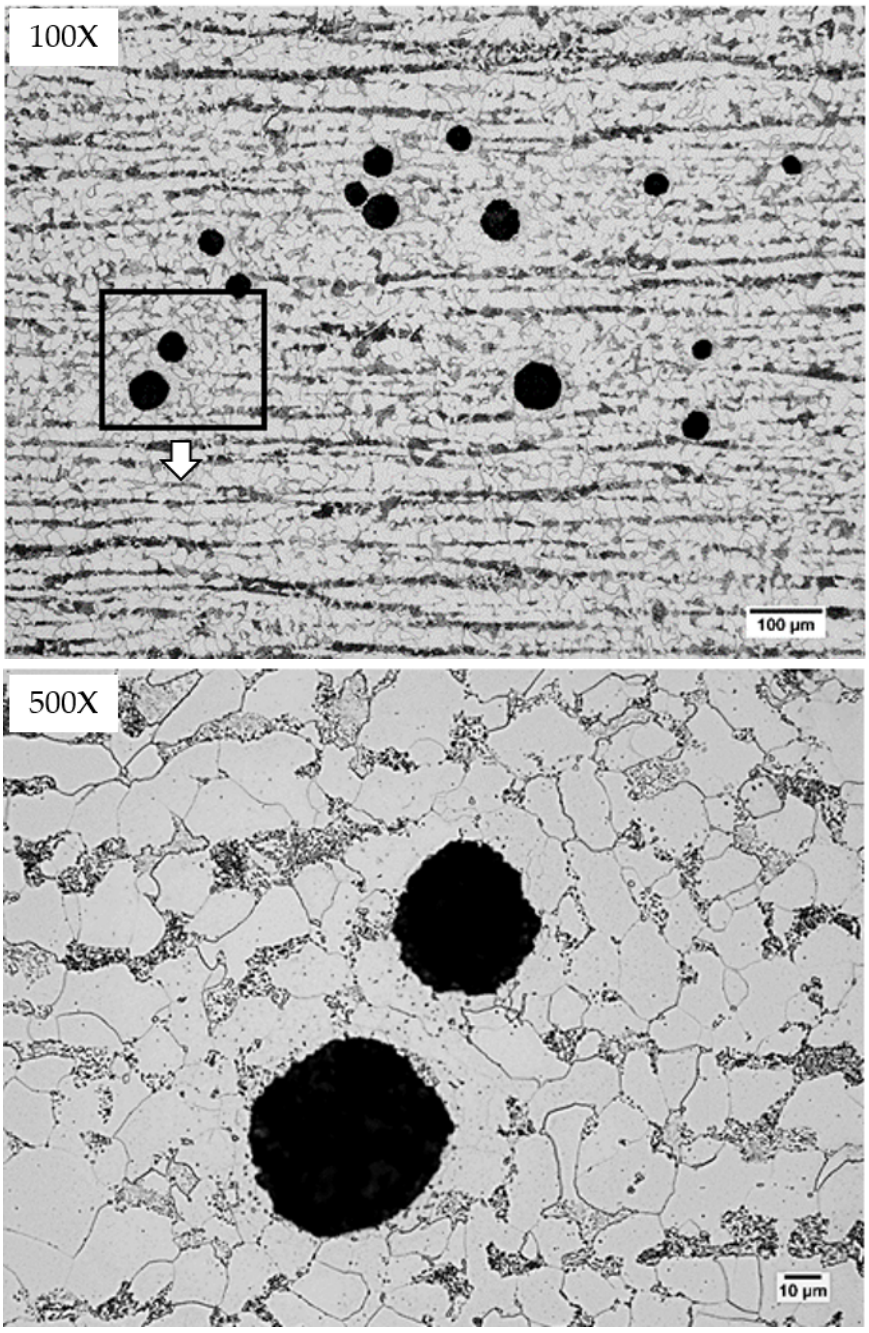


Figure 28. Optical micrographs, showing evidence of random graphitization in the base metal remote from the HAZ on CW-A (A2 Base Metal), 2% Nital etch.

Circumferential Weld (CW-B)

CW-B consisted of a circumferential weld between base metals B1 and B2. Cross-sectional specimens were extracted for metallurgical examination from CW-B weldment. Figure 29 shows the cross-sectional macrograph of CW-B. Graphitization was only observed in the B1 side of the weld deposit. Graphitization was not observed at any location of B2. The maximum extent of graphitization in B1 was observed just outside of the visible HAZ, and were oriented parallel to the primary plate rolling direction. Graphitization observed in the base metal B1 is a planar type. Graphitization in the base metal remote from the fusion line was random and isolated in B1. Figure 30 shows optical micrographs from the base metal just outside of the HAZ in B1. Evidences of randomly dispersed graphite nodules were also observed in the B1 FGHAZ (see Figure 31). Graphitization was not observed in the weld deposit and the coarse-grained heat-affected zone (CGHAZ). B1 and B2 base metals were operating under the same conditions but B1 exhibited graphitization and B2 did not. The non-occurrence of graphitization in the B2 base metal is attributed to its lower aluminum content compared to the base metal B1 (0.002 wt. % vs. 0.045 wt.%). Additional micrographs from the CW-B weldment exhibiting graphitization is presented in Appendix B.

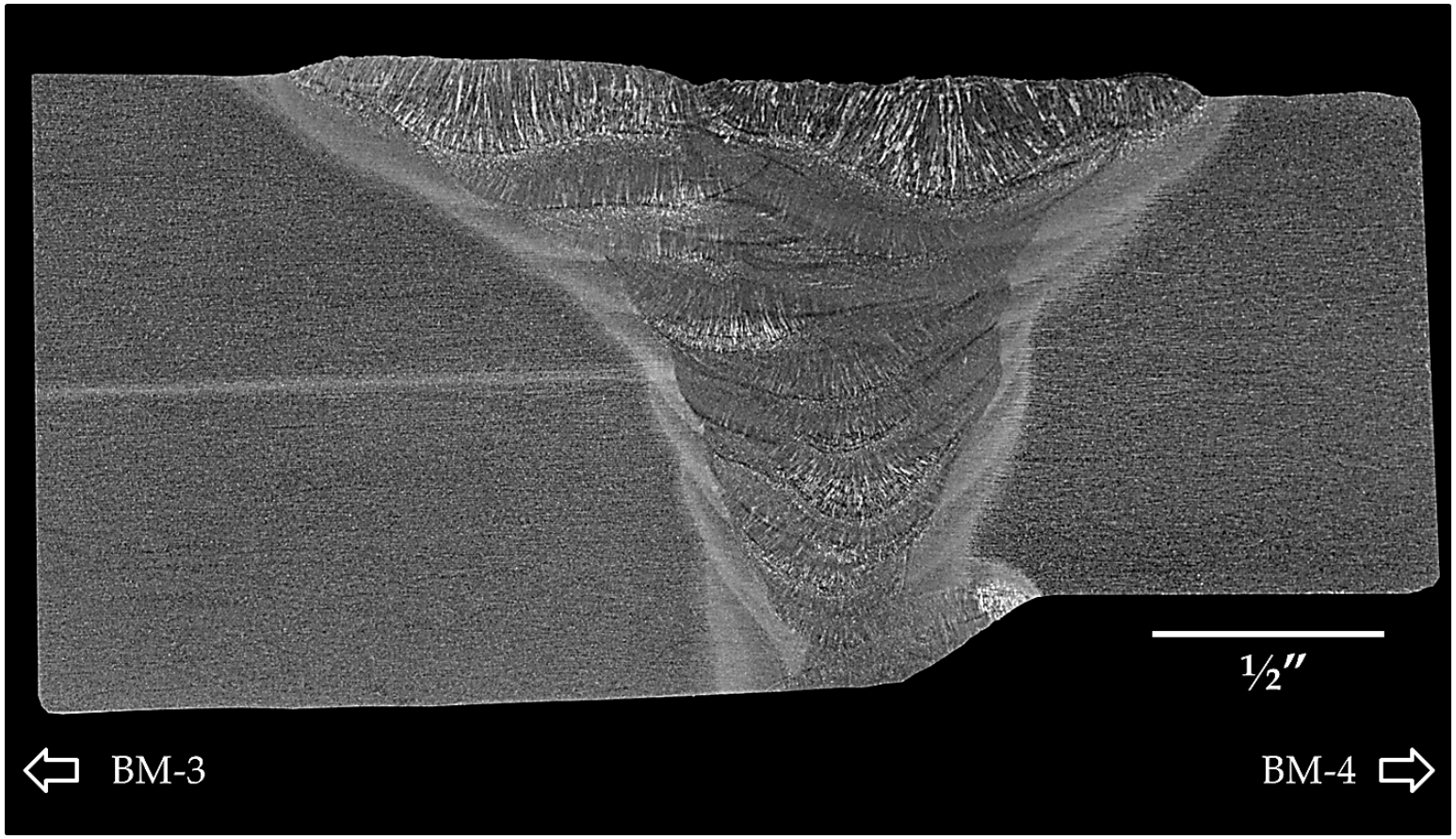


Figure 29. Macrograph of a circumferential weld, CW-B, 2% Nital etch.

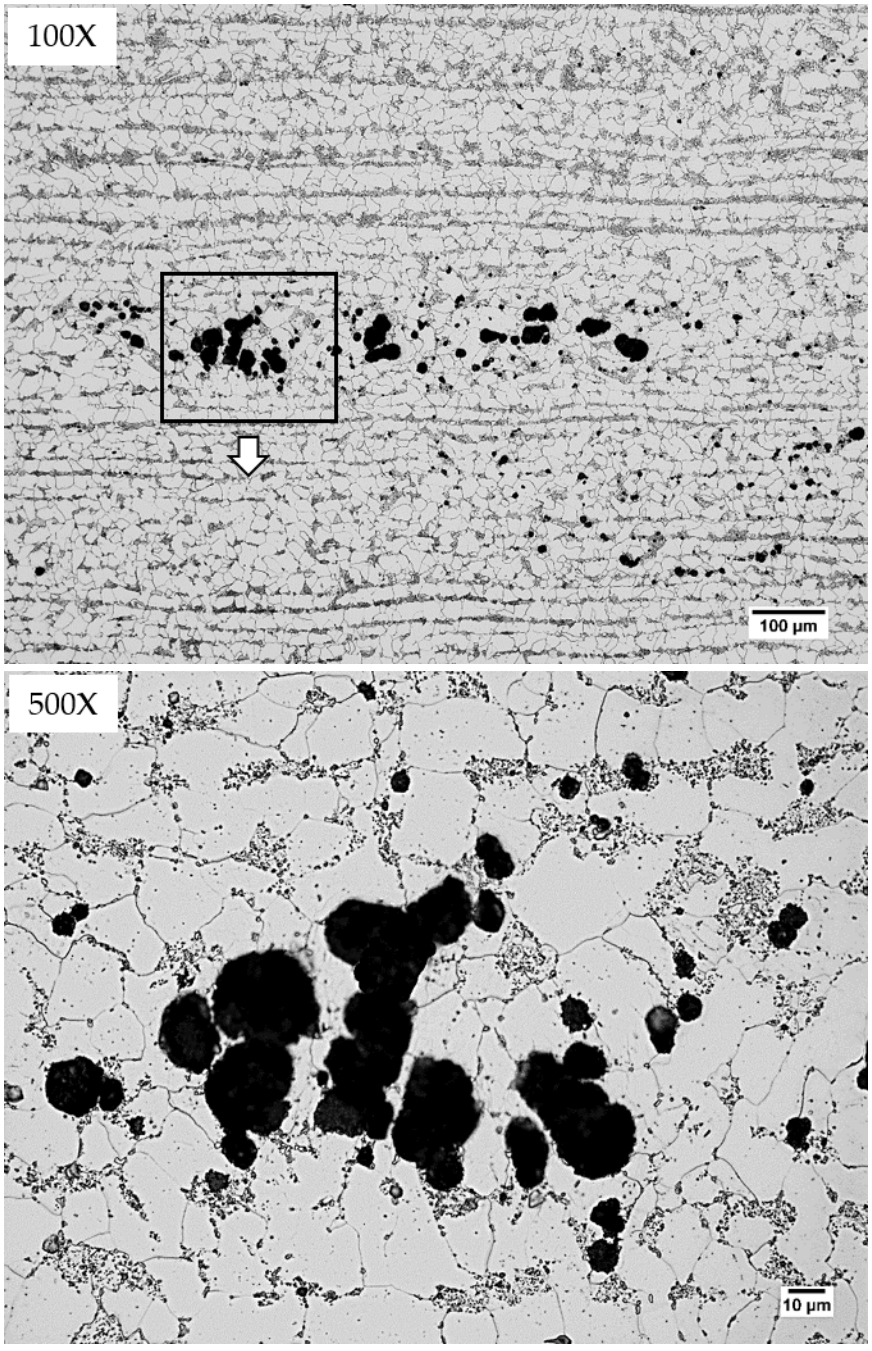


Figure 30. Optical micrographs, showing planar graphitization in the base metal just outside of the HAZ of CW-B, 2% Nital etch.

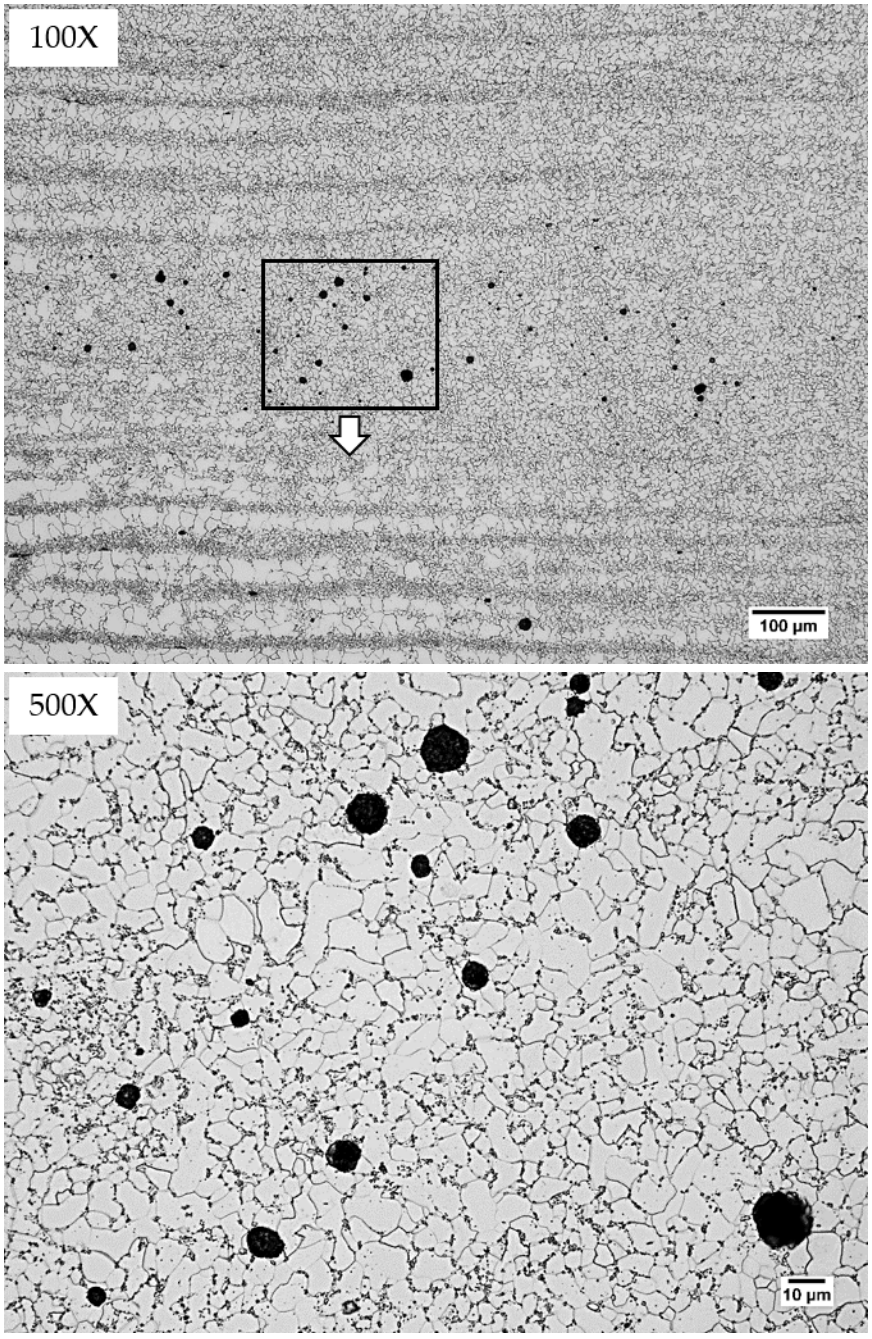


Figure 31. Optical micrographs showing random and isolated graphitization in the FGHAZ in CW-B, 2% Nital etch.

Circumferential Weld (CW-C)

CW-C consisted of a circumferential weld between base metals C1 and C2. Multiple cross-sectional specimens were extracted from CW-C for metallurgical examination from various circumferential positions. All specimens exhibited similar extent of graphitization. Figure 32 shows a cross-sectional macrograph of CW-C circumferential weld. Graphitization was observed in the base metal C1 side (base metal and HAZ); however, was not observed at any locations of the base metal C2. The non-occurrence of graphitization in the base metal C2 is attributed to its lower aluminum content compared to the base metal C1 (0.045 wt.% vs. 0.002 wt.%). Graphitization in C1 was primarily observed just outside of the visible HAZ and exhibited chain-type morphology. Random and isolated graphitization was observed remote from the weld deposit. Figure 33 shows example of graphitization observed in the base metal just outside of the HAZ. Figure 34 depicts example of graphitization in the base metal remote from the HAZ. Evidences of randomly dispersed graphite nodules were observed in the CGHAZ and FGHAZ. Graphitization was not observed in the weld deposit. Additional micrographs from CW-C weldment exhibiting graphitization is presented in Appendix B.

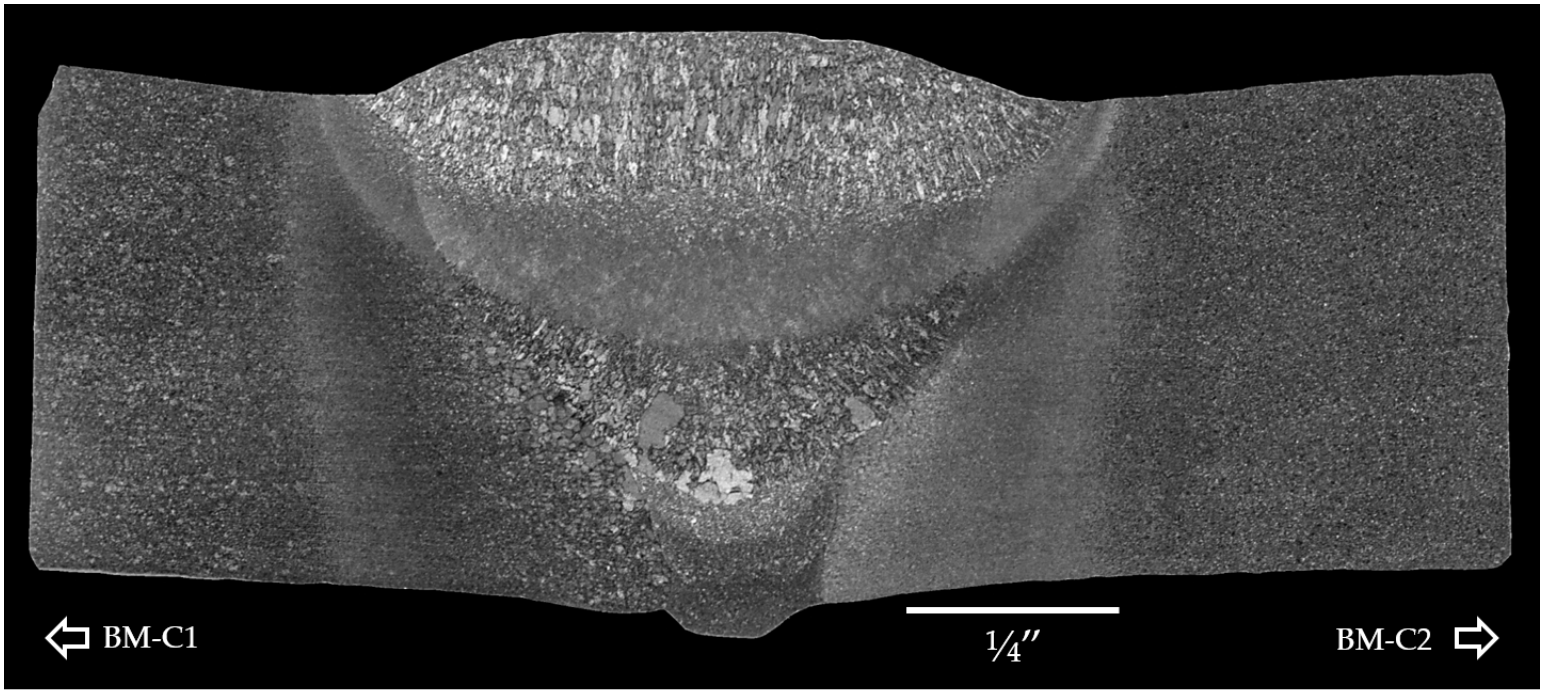


Figure 32. Weld C - Circumferential weld macrograph, 2% Nital etch.

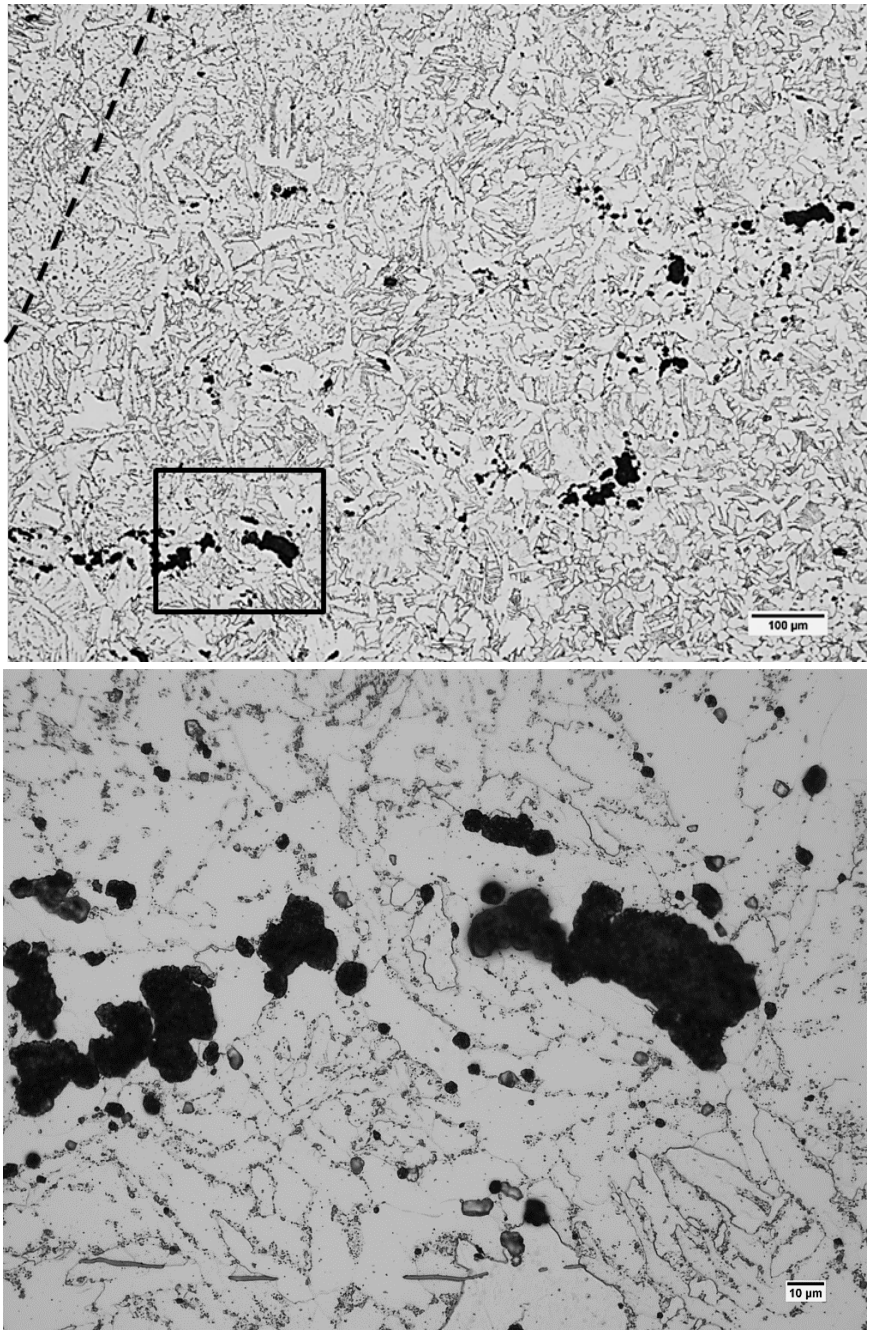


Figure 33. Optical micrographs showing planar graphitization, A) 100X, and B) 500X in CW-C (C2) base metal HAZ, 2% Nital etch.

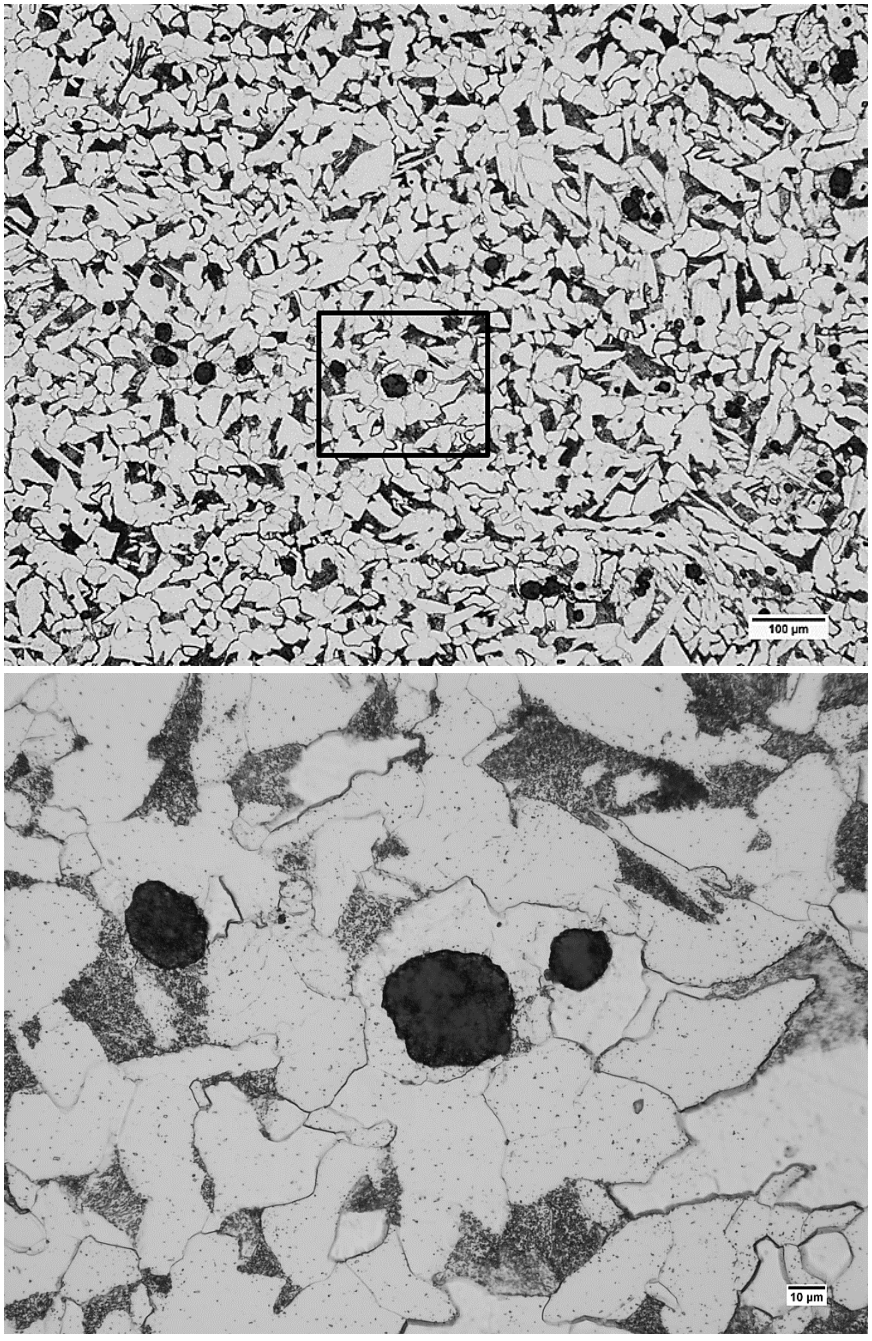


Figure 34. Optical micrographs showing isolated graphitization, A) 100X, and B) 500X in C2 base metal, 2% Nital etch.

Longitudinal Seam Weld (LSW-D)

Cross-sectional specimen for metallurgical examination was extracted from the longitudinal seam welded pipe section LSW-D. Graphitization was observed in the base metal and the HAZ (only FGHAZ). No evidence of graphitization was observed in the weld deposit. Graphitization was primarily observed in the base metal just outside of the visible HAZ, which exhibited chain-type morphology. Random and isolated form of graphitization was observed in the base metal remote from the weld deposit. Graphitization observed in the FGHAZ was to a lower extent compared to the base metal region just outside of the HAZ. Graphitization in LSW-D was similar to what was observed in the samples (CW-A, CW-B and CW-C) discussed earlier. Micrographs from LSW-D is presented in Appendix B.

Longitudinal Seam Weld (LSW-E)

Cross-sectional specimen for metallurgical examination was extracted from the longitudinal seam welded pipe LSW-E. Graphitization in LSW-E was observed to a reduced extent compared to the rest of the materials examined in the current study. Graphitization was only observed in the base metal was random and isolated. The low-level of graphitization in LSW-E can be attributed

to its low aluminum content compared to the rest of the materials. Related micrographs from LSW-E is presented in Appendix B.

5.1.2 Cryo-cracking

Cryo-cracking study was performed on CW-A weldment on samples extracted from both A1 and A2 base metal. Both samples A1 and A2 present similar results with regards to the extent and location of graphitization. The result presented herein only correspond to SEM fractographic examination performed on the A2 base metal. Figure 35 shows the location of sample extraction for cryo-cracking. Samples for cryo-cracking was extracted parallel to the weld fusion line and a sharp ~2 mm notch, perpendicular to the weld fusion line was placed using a dremel tool. The notch was made circumferentially around the sample to direct the cryo-cracking along the desired path. Sample was fractured at liquid nitrogen temperature (-196°C, -320°F) using a rapid force. Fracture surface was examined using SEM, which allowed examination on the extent, location and morphology of graphitization. Figure 36 shows a macrograph of the cryo-cracked fracture surface and the macrograph showed the presence of weld deposit, HAZ, and the base metal. Note: evidence of graphitization was observed just outside of the HAZ, even in a low magnification macrograph.

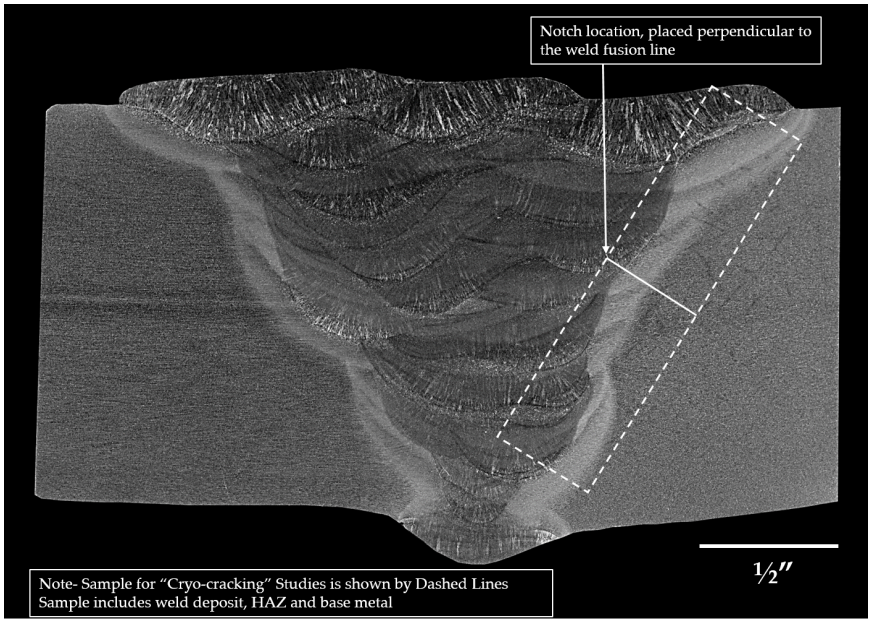


Figure 35. Cryo-cracking sample extraction location is shown by dashed lines. ~2 mm deep notch (shown by arrow) was placed perpendicular to the weld fusion line to propagate fracture along the desired location.

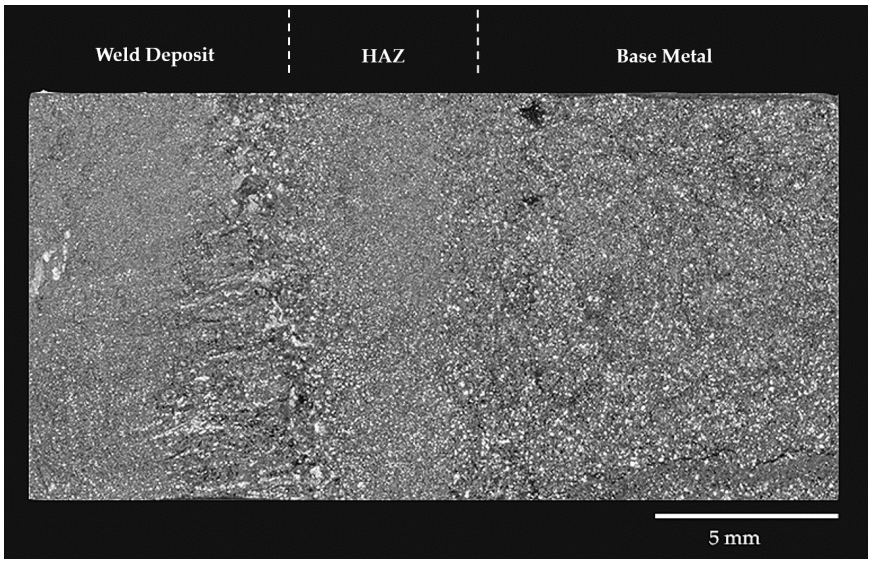


Figure 36. Cryo-cracking fractograph showing various regions of the weldment: weld deposit, HAZ and the base metal. Note the presence of graphite observed even at low magnification fractograph.

A three dimensional pseudo-schematic depicting the presence of graphite in a cryo-cracked fracture surface along with the polished and etched optical micrograph is presented in Figure 37. White arrows indicate graphite nodules. A chain-type graphitization was observed in the base metal just outside of the optically visible HAZ. Random and isolated graphite nodules were observed in the base metal remote from the HAZ. The difference in extent of graphtiization was clearly apparent between the base metal region just outside of the HAZ and the repote from HAZ. Figure 38 and Figure 39 depict higher magnification SEM fractographs from the base metal region just outside of the visible HAZ. Fractographs showed that graphite nodules grew in a rosette pattern, initiated at the center and grew on outward direction. Energy dispersive spectroscopy (EDS) examination of the center of the nodule showed the presence carbon. However, with regards to aluminum and silicon, which has been previously espoused in the literature by various investigators being influential to nucleation of graphite nodules was not detected at/or around graphite nodules in multiple EDS examination attempts. This appear to suggest that aluminum or silicon may have no effect on nucleation of graphite nodules.

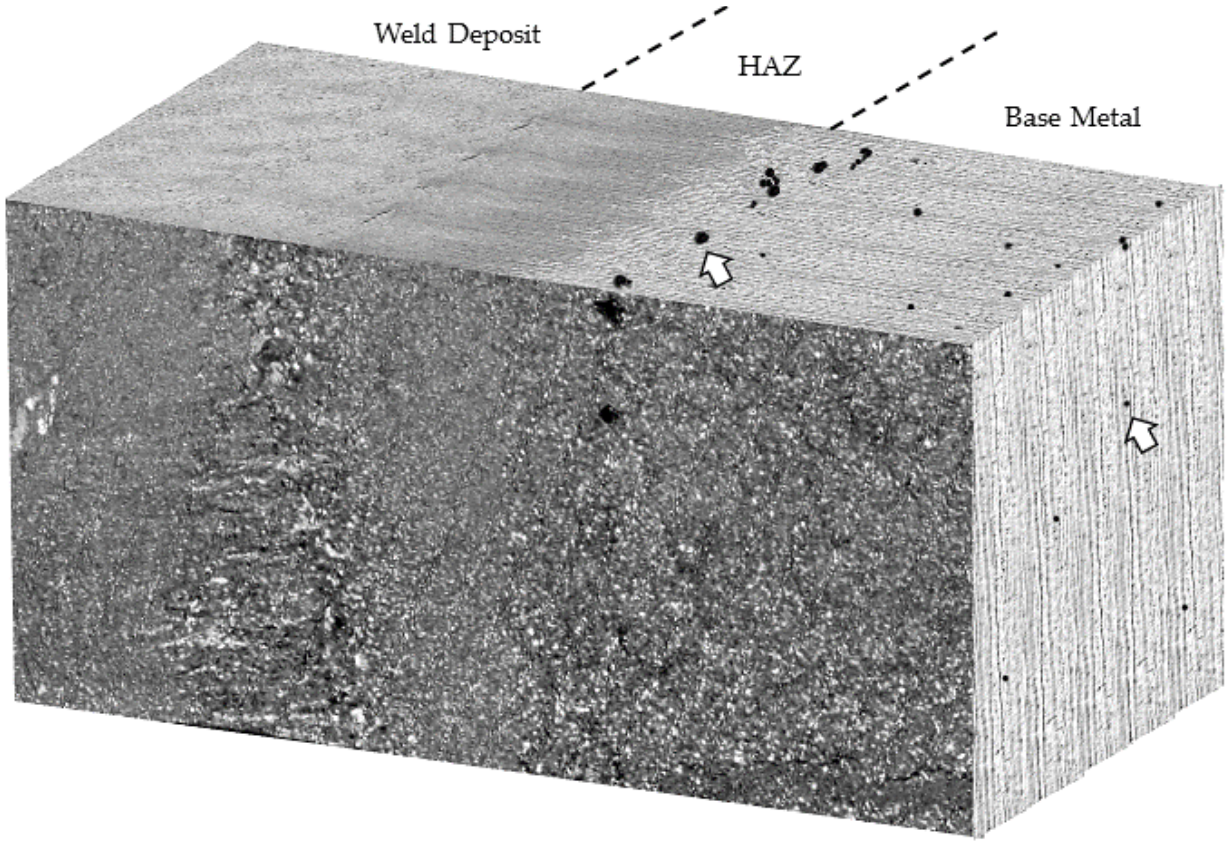


Figure 37.Three dimensional schematic illustrating the presence of graphite in a cryo-cracked fracture surface along with the polished and etched optical micrograph. White arrows indicate typical graphite nodules. Graphitization was primarily located just outside of the visible HAZ and random/isolated graphite nodules were observed in the base metal remote from the HAZ.

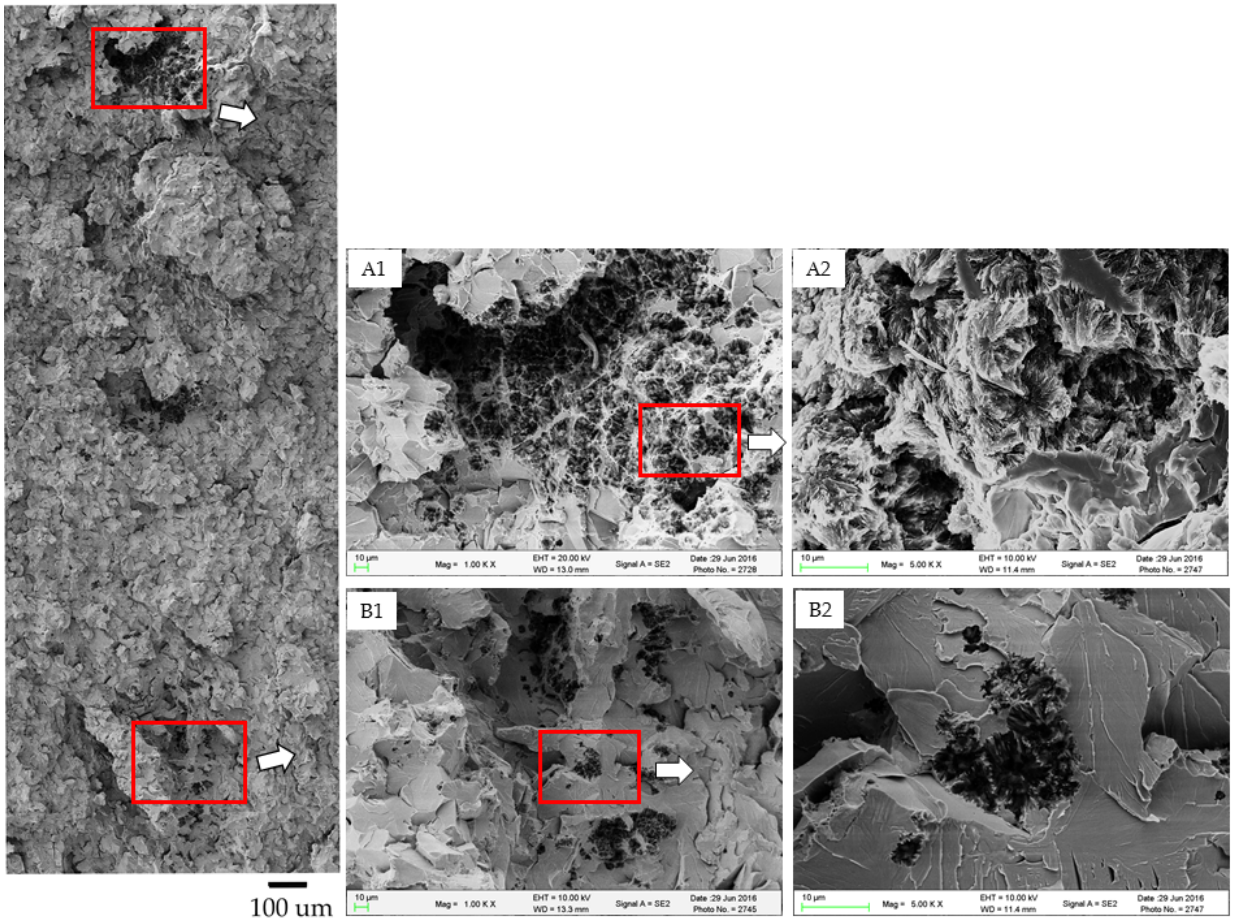
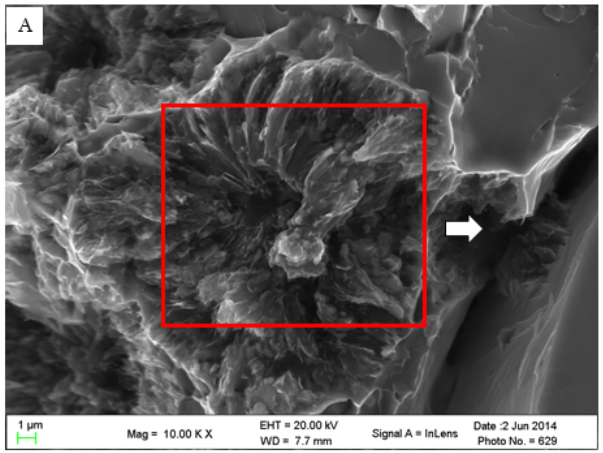
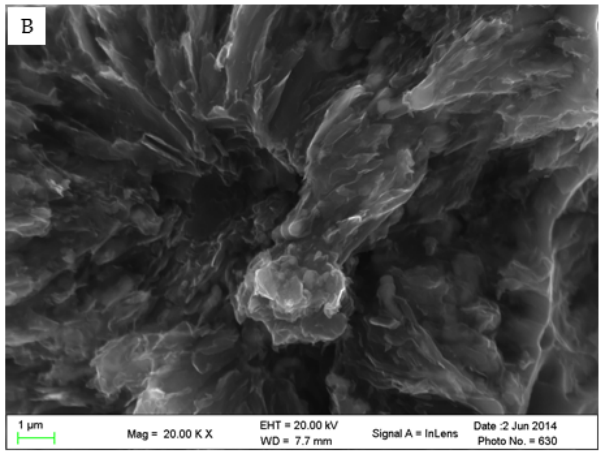
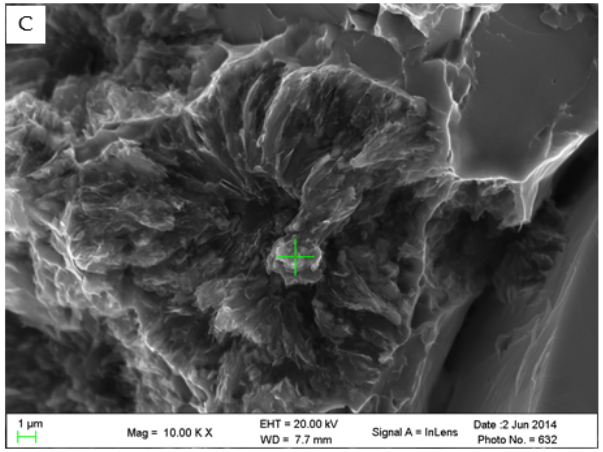
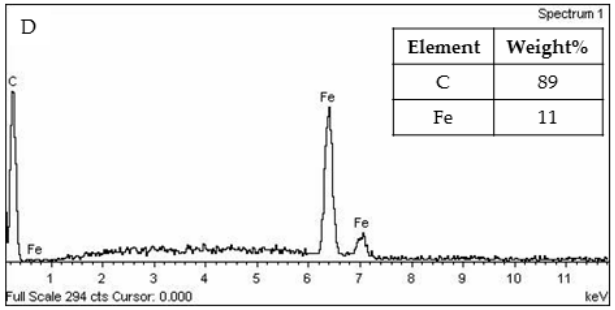


Figure 38. SEM cryo-cracked fractographs (A1, B1 = 1000X and A2, B2 = 5000X of the region just outside of the visible HAZ, showing agglomeration of graphite nodules. Higher magnification SEM fractographs are shown in Figure 39.









EDS spectrum of the graphite nodule, shown by the green-cross shown on left (Figure C)

Figure 39. SEM cryo-cracked fractographs of graphite nodule exhibited rosette pattern (i.e. initiated at the center and grew in outward direction. EDS examination conformed graphite nodule.

5.1.3 Effect of Aluminum on Graphitization

Aluminum is the most discussed element with regards to graphitization in carbon steels, however its true influence on graphitization is not fully understood [9, 11, 12, 16-18, 45-51]. A literature survey on the early observations with regards to the effect of aluminum on graphitization is presented in section 2.4.3. The early observations on aluminum being a graphitizer have been based solely on empirical observations using metallography to determine the presence of graphite and chemical analysis for aluminum content. No clear observations of graphite nodules nucleating from aluminum oxide/nitride particles have been observed. The metallographic examination results in the current study supported the generally accepted hypothesis on aluminum increasing the extent of graphitization. Tables 8-9 show the effect of aluminum content for the occurrence of graphitization in carbon and C-½ Mo steels. Figure 40 shows the correlation between the aluminum content and the extent of graphitization observed in metallographic specimens. An aluminum content of ~0.005 wt.% was found to be the threshold amount for occurrence of graphitization in the carbon steels investigated in the current study. However, the presence of nucleating agents associated with aluminum (oxide or nitride) was not detected in or around graphite nodules when examined using EDS.

Table 8. Table showing the effect of aluminum on graphitization in service-exposed (17 years at 800°F) carbon steel materials. An aluminum content of 0.005 wt.% found to be the threshold amount for occurrence of graphitization.

	LSW-D	CW-A-A1	CW-B-B1	CW-C-C2	CW-A-A2	LSE-E	CW-C-C1	CW-B-B1
Aluminum	0.047	0.046	0.045	0.035	0.014	0.006	0.003	0.002
Carbon	0.18	0.23	0.18	0.20	0.23	0.26	0.12	0.18
Silicon	0.24	0.25	0.25	0.29	0.24	0.20	0.16	0.20
Graphitization	Planar	Planar	Planar	Planar	Planar	Isolated/Minimal	None	None

Chemical composition expressed in weight percentage.

Table 9. Table showing the effect of aluminum on graphitization in C-½ Mo materials subjected to laboratory heat-treatment studies at 1000°F for 4000 hours.

	Sample 1	Sample 2	Sample 3
Aluminum	0.014	0.034	0.004
Carbon	0.19	0.26	0.11
Molybdenum	0.48	0.43	0.54
Silicon	0.23	0.21	0.20
Graphitization	None	Yes**	None

Chemical composition expressed in weight percentage

** Graphitization along grain boundaries and triple-point junctions was observed after 500 hours at 1000°F

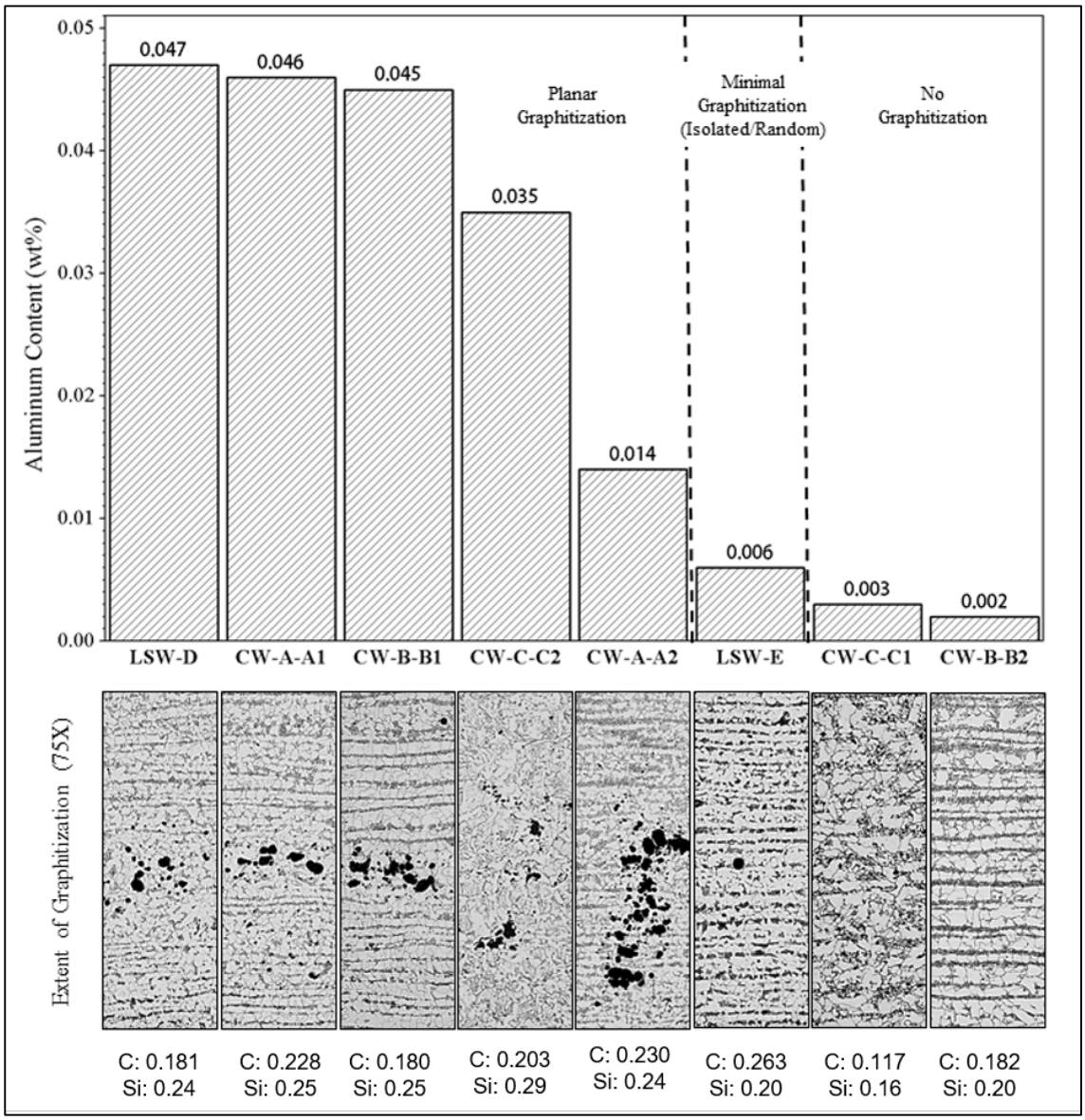


Figure 40. Effect of aluminum on graphitization of service-exposed carbon steel studied in the current project. An aluminum content of 0.005 wt.% found to be the threshold amount for occurrence of graphitization.

The EDS measurements were performed on both polished/etched and also on cryo-cracked fracture surfaces. The aluminum content on the eight service-exposed carbon steel materials ranged from 0.002 wt.%-0.047 wt.% and three heat-treated C-½ Mo materials ranged from 0.004 wt.%-0.034 wt.%. The level of aluminum present in these materials are on the lower end of the detectability limit of the modern day state-of-the-art chemical analysis techniques like Auger electron spectroscopy (detectability limit of the instrument at ORNL is 0.05 wt.%), thus was not approached.

The major source of carbon during graphitization reaction is cementite which is located within pearlite colonies. In initial stages of graphitization, nodules of graphite are observed to nucleate primarily at ferrite-cementite interface. Examples of graphite nucleating along the ferrite-cementite interface after 500 hours of exposure at 1000°F is shown in Figure 41 and Figure 42. Pearlite forms from a diffusional transformation of austenite resulting in a cooperative growth of cementite and ferrite. Since, the transformation is diffusion controlled and occurs at a fairly high temperature (~700°C), both substitutional and interstitial elements to equally partition. Aluminum and silicon which has partition coefficient ($K = C_{cementite}/C_{Ferrite}$) less than one, thus will partition to ferrite.

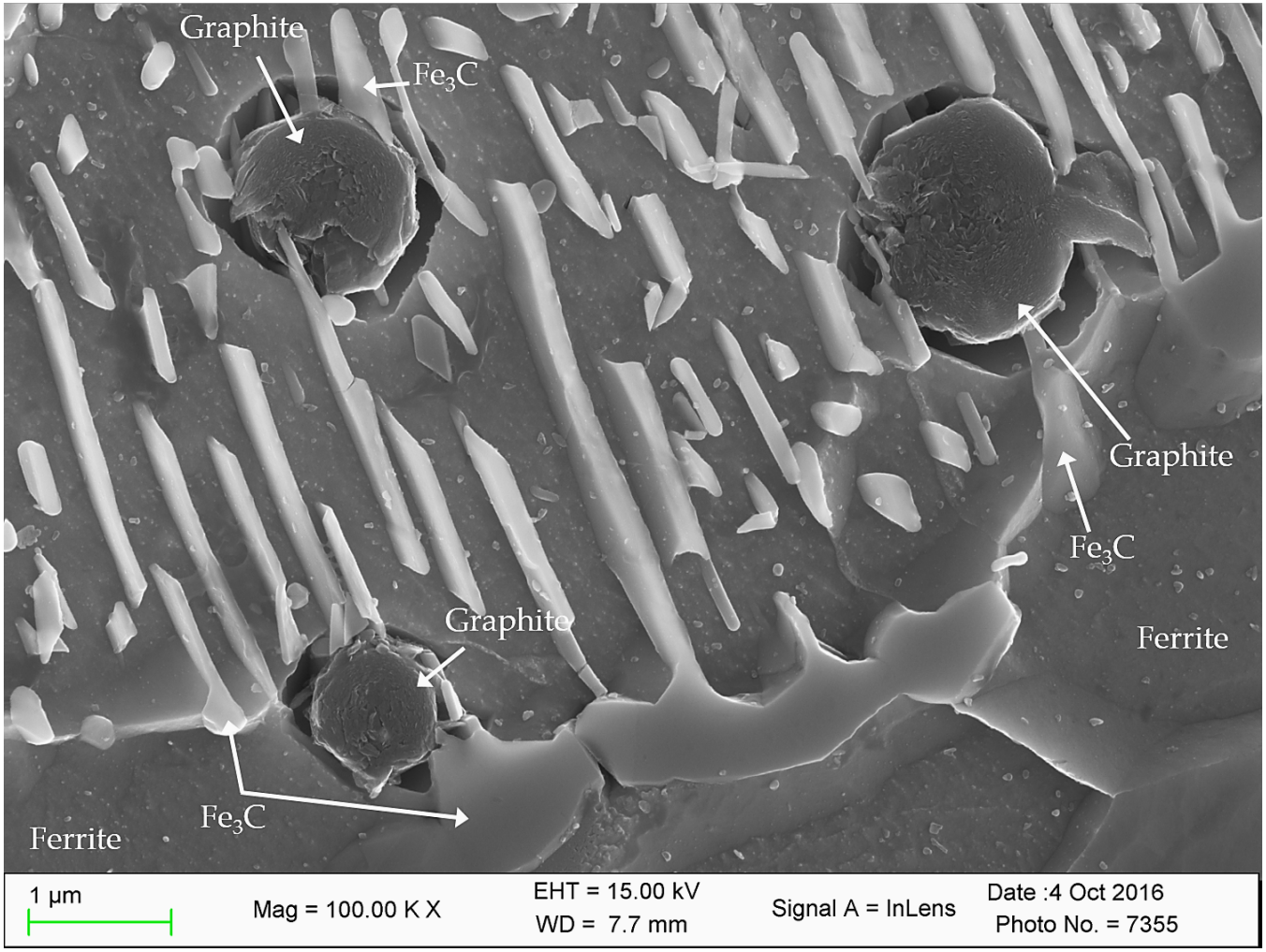


Figure 41. SEM micrograph showing nucleation of graphite nodules along ferrite-cementite interface with in a pearlite colony (observed after 500-hours exposure at 1000°F).

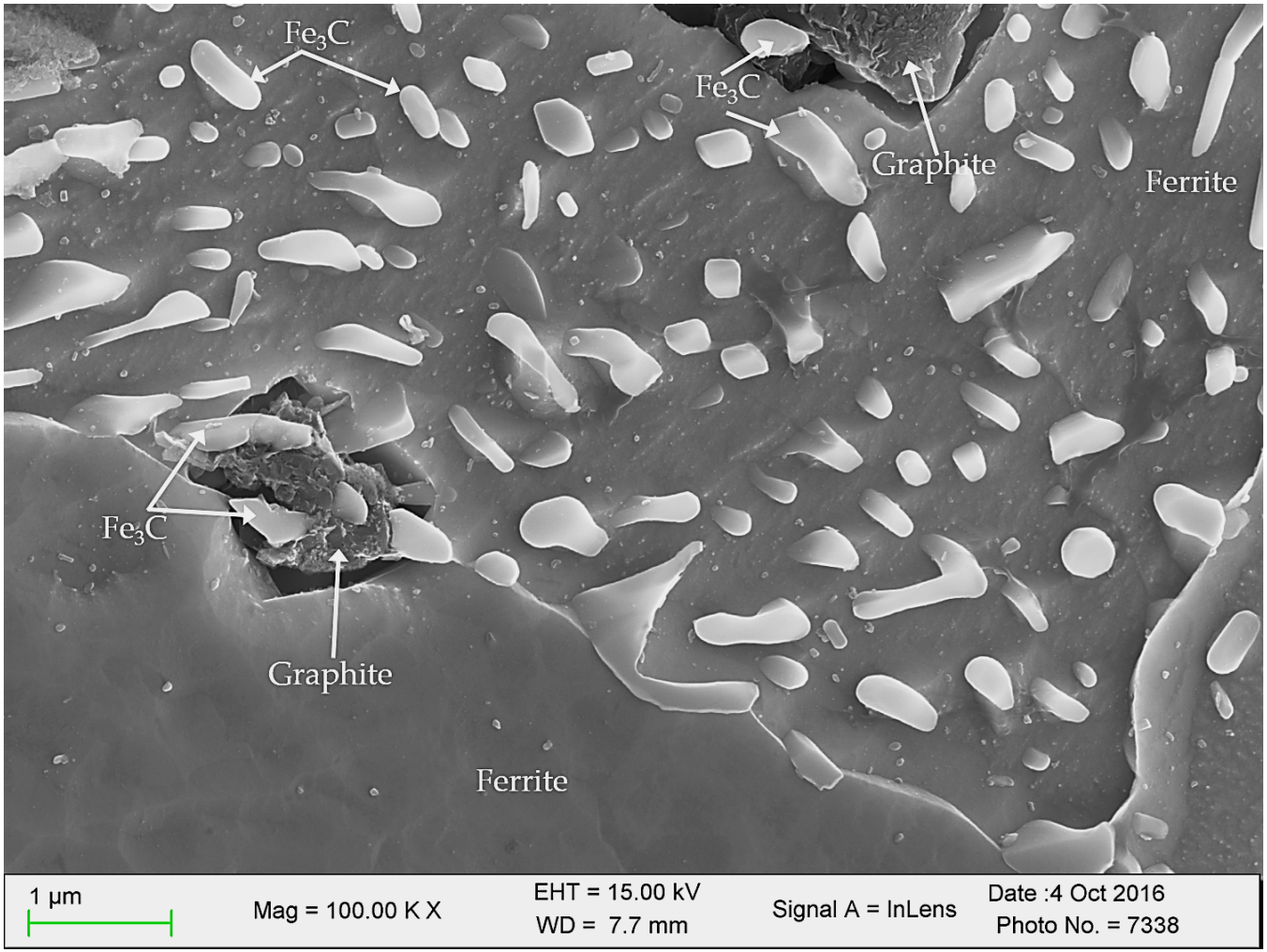


Figure 42. SEM micrograph showing nucleation of graphite nodules along ferrite-cementite interface with in a pearlite colony (observed after 500-hours exposure at 1000°F).

Carbide forming elements, such as manganese, chromium, molybdenum, etc. has partition coefficient ($K = C_{cementite}/C_{Ferrite}$) greater than one, thus will partition to cementite. This was experimentally depicted by H. Bhadeshia using atom probe tomography measurements across ferrite-cementite lamella within a pearlite colony (Figure 43)[90].

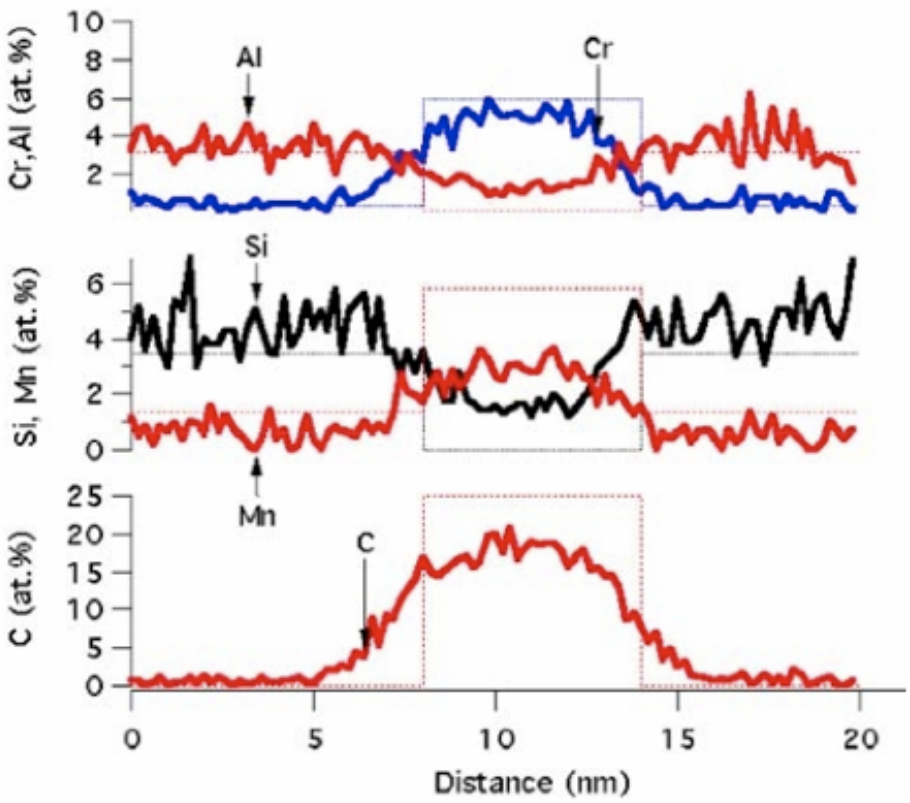


Figure 43. Atom probe tomography measurements across ferrite-cementite lamella in a pearlite colony in a low carbon steel. (square box denote across cementite region)[90].

Thus, a hypothesis to support empirically observed behavior on the effect of aluminum on the occurrence of increased amount of graphitization, based on thermodynamic principles, has been postulated. Rather than aluminum acting as a nucleation agent, we believe that aluminum acts to accelerate in the rate of graphitization by following reasons:

1. <u>Decreasing Solubility of Carbon in Ferrite</u>

Partition of aluminum in ferrite results in decreased solubility limit of carbon in ferrite, thus increases the tendency for atoms to leave alpha-solid solution. Increase in aluminum or silicon results in decrease of solubility of carbon in ferrite. This is experimentally shown for both low and high levels of aluminum. Figure 44 shows the solubility of carbon differential as a function of alloying elements[91].

2. <u>Increasing Metastability of Cementite by Increasing Carbon Activity</u>

The graphitization reaction is shown below, and the major driving force for the reaction to proceed forward is the free energy change during the reaction.

$$Fe_3C \rightarrow 3Fe + C\ (graphite)$$

$$\Delta G = -RT \ln K$$

where, R is gas constant, T is temperature (kelvin), and K is equilibrium constant, which is directly proportional to activity.

$$K = \frac{[a_c][[a_{Fe}]^3}{[a_{Fe3C}]}$$

Thus, increase in carbon activity increase the free energy change for the graphitization reaction, thus resulting in increased amount of graphitization with increased aluminum content. This, results in increase of cementite metastability thus increasing tendency of graphitization.

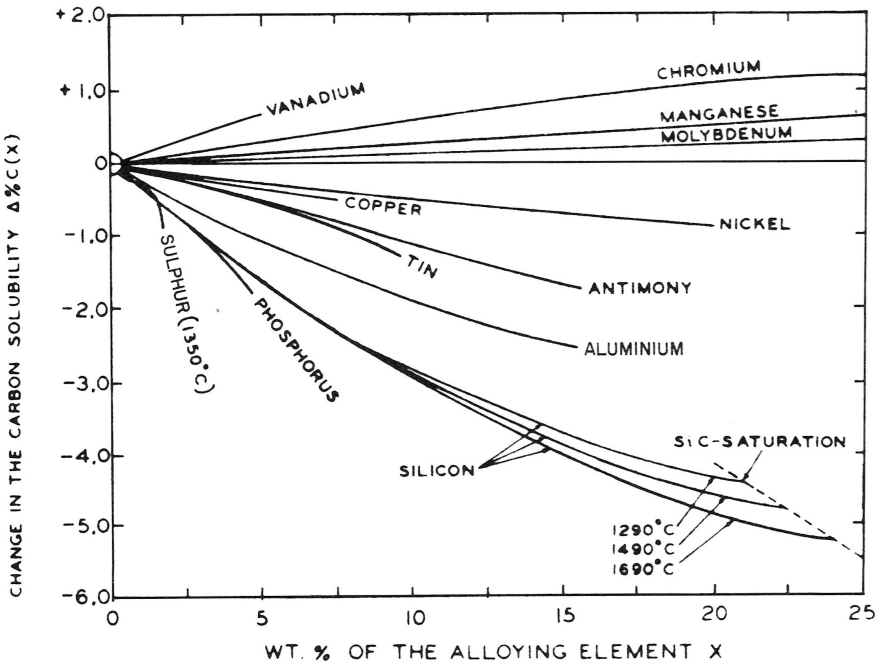


Figure 44. Change in solubility of carbon in iron as a function of alloying elements [91].

5.1.4 Weld Related Graphitization

Graphitization in the carbon steels examined in the current study was principally observed to be aligned in a narrow band immediately outside of the optically visible base metal weld heat-affected zone (HAZ). A composite of optical micrographs (50X) in Figure 45 depicts the various regions of the base metal heat-affected zone, and clearly shows that graphite nodules are located outside of the base metal HAZ in a region called the subcritical HAZ (SCHAZ). This region is so named as to reflect that the maximum temperature during welding is below the lower critical transformation temperature of steel (Ac_1 temperature). The Ac_1 temperature is related to the Ae_1 temperature but is higher than Ae_1 due to the effect of heating rate. Higher magnification optical micrographs (200X) of all pertinent HAZ regions are shown in Figure 45. The base metal adjacent to graphite nodules (Figure 45) shows no optically distinguishable difference when compared to the base metal remote from the HAZ. To further understand the susceptibility of the SCHAZ region to graphitization, it is critical to study the weld thermal cycle experienced by this region.

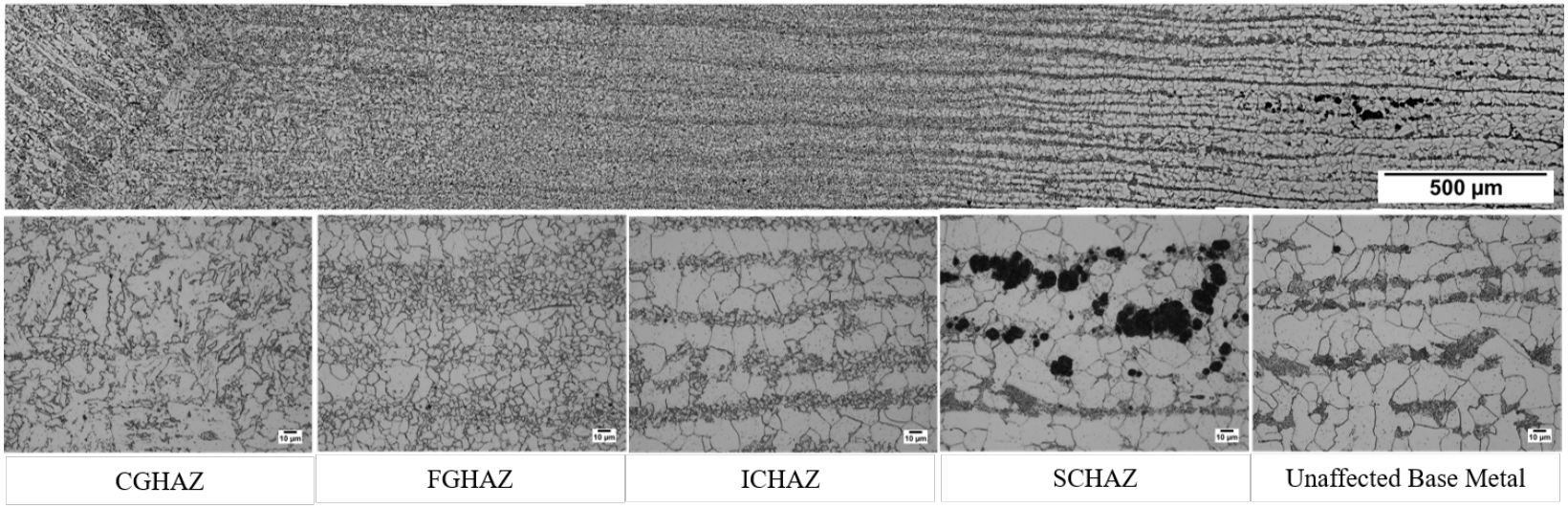


Figure 45. Composite (50X) and higher magnification (200X) optical micrographs showing various regions of the heat-affected zone (HAZ). Graphite nodules were primarily observed in the SCHAZ. Note: the microstructure (ferrite and pearlite) adjacent to the graphite nodules in the SCHAZ is optically identical to that of the unaffected base metal, 2% Nital etch.

As-discussed in detail in the literature-review section (2.3.3), some of the earlier investigators believed that the most graphitization susceptible region is the intercritical heat-affected zone (ICHAZ), which pertains to peak temperatures above the lower critical transformation temperature (Ac_1) and other researchers espoused that it is below the Ac_1 temperature and thus in the SCHAZ [2, 7, 11, 24, 43, 45-49].

To clarify that the weld thermal cycle peak temperature for the most graphitization susceptible region, it is important to understand the various HAZ regions. The HAZ is generally divided into four regions which are defined by the peak temperature of the thermal cycles experienced during welding: coarse-grained HAZ (CGHAZ), fine-grained HAZ (FGHAZ), intercritical HAZ (ICHAZ), and subcritical HAZ (SCHAZ). The microstructure and the resulting properties of these separate regions pertain to the specific peak temperatures experienced during the thermal cycle. An example of weld thermal cycles experienced in the various HAZ regions is shown in Figure 46. These particular thermal cycles are characteristics of a 1" (25.4 mm) carbon steel plate (ASTM A516-70) with an energy input of 50 KJ/inch (no preheat). A 50 KJ/inch energy input is typical of the shielded metal arc welding (SMAW) conditions used for carbon steels. The microstructure in the various HAZ regions depends on the

weld thermal cycle and the peak temperature with respect to the critical transformation temperatures (Ac_1 and Ac_3). Microstructures for each of the HAZ regions are embedded in Figure 46 with reference to their thermal cycles. Since, welding is a non-equilibrium process, the critical transformation temperatures will depend on thermal cycle heating rates. The thermal cycle heating rates during welding are rapid and thus on-heating transformation temperatures will be higher than the equilibrium transformation temperatures. Since, the region of interest in this investigation is the SCHAZ, we have only considered the identification of the lower critical transformation temperature (Ac_1) in this discussion. The CGHAZ, FGHAZ, ICHAZ, and SCHAZ thermal cycles presented (Figure 46) exhibit different average heating rates of 550F°/sec, 400F°/sec, 270F°/sec, and 160F°/sec, and also different cooling rates of 180F°/sec, 125F°/sec, 90F°/sec, and 75F°/sec, respectively. The average heating/cooling rates for the CGHAZ, FGHAZ and ICHAZ were obtained from their calculated thermal cycles pertaining to the temperatures of the lower critical and upper critical transformation temperatures (Ac_1 and Ac_3). The average heating/cooling rates for the SCHAZ region were obtained over the temperature range of 932°F (500°C) to 1292°F (700°C). The on-heating lower critical transformation

temperature (Ac_1) for the CGHAZ region (heating rate of 550F°/sec) was determined using Gleeble dilatometry and was found to be 1410°F (766°C).

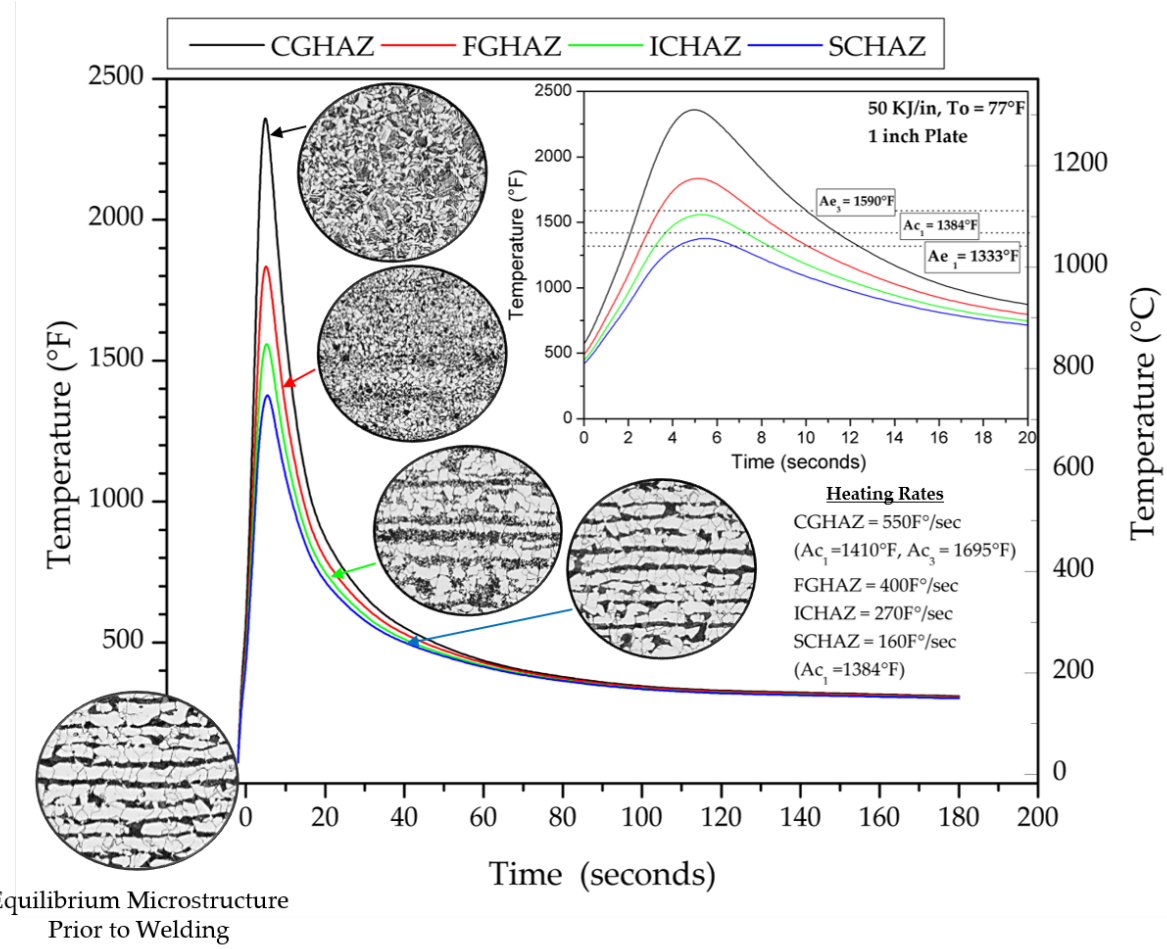


Figure 46. Weld thermal cycles and the resulting microstructures of the various HAZ regions for a typical carbon steel (ASTM A516-70) experiencing a weld energy input 50 KJ/inch (1″ plate, no preheat). Thermal cycles for times 0-24 seconds shown in the inset plot illustrates the difference in heating/cooling rates for various HAZ regions.

The equilibrium transformation temperature (Ae_1) with a slow heating rate for the same base metal was determined to be 1333°F (723°C). Thus, to simulate the microstructure of the primarily graphitized region (SCHAZ), it is imperative to know the exact lower critical transformation temperature upon heating (Ac_1) based on the heating rate pertaining to the thermal cycle in the SCHAZ.

5.1.4.1 Simulation of SCHAZ Microstructure using the Gleeble

The most readily graphitized region is approximately 2.5-3.0 mm away from the fusion line and pertains to a heating rate of 160F°/sec (Energy Input = 50 KJ/inch, 1" plate, no preheat). A thermal cycle simulation was performed, using the Gleeble for a peak temperature above the lower critical transformation temperature of 1425°F (774°C) with an energy input of 50 KJ/inch (1" plate, no preheat). Dilatometry was used during the thermal cycle simulation to define the lower critical transformation temperature by characterizing dilation. The effective lower critical transformation temperature (Ac_1) was determined to be 1384°F (751°C) (as shown in Figure 47). As previously stated, the general consensus in the literature regarding the peak temperature of the most readily graphitized region is either that the peak temperature is above the Ac_1 or it is below Ac_1.

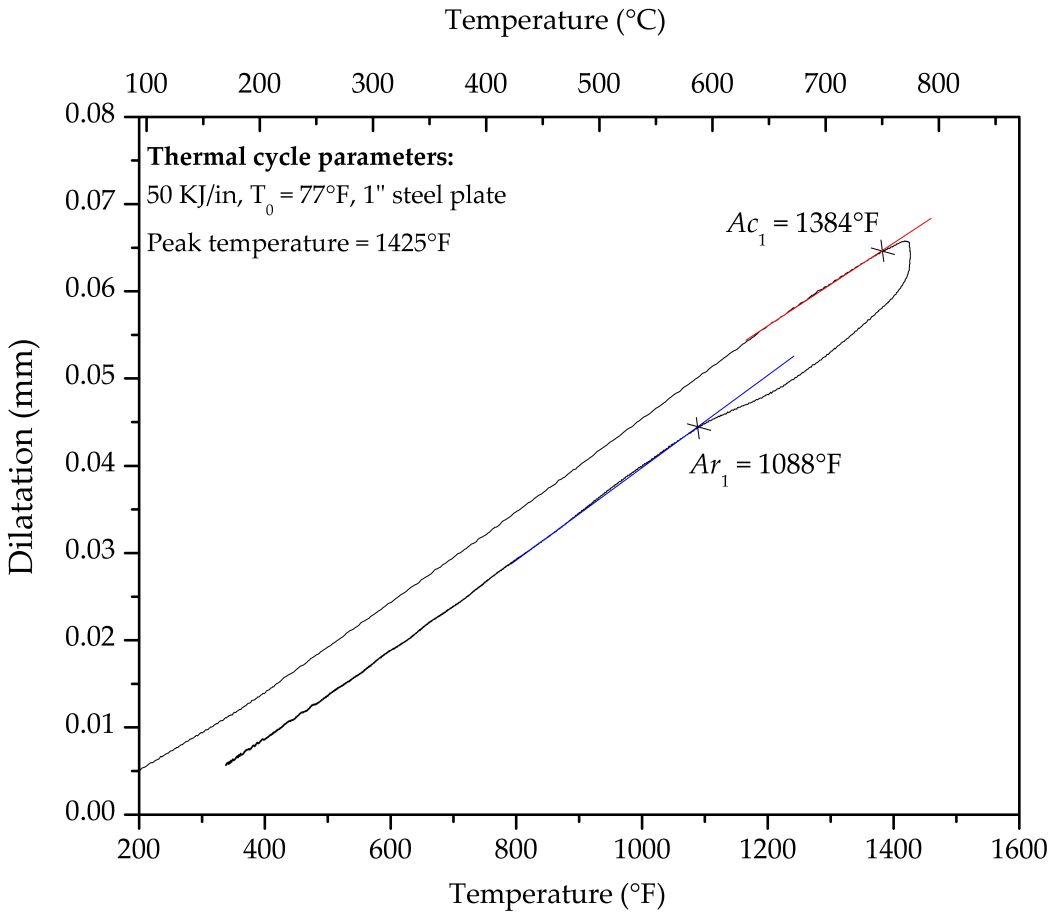


Figure 47. Dilatometry curve showing on-heating (Ac_1) and on-cooling (Ar_1) transformation temperatures for the heat-affected zone peak temperature cycle of 1425°F (774°C) and an energy input of 50 KJ/inch (1" plate, no preheat). Note that the lower critical transformation temperature Ac_1 is 1384°F (751°C).

To clarify this mixed-view, a microstructural simulation for a peak temperature just above (1425°F/774°C) and just below (1380°F/749°C) the Ac_1 temperature (1384°F/751°C) was performed. Figure 48 shows the respective thermal cycles used for microstructural simulation. Note that these thermal cycles are virtually identical with regards to the heating/cooling rates and the only difference is the peak temperature. Dilatometry was used during each of these thermal simulations. Figure 49 shows dilatation curves for a peak temperatures of 1380°F (749°C) and 1425°F (774°C). The dilatation curve for 1380°F (749°C) does not show any indication of transformation, however a 1425°F (774°C) peak temperature shows evidence of transformation. Thus, the upper temperature limit of the primary, most readily graphitized region (SCHAZ), corresponds to peak temperatures below the lower critical transformation temperature (Ac_1) of 1384°F (751°C). Therefore, a simulation temperature of 1380°F (749°C) was utilized in this study to evaluate the potential for graphitization in the SCHAZ region.

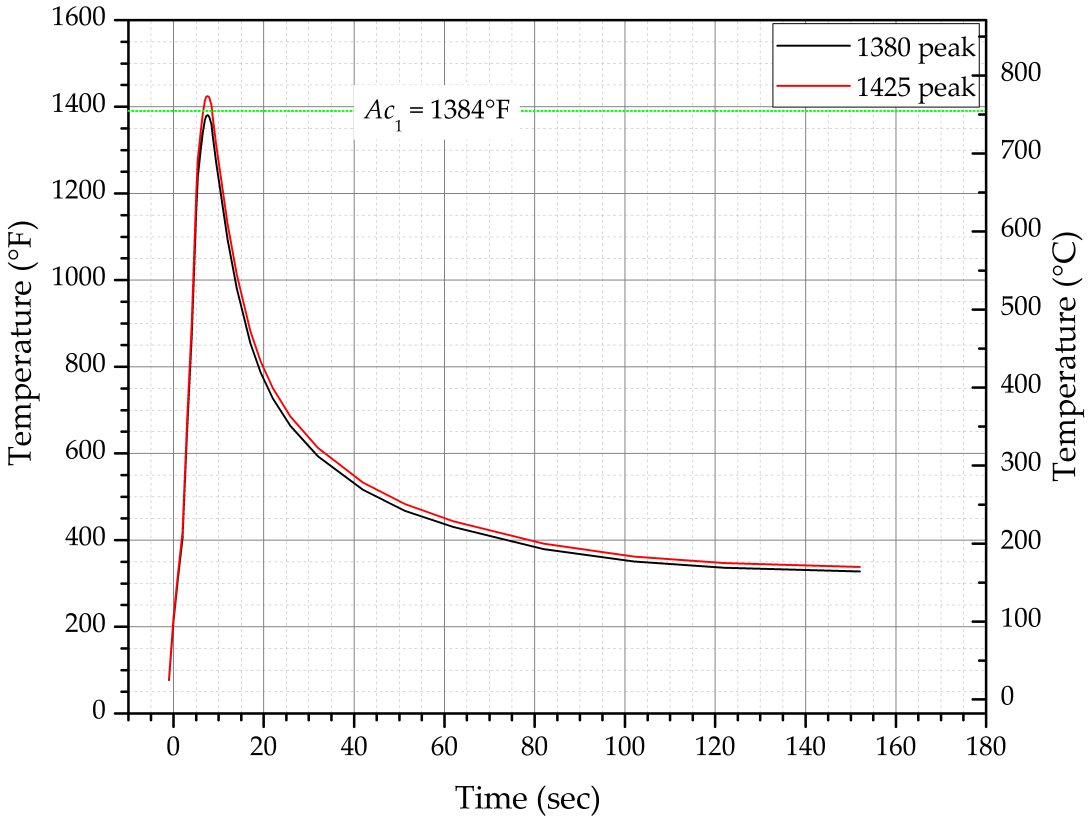


Figure 48. Weld thermal cycles for a peak temperature of 1425°F (774°C) and 1380°F (749°C). These temperatures were selected to simulate the microstructure above and just below the effective lower critical transformation temperature (Ac_1 =1384°F/751°C). Ac_1 position is indicated by the green line. Note that these thermal cycles are identical with regards to heating/cooling rates and the only difference is the peak temperature.

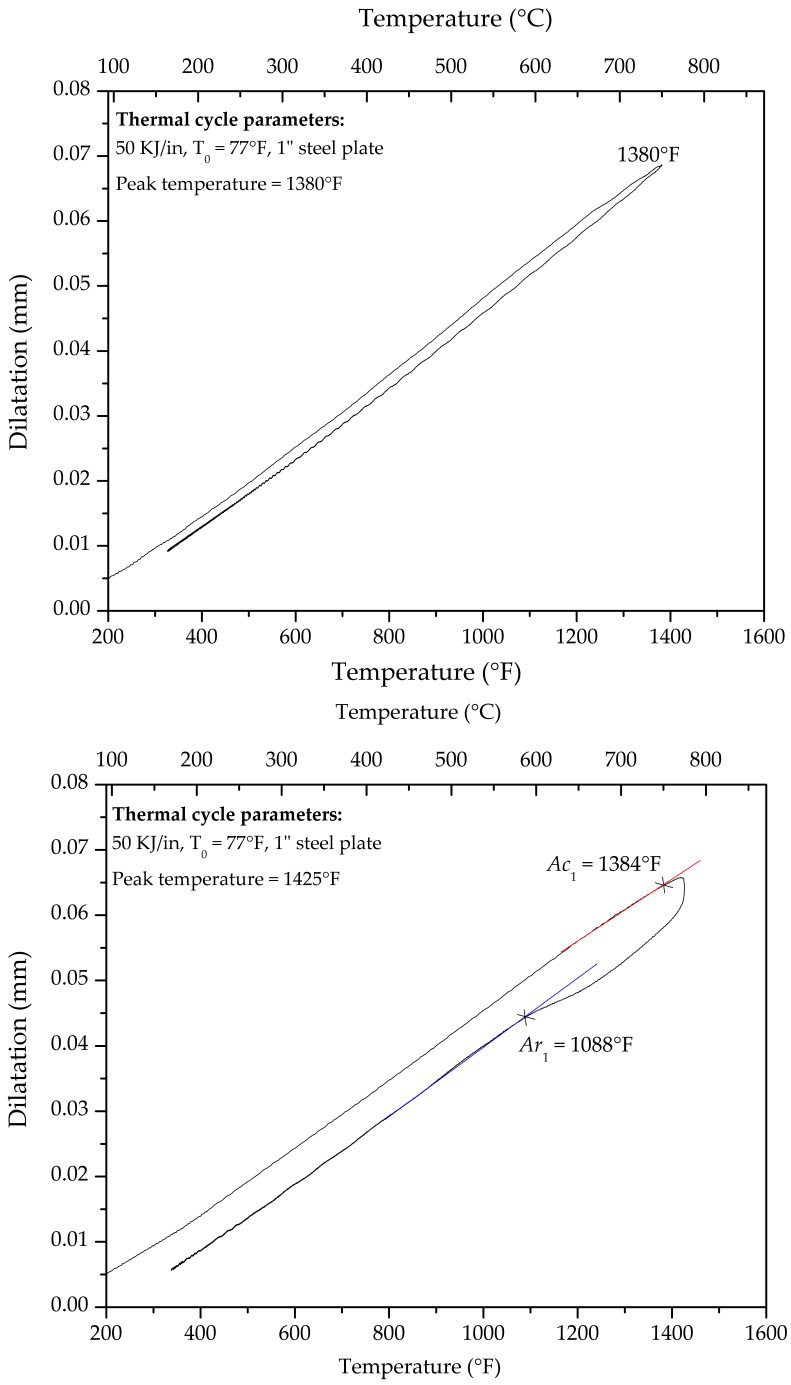


Figure 49. Dilatation curves for thermal cycles simulated at peak temperatures 1380°F and 1425°F. Note: No evidence of transformation was observed for a 1380°F peak temperature.

5.1.4.2 Metallographic Examination of the Gleeble Simulated Samples

Metallographic examination was conducted on Gleeble simulated samples for peak temperatures of 1380°F (749°C) and 1425°F (774°C). Figure 50 shows comparative optical micrographs prior to simulation and after the simulation both below (1380°F/749°C) and above (1425°F/774°C) the Ac_1 temperature. The optical micrographs clearly depict evidence of partial transformation in the sample simulated at a peak temperature of 1425°F (774°C). However, there is no optically discernible difference in microstructure between the sample prior to simulation and the sample simulated at a peak temperature of 1380°F (749°C). The base metal region adjacent to the primary graphitized region just outside of the visible HAZ also showed no discernible difference as compared with base metal remote from the HAZ. Thus, the region of maximum graphitization corresponds to a temperature just below the effective lower critical transformation temperature (Ac_1). The results of the microstructural observations in both the service-exposed and the 1380°F (749°C) simulated samples together with the findings from the literature survey were used to propose a hypothesis for the mechanism of increased amount of graphitization occurring just outside of the optically visible HAZ (below 1384°F/751°C in the current case).

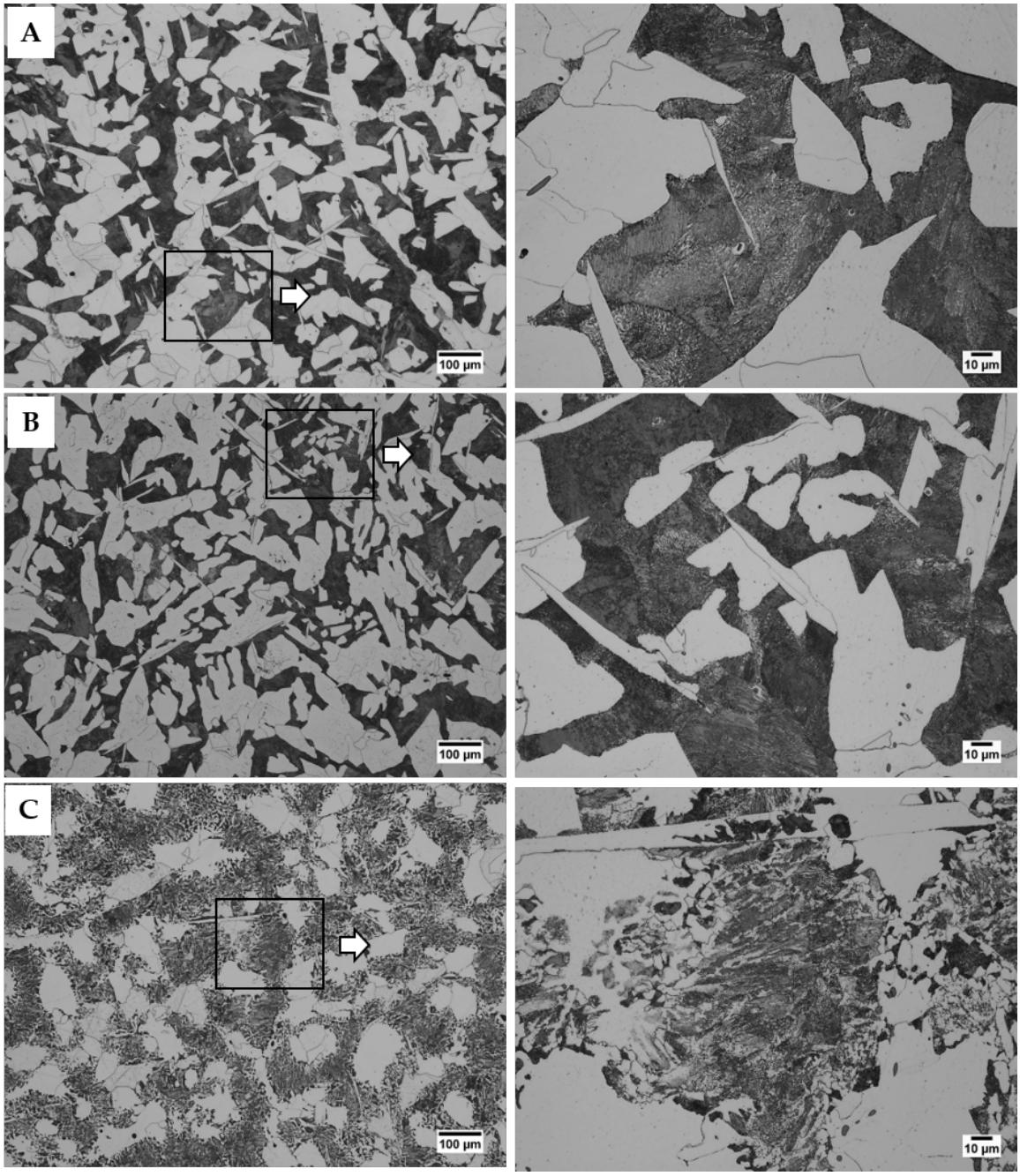


Figure 50. Comparative optical micrographs at 60X and 300X, A) Equilibrium microstructure B) Simulated to a peak temperature of 1380°F, and C) Simulated to a peak temperature of 1425°F.

5.1.4.3 Hypothesis Related to the Increased Amount of Graphitization in the SCHAZ

The subcritical heat-affected zone (SCHAZ) region is exposed to peak temperatures below the lower critical transformation temperature (Ac_1) of 1384°F (751°C). The HAZ region simulated at a peak temperature of 1380°F (749°C) did not show any optically discernible microstructural difference when compared to the base metal prior to simulation (see Figure 50). When the hypoeutectoid steel used in this program is heated to a temperature of 1380°F (749°C) during welding, the solubility of carbon in alpha-ferrite reaches its maximum solubility (~0.025 wt.% C). The solubility of carbon in alpha-ferrite at room temperature is ~0.002 wt.%. This is shown by the solvus line (for alpha-ferrite) on the Iron-carbide (Fe- Fe_3C) diagram in Figure 51. Note that this phase diagram is not drawn to scale in order to accentuate the alpha-ferrite region for improved interpretation. The change in solubility of carbon in alpha-ferrite between a peak SCHAZ temperature of 1380°F (749°C) and room temperature is approximately 90 percent. For complete understanding on mechanisms behind the increased amount of graphitization in the SCHAZ, it is important to study the microstructural and compositional changes before, during, and after welding.

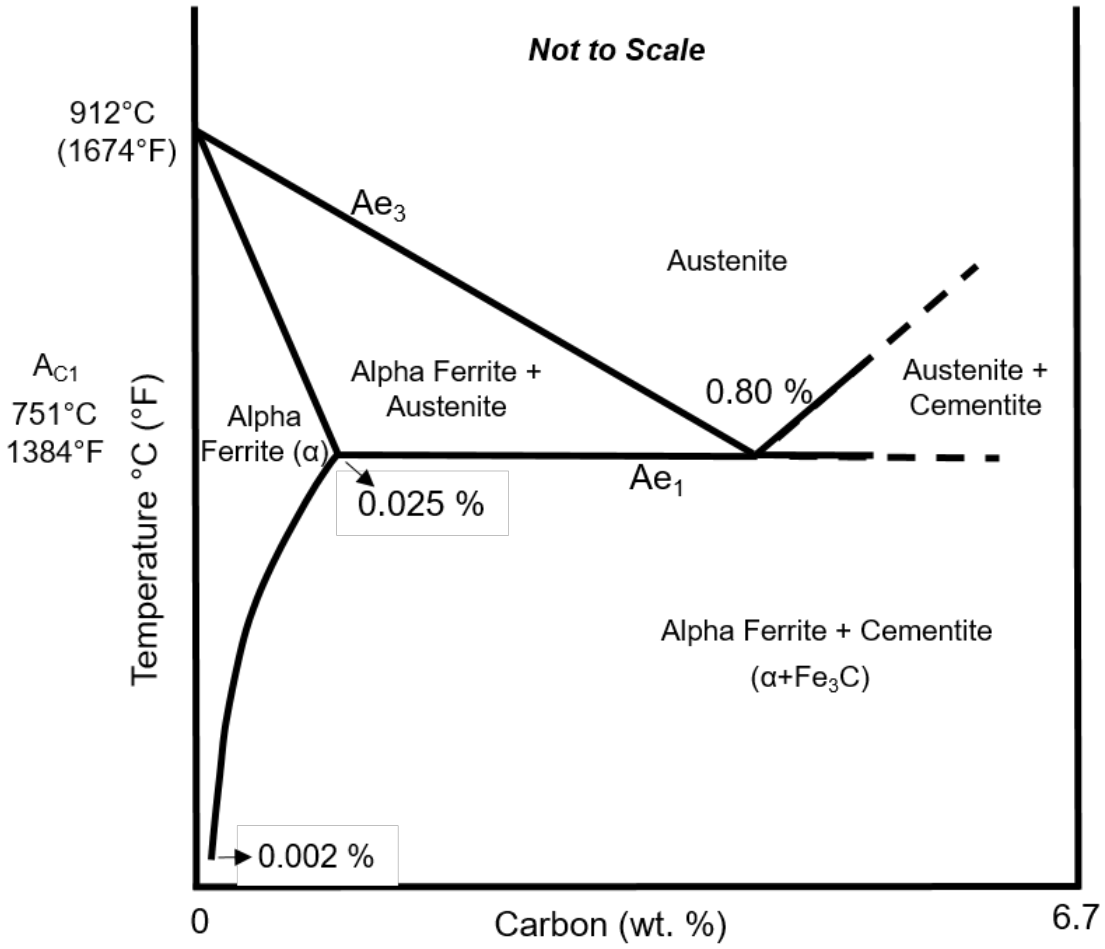


Figure 51. Schematic of Fe- Fe_3C diagram re-drawn to show the solubility difference of carbon in alpha-ferrite as a function of temperature. This phase diagram is not drawn to scale to accentuate the alpha-ferrite region.

The microstructural changes in the SCHAZ can be described in four parts with respect to the thermal history and compositional viewpoints.

1. Step I: Prior to welding (Hypoeutectoid steel at ambient temperature)

2. Step II: During welding (Hypoeutectoid steel is heated to a temperature at or just below its Ac_1)

3. Step III: During cooling (Hypoeutectoid steel is cooled to ambient temperature)

4. Step IV: Hypoeutectoid steel component is placed in service at elevated temperature below the Ac_1 temperature (e.g. 800°F/427°C)

Step I: Prior to welding (Hypoeutectoid steel at an ambient temperature)

Typical microstructure in the SCHAZ region consists of alpha-ferrite and pearlite (ferrite + cementite). This is schematically shown in Figure 52 with the ferrite-cementite ($Fe-Fe_3C$) interface between a pearlite colony and ferrite grain is indicated.

Prior to the start of welding, the hypoeutectoid steel is at ambient temperature (T_1), as is indicated on the phase diagram in Figure 53. The maximum solubility of carbon in ferrite at T_1 is ~0.002 wt. % and cementite, an

intermetallic compound, with 6.7 wt. % carbon. The carbon levels at the ferrite-cementite interface for T_1 are shown in the concentration profile. The original ferrite-cementite interface position prior to welding is indicated by a dashed line and the ferrite is at a composition of ~0.002 wt. % carbon

Step II: During welding (Hypoeutectoid steel is heated to a temperature at or just below Ac_1)

During welding, the SCHAZ region is heated to a temperature at or just below the Ac_1 temperature. The solubility limit of carbon in ferrite increases with an increase in temperature and reaches its maximum solubility limit at the Ac_1 temperature (increases from ~0.002 wt.% to ~0.025 wt. %). The composition limit of carbon in cementite however remains the same at 6.7 wt.%. Because of the increased solubility of carbon in ferrite and the carbon concentration difference between alpha-ferrite and cementite, some of the cementite must decompose and the carbon diffuses into ferrite. This increases the ferrite carbon concentration and develops a carbon gradient in the ferrite. This postulated concentration gradient at the peak temperature of 1380°F/749°C [just below the Ac_1 temperature at T_2] is shown in Figure 54. It is assumed that the ferrite-cementite interface remains in a localized equilibrium condition (within a few atomic distances from the interface), and the carbon concentration in the

ferrite proceeds towards ~0.025 wt. % C. The ferrite away from the ferrite-cementite interface develops a carbon concentration gradient by diffusion. It is axiomatic that the increase in solubility of carbon also results in dissolution of a portion of the cementite and thus the thickness of cementite platelets is reduced. This is schematically shown in Figure 54. Dashed lines show the original ferrite-cementite interface, and black arrows illustrate the direction of interface movement and red arrows indicate the direction of carbon diffusion from cementite toward the ferrite maximum solubility.

Step III: During cooling to an ambient temperature after welding

When the steel is cooled to ambient temperature (T_1) after welding from temperature (T_2) (1380°F/749°C), just below Ac_1, the alpha-ferrite follows the decreasing the solubility limit (solvus) of carbon in ferrite from ~0.025 wt. % C toward the solubility limit of ~0.002 wt. % C at T_1. Since, welding thermal cycles involve rapid cooling (75F°/sec), the time interval to reach ambient temperature does not permit all of the carbon in ferrite at T_2 to completely level the concentration gradient and concomitantly re-form cementite. Soluble carbon from the region immediately adjacent to the ferrite-cementite interface reacts to form cementite. Ferrite reaches a local equilibrium (within a few atomic distances from the ferrite-cementite interface) with a carbon concentration of 0.002 wt.%.

However, with decreasing diffusivity of carbon with temperature/time, some excess carbon is retained in the alpha-ferrite resulting in a supersaturated solution of carbon in alpha-ferrite. The carbon concentration in alpha-ferrite shows a decreasing gradient away from the ferrite-cementite interface as depicted as a double gradient in Figure 55. Because of the reduced solubility of carbon at ambient temperature, excess carbon in the ferrite is either rejected as graphite nuclei or forms cementite particles. This is schematically depicted in the microstructural illustration in Figure 55. The thickness of cementite platelets re-grow (increase) and the repositioned ferrite-cementite interface is shown in Figure 55. Comparative SEM micrographs at 50KX, 100KX and 200KX prior to simulation and after the 1380°F (749°C) weld thermal cycle simulation, reveals evidence of precipitation of nanoscale particulates (20-50 nm) of excess carbon in the form of graphite and/or cementite.

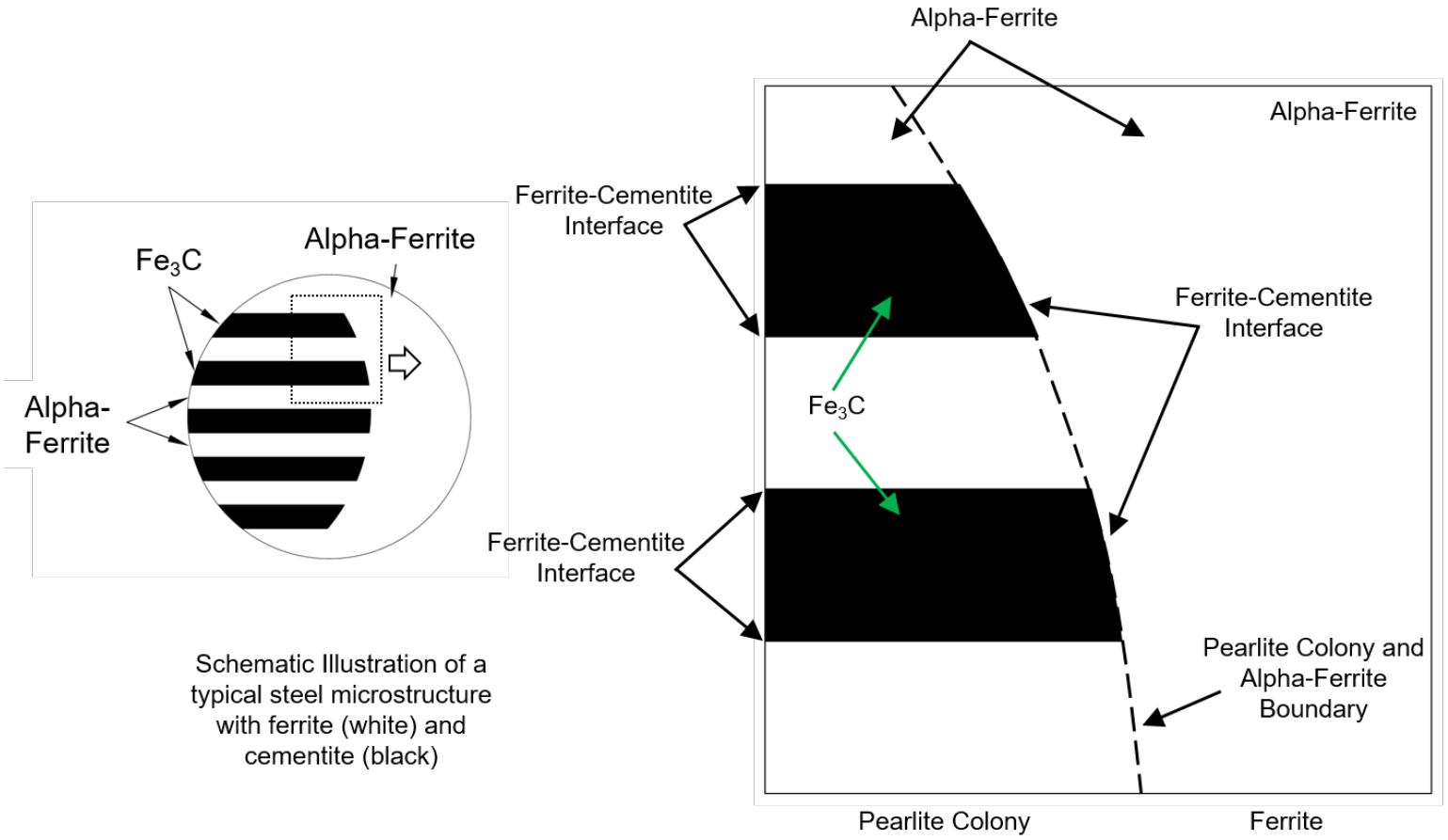


Figure 52. Schematic illustration of a typical microstructure in hypoeutectoid steel, consisting of microconstituents ferrite and pearlite.

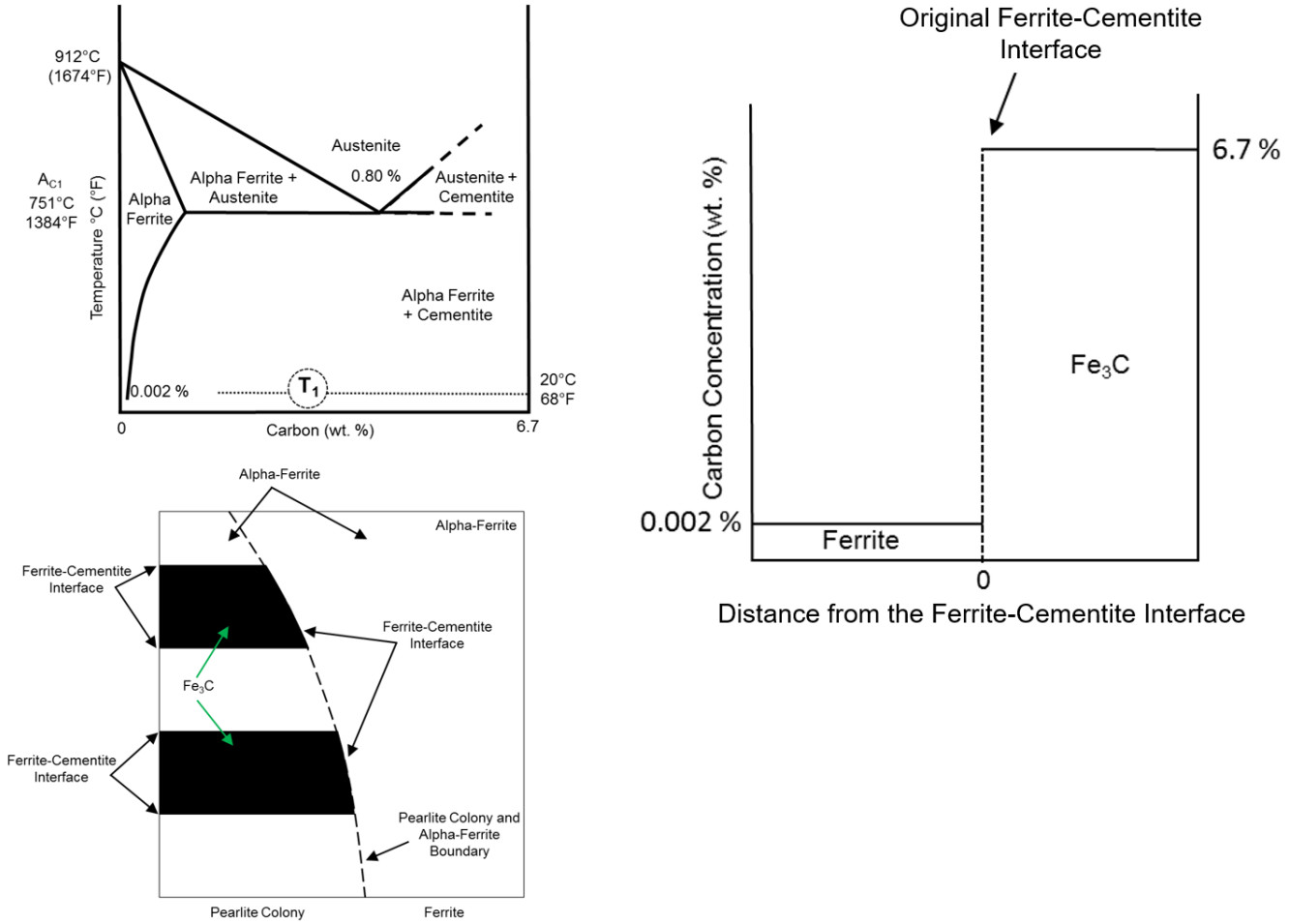


Figure 53. Step I – Hypoeutectoid steel at ambient temperature (T_1) prior to welding. Schematic illustration of a typical hypoeutectoid steel microstructure with ferrite (white) and cementite (black).

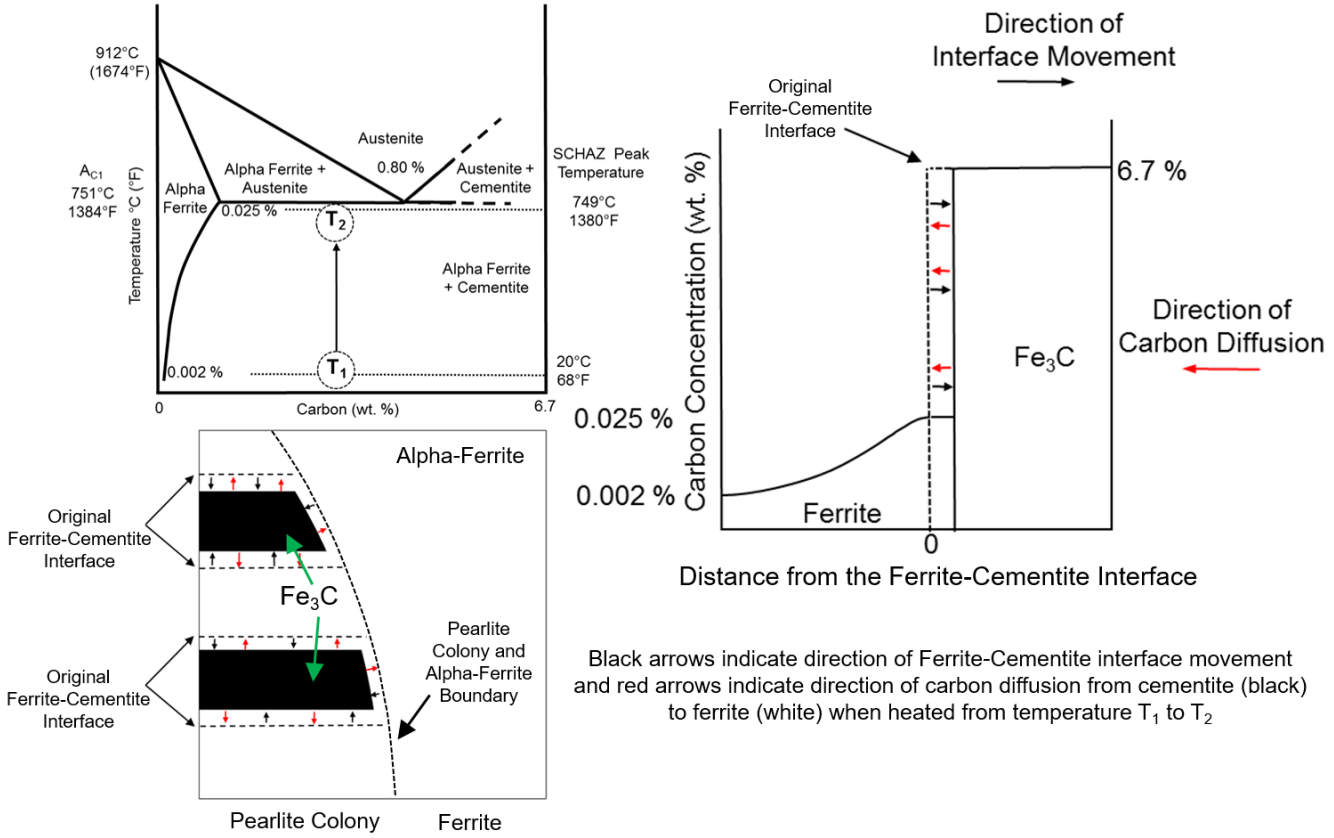


Figure 54. Step II – Hypoeutectoid steel is heated rapidly (~160F°/sec) during welding from ambient temperature (T_1) to a temperature below the lower critical transformation temperature Ac_1 (T_2).

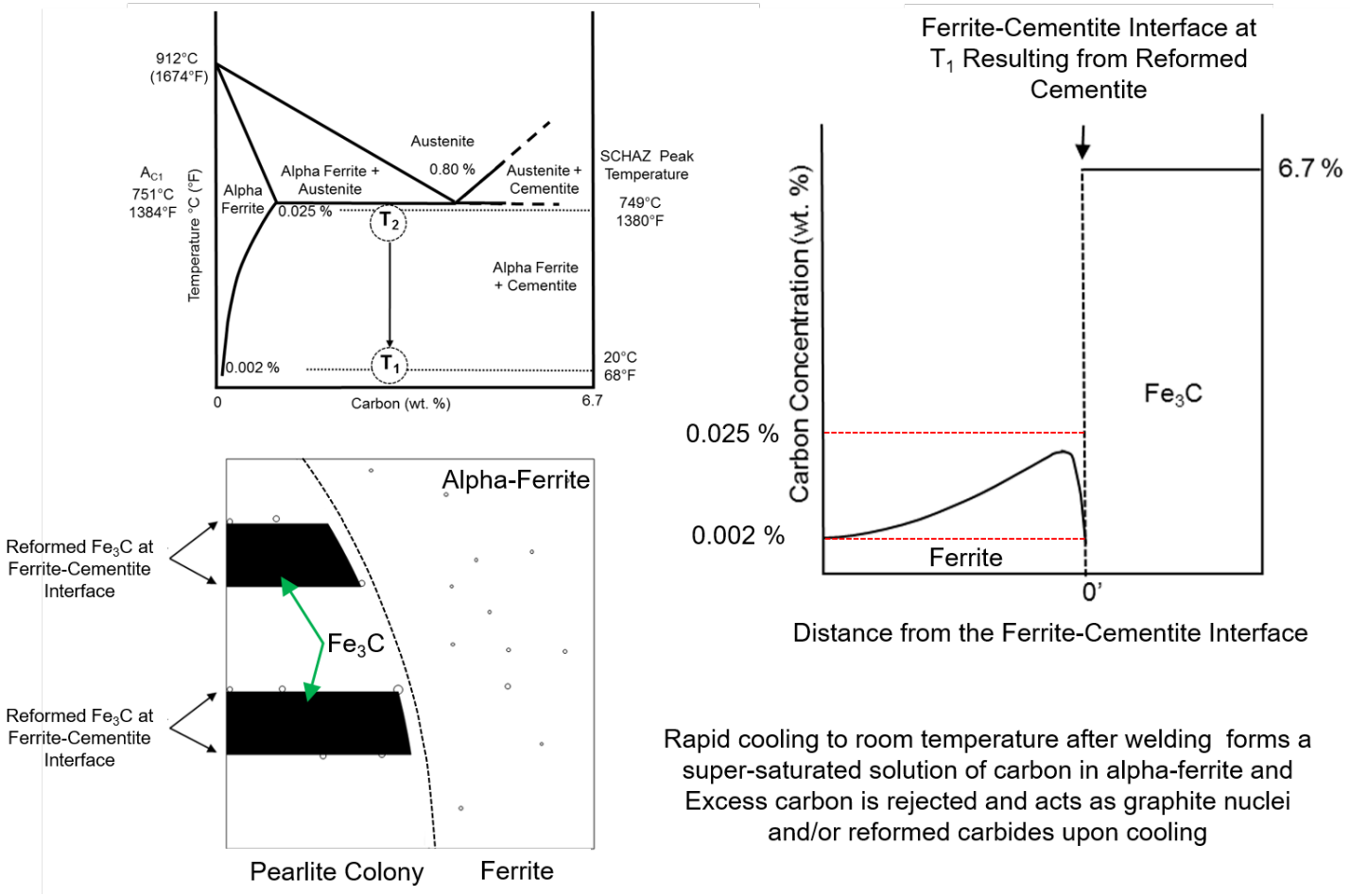


Figure 55. Step III – Hypoeutectoid steel is rapidly cooled (~75F°/sec) from a temperature below the lower critical transformation temperature Ac_1 (T_2) to ambient temperature (T_1) after welding.

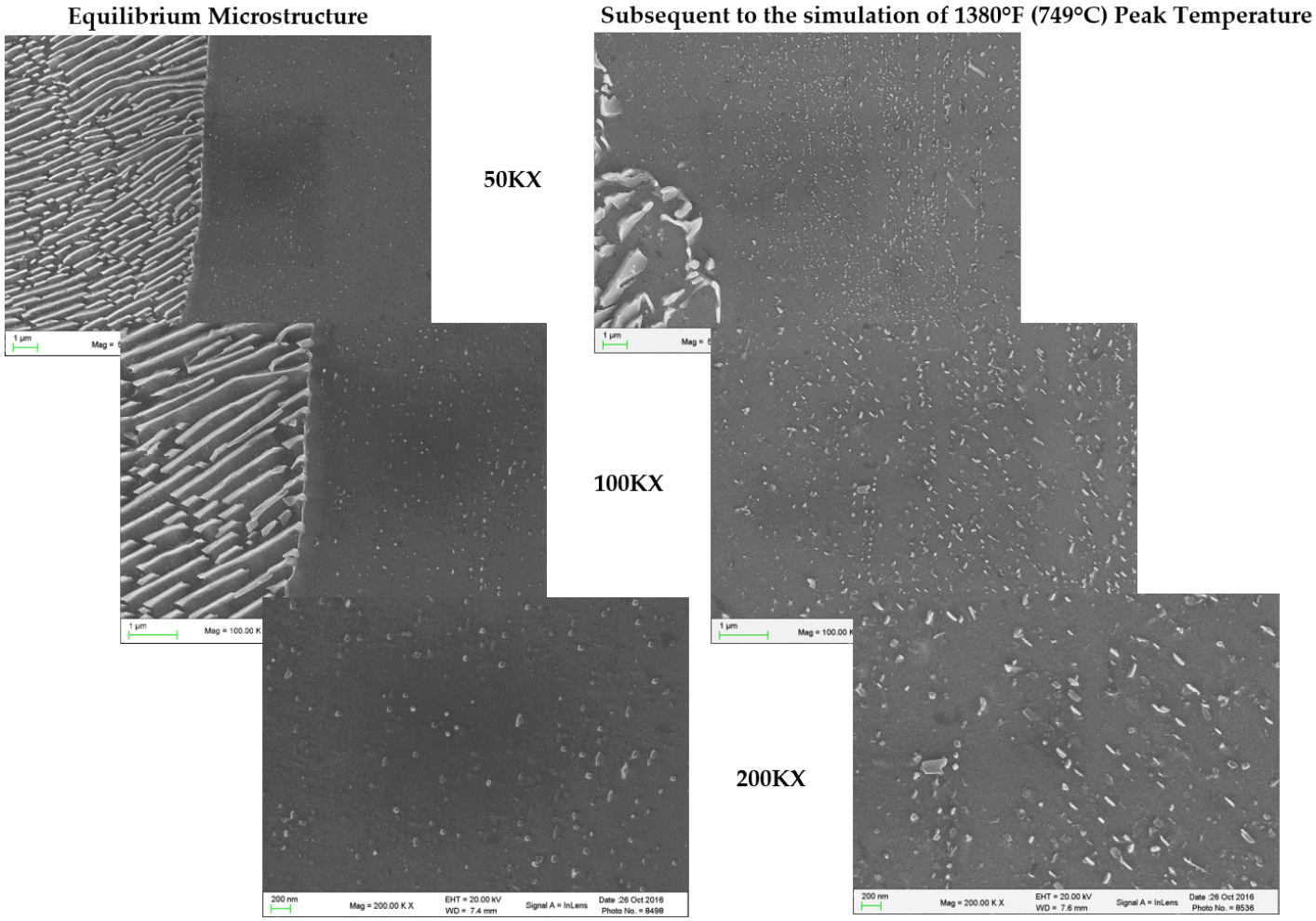


Figure 56. Comparative SEM micrographs prior to simulation (equilibrium microstructure, left) and subsequent to the simulation of 1380°F (749°C) peak temperature.

Step IV: When the welded hypoeutectoid steel component is placed in longtime service at ~800°F/427°C

When the hypoeutectoid steel component is placed in service at a typical steam service temperature of 800°F (427°C), the solubility limit for carbon in ferrite increases to ~0.008 wt. % C from the room temperature limit of ~0.002 wt. % C. Cementite is metastable and when provided with sufficient energy to overcome the thermal activation barrier, decomposes to form ferrite and graphite. The nanoscale particulates precipitated as described above act as nuclei for graphite formation and subsequent growth.

$$Fe_3C \rightarrow 3Fe + C \text{ (graphite)}$$

In addition, because of the increased solubility of carbon in ferrite and the metastable nature of cementite, carbon from Fe_3C diffuses into the alpha-ferrite and enhances graphite growth. The dissolution of cementite reduces cementite platelet thickness. The carbon atoms diffuse and form on the already nucleated graphite at the ferrite-cementite interface or in the alpha-ferrite. This is schematically shown in Figure 57. Dashed lines show original ferrite-cementite interface, black arrows illustrate the direction of interface movement and red arrows indicate the direction of carbon diffusion. Figure 58 (50KX and 100KX) and Figure 59 (100KX) shows microstructural evidence of graphite nucleation

along ferrite-cementite interfaces, after 500 hours of exposure at 1000°F (538°C). The temperature of 1000°F (538°C) is higher than a typical operating temperature of the steel components under investigation 800°F (427°C) but it was selected to accelerate the graphitization reaction rate during aging studies (diffusivity of carbon increases with temperature and no phase transformation occur between 800°F and 1000°F).

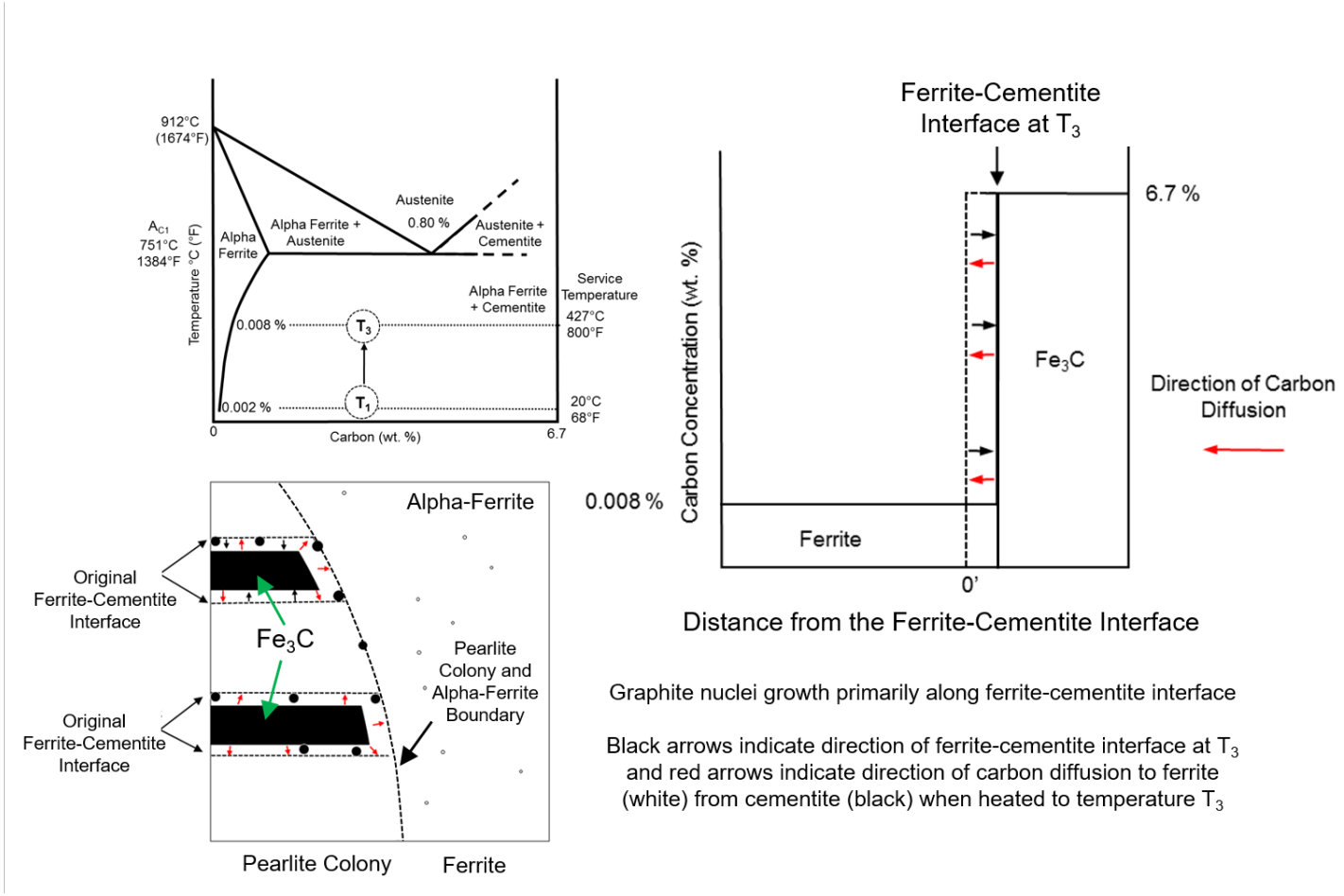


Figure 57. Step IV – Welded hypoeutectoid steel component is heated from ambient temperature (T_1) to a typical service temperature (T_3) of ~800°F/427°C.

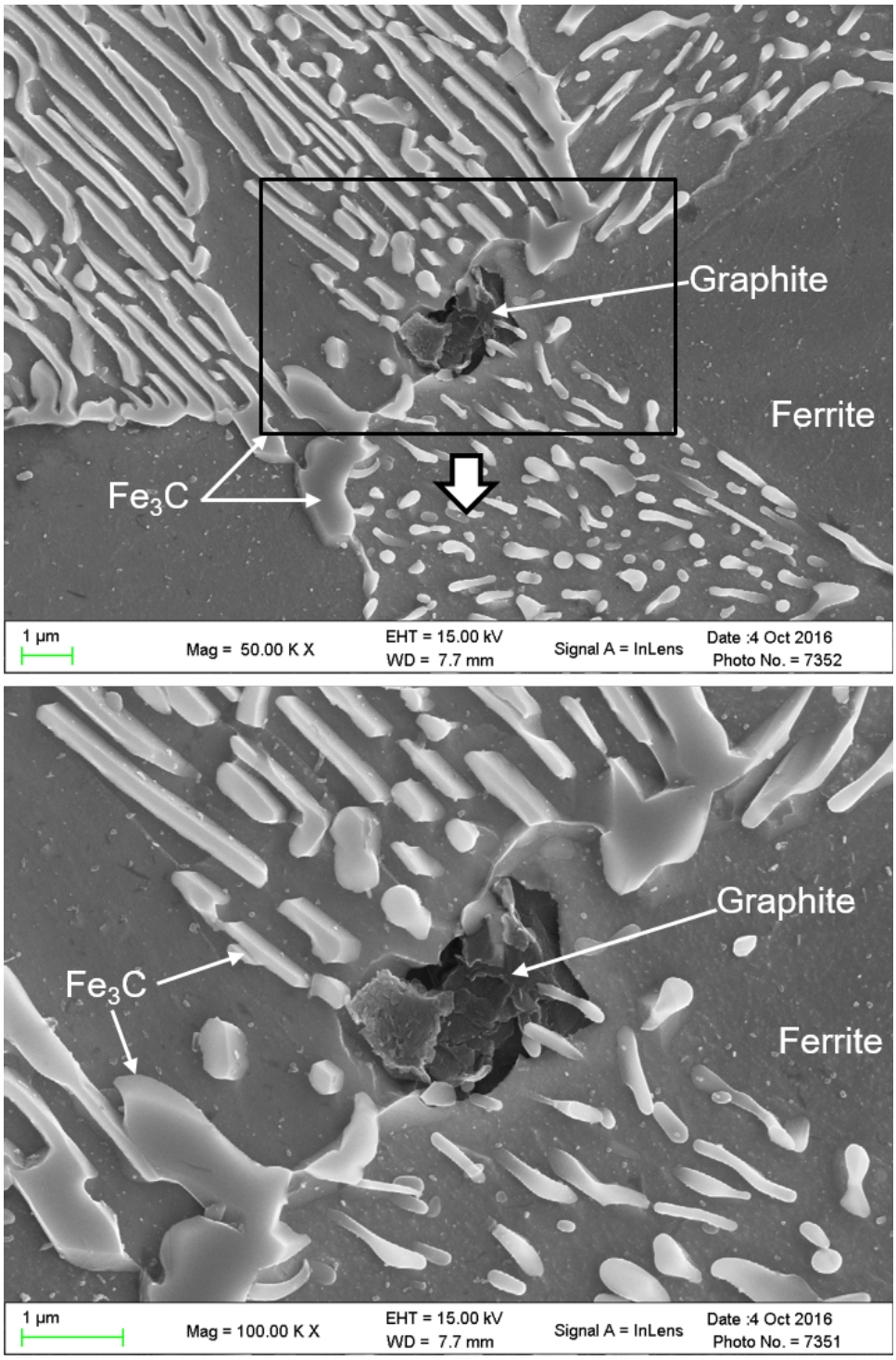


Figure 58. SEM micrographs showing evidence of graphitization at ferrite-cementite (Fe-Fe_3C) interface. Graphitization was observed after 500 hours of exposure at 1000°F (538°C).

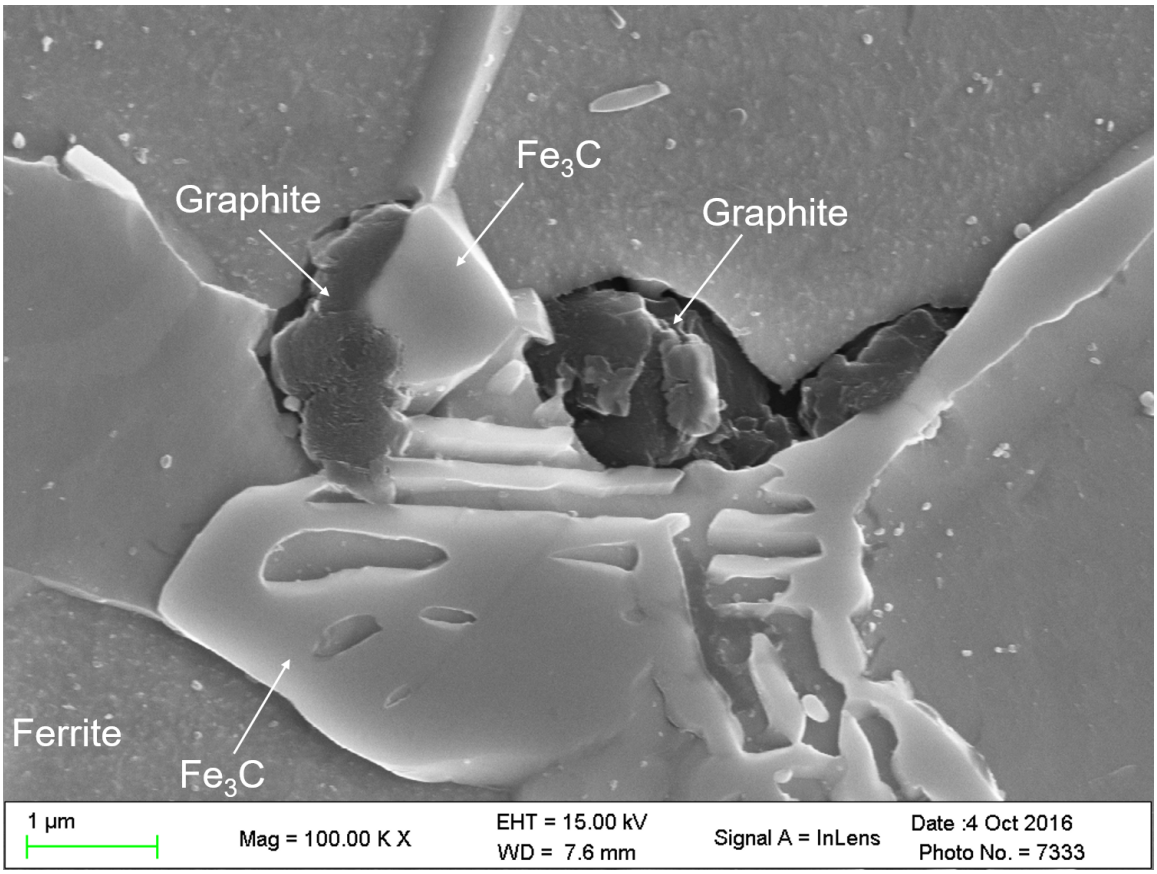


Figure 59. SEM micrograph showing evidence of graphitization at ferrite-cementite (Fe-Fe_3C) interface. Graphitization was observed after 500 hours of exposure at 1000°F (538°C).

Secondary Influence of Aluminum and Silicon on Increased Graphitization in SCHAZ

Aluminum and silicon are probably the most discussed element with regards to graphitization in carbon steels [9, 11, 12, 16-18, 45-51]. Aluminum is primarily added as a deoxidizing element along with silicon during the steel making process to minimize porosity. With regards to graphitization, it is considered significant that, when steels are to be operated in an elevated temperature range, de-oxidation practice (primarily aluminum) has a significant influence on occurrence of graphitization. However, there has been no significant explanation in the literature on why aluminum de-oxidized steels graphitize more easily than those steels without aluminum are only anecdotal considerations. This has influenced how researchers perceive graphitization to date. An influence of aluminum or silicon on the occurrence of graphitization is offered below (for a detailed discussion see section 5.1.3).

Rather than aluminum or silicon acting as a nucleation agent for graphite nuclei, we believe that aluminum/silicon act to accelerate in the rate of graphitization by influencing carbide stability and carbon solubility. Aluminum/silicon partition to ferrite during the transformation of austenite to pearlite and this results in a decrease in the solubility limit of carbon in ferrite.

The decreased solubility of carbon in ferrite results in an increase of carbon activity thus increasing the tendency for carbon to precipitate as graphite.

The increased amount of graphitization in the SCHAZ region may be exacerbated by the segregation of both aluminum and silicon from the adjacent intercritical heat-affected zone (ICHAZ) region during welding. Aluminum and silicon have higher solubility in austenite (γ) compared to ferrite (α). Figure 60 shows the Fe-Al binary phase diagram and Figure 61 shows Fe-Si binary phase diagram. The pertinent regions of the Fe-Al and Fe-Si phase diagrams is enlarged in the inset to accentuate the difference in solubility of aluminum/silicon in austenite (γ), austenite + ferrite ($\gamma + \alpha$) and ferrite (α)[92]. The solubility of aluminum in austenite is 0.35 wt.% and in the austenite + ferrite ($\gamma + \alpha$) region is 0.62 wt.% and 18 wt.% in ferrite (α) at a temperature of 1832°F (1000°C). Silicon has a one order of magnitude higher solubility in ferrite than in austenite. Thus, aluminum or silicon, primarily from the ICHAZ region (which partially transforms to austenite) diffuses towards the SCHAZ region. The major driving force behind the diffusion of aluminum/silicon is the solubility differential of aluminum/silicon in ferrite versus austenite. Any aluminum or silicon which diffuses from the ICHAZ to the SCHAZ will most likely segregate to grain boundaries upon cooling.

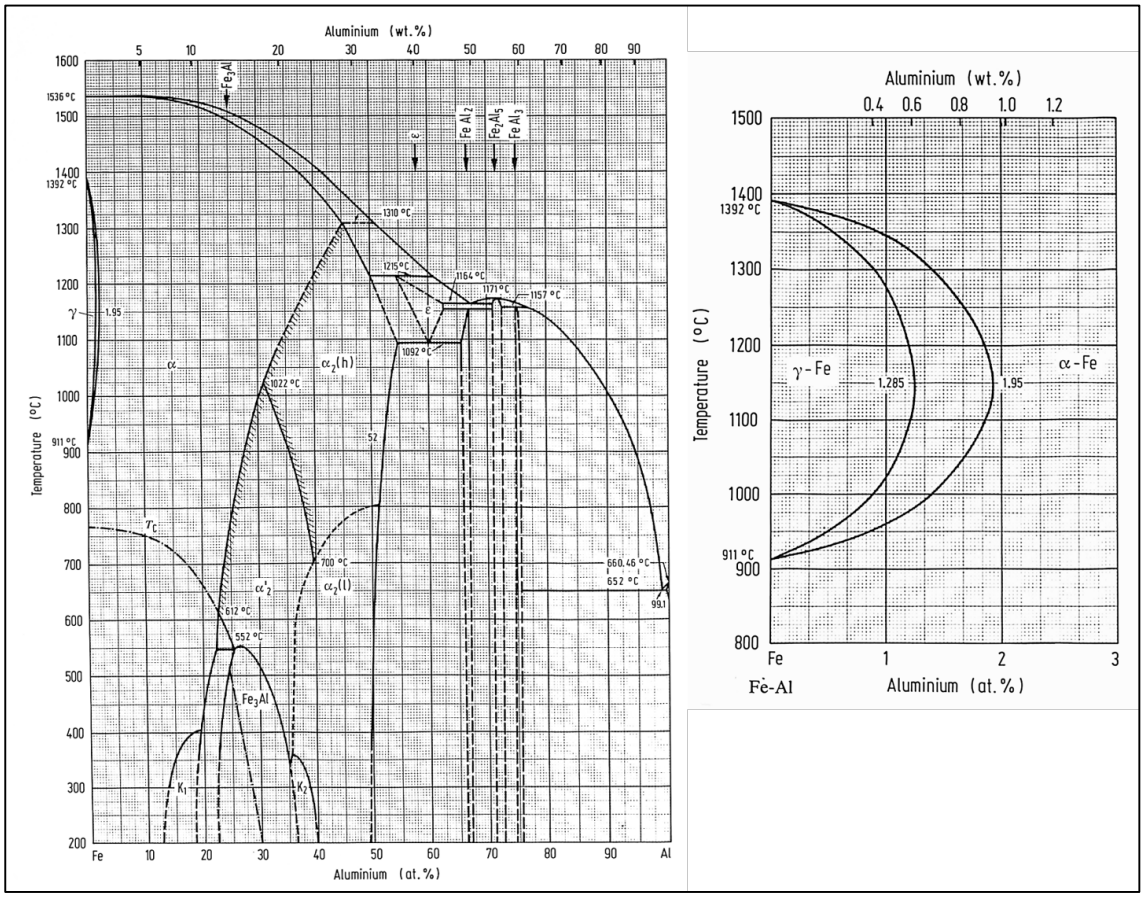


Figure 60. Iron-Aluminum (Fe-Al) binary phase diagram (left), Portion of (Fe-Al) phase diagram emphasizing the region showing the difference of solubility of aluminum between austenite and ferrite (right) [92].

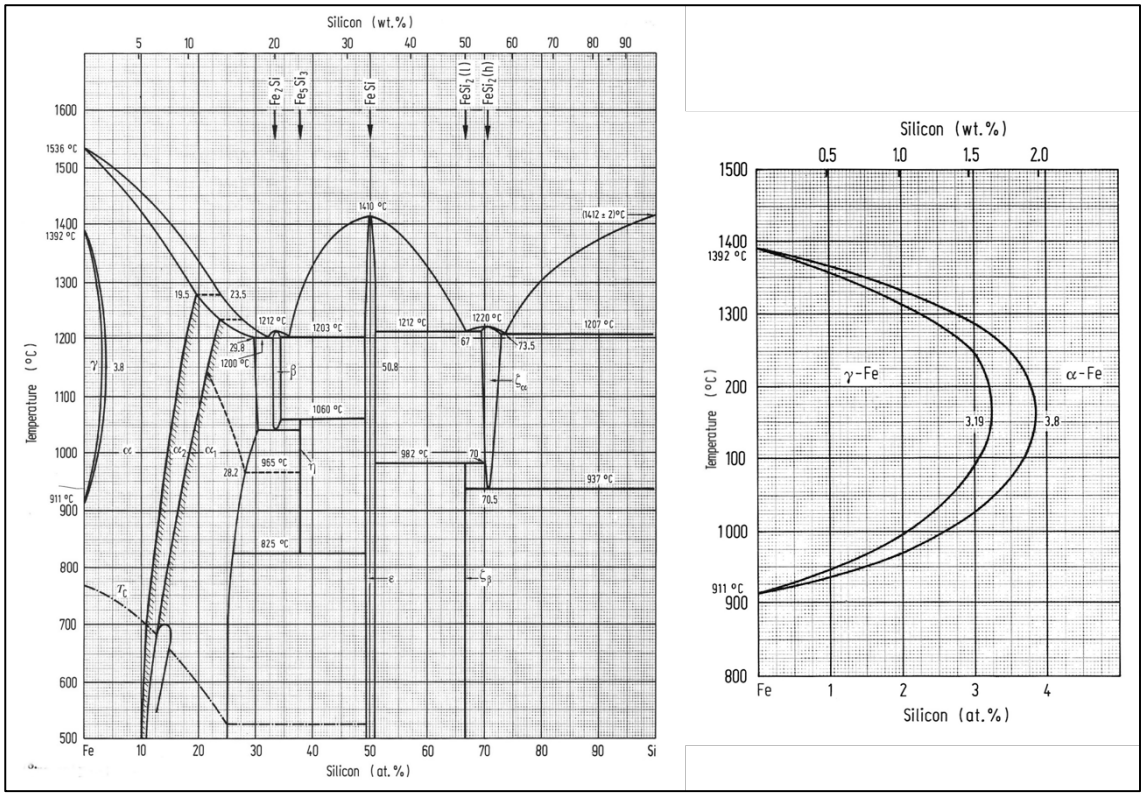


Figure 61. Iron-Silicon (Fe-Si) binary phase diagram (left), Portion of (Fe-Si) phase diagram emphasizing the region showing the difference of solubility of silicon between austenite and ferrite (right) [92].

When the welded components are placed in service at elevated temperatures, these aluminum/silicon rich boundaries may influence the stability of Fe_3C and result an increase in graphitization in the SCHAZ region. However, because of the low diffusivity of aluminum and silicon in iron, it is difficult to conclusively state the true role of these elements, when present, on the increased amount of graphitization in the SCHAZ.

We have made multiple attempts to measure segregation of aluminum or silicon in the SCHAZ regions during welding using energy dispersive spectroscopy (EDS). However, because of the low levels of aluminum and silicon present in the steel in this investigation, conclusive evidence on enrichment of aluminum/silicon in the SCHAZ was not acquired and thus the influence of aluminum/silicon on graphitization is of a hypothetical nature, which if accurate, answers the earlier claims of investigators who espoused the role of aluminum as critical key for graphitization. However, the work herein indicates that the aluminum and silicon affect is ancillary with regard to the graphitization in the SCHAZ in carbon steel.

5.2 In Situ Inspection for Graphitization

Graphitization has been a continued industry concern with regards to in service detectability to prevent shutdown during the operation for inspection. A protocol to evaluate graphitized steel components using both non-destructive (ultrasonic) and destructive (core sample) extraction was studied. Ultrasonic inspection studies were performed with an assistance of Level III - NDE technician from Team Industrial Services Inc. Examination of graphitized components was performed by studying the efficacy of core samples extraction for evaluation of graphitization in service. Core sample extraction was accomplished using Weldcore® Technology with an assistance of Nelson Mandela Metropolitan University (NMMU), South Africa. Repair weldability of the core extraction site was also performed with an assistance of NMMU.

5.2.1 Ultrasonic Inspection

Ultrasonic examination to evaluate the detectability of the presence and extent of graphitization was performed using modern state-of-the-art techniques. The major objective of NDE (non-destructive examination) studies was to enhance ultrasonic inspection capabilities for detection of graphitized materials. Linear phased array, focused phased array, and annular phased array were all

utilized to examine the graphitized components. The results reported herein only contain the results using focused phased array technique, called "Variable Focus Matrix Phased Array" which showed the most improved detectability of graphitization. This study was performed with the assistance of a Level III - NDE technician from Team Industrial Services Inc. Two circumferential welds (CW-A and CW-B) were selected based on the prior metallographic examination results. A summary of the metallographic examination results are provided herein:

Metallographic Examination Summary of CW-A:

Circumferential weld A (CW-A) consists of base metals A1 and A2, and graphitization was observed on both A1 and A2 base metals. Graphitization was not observed in the weld deposit. Both base metals exhibited similar extent of graphitization. The maximum extent of graphitization was observed in the region along the plate mid-wall just outside of the optically visible HAZ for both A1 and A2 base metals. A reduced extent (isolated/scattered) of graphitization was observed in the base metal remote from the HAZ. Although the overall extent of graphitization was similar in the A1 and A2 base metals, graphitization in the A1 base metal was oriented parallel to the plate rolling direction as compared to the A2 base metal which exhibited nodules parallel to the weld

fusion line. Figure 62 shows optical micrographs exhibiting graphitization observed in base metals A1 and A2.

Metallographic Examination Summary of CW-B:

Circumferential weld B (CW-B) consists of base metals B1 and B2. Graphitization was observed only in the B1 base metal. Similarly, to CW-A, the maximum extent of graphitization was observed in the base metal just outside of the optically visible HAZ. Isolated/scattered graphitization was observed away from the HAZ and was to a reduced extent when compared to the base metal adjacent to the HAZ. Graphite nodules were oriented parallel to the plate rolling direction in the B1 base metal. Graphitization was not observed at any locations in the B2 side (base metal, HAZ and the weld deposit). The ultrasonic inspection of the B2 base metal was used for comparison purposes and thus was used to obtain a typical ultrasonic response of non-graphitized material exposed in the same service-environment for a similar extent of time.

Summary of Ultrasonic Inspection Results:

Ultrasonic inspection was performed on both CW-A and CW-B using a focused phased array technique with both 5 and 10 MHz probes. The major ultrasonic indications were observed just outside of the visible HAZ (location of maximum graphitization). However, the intensity of the indications was too

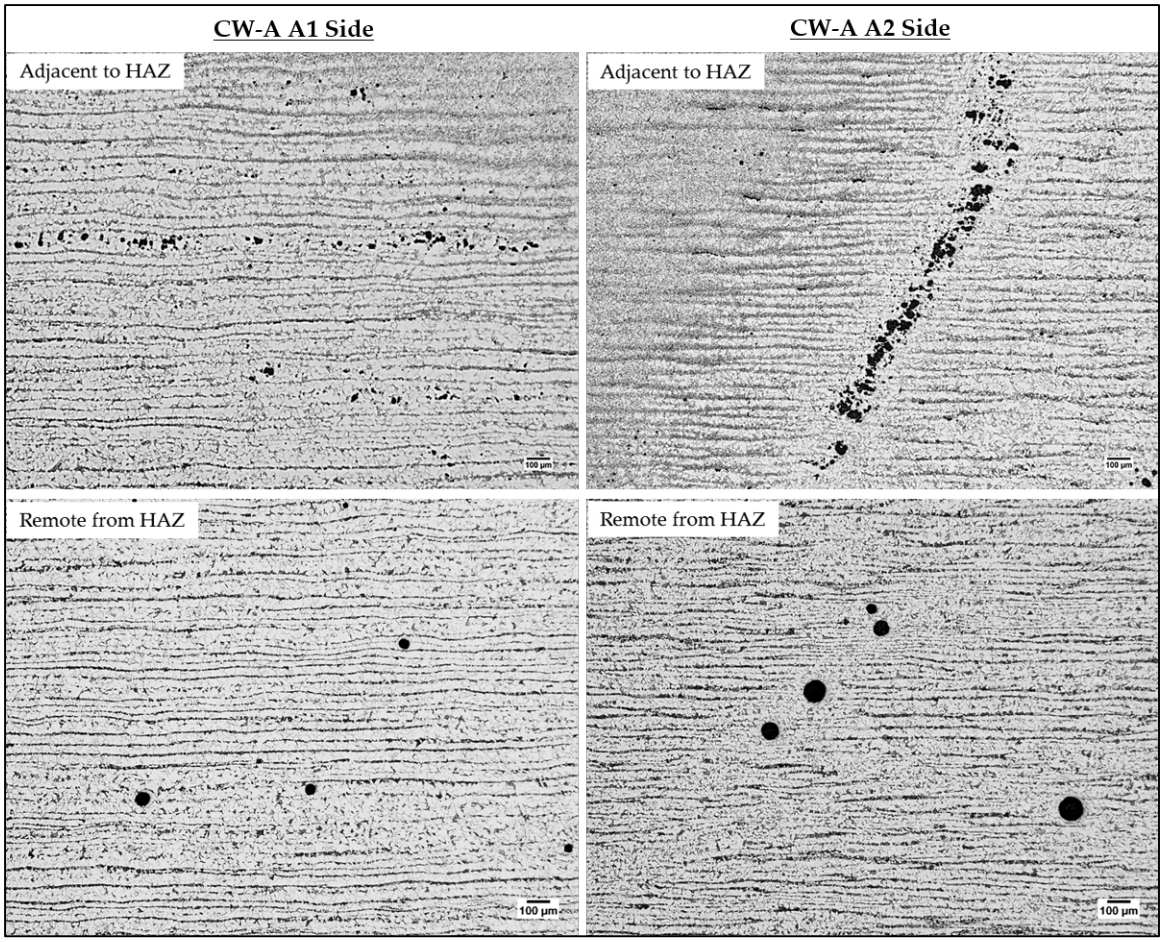


Figure 62. Optical micrographs (50X) from CW-A weldment showing the extent and orientation of graphitization on A1 and A2 base metals.

weak to conclusively determine if they were a result of the presence of graphite nodules. Thus, a comparative approach was devised to evaluate the ultrasonic reflection response between the base metal regions adjacent to the HAZ (maximum graphitized region) and the base metal regions away from the HAZ (reduced graphitization regions). Figure 63 shows the ultrasonic scans using a 10 MHz focused phased array probe showing S-scan, A-scan, B-scan, and C-scan on the CW-B B2 base metal. No relevant indications were detected, which is in agreement with the metallographic examination results. Figure 64 shows the ultrasonic examination results with a 10 MHz focused phased array probe on CW-B B1 base metal. Heavy reflections oriented in the laminar-type (flat) direction was detected. The major reflections were observed adjacent to the weld and the degree of ultrasonic response reduced further away from the weld. Figure 65 shows ultrasonic examination results using a 10 MHz focused phased array probe on CW-A A1 base metal. The indications appear to be strongest in the close proximity of the weld and the intensity decreases but stays relatively consistent further away from the weld deposit. The indications were laminar-type, i.e. oriented parallel to the plate rolling direction (this is similar to graphite orientation shown in the metallographic examination results). Figure 66 shows the ultrasonic examination

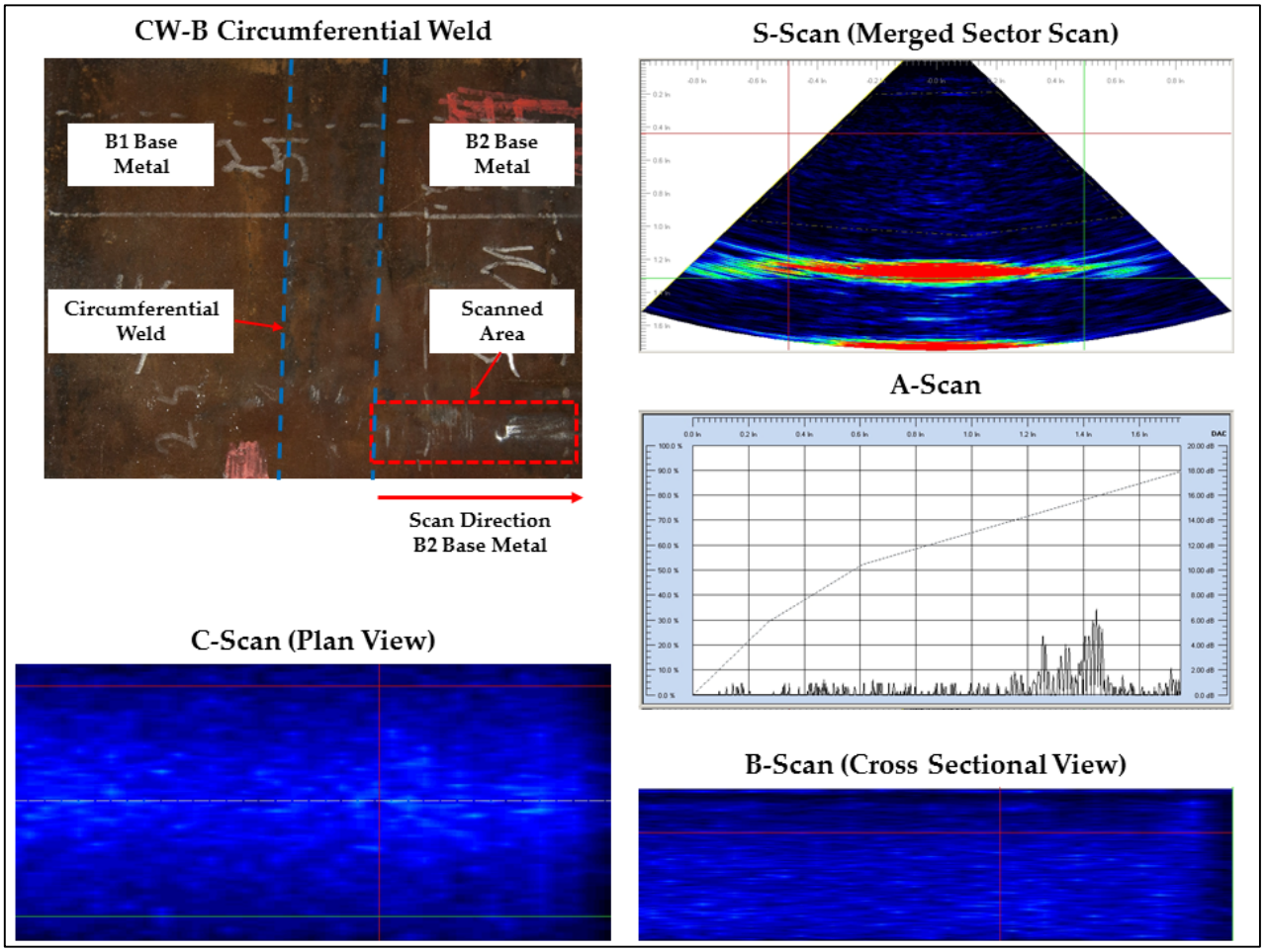


Figure 63. Ultrasonic examination of CW-B, B2 base metal. Red dashed box shows area used for ultrasonic scan. No indications were observed remote from the fusion line.

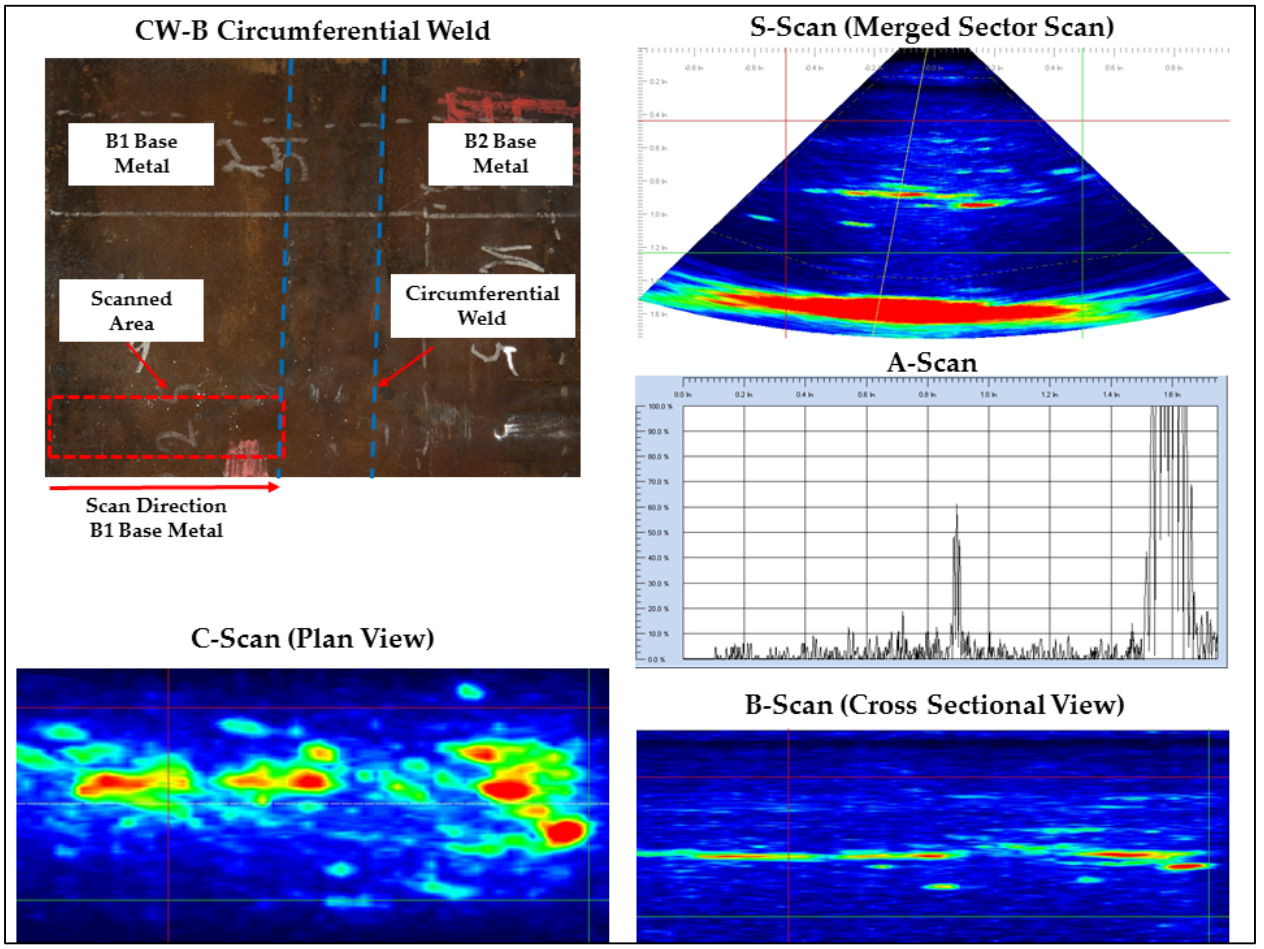


Figure 64. Ultrasonic examination of CW-B, B1 base metal. Red dashed box shows area used for ultrasonic scan. The major UT reflections were observed adjacent to the fusion line and the intensity decreases remote from the fusion line.

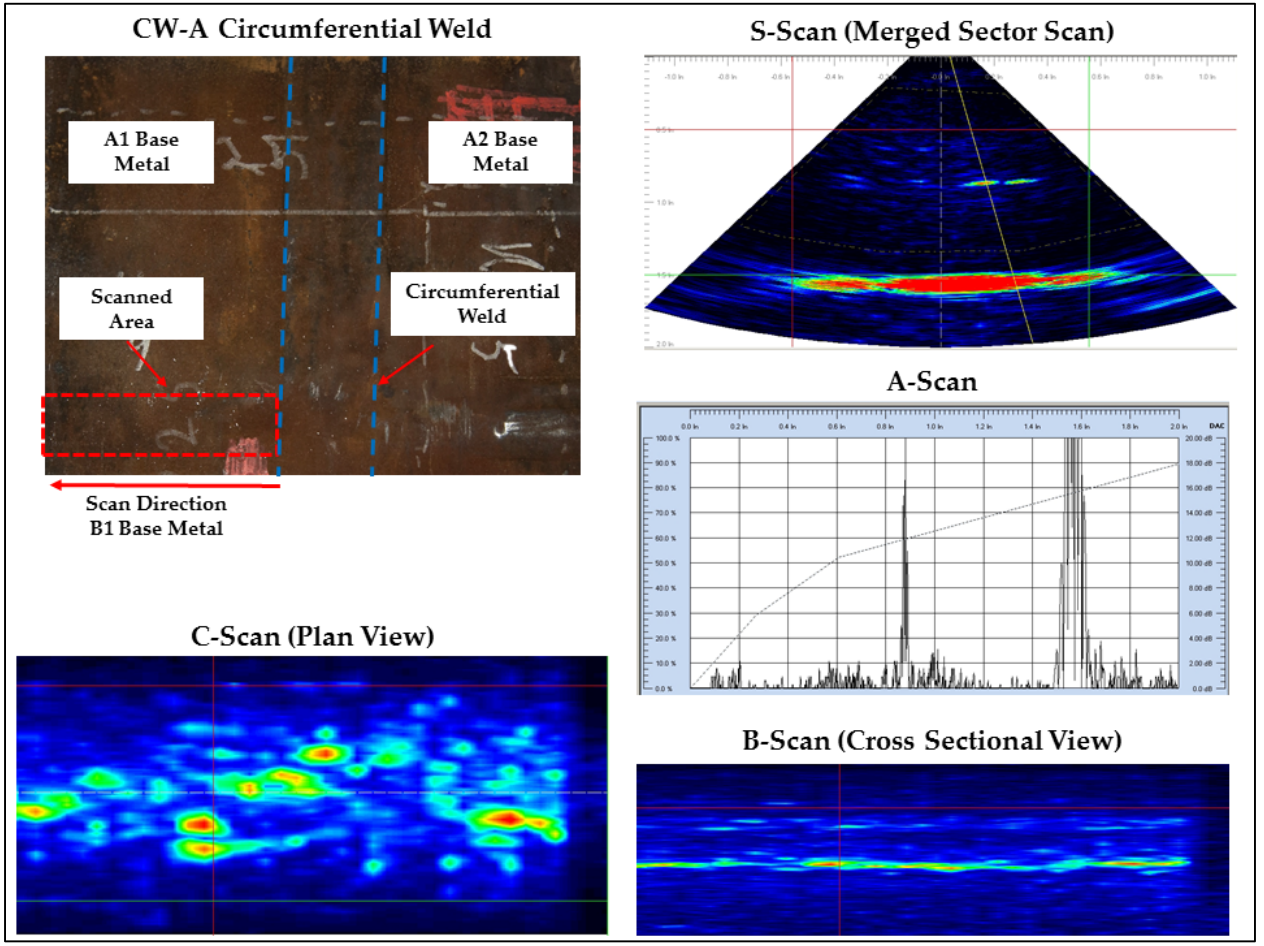


Figure 65. Ultrasonic examination of CW-A, A1 base metal. Red dashed box shows area used for ultrasonic scan. The major UT reflections were observed adjacent to the fusion line and the intensity decreases remote from the fusion line.

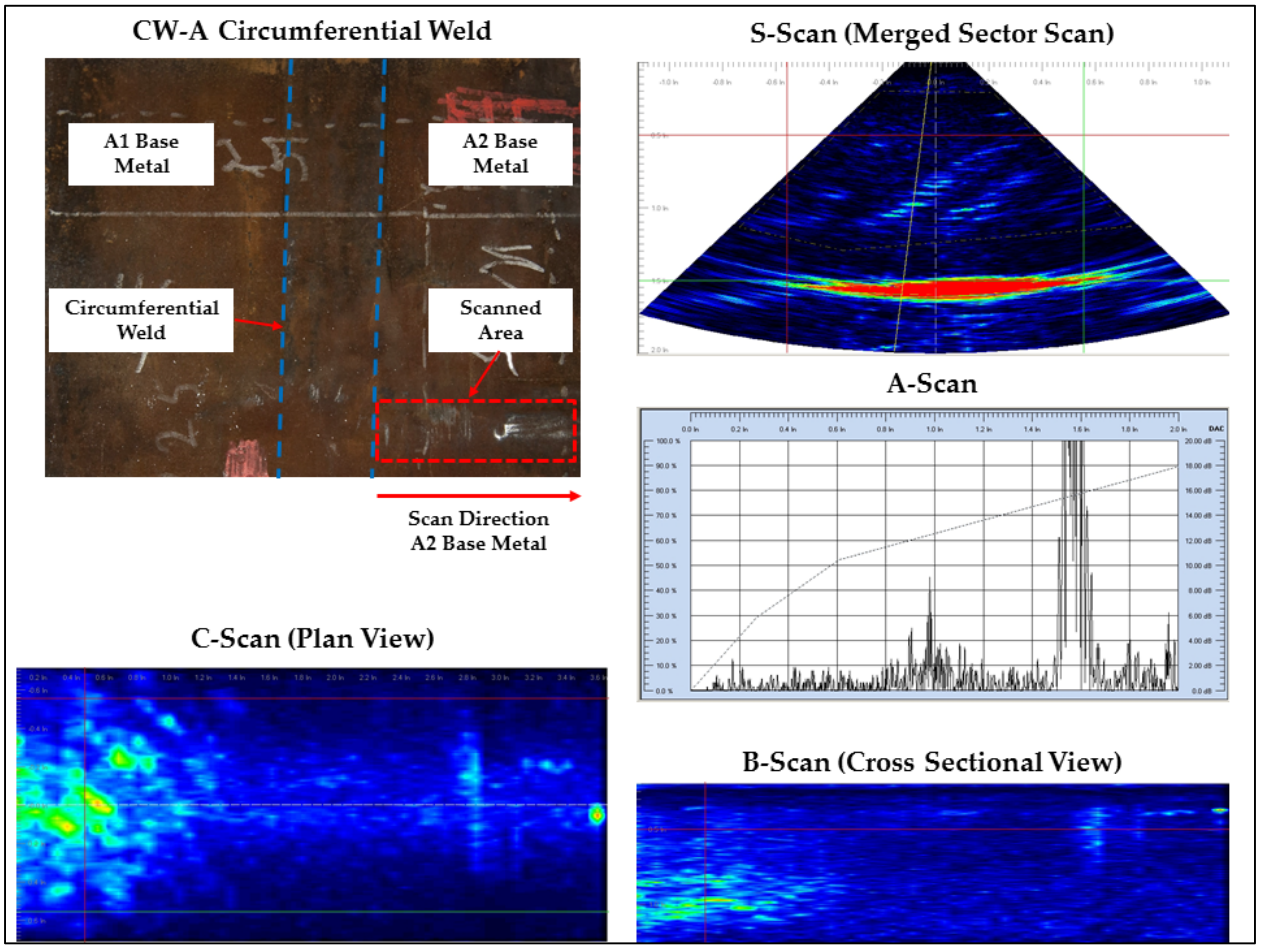


Figure 66. Ultrasonic examination of CW-A, A2 base metal. Red dashed box shows area used for ultrasonic scan. The major UT reflections were observed adjacent to the fusion line and the intensity decreases remote from the fusion line.

results using a 10 MHz focused phased array probe on CW-A A2 base metal. The ultrasonic indications appear with high intensity adjacent to the weld and the amplitude drops off significantly further away. The indications were oriented 45 degrees to the plate rolling direction (see sector scan in Figure 66). The orientation of indications agreed to metallographic examination results shown in Figure 62.

The inspection results showed a clear difference in the ultrasonic response between graphitized regions versus non-graphitized regions during examination of CW-A and CW-B weldments. The improvement in the detectability of the presence of graphite was observed with the latest transducers using Variable Focus Matrix Phased Array. The varying extent of the ultrasonic responses are difficult to ascribe to the occurrence of graphitization at this time; however, progress has been made for ultrasonic examination of graphitized components. This comparative method provides information whether the component requires further evaluation using metallographic examination. Further studies with improved ultrasonic inspection techniques should however must be carried out to clarify responses for the evaluation of graphitized components.

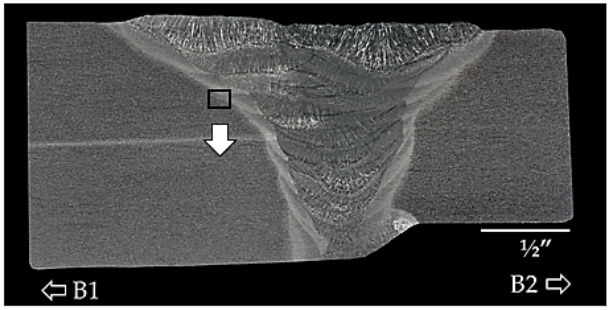
5.2.2 Weldcore® Technology

Two carbon steel circumferential welds designated CW-A and CW-B, which were selected for the ultrasonic inspection studies were also subjected to the core extraction and repair welding studies using Weldcore® Technology. CW-A and CW-B were selected based on their metallographic examination results, as these two weldments exhibited the most extensive graphitization compared to the other materials examined. CW-A consisted of base metals A1 and A2, and CW-B consisted of base metals B1 and B2. Graphitization was observed on both A1 and A2 base metals. CW-B showed graphitization only on the B1 base metal. Graphitization was not observed in any locations of B2 base metal. The maximum extent of graphitization (planar morphology) was observed in the base metal just outside of the optically visible HAZ for both weldments at the location which was exposed to peak temperatures just below the lower critical transformation temperature (Ac_1) during welding. The Ac_1 temperature this region (SCHAZ) was determined to be 1384°F (751°C). Because of the severity of graphitization observed in the base metal region just outside of the optically visible HAZ, this region was selected for core extraction and repair welding studies using friction tapered hydro pillar processing (FTHPP). Figure 67 shows optical macrographs with core extraction locations outlined by red

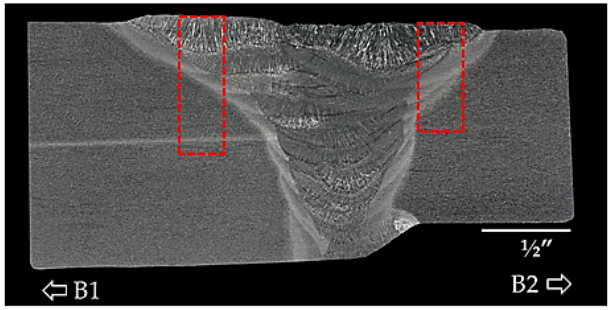
dashed lines. The core extraction locations were selected such that the core samples include a portion of base metal from the plate mid-wall region, which exhibited maximum extent of graphitization and also the regions from the weld deposit and HAZ. This methodology allowed in-situ extraction of specimen which could be utilized for metallurgical characterization and mechanical testing without having to section the entire component.

Metallurgical Examination of Extracted Cores

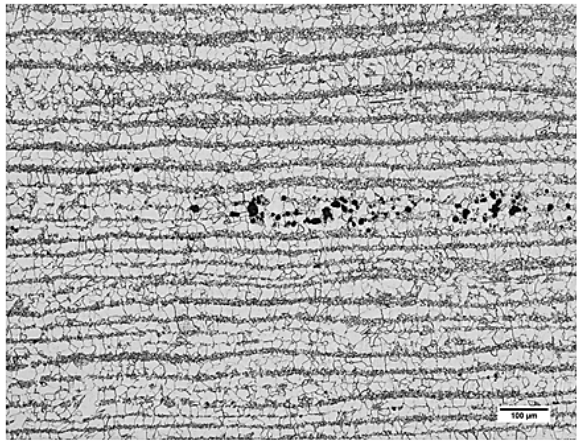
The extracted core samples were 0.31" (8 mm) in diameter and contained approximately ½ of the component wall thickness. Metallurgical examination of the extracted core samples was performed to determine if the in situ core extraction process would be a representative of extent of graphitization present in these components. Figure 68-a shows a photograph of the extracted core sample and Figure 68-b shows the cross-sectional macrograph of the core sample. The macrograph shows that the extracted core sample consisted of regions containing the weld deposit, heat-affected zone (HAZ), and the base metal. Optical microscopic examination of the core sample showed the maximum extent of graphitization was present in the base metal just outside of the visible HAZ (Figure 68-c) and random/isolated type graphitization was observed in the base metal remote from the HAZ (Figure 68-d).



(a) Location of Primary Graphitization



(b) Core Extraction Location



(c) Optical micrograph in the region just outside of the visible HAZ

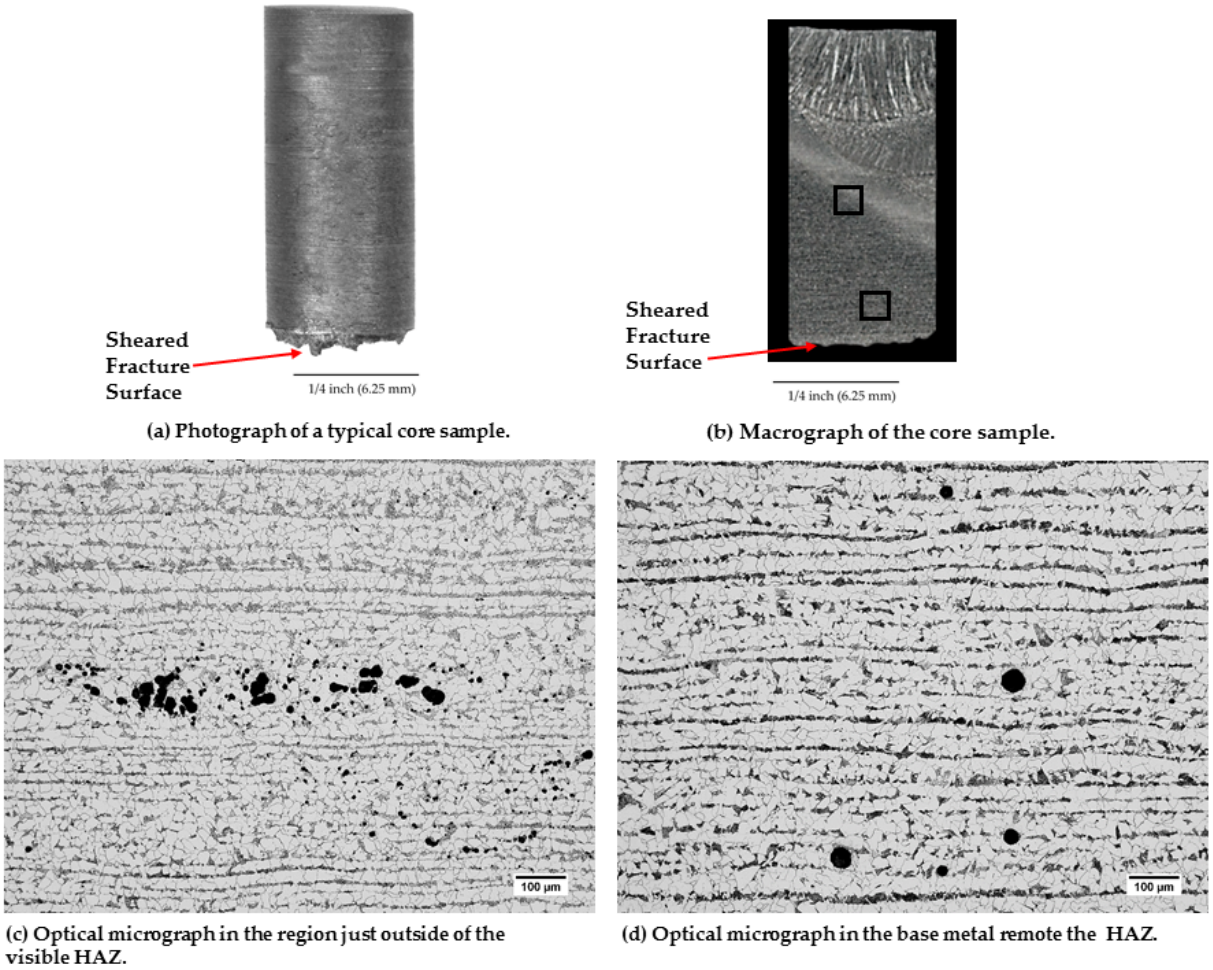
- Red dashed boxes showing the locations of core extraction site.
- Approximately 8 mm diameter cores; 15 mm long on the B1 side and 10 mm on the B2 side were extracted.

Wall-thickness B1 = 1 3/8″ (35 mm)

Wall-thickness B2 = 1″ (25.4 mm)

- Dashed red boxes show approximate location of core extraction.
- Locations were selected such that the extracted sample includes the region just outside of the HAZ, where graphitization was primarily observed.

Figure 67. Core extraction procedure, a) Location showing the most graphitization susceptible region which was selected for core extraction to examine extent of graphitization in the component, and b) Dashed red boxes in the macrograph shows approximate core extraction location on CW-B circumferential weldment.



(a) Photograph of a typical core sample.

(b) Macrograph of the core sample.

(c) Optical micrograph in the region just outside of the visible HAZ.

(d) Optical micrograph in the base metal remote the HAZ.

Figure 68. Metallographic examination of the core sample extracted from CW-B.

Graphitization was not observed in the weld deposit or the HAZ. These metallurgical examination results are comparable to what was previously observed in examination of full-wall cross-sectional metallurgical specimens. Thus, core extraction appears to be a viable approach for in situ evaluation of graphitized components.

Repair-Welding

Figure 69 shows a photograph of the core and the core extraction site prior to the repair welding. The core removal sites were subsequently repaired by friction tapered hydro pillar processing (FTHPP) using ASTM A516-70 carbon steel plug material. Figure 70 shows a photograph of a completed typical FTHPP weld prior to sectioning the excess plug (consumable) material. Evidence of flash formation as a result of plastic flow and upsetting force was observed (see Figure 70 indicated by a red arrow). Figure 71 shows the position of the plug material with respect to the original girth weld. Figure 72 shows the macrograph of the completed FTHPP weld prior to sectioning the excess plug material and FTHPP weld macroscopically showed 100% bonding with no defects along the interface. Plastic flow and evidence of flash formation is evident on the top surface, result of forging force during the last stage.

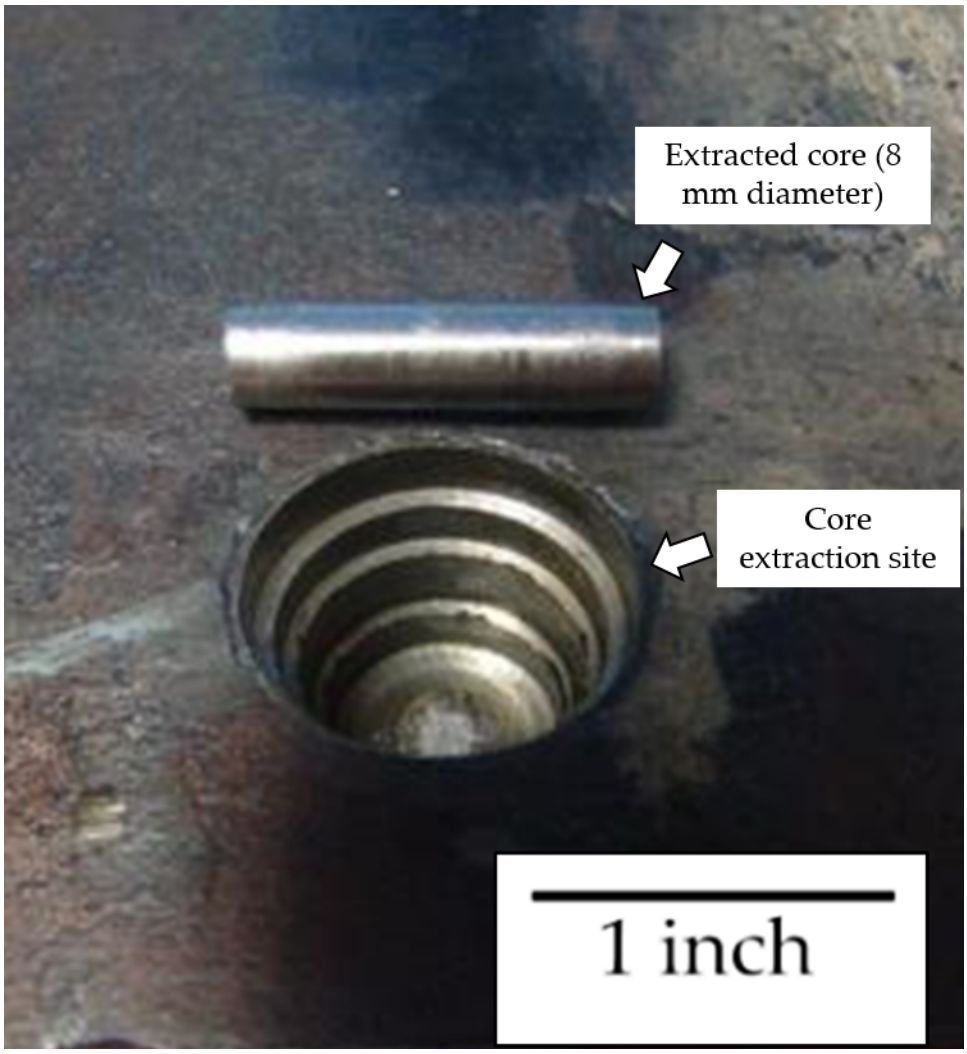


Figure 69. Photograph showing the extracted core and core extraction site prior to finishing for repair welding.



Figure 70. Photograph showing the completed FTHPP weld prior to sectioning the excess plug material. Red arrow shows flash formation of the consumable tool as a result of plastic deformation.

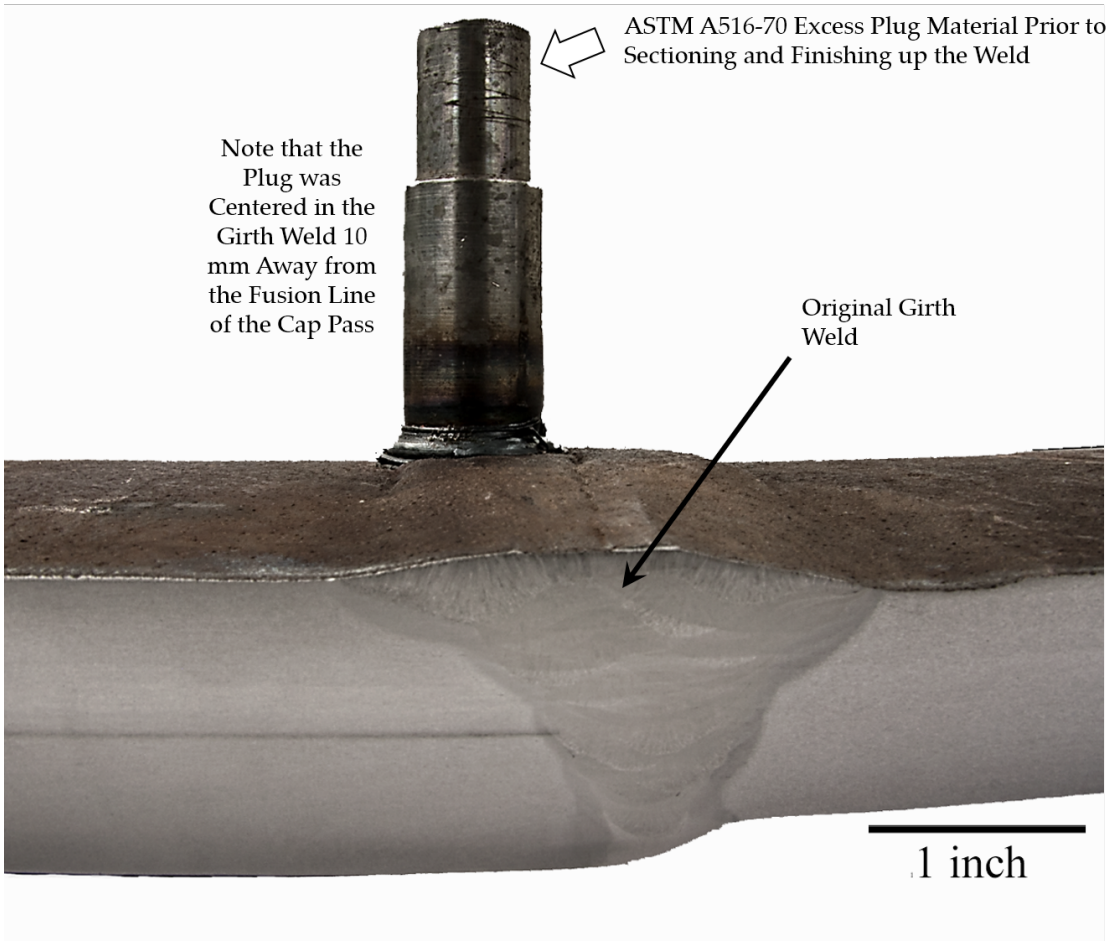


Figure 71. Cross-sectional view of the completed FTHPP weld showing the position of the consumable (Plug Material) with respect to the fusion line, 10% Nital etch.

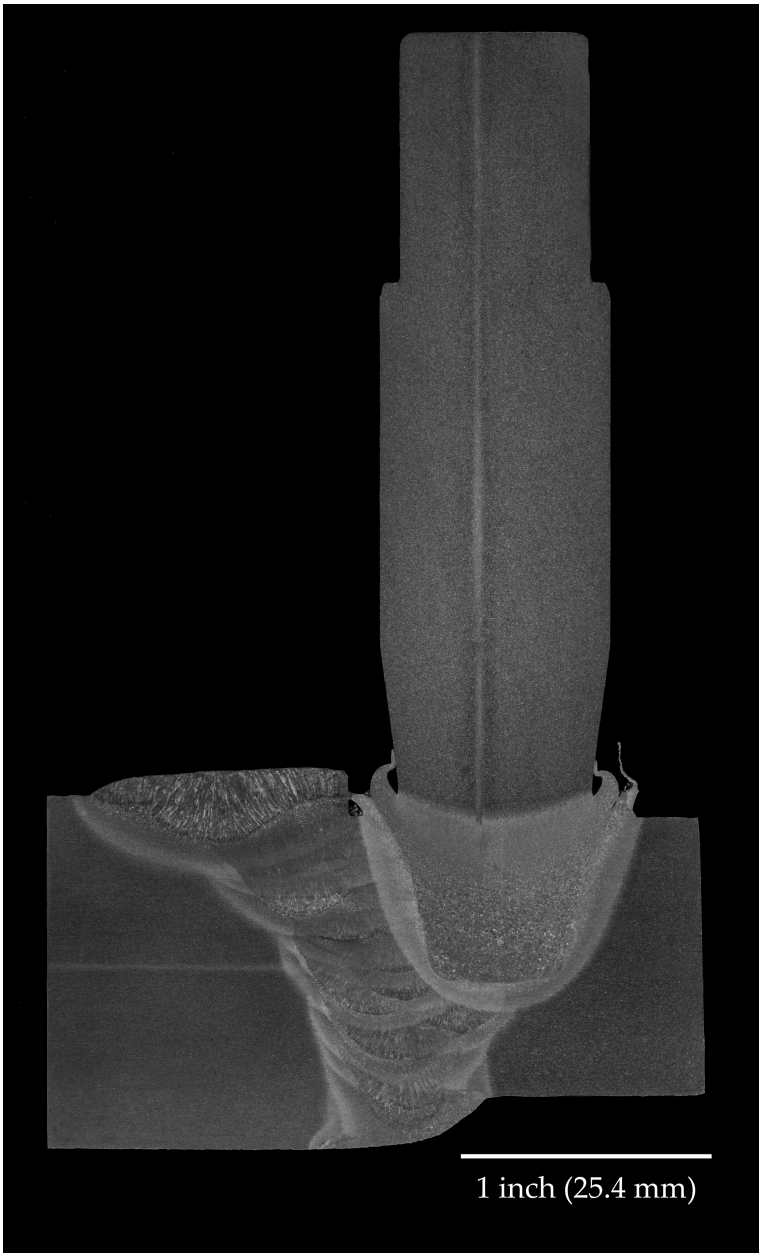


Figure 72. Macrograph showing completed FTHPP weld, 10% Nital etch.

Eight welds were prepared on the CW-A weld and four welds were prepared on CW-B weld. FTHPP welding parameters (consumable type, downward force, rotational speed, forging force, etc.) was kept constant in for all twelve welds. Figure 22 shows the process parameters used in all the twelve FTHPP welds. One of the welds from CW-B was utilized for thermal cycle acquisition during FTHPP welding. The results from the friction welding studies of CW-A and CW-B welds are discussed below.

CW-A – FTHPP Weld

Microstructural Assessment

A total of eight FTHPP welds were prepared on the CW-A weldment for microstructural evaluation, mechanical properties determination, and heat-treatment studies. A total of four welds were prepared on A1 base metal and four were prepared on A2 base metal. Six FTHPP welds were utilized for creep studies. Figure 73 shows a cross-sectional macrograph of the FTHPP plug welds on the CW-A weldment. The macrograph showed 100% bonding along the interface (bond line) for both base metals and original CW-A arc weld. Figure 74 shows optical panorama of the plug weld showing evidence of plastic flow and 100% bonding along the friction weld interface.

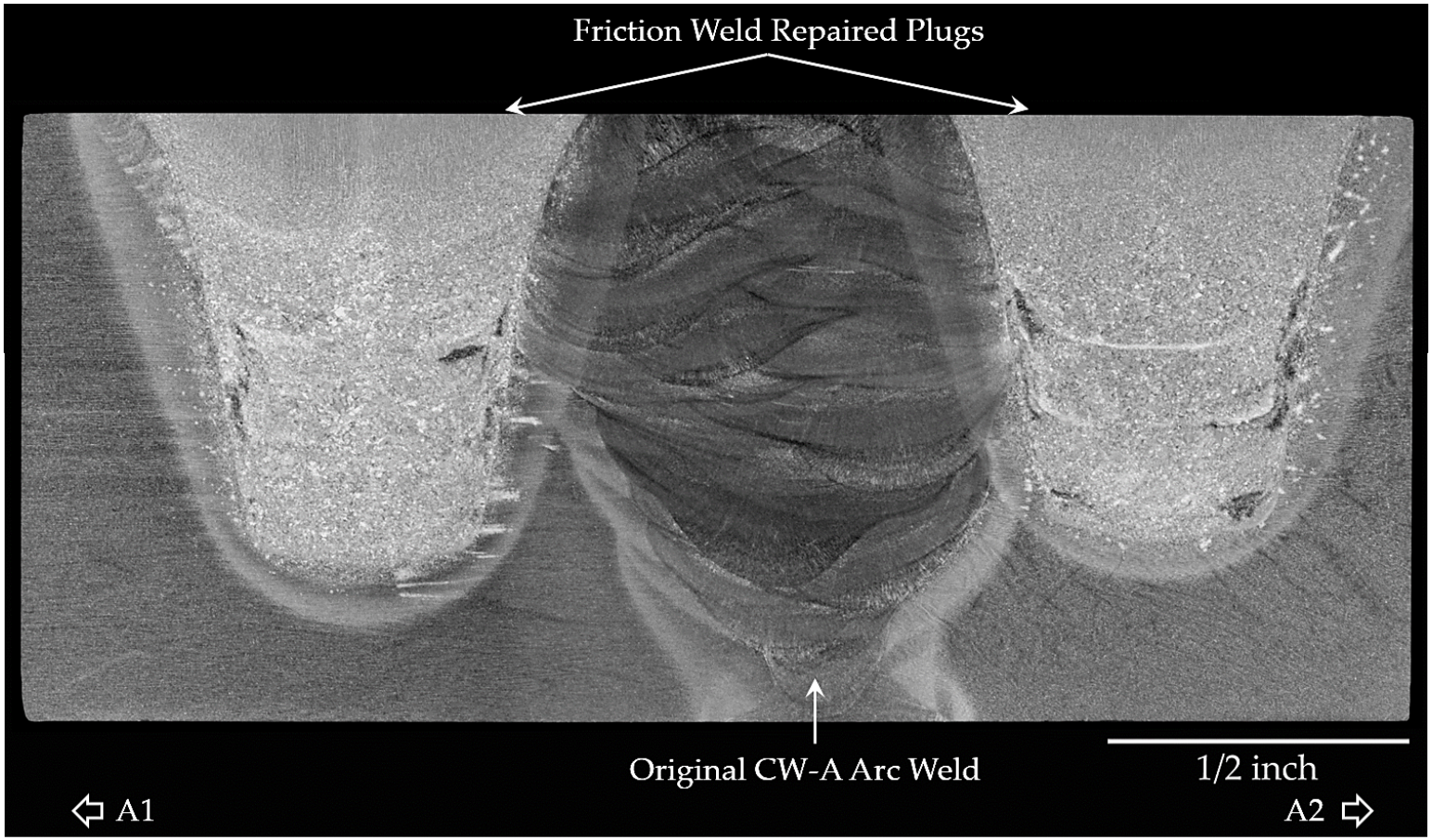


Figure 73. Cross-sectional macrograph showing the friction weld repaired plugs on the CW-A arc weld, 2% Nital etch.

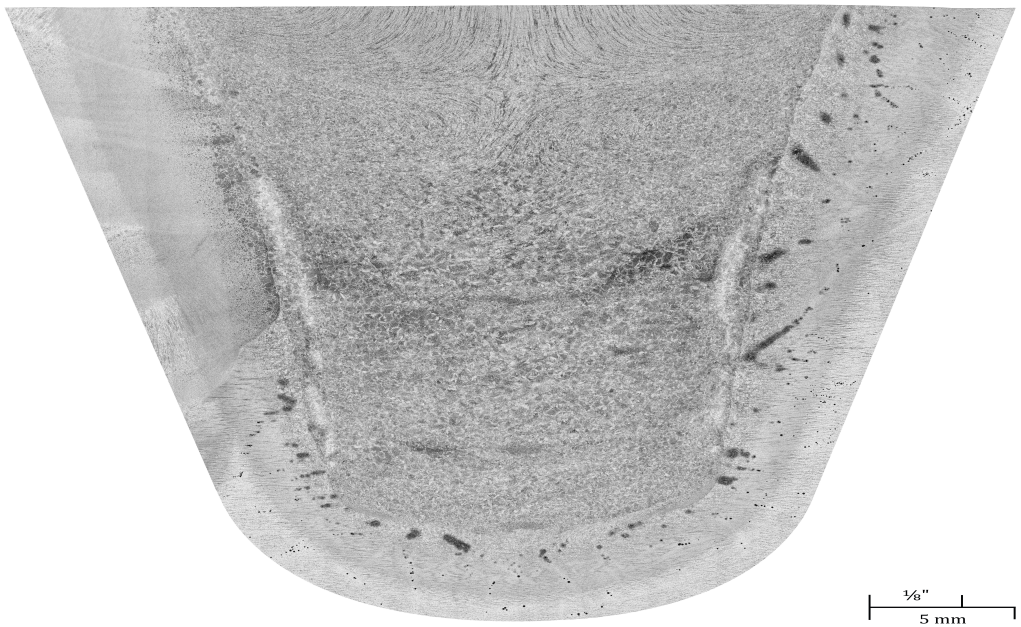


Figure 74. Panorama of the FTHPP weld showing evidence of dusting around graphite nodules adjacent to the interface.

The friction weld HAZ showed a dark appearing region when examined optically appears as “dusting”, which was a result of diffusion of carbon from graphite nodules to adjacent areas, resulting in a carbon rich region in the immediate vicinity of graphite nodules. Figure 75 and Figure 76 show a panorama of the friction weld HAZ exhibiting preferential dark-etching regions in the areas immediately adjacent to pre-existing graphite nodules in the FTHPP weld HAZ. The previously graphitized regions remote from the friction weld HAZ do not show any evidence of dusting. SEM was used for further understanding of the microstructure that was observed in the friction weld HAZ. The optical and SEM micrographs show the formation of complex microconstituents, as a result of partial melting of the carbon-enriched austenitic region surrounding the graphite nodules. This carbon-enriched austenitic region adjacent to the graphite nodule partially melted which upon cooling transformed to Ledeburite (austenite and cementite). The final microstructure of the “dusted” region consists of pearlite (lamellar structure) and proeutectoid cementite. The plug weld HAZ of both A1 and A2 base metals showed similar microstructural results. SEM micrographs from the friction weld HAZ showing complex high carbon microconstituents are shown in Figure 77-80. The resulting increase of hardness with formation of proeutectoid cementite is shown in Figure 81.

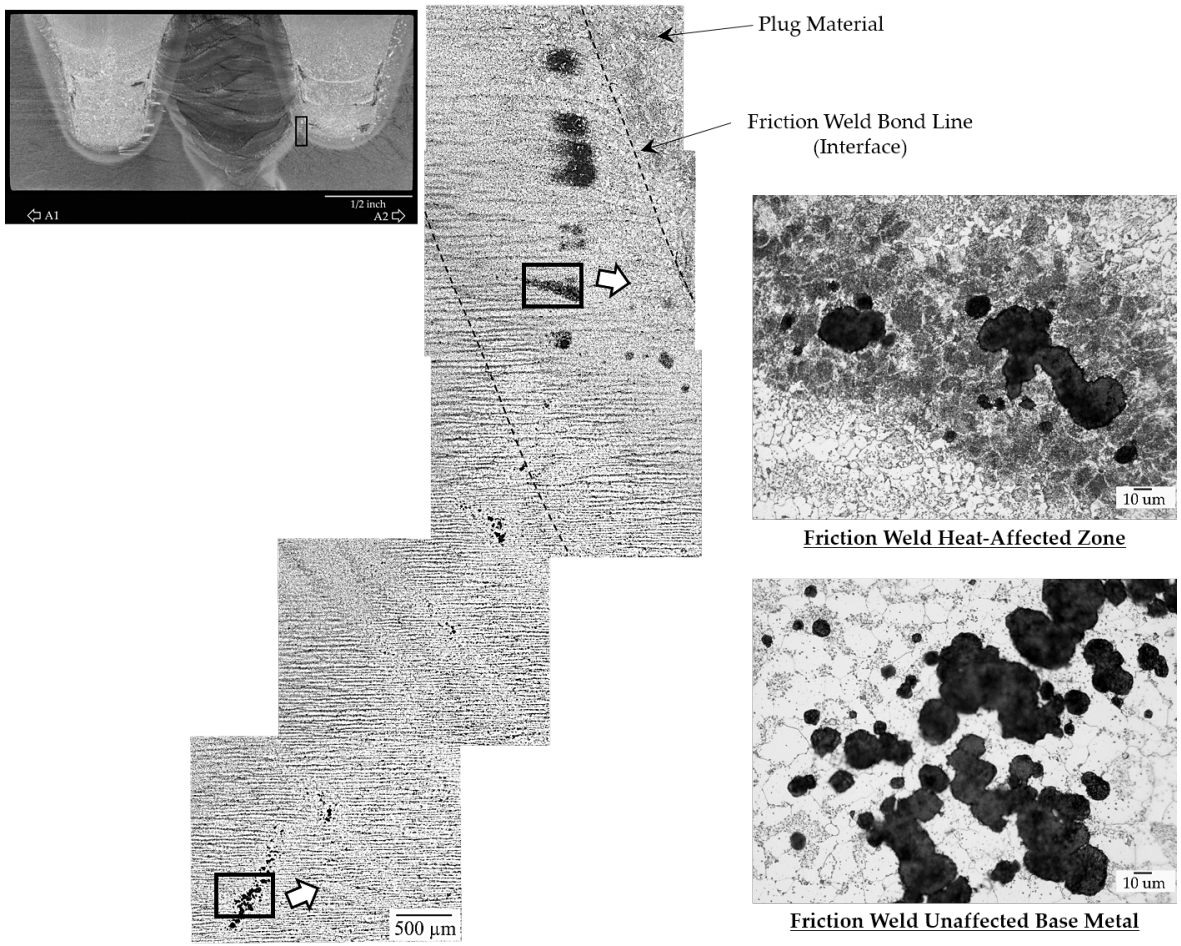


Figure 75. Diffusion of carbon from graphite nodule resulted carbon rich region in immediate vicinity which optically appear as carbon "dusting" in the friction weld HAZ. Graphite nodules remote from the weld deposit did not exhibit any evidence of "dusting" appearance, 2% Nital etch.

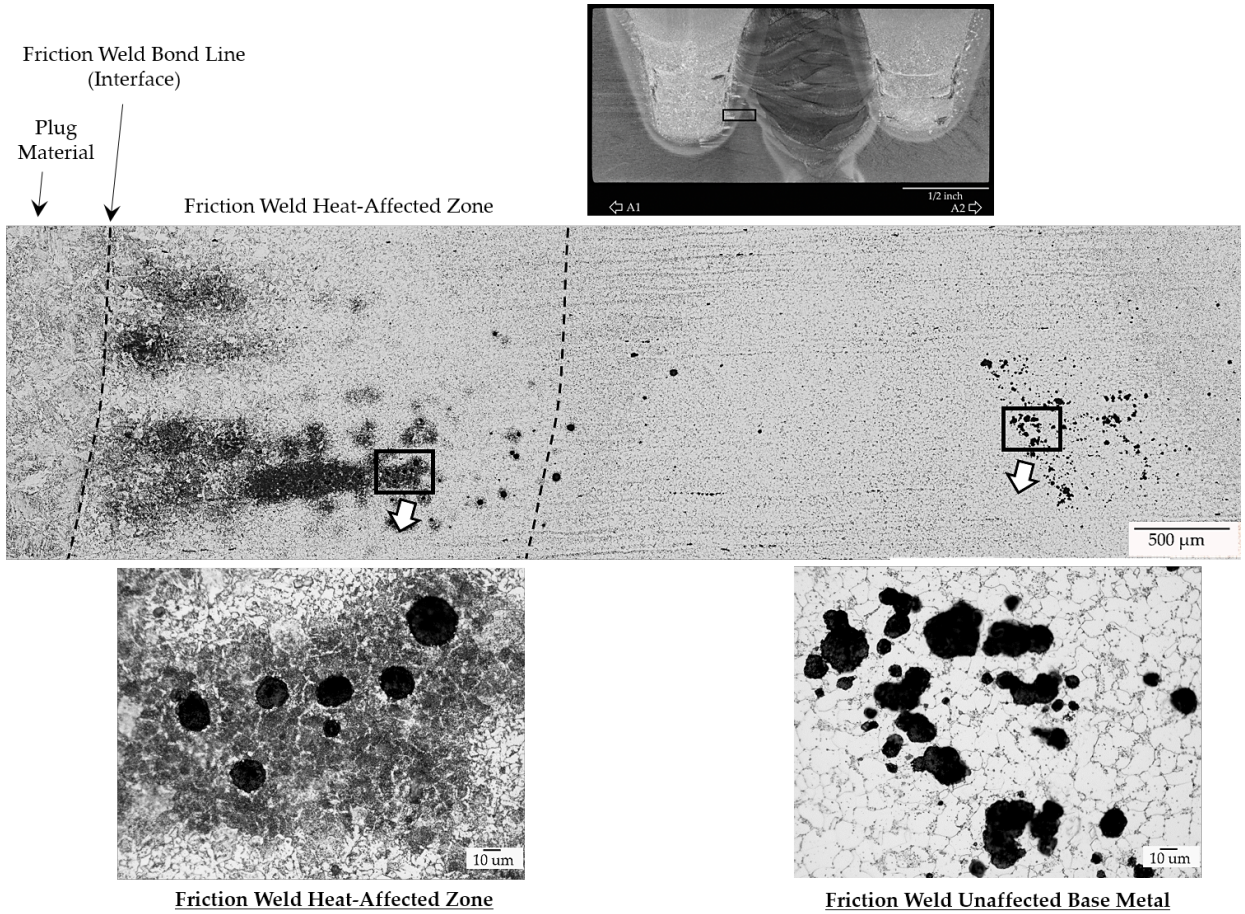


Figure 76. Diffusion of carbon from graphite nodule resulted carbon rich region in the immediate vicinity, which optically appear as carbon "dusting" in the friction weld HAZ. Graphite nodules remote from the interface did not exhibit "dusting" appearance, 2% Nital Etch.

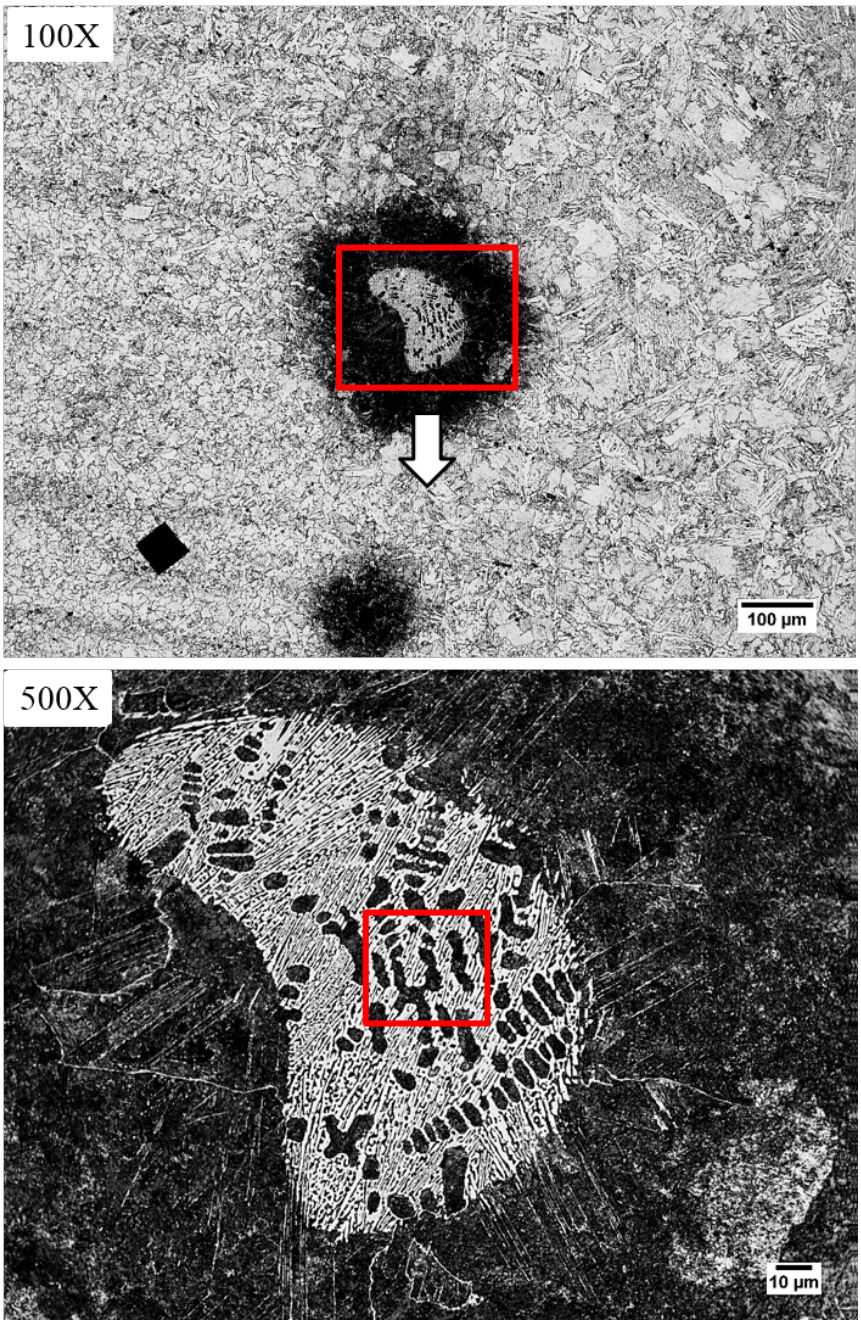


Figure 77. Partial melting adjacent to graphite nodule in accordance to constitutional liquation, 2% Nital Etch.

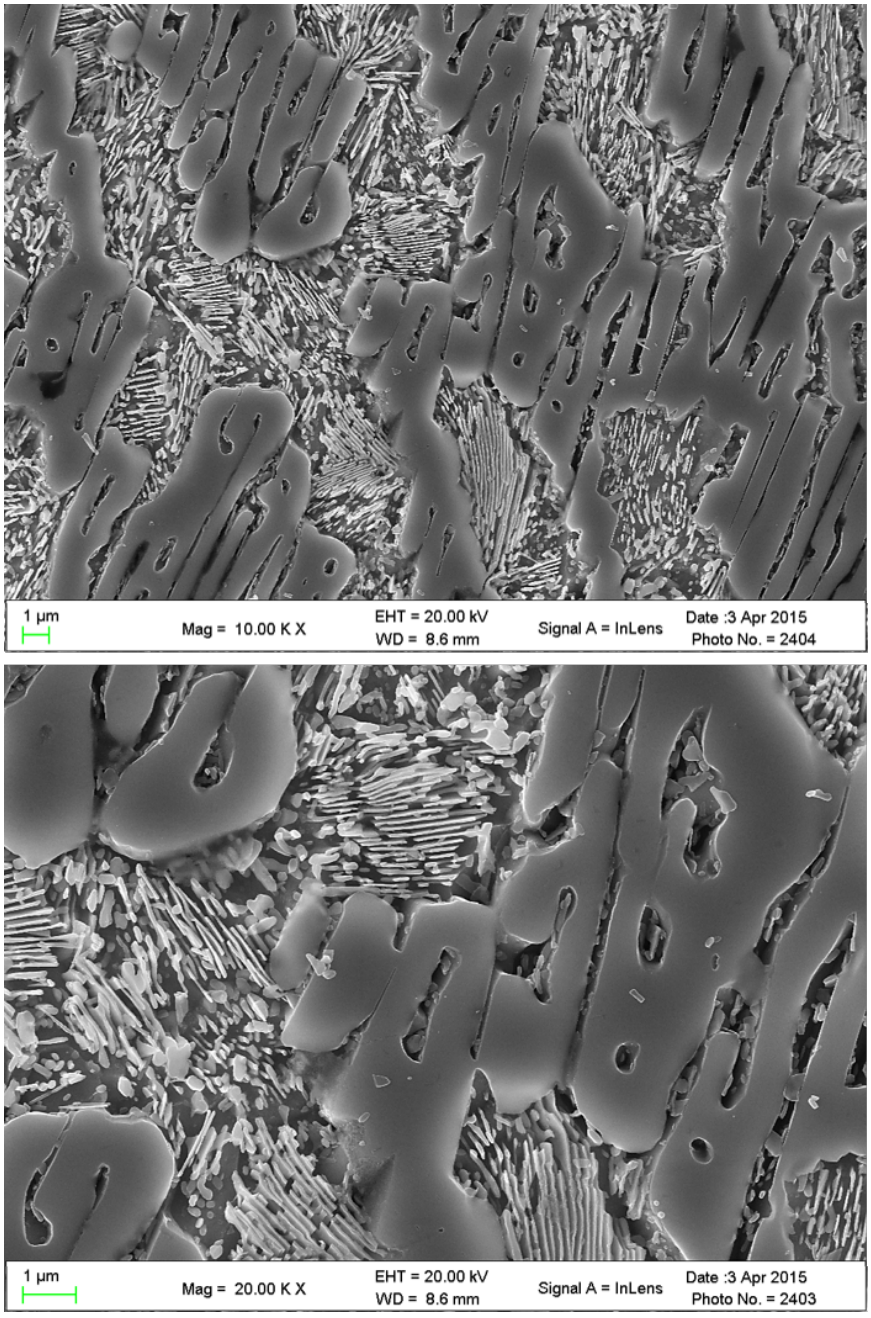


Figure 78. SEM Micrographs of the boxed region from Figure 77, showing formation of pro-eutectoid cementite and pearlite (lamellar structure).

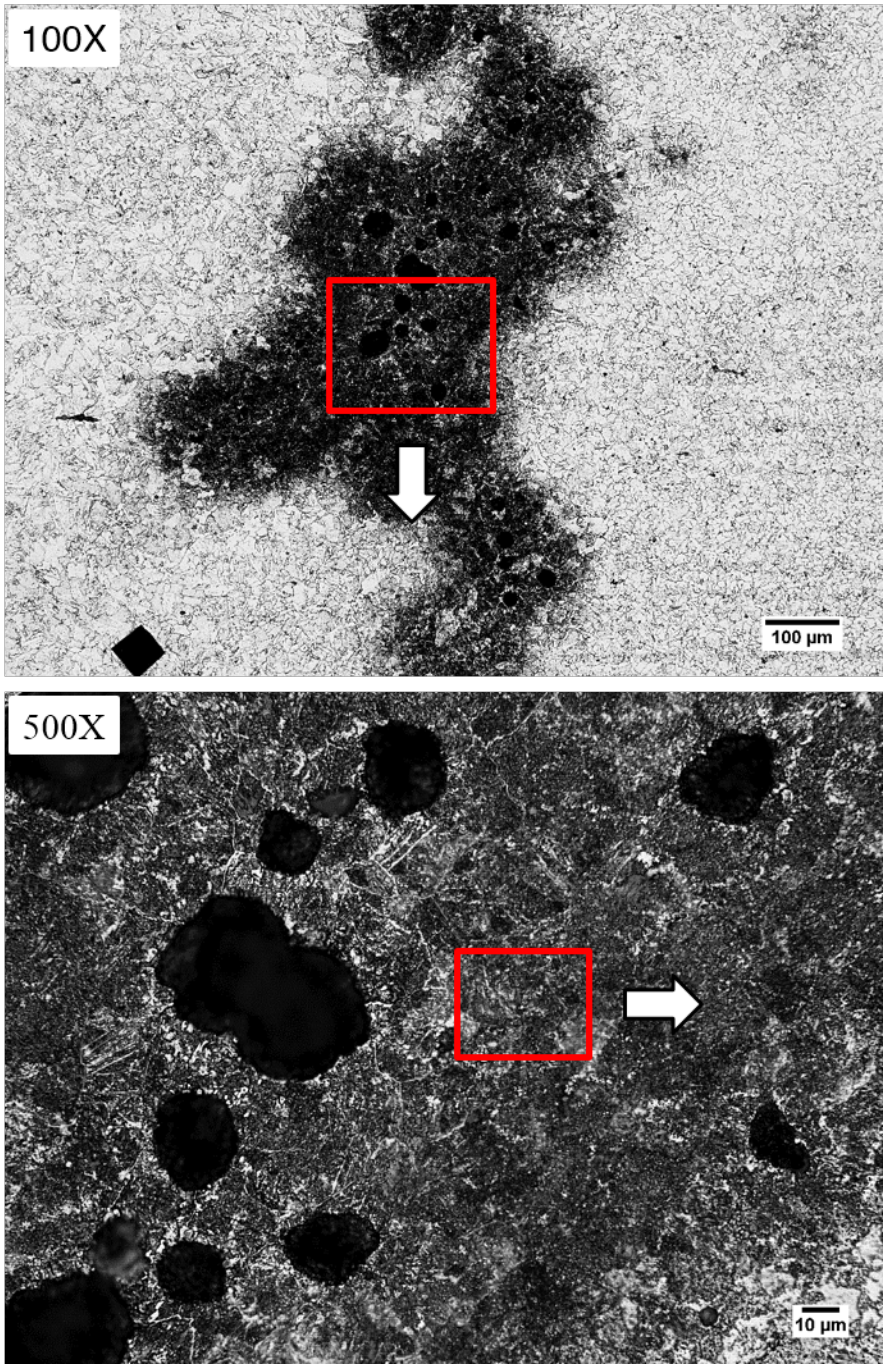


Figure 79. Diffusion of carbon from pre-existing graphite nodules resulting in dusted region, 2% Nital etch.

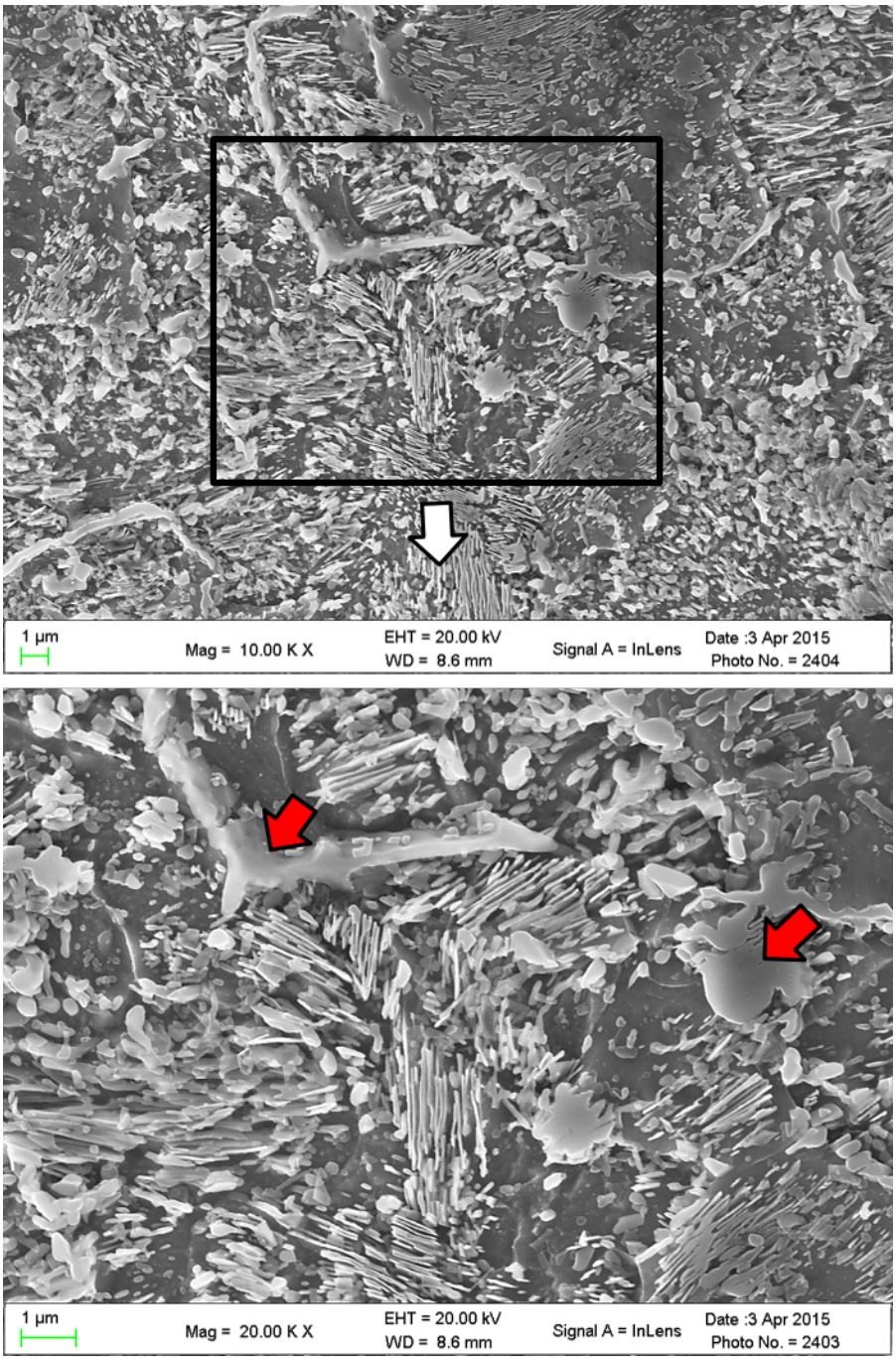


Figure 80. SEM Micrographs of the boxed region from Figure 79, showing formation of pro-eutectoid cementite (shown by red arrows) and pearlite (lamellar structure).

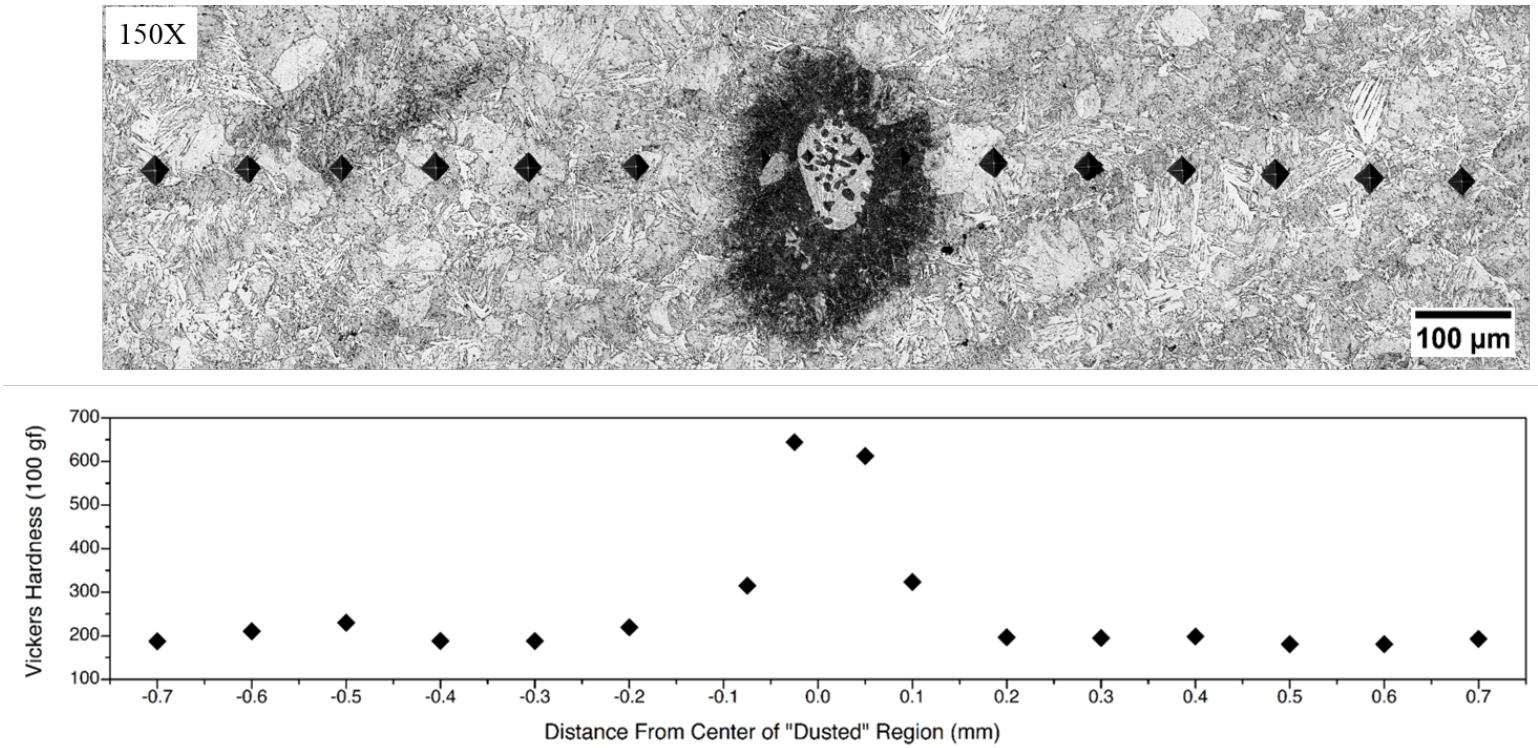


Figure 81. Hardness traverse (100 gf) across the dusted region (as shown in micrograph) showing peak hardness of 650 HV. Average hardness outside the dusted region = 200 HV.

CW-B – FTHPP Weld

Microstructural Assessment

A total of four FTHPP welds were prepared on CW-B weldment for microstructural, mechanical properties, and heat-treatment studies. A total of three welds were prepared on B1 base metal and one weld was prepared on B2 base metal. B2 base metal did not exhibit any evidence of graphitization, and thus was utilized for comparative purposes. The CW-B FTHPP weld showed 100% bonding along the interface (bond line) for both base metals and original CW-B arc weld.

Metallurgy of FTHPP HAZ Microstructure

During friction welding plug repair, the region adjacent to a graphitized section of the carbon steel base metal behaves similarly to a nodular cast iron because of the prior presence of the graphite nodules in the parent material. These pre-existing graphite nodules adjacent to the interface between the plug and the parent material are typically heated to peak temperatures ranging from the lower critical transformation temperature (Ac_1) to temperatures greater than the eutectic temperature (2075°F) during FTHPP welding. The peak temperature experienced by pre-existing graphite nodules depends on their distance from the

interface between the plug weld and the parent material. As a result of this thermal exposure, carbon from the graphite nodules begins to diffuse into the adjacent austenite matrix (transformed from ferrite/pearlite when heated to temperatures greater than Ac_1). The diffusion of carbon away from graphite nodules results in a carbon gradient in the adjacent austenite matrix. Since the heating/cooling rates are rapid during friction welding, the time spent at an elevated temperature is short and the carbon from the graphite nodules can only diffuse a limited distance from the graphite-austenite interface. The diffusion of carbon from a graphite nodule concomitantly results in a reduction of the size of the graphite nodule. Upon cooling, the carbon rich regions adjacent to graphite nodule precipitate as carbides termed as "dusting" or "dusted" in this document. The "dusted" region surrounding a graphite nodule, resulting from carbon diffusion during friction welding, has a radius on the order 200-500 μm around the graphite core. The degree of "dusting" depends on the distance of the graphite nodule from the weld interface (i.e. on the peak temperature reached by a pre-existing graphite nodule), which will determine the resulting microstructure/mechanical properties (strength and toughness) in these "dusted" regions. FTHPP thermal cycle study was performed to determine the time/temperature behavior during friction weld thermal cycle.

5.3 Mechanical Testing

5.3.1 ASME Section IX Bend Test

ASME IX guided bend test was performed to examine the bend ductility of the graphitized component and also the ductility of the friction repair welded component. Bend sample was machined to evaluate the ductility of the most graphitized region (base metal region just outside of the HAZ). CW-A weldment which exhibited the highest extent of graphitization was selected for bend testing. Bend specimen showed embrittling nature of the graphitized region, however the graphitization extent of 1 volume percent did not appear affect the bend ductility of the weldment which was fully ductile in all regions with 20% outer-fiber strain (plastic flow). The opening along the graphitized region just outside of the visible HAZ in the base metal was observed, however was less than 1/8″ (3 mm).

ASME-IX guided side bend test was also performed on two specimens (3/8″-wide) prepared on CW-B friction weld. One bend specimen consisted of the weld prepared on the graphitized side and the second specimen consisted on the non-graphitized side. Bend specimens were extracted such that the center of the specimen is located at the center of the friction plug weld. The friction weld was fully ductile in all regions (plug material, HAZ, and bond line) with 20%

outer-fiber strain (plastic flow). A discontinuity (tear) was observed along the bond line (interface) at the bottom of the friction weld, however the width of the discontinuity observed is within the maximum allowed 1/8" (3 mm) per ASME Section IX acceptance criteria[93].

5.3.2 Creep Testing

An extensive creep study was performed on all the materials (service-exposed and friction weld repaired) received for the current study. A total of 30 specimens were tested for a period of more than a year. Creep testing was performed using the protocols shown in Figure 23. Creep data was utilized to obtain the steady state creep rates for different temperature and stress combinations. All the creep data available in literature with regards to graphitization were performed at temperatures greater than 1000°F, which is rather higher than the typical operating temperatures of the materials susceptible to graphitization. Creep testing was performed at temperature ranges of 850°F-950°F and at stresses of 4.4 ksi-10 ksi. Creep data was normalized to a typical operating temperature of 800°F and 10 ksi to obtain steady state creep rates for the graphitized materials.

Figure 82 shows a creep curve used in the current study for the circumferential weld CW-A. Stress and temperatures were periodically varied to

obtain steady state creep rates for various temperature (850°F-950°F) and stress combinations (4.4 ksi – 10 ksi). Table accompanying the Figure 82 provides steady state creep rate for different temperature stress combinations. Creep curves were normalized to the typical operating temperature of power plant for carbon steel component of 800°F. The time-temperature extrapolation was performed using Larson-Miller Parameter (LMP), with constant of 15. Normalized creep curve is shown in Figure 81.

$$LMP = Temperature\ (\log t + C)$$

where, T = Temperature (Kelvin or Rankine)
t = time (hours), C = Constant, 15 for Graphitized components

Similarly, creep data was obtained for each weldment subjected in this study (CW-B, CW-C, LSW-A1, LSW-D, and LSW-E). The respective creep curves at various temperatures and stress combination are shown are shown in Appendix C. Three duplicate specimens were tested for each material. Creep results showed no significant influence of graphitization on creep performance of these weldments. The steady creep rates were derived for graphitized weldments as a function of stress and temperature are shown in Table 10 and Table 11.

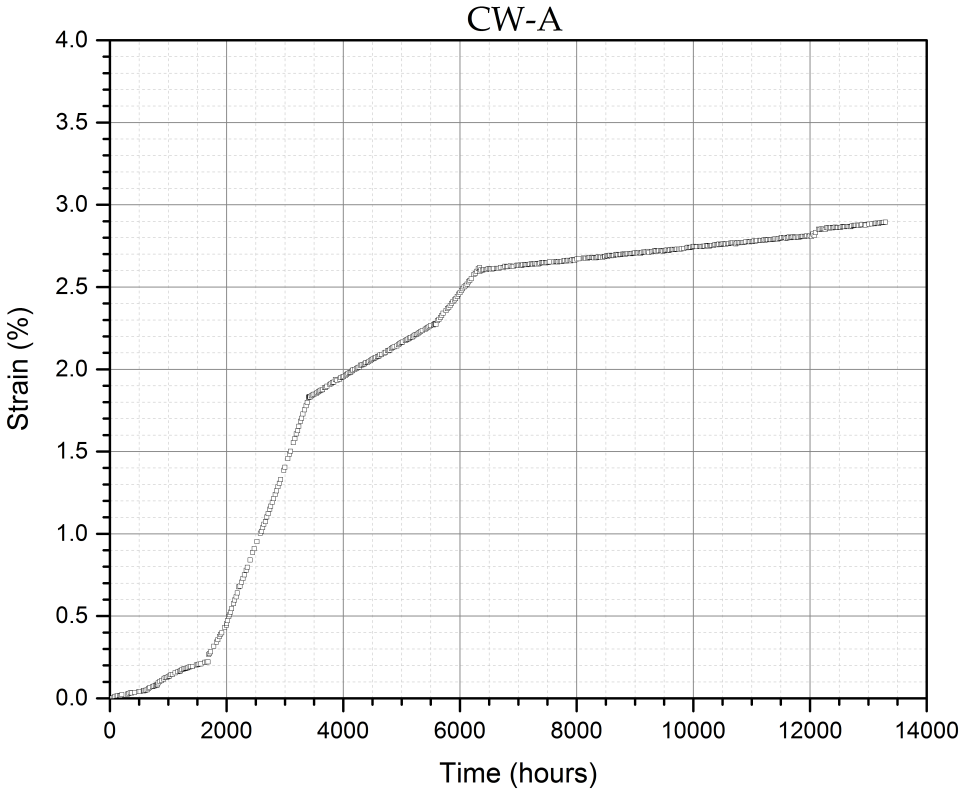


Figure 82. Creep curve for CW-A circumferential weld. Creep testing conditions and steady sate creep rate provided in Table below.

Test Time (hours)	**Temperature (°F)**	**Stress (ksi)**	**Steady State Creep Rate (%/hr x 10^{-4})**
574	900	4.4	0.8
234	950	4.4	1.6
878	900	8	1.7
313	950	8	6.8
1419	950	10	9.6
2154	900	10	2.1
768	925	10	4.5
6955	850	10	0.4

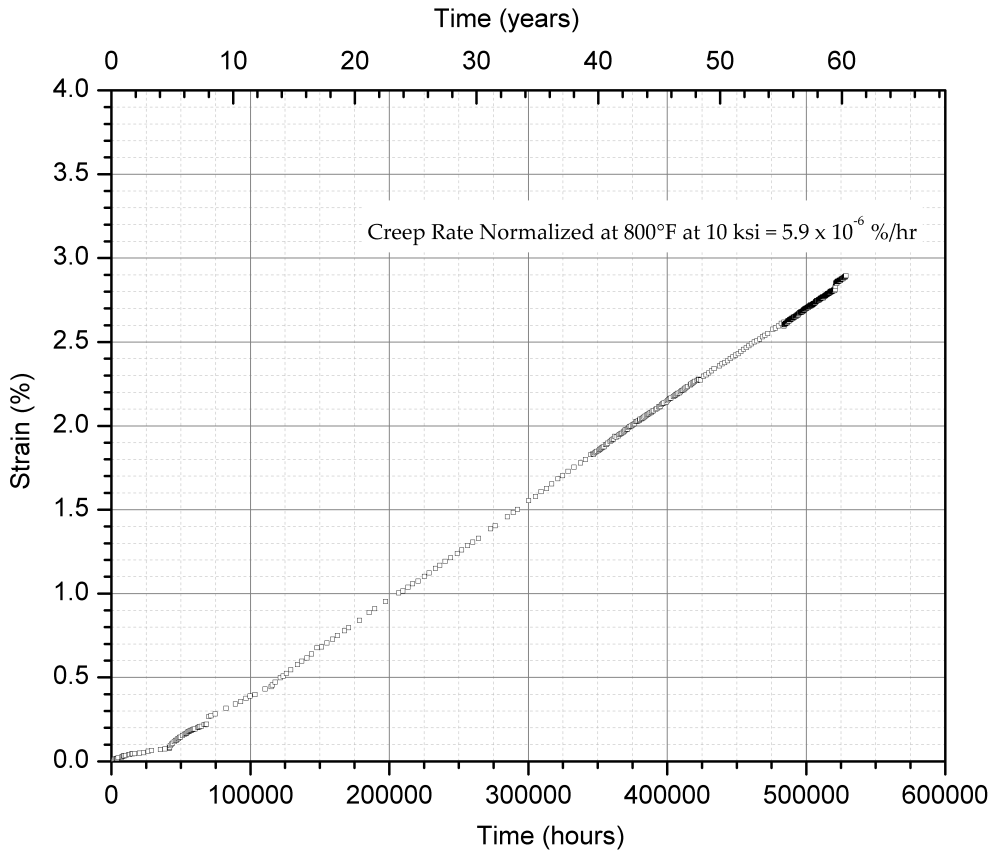


Figure 83. Normalized creep curve to obtain steady-state creep rate for a typical operating temperature of 800°F for CW-A. Normalization was performed using Larson Miller Parameter, with constant of 15.

Table 10. Steady creep rate (%/hr x 10^{-4}) for graphitized carbon steel samples tested at 10 ksi (68.9 MPa) stress as a function of temperature.

Temperature	Circumferential Welds			Longitudinal Seam Welds			Friction Repair Weld
(°F/°C)	CW-A	CW-B	CW-C	LSW-A1	LSW-D	LSW-E	CW-A
850°F (454°C)	--	1.0	0.6	2.2	0.8	2.7	1.6
900°F (482°C)	2.1	4.1	1.8	10.3	3.1	11.5	7.4
925°F (496°C)	--	10.8	4.8	26.1	7.9	30.8	30.6
950°F (510°C)	9.6	23.0	8.5	43.5	20.2	55.9	--

-- Sample was not tested at this condition

Table 11. Steady creep rate (%/hr x 10^{-4}) for graphitized carbon steel samples tested at a temperature of 900°F (482°C) as a function of stress.

Temperature	Base	Circumferential Welds			Longitudinal Seam Welds			Friction Repair Weld
(°F/°C)	Metal	CW-A	CW-B	CW-C	LSW-A1	LSW-D	LSW-E	CW-A
4.4 (27.6)	0.7	0.8	--	0.4	--	--	--	--
8 (55.2)	2.6	1.7	--	--	--	--	--	--
10 (68.9)	--	2.1	4.1	1.8	10.3	3.1	11.5	7.4

-- Sample was not tested at this condition

Figure 84 shows the log-log plot of the effect of temperature on the steady state creep rate for all the materials tested at 10 ksi. The creep rates increase with the increase of temperature. However, the presence and different extent of graphitization does not appear to have a significant influence in creep behavior. CW-A was the most graphitized material received in this study thus an extensive study was performed to examine the creep properties. A total of 14 specimens were prepared from CW-A, 12 cross welds and 2 base metals specimens. Figure 85 shows the steady state creep rate as a function of temperature for different stress conditions for CW-A. The steady state creep rate increased as a function of temperature and stress.

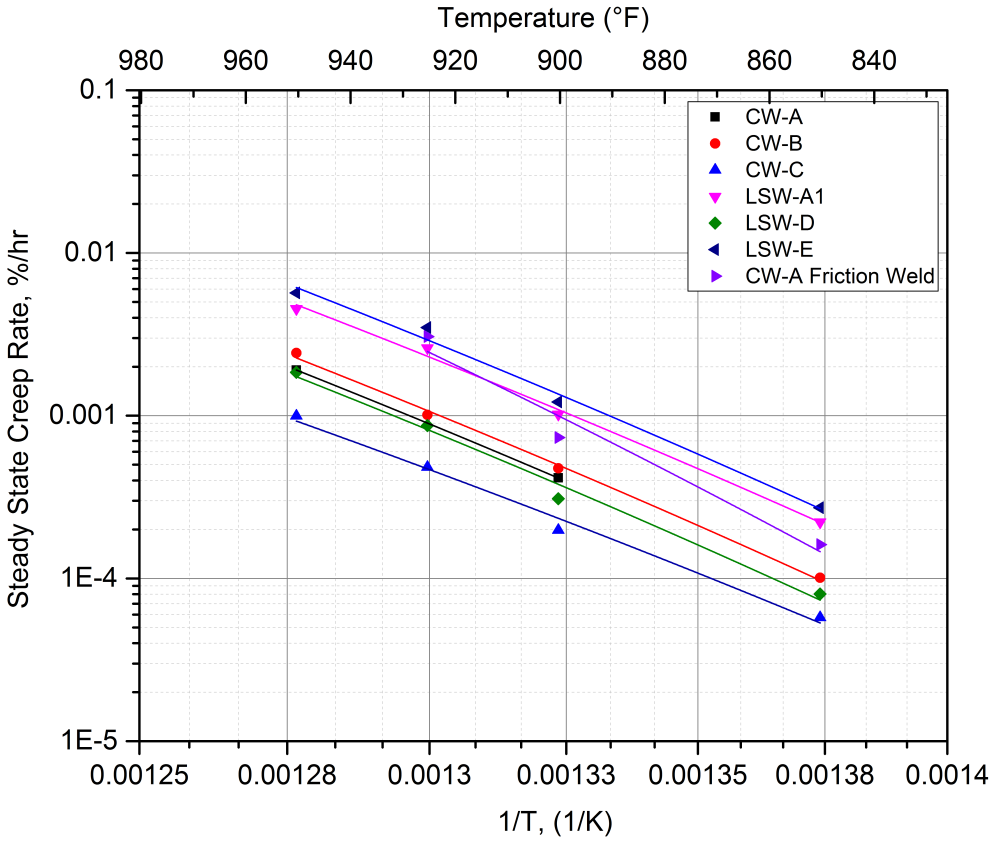


Figure 84. Steady creep rate for graphitized carbon steel samples tested at 10 ksi (68.9 MPa) stress as a function of temperature.

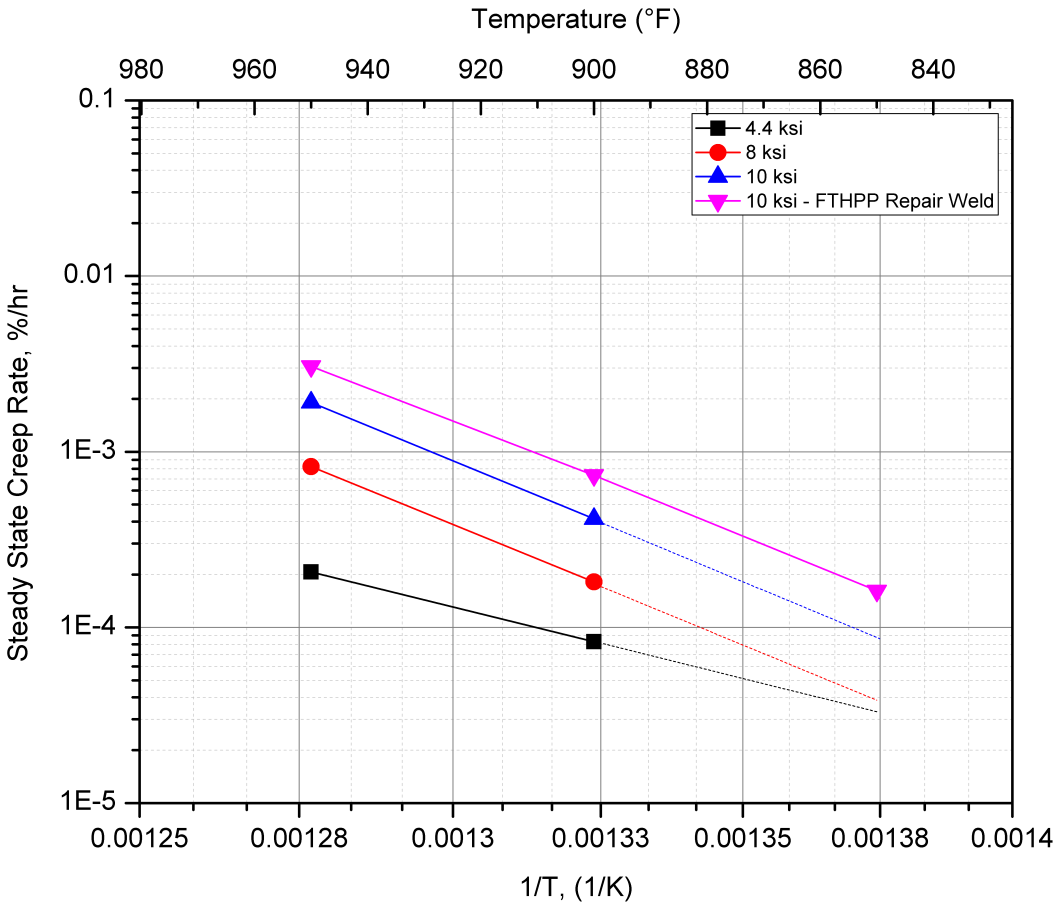


Figure 85. Steady creep rate for CW-A as a function of temperature for different stresses.

Metallurgical Examination of Creep Tested Friction Welded Specimens

Three "jumbo" specimens (designated as CW-A-FW-1, CW-A-FW-1, and CW-A-FW-3) with a cross-sectional area of 1 in^2 (645 mm^2) consisting of two plug welds and a circumferential weld were machined. A photograph showing both the cross-sectional and the top-view of the cross-weld creep specimen prepared from friction welded sample is shown in Figure 86. All three specimens were machined to exact dimensions. Creep specimens were tested at different time-temperature combinations (as shown in Figure 87) so that steady-state creep rate at different temperature can be obtained.

Metallographic Examination of Creep Samples (Service-Exposed)

Post creep test metallographic examination was performed on all the samples to evaluate for creep damage. Samples were examined to characterize the effects of pre-existing graphite on creep performance. Also, the effect of creep tests (temperature and stress) on the morphology and extent of pre-existing graphite nodules were examined.

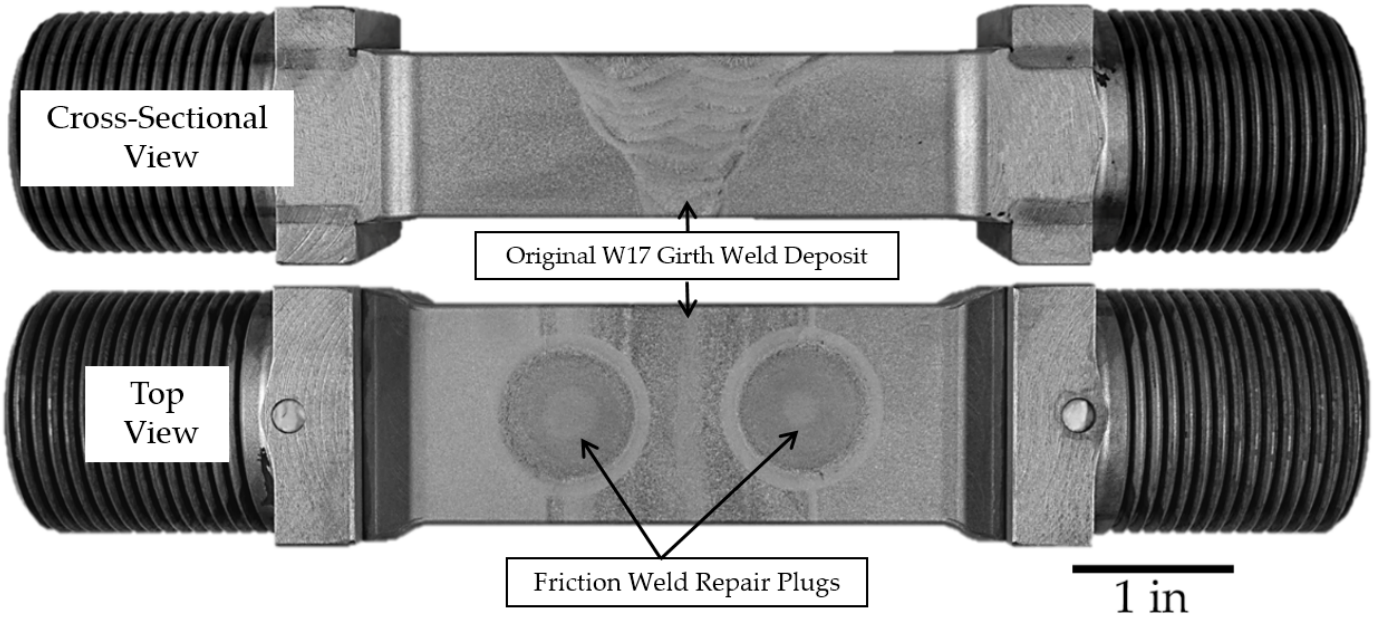


Figure 86. Photograph of a full-wall cross-weld creep specimen (CW-A-1), showing two friction weld repaired plugs on either side of the girth weld, RA = 1%, 2% Nital Etch.

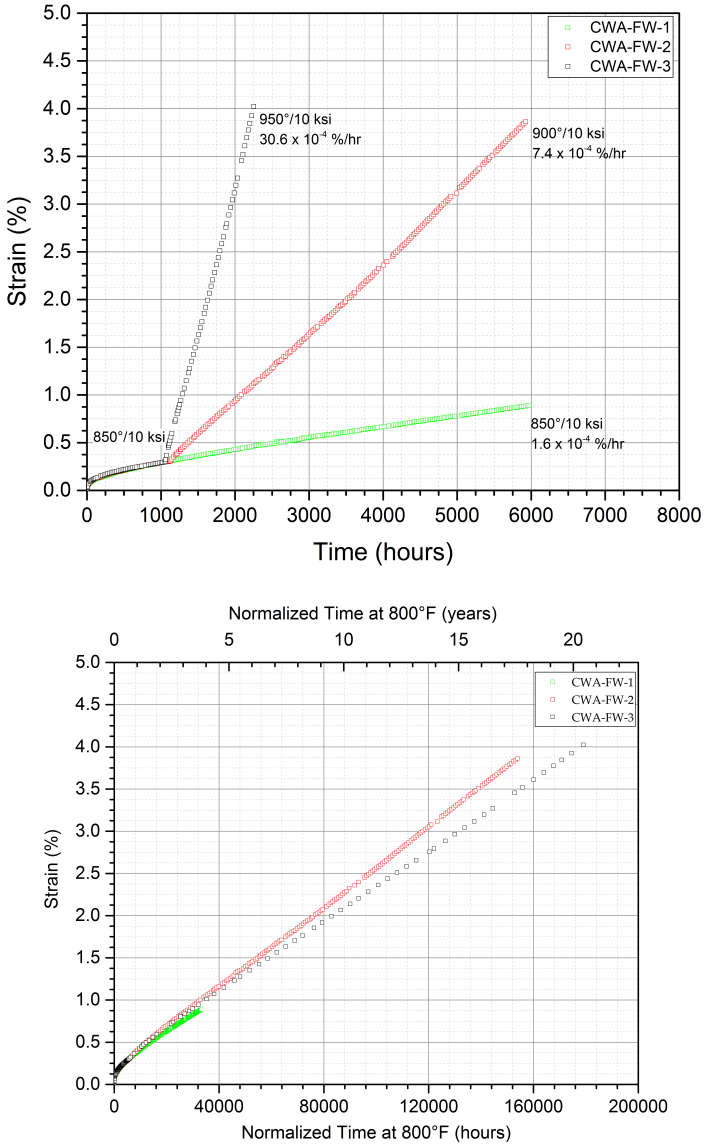


Figure 87. Creep Curve (Top) for friction welded specimens from CW-A and normalized creep curves (bottom) for friction welded specimens at 800°F using LMP constant C= 15.

5.4 Heat-Treatment Studies

Heat-treatment studies were performed for further understanding of the graphitization morphology with regards to nucleation and growth theory. Heat-treatment study was performed on the service-exposed material (removed after 17 years in service at 800°F/427°C) to examine if there is a continued growth of graphite nodules, friction repair welded components to study efficacy of repair welding on elevated temperature exposure and non-graphitized carbon and carbon-½molybdenum (C-½ Mo) steels to evaluate susceptibility for graphitization.

1. Heat-treatment studies on service-exposed and friction-repaired materials

Aging studies were performed on various service-exposed (800°F/427°C for 17 years) materials for evaluation of addition time on pre-existing graphite nodules. Samples were subjected to multiple aging treatments and were periodically examined. Temperatures for heat-treatment studies were selected higher than the typical operating temperature to accelerate the reaction rate. Metallographic examination of heat-treated samples did not exhibit any influence of additional time at elevated temperatures on the extent and the morphology of graphite. Figure 88 shows comparative the optical micrographs before and after the heat-treatment. The additional heat-treatment on the

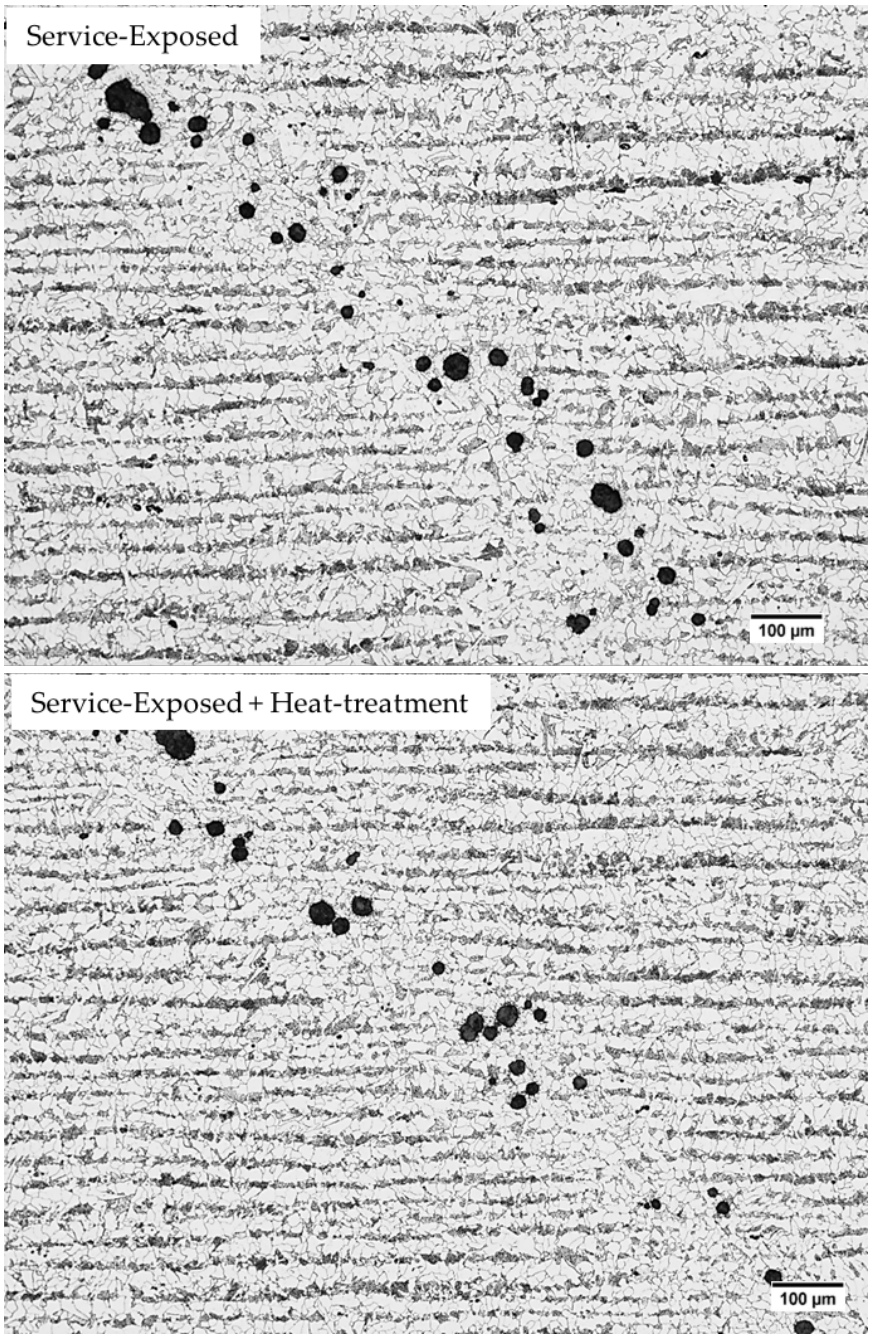


Figure 88. Comparative optical micrographs in service-exposed (17 years at 800°F) and additional heat-treatment studies (900°F/567 hours + 950°F/168 hours). Heat-treatment is equivalent to ~11 years at a typical service-temperature of 800°F.

service-exposed material is approximately equivalent to 11 years at a typical service-temperature of 800°F (427°C) determined using Larson-Miller Parameter (C=15). As-discussed earlier in the creep examination section, the additional time (equivalent to more than 100 years 800°F) at elevated temperatures (850-950°F) along with stress (4.4 ksi-10 ksi) during creep testing, do not appear to influence the extent or morphology of graphite nodules observed in service-exposed materials. This suggest that the spheroidized pearlite, ferrite, and pearlite that was observed in service-exposed materials have acquired close-to equilibrium state. This is shown in comparative SEM micrographs in Figure 89, obtained in CW-A weldment (after 17 years of service at 800°F). Prior pearlitic regions adjacent to graphite nodules are completely spheroidized. Higher magnification SEM micrographs at 50KX and 100KX is shown in Figure 90. Heat-treatment performed on the samples extracted friction weld HAZ, showed nucleation of "new" graphite nodules (~5-7 microns) in size. However, the "new" nodules were only observed in the "dusted" region thus did influence the overall integrity and the creep performance of the welded joint. Figure 91 shows comparative SEM micrographs before and after creep testing, exhibiting increase in volume fraction of new nodules in HAZ with time.

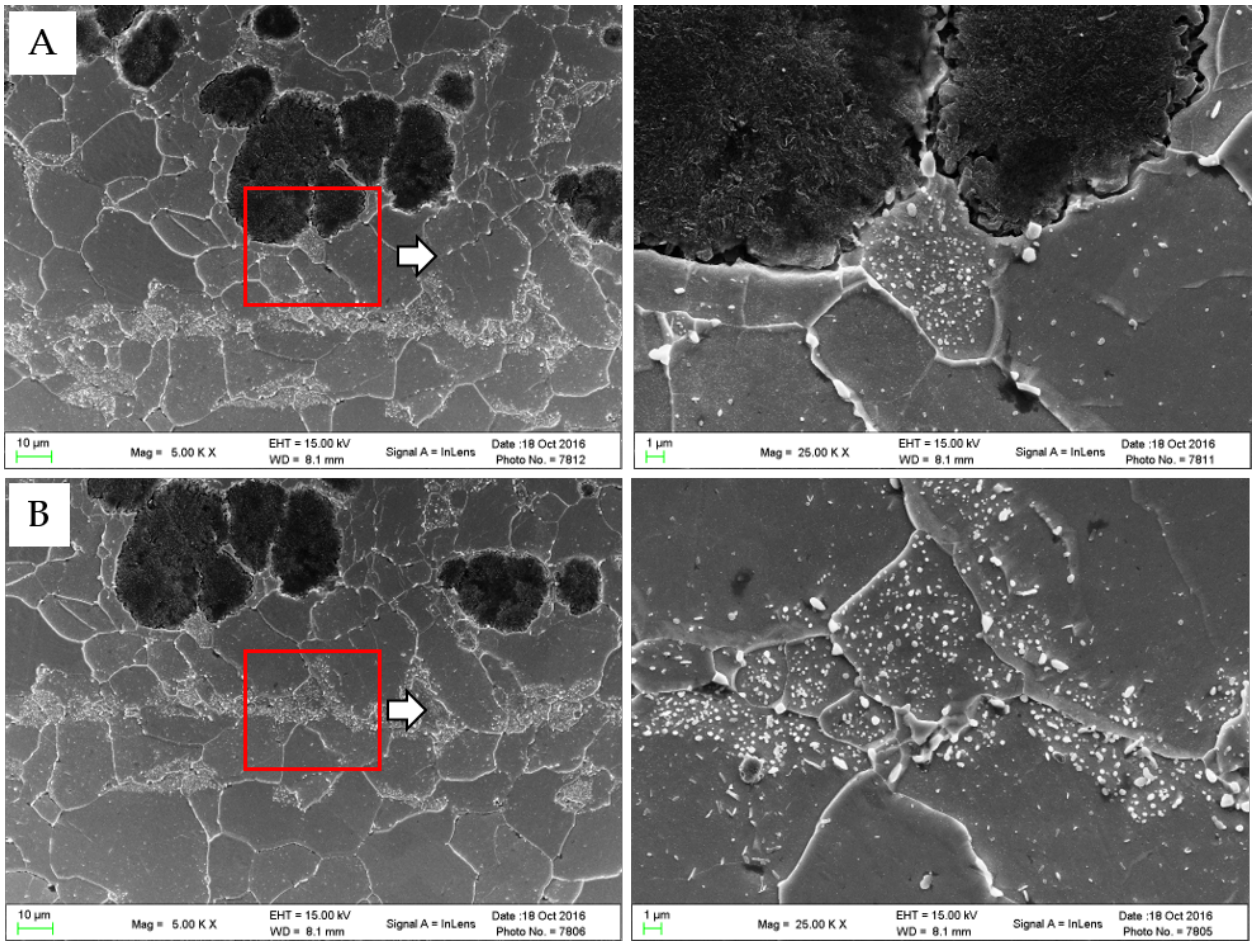


Figure 89. SEM micrographs on CW-A, A) Prior pearlitic region adjacent to graphite nodule, B) Prior pearlitic region further away from graphite nodule. Micrographs show that prior pearlitic region is completely spheroidized.

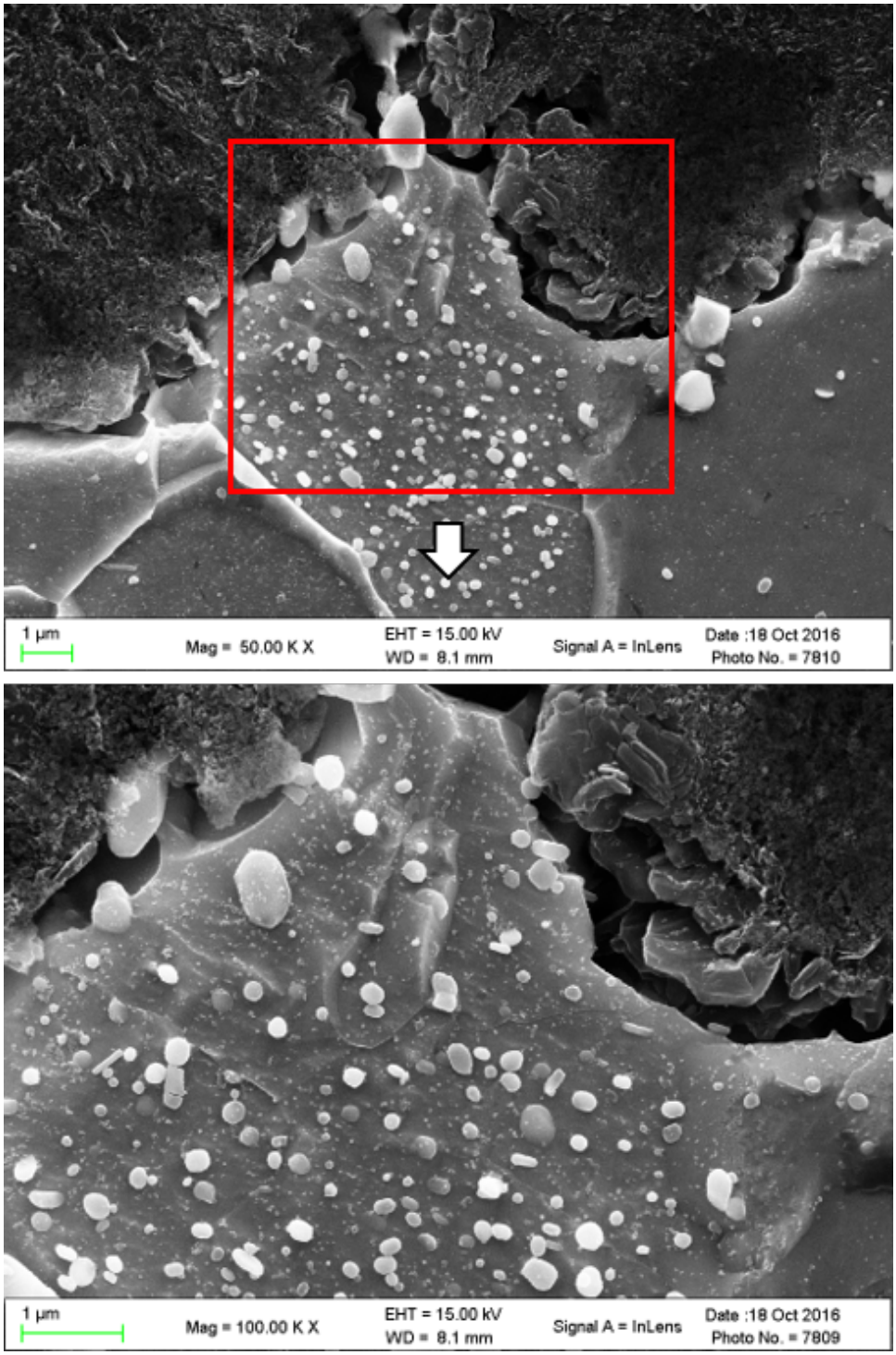


Figure 90. SEM micrographs (50kx and 100kx) from location A in Figure 89. Note that the prior pearlitic region is completely spheroidized and carbon denuded.

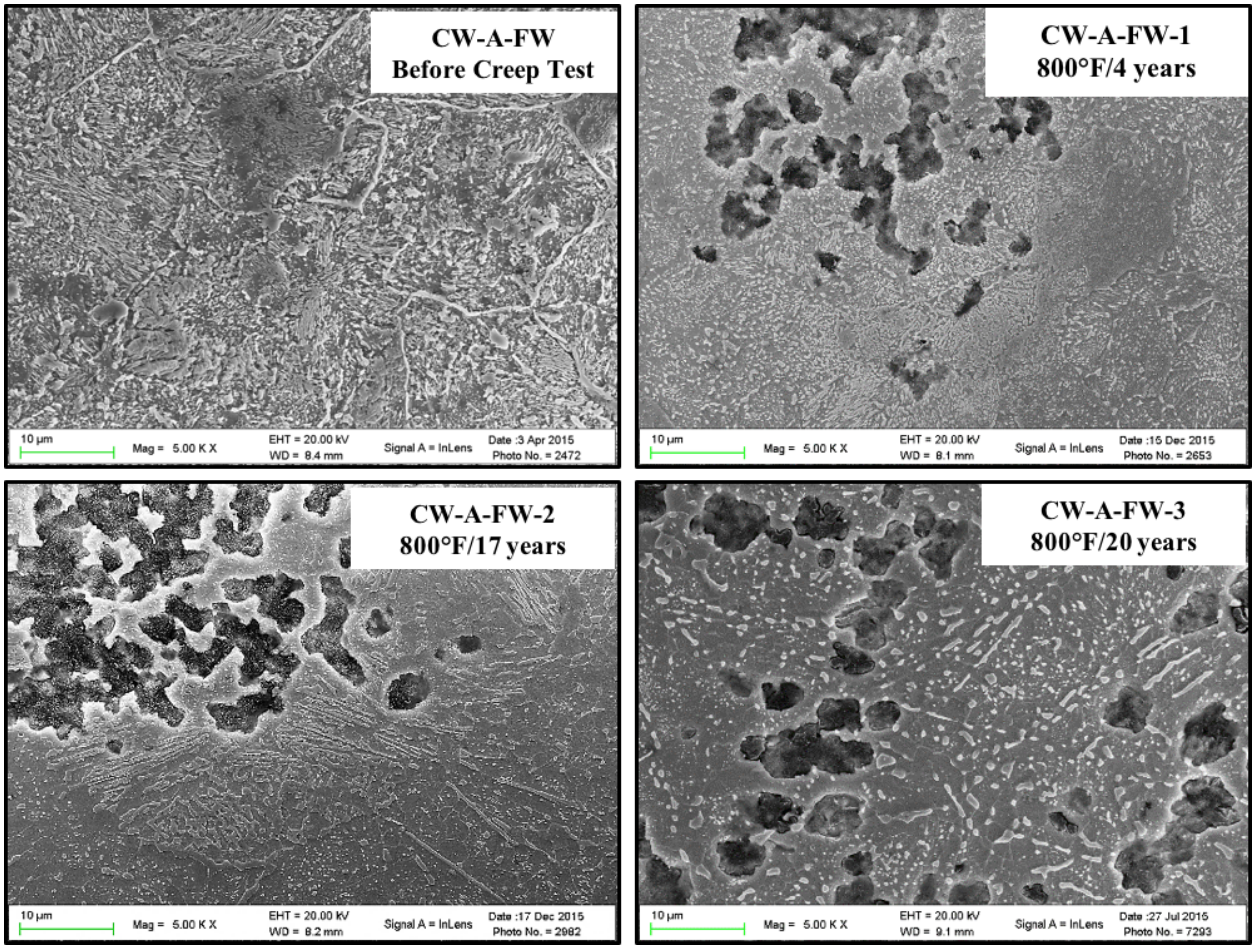


Figure 91. Comparative SEM micrographs before and after creep tests (different time) in the "dusted" region in friction weld HAZ showing evidence of nucleation of "new" graphite nodules.

2. Heat-treatment studies on non-graphitized C-½ Mo steels

Three non-graphitized C-½ Mo steel materials (Sample #1 0.014 wt.% Al, Sample #2: 0.034 wt.% Al and Sample #3: 0.004 wt.% Al) with varying amount of aluminum content was subjected to heat-treatment studies. Samples were evaluated after 50, 100, 250, 500, 1000, 2000, and 3000 hours at 1000°F (538°C). Comparative SEM micrographs at 25 KX after 0, 50, 100, and 250 hours are shown in Figure 92. The first 250 hours at 1000°F (538°C) exhibited primarily spheroidization behavior. The degree of spheroidization increased with time. First evidence of graphite formation (~200 nm-500 nm in size) was observed after 250 hours at 1000°F (538°C) along the Fe-Fe_3C interface, as shown in Figure 93. Graphite nodules showed rapid growth with time, comparative SEM micrographs after 500, 1000, 2000, and 3000 are shown in Figure 94. Nucleation of graphite nodules was observed to be interface controlled, and was commonly observed along Fe-Fe_3C interface, grain boundaries or the matrix-inclusion interface. Figure 95 provides an illustration of graphite nucleation and growth along Fe-Fe_3C interface and along perlite-ferrite boundary. SEM micrograph of Graphite nucleation and growth showed a typical sigmoidal type-behavior, as shown in Figure 96. The overall transformation rate included initial incubation

period, followed by rapid growth of graphite nodules, and eventual saturation after acquiring an equilibrium state.

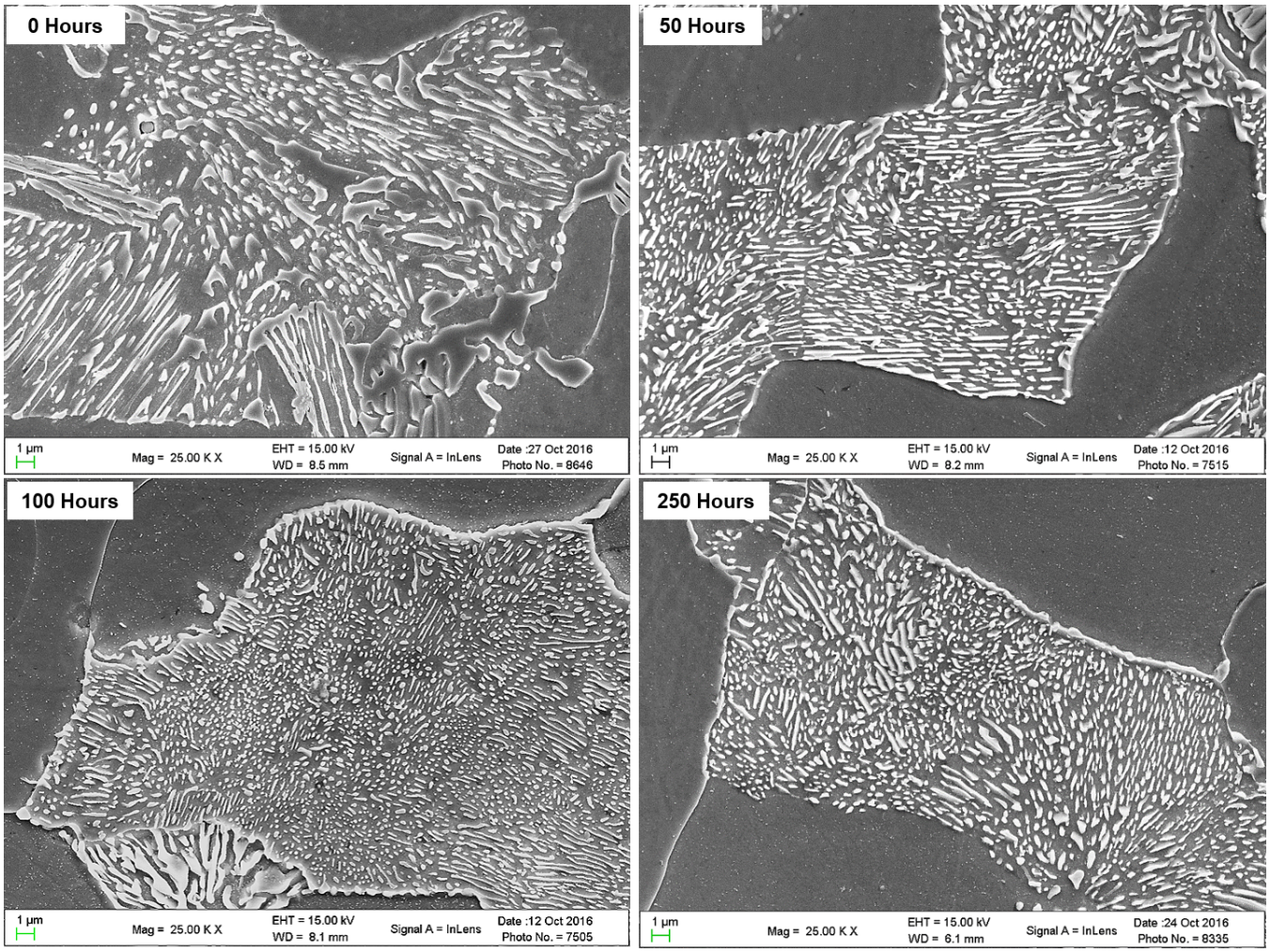


Figure 92. Comparative SEM micrographs (25 KX) after 0, 50, 100, and 250 hours of exposure at 1000°F (538°C).

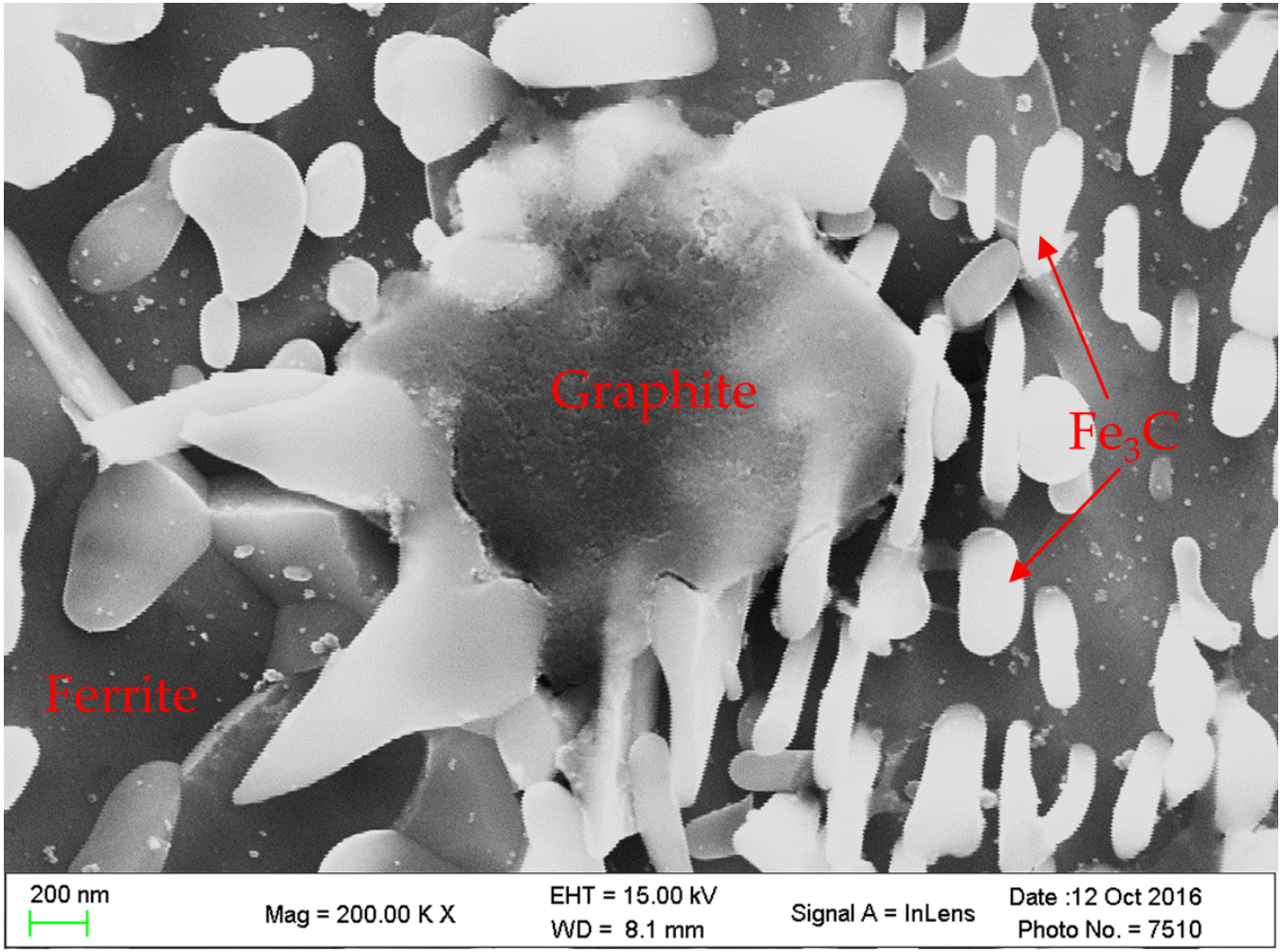


Figure 93. SEM micrograph showing evidence of graphitization along the ferrite-cementite interface (~500 nm) at 200 KX, observed after 250 hours at 1000°F (538°C).

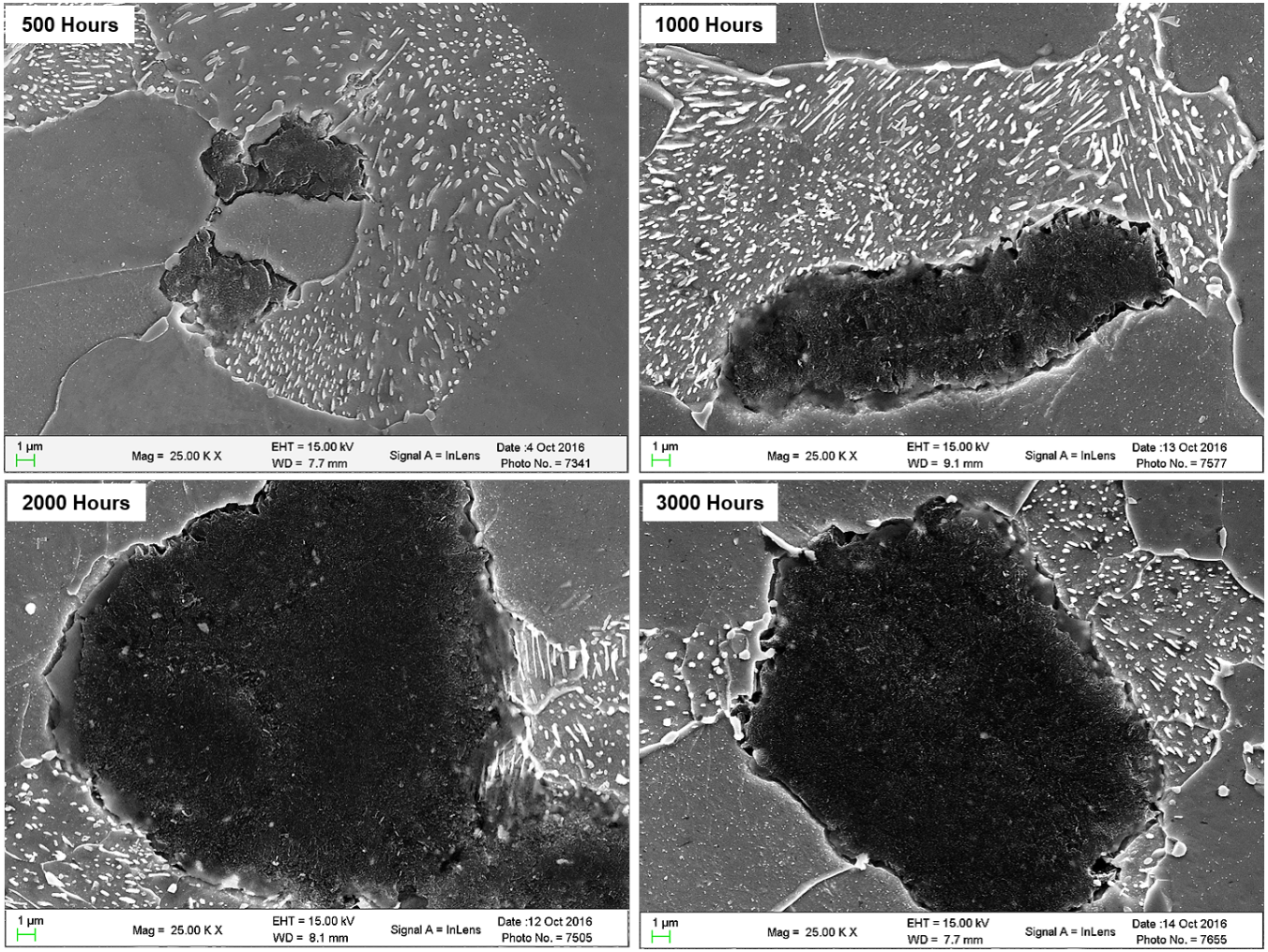


Figure 94. Comparative SEM micrographs (25 KX) after 500, 1000, 2000, and 3000 hours of exposure at 1000°F (538°C).

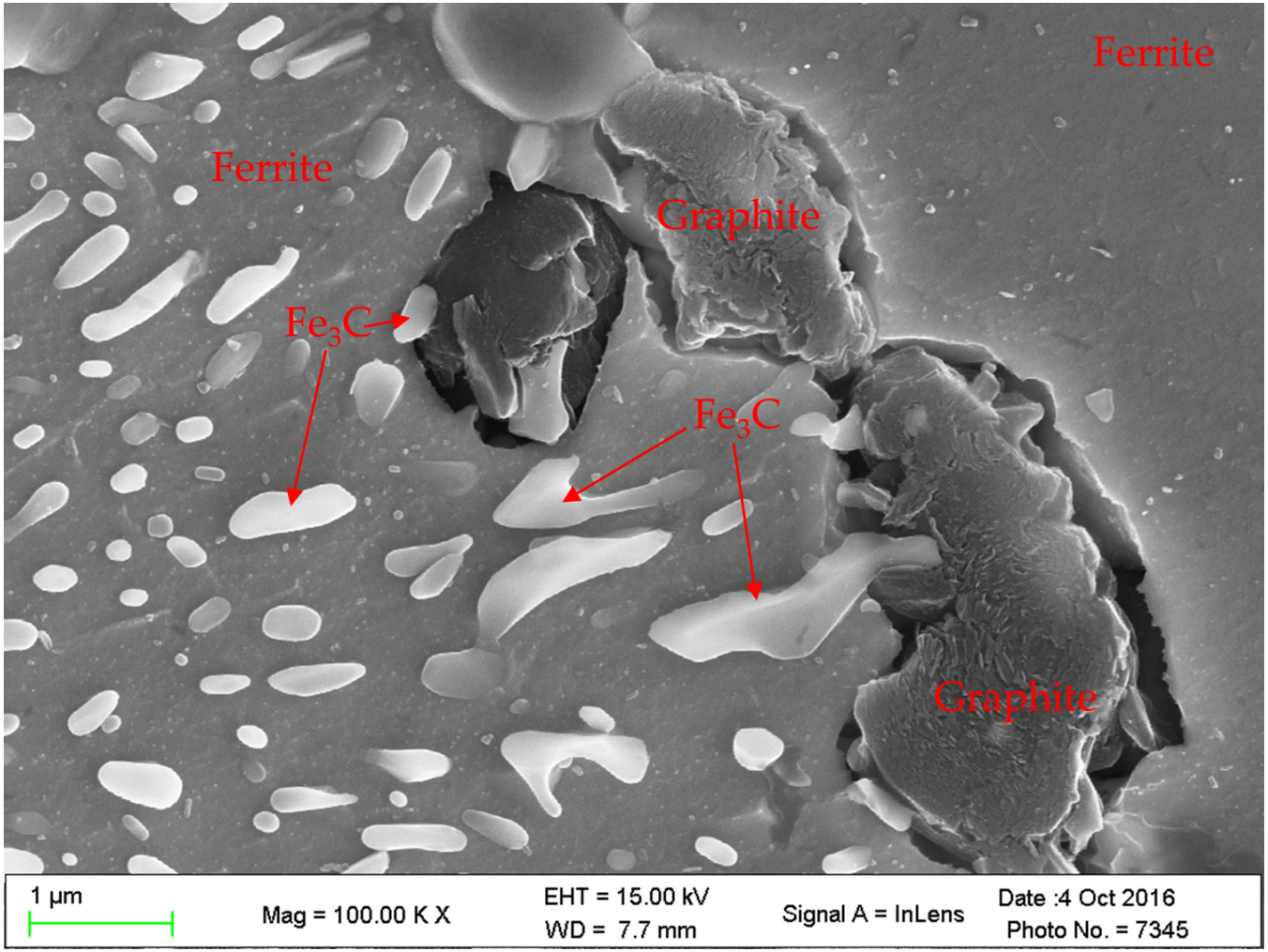


Figure 95. SEM micrograph showing graphitization along Fe-Fe3C interface and along pearlite-ferrite boundary.

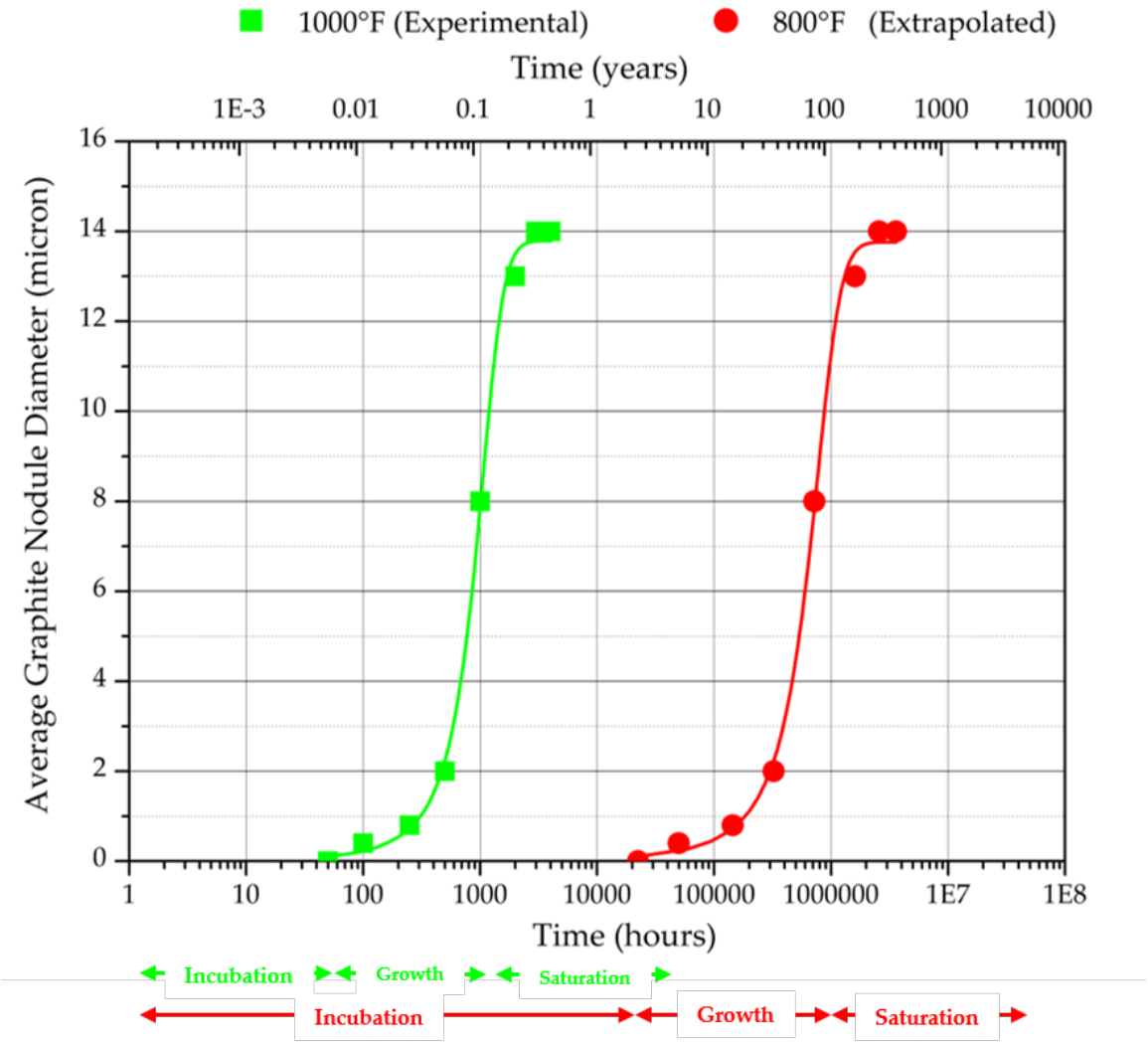


Figure 96. Average graphite nodule diameter as a function of time. The nodule growth rate showed a typical Avrami type transformation, which exhibited initial incubation period, which followed a rapid growth stage and acquired an equilibrium state.

Chapter 6 - Conclusions

Five ex-service carbon steel weldments were submitted after 17 years of service at 800°F (427°C) for metallurgical characterization to evaluate the presence of graphite and for remaining life assessment studies using creep studies. Three C-½ Mo materials with no prior evidence of graphitization were also utilized for heat treatment studies for further fundamental understanding. Following conclusions were drawn from the examination of all the materials evaluated with regards to the fundamental causes of graphitization and the remaining life assessment studies.

6.1 General Conclusions:

1. Microstructure of base metal after 17 years of service at 800°F (427°C) consisted of ferrite, spheroidized pearlite, and graphite. ASTM grain size ranged from #5-8.

2. Graphitization was primarily observed just outside of the optically visible HAZ in the base metal on the outer band which was exposed to a temperature just below the lower critical transformation temperature (A_{C_1}). These regions pertain to the subcritical heat affected zone

(SCHAZ). Graphitization observed in the SCHAZ exhibited planar morphology. A supporting hypothesis on the increased amount of graphitization on the SCHAZ region is proposed in this study.

3. Graphitization in the base metal remote from the HAZ were isolated/random and was observed to a lower extent compared to the base metal region just outside of the visible HAZ.

4. Graphite nodules were primarily located along the middle-third of the pipe wall. Graphitization was not observed in the weld deposit, which was attributed to its low carbon content.

5. Quantitative metallography using both ASTM E562 manual point count method and automated image analysis was performed to examine the volume fraction of graphite. The maximum graphite volume fraction for a through wall-region (1"-wall) in a 35 mm^2 band of the most graphitized material (CW-A) was only on the order of 1%. A through-wall volume fraction of the graphite nodules remote from the HAZ was less than 0.5 %.

6. Metallographic examination showed a general agreement with regards to the aluminum content. Materials with increased aluminum content showed presence of graphitization. However, the maximum extent of

graphitization was not observed in a sample with highest aluminum content. The two weldments with the lowest aluminum content (< 0.05 wt.%) did not exhibit any evidence of graphitization.

7. Energy dispersive spectroscopy (EDS) examinations did not show any evidence of aluminum or its oxide/nitride at or around graphite nodules to indicate if aluminum had any role in nucleation of new graphite nodules.

8. ASME IX Bend tests were performed to evaluate the bend ductility of the most graphitized region. CW-A weldment which exhibited the highest extent of graphitization was selected for bend testing. Bend specimen showed embrittling nature of the graphitized region, however the graphitization extent of 1 volume percent did not appear affect the bend ductility of the weldment which was fully ductile in all regions with 20% outer-fiber strain (plastic flow). The opening along the graphitized region just outside of the visible HAZ in the base metal was less than 1/8″ after 20% strain.

6.2 In Situ Inspection Studies Conclusions:

1. In situ inspection studies were performed on graphitized components using both non-destructive and destructive methods. Non-destructive evaluation using modern state-of-the-art ultrasonic inspection was performed with an assistance of level III NDE expert from Team Industrial Services. Destructive evaluation, using core sample extraction (~1/2 –wall) was performed with an assistance of Nelson Mandela Metropolitan University (NMMU), South-Africa.
2. A new protocol for evaluating the presence/extent of graphite nodules using ultrasonic methods was performed using "Variable Matrix Array". The ultrasonic inspection showed good progress with regards to the detectability of the graphitized components using a comparison method.
3. A core sample extraction performed using Weldcore technology was studied.
4. Core sample showed good representation of a typically observed graphitization in a through-wall cross-sectional metallurgical specimen.
5. Repair welding of the core extraction sites was performed using friction tapered hydro pillar processing (FTHPP).

6. All the twelve FTHPP friction plug welds showed 100% bonding along the interface. ASME IX Bend specimen used to evaluate the friction weld repaired joint showed material was fully ductile with 20% outer-fiber strain (plastic flow). A defect/opening along the friction weld interface was observed, however they were less than 1/8" (3 mm) for ASME weld qualification.
7. Microstructure of the plug base metal was fully bainitic subsequent to friction weld repair, suggesting the temperature of the plug was heated to a temperature above upper critical transformation (Ac_3) and followed by a rapid cooling. Plug base metal prior to FTHPP welding consisted ferritic and pearlitic microstructure. The average hardness of the plug base metal increased to 192 HV (88 ksi) from 130 HV (62 ksi) subsequent to FTHPP.
8. Microstructure of the plug weld HAZ (location of pre-existing graphite nodules) showed presence of complex microstructural constituents consisting of eutectic microstructures (Ledeburite and Cementite) as a result of nodule resolution in accordance to constitutional liquation. Nodule resolution resulted in carbon rich region adjacent to graphite nodules, which optically appeared as "dusting".

9. Nucleation of graphite nodules (~1-2 μm diameter) was observed in the friction weld HAZ ("dusted" region) subsequent to creep testing and additional aging studies of the friction repair welded specimen. However, nucleation of "new" graphite nodules did not appear to influence the creep performance of the welded component.

6.3 Creep Studies Conclusions:

1. Total of 29 creep specimens which involved materials in both service-exposed and friction weld repaired state were tested over a period longer than one year.
2. Steady state creep rates for graphitized materials for temperatures ranging (800-950˚F) and stresses (4.4 ksi-10 ksi) were generated.
3. Creep performance was not influenced by the presence of graphite. This seems to suggest that 1 volume fraction of graphite did not appear to influence the creep performance of these welded piping components.
4. Remaining life estimation was made on the graphitized components using Larson-Miller Parameter, constant (C) of 15. Even the most graphitized material showed a long remaining service life greater than 40 years.
5. Additional temperature/stress during the creep testing did not alter morphology/extent of the prior presence of show any influence on the

presence of graphite nodules, i.e. no changes in ex-service graphitization morphology were ascribed to creep testing.

6. Creep damage (cavitation and micro-fissuring) was only observed in two creep specimens; the damage was minor. However, creep damage observed in these samples was not attributed to prior presence of graphite nodules.
7. No creep related damage, cavities or fissures were observed during creep studies in the friction weld repaired components to suggest any issues with the longevity of the repair welded components.

6.4 Effect of Aluminum on Graphitization

1. In earlier investigations of the graphitized components, it has been proposed that aluminum acts as a nucleating agent for graphite nodule (either by forming aluminum oxide or nitride), but in the current study evidence of aluminum oxide/nitride associated with nucleation of graphite nodules was not observed.

2. Metallographic examination generally agreed with regards to the aluminum increasing graphitization, i.e. increased aluminum content resulted in graphitization. The two weldments with the lowest aluminum

content (< 0.05 wt.%) did not exhibit any evidence of graphitization. However, the maximum extent of graphitization was not observed in a sample with highest aluminum content.

3. Thus, it is believed that aluminum acts a graphitizer rather by un-stabilizing the carbides and by lowering solubility of carbon in iron rather than acting as a nucleating agent. A supporting hypothesis on the increased amount of graphitization with regards to the influence of aluminum on graphitization has been proposed in this study.

6.5 Weld Related Graphitization

1. Graphitization was primarily observed just outside of the optically visible HAZ in the base metal on the outer band which was exposed to a temperature just below the lower critical transformation temperature (Ac_1). These regions pertain to the subcritical heat affected zone (SCHAZ). Graphitization observed in the SCHAZ exhibited planar morphology. A supporting hypothesis on the increased amount of graphitization on the SCHAZ region was proposed in this study.

2. A hypothesis to support the increased amount of graphitization in SCHAZ was proposed in the current study. The increased amount of

graphitization was attributed to the carbon solubility differential between in ferrite as a function of temperature when the material is heated to the SCHAZ temperature.

3. The peak temperature with regards to the outer band of the HAZ, where graphitization is mostly observed was determined using dilatometry and post metallographic examination. The peak temperature was found to be just below the effective lower critical transformation temperature.

List of References

1. API Recommended Practice 571., *Damage Mechanisms Affecting Fixed Equipment in the Refining Industry*. 1st ed. 2003, Washington, D.C.: American Petroleum Institute. Division of Refining.
2. Smith, G. V. and Brambir, S. H., *Graphitization of Welded and of End-Quenched Carbon and Molybdenum Steels.* Welding Journal, 1945 (March).
3. Smith, G. V., MacMillan, J. A., and Dulis, E. J. *Some Aspects of Graphitization in Steel*. in *American Society for Metals -- Meeting, Oct 23-27 1950*. 1950. Cleveland, OH, United States: American Society for Metals.
4. Port, R. D., Mack, W. C., and Hainsworth, J., *The Mechanisms of Chain Graphitization of Carbon and Carbon Molybdenum Steels.* Heat Resistant Materials, 1991: p. 587-594.
5. Port, R. D. and Herro, H. M., *The Nalco Guide to Boiler Failure Analysis*. 1991, New York: McGraw-Hill. vi, 293 p.
6. Kinzel, A. B. and Moore, R. W., *Graphitization in Low-Carbon Steel.* Transactions of American Institute of Mining and Metallurgical Engineers, 1935. **116**.
7. Emerson, R. W. and Morrow, M., *Further Observation of Graphitization in Aluminum-Killed Carbon-Molybdenum-Steel Steam Piping* Transactions of ASME, 1946. **68**: p. 597-607.
8. Wells, C., *Graphitization of High Purity Iron Carbon Alloys.* Transactions of American Society of Metals, 1938. **26**: p. 289-357.
9. Austin, C. R. and Fetzer, M. C., *Factors Controlling Graphitization of Carbon Steels at Subcritical Temperatures.* Transactions of American Society of Metals, 1945. **35**.
10. Emerson, R. W. *Carbide Instability of Carbon-Molybdenum Steel Piping*. in *Graphitization of Steel Piping*. 1945. New York, New York: Annual Meeting of The American Society of Mechanical Engineers.
11. Hoyt, S. L. and Williams, R. D., *Progress Report on Graphitization of Steam Lines.* Welding Journal, 1945(May): p. 274-s.
12. Kerr, H. J. and Eberle, F., *Graphitization in Low-Carbon and Low-Carbon-Molybdenum Steels.* Welding Journal, 1945 (February).
13. Kerr, H. J. and Eberle, F. *Graphitization Caused by Testing Conditions on Carbon-Molybdenum Tubular Creep-Test Specimens*. in *Graphitization of Steel Piping*. 1945. New York, New York: Annual Meeting of The American Society of Mechanical Engineers.
14. Smith, G. V. and Miller, R. F. *A Possible Means of Avoiding Local Graphitization of Steels in Service at Elevated Temperatures*. in *Graphitization of*

Steel Piping. 1945. New York, New York: Annual Meeting of The American Society of Mechanical Engineers.

15. Timmons, G. A., *Graphitization of Carbon-Molybdenum Steel in High Temperature Steam Piping.* Welding Journal, 1946 (January).
16. Weaver, S. H., *General Discussion of Graphitization Papers.* Transactions of the American Society of Mechanical Engineers, 1946. **68**: p. 631.
17. White, A. E., *Graphitization of Steels at Elevated Temperatures.* Metals Progress, 1947. **52**(September).
18. Smith, G. V., *Graphitization of Low-Carbon Low-Alloy Steel- An Appraisal of Literature.* Welding Journal, 1948. **27**(6): p. 277-284.
19. Mahoneu, C. H. and Dritt, W. S., *Oak Ridge Reports on Graphitization in H-P Steam Lines.* Power Engineering, 1959. **63**(3): p. 68-69.
20. Rohrig, I. A., *Williamsburg Station Accident Investigation.* 1977.
21. McDonald, C., Arnold, J., and Henry, J., *Grain Boundary Graphitization in P1 (C-1/2 Mo) Alloy Pipe.* Proceedings of the ASME Pressure Vessels and Piping Conference, 2012. **6**: p. 645-656.
22. Ghosh, D., et al., *High-Temperature Graphitization Failure of Primary Superheater Tube.* High Temperature Materials and Processes, 2015. **34**(8): p. 777-781.
23. Furtado, H. C. and Le May, I., *Evaluation of an Unusual Superheated Steam Pipe Failure.* Materials Characterization, 2003. **49**(5): p. 431-436.
24. Thielsch, H., Phillips, E. M., and Jerome, J. E. R., *Considerations in Evaluation of Graphitization in Piping Systems.* Welding Journal, 1955. **34**(6): p. 286-294.
25. ASM International. Handbook Committee. and Knovel (Firm), *ASM handbook. Volume 1, Properties and Selection: Irons, Steels, and High-Performance Alloys*, 1990, ASM International,: Materials Park, OH. p. xi, 1063 p.
26. Port, R. D. *Non-Weld Related Graphitization Failures*. in *Corrosion 89*. 1989. New Orleans Convention Center, New Orleans, Louisiana: Proceeding of the 4tth NACE Annual Conference.
27. Kotwica, D. J., *Graphitization-Related Failure of a Low-Alloy Steel Superheater Tube*, in *Handbook of Case Histories in Failure Analysis*. 1992, ASM International
28. Schwartz, H. A., *Conversion of Solid Cementite into Iron and Graphite.* Iron and Steel Institute -- Journal, 1938. **138**(2): p. 205-235.

29. Darken, L. S. and Gurry, R. W., *Free energy of formation of cementite and the solubility of cementite in austenite.* Journal of Metals, Metallurgical Society of AIME, 1951. **3**: p. 1015-1018.
30. Darken, L. S. and Gurry, R. W., *Physical Chemistry of Metals*. Metallurgy and Metallurgical Engineering Series. 1953: McGraw-Hill Book Company, Inc. 535 pages.
31. Chipman, J., *Thermodynamics and Phase Diagram of the Fe-C System.* Metallurgical Transactions, 1972. **3**(1): p. 55-64.
32. Bhadeshia, H. K. D. H. and Honeycombe, R. W. K., *Steels : Microstructure and Properties*. 3rd ed. 2006. xi, 344 pages.
33. Sauveur, A., *The Metallography of Iron and Steel*. 1st ed. 1912, Cambridge, Mass.,: Sauveur and Boylston. xvi, 413 p.
34. Sauveur, A., *The Metallography and Heat Treatment of Iron and Steel*. 2d ed. 1916, Cambridge, Mass.,: Sauveur and Boylston. xvi, 486 p.
35. Croker, S. and Bailey, A. D., *Research on Graphitization of Piping is Under Way - Progress Report No. 1 on Survey of Graphitization of Piping.* Edison Electric Institute -- Bulletin, 1943. **11**(10): p. 307-308.
36. Anon, *Research on Graphitization of Piping is Under Way.* Edison Electric Institute -- Bulletin, 1944. **12**(4): p. 125-126.
37. Bailey, A. D. and Croker, S., *Fundamental Investigation of Graphitization of Piping - Progress Report No. 2.* Edison Electric Institute -- Bulletin, 1944. **12**(4): p. 125-126.
38. Anon, *Fundamental Investigation of Graphitization of Piping.* Edison Electric Institute -- Bulletin, 1945. **13**(7): p. 209-211.
39. Hankinson, L. E. and Purcell, T. E., *Fundamental Investigation of Graphitization of Piping - Progress Report No. 3.* Edison Electric Institute -- Bulletin, 1945. **13**(7): p. 209-211.
40. Anon, *Fundamental Investigation of Graphitization of Piping.* Edison Electric Institute -- Bulletin, 1946. **14**(2): p. 48-52.
41. Hankinson, L. E. and Bailey, A. D., *Final Progress Report - Fundamental Investigation of Graphitization of Piping.* Edison Electric Institute -- Bulletin, 1948. **16**(2): p. 43-44.
42. Emerson, R. W. *Carbide Instability of Carbon-Molybdenum Steel Piping*. in *Graphitization of Steel Piping*. 1943. New York, New York: Annual Meeting of The American Society of Mechanical Engineers.

43. Rossheim, D. B., et al., *Recent Experience in Examination of High-Temperature Catalytic-Cracking Pressure Equipment.* American Society of Mechanical Engineers -- Transactions, 1952. **74**(7): p. 1099-1122.
44. Nuchols, J. B. and McGuffey, J. R., *Graphitization Failures in Piping.* Mechanical Engineering, 1959. **81**(5): p. 43-45.
45. Austin, C. R. and Fetzer, M. C., *Effect of Composition and Steelmaking Practice on Graphitization below the A1 of Eighteen One Percent Plain Carbon Steels.* Transactions of the American Institute of Mining and Metallurgical Engineers, 1941. **145**: p. 213-224.
46. Kerr, H. J. and Eberle, F., *Discussion on Graphitization in Low-Carbon and Low-Carbon-Molybdenum Steels.* Welding Journal, 1945 (June).
47. Wilson, J. G., *Graphitization of Steel in Petroleum Refining Equipment and The Effect of Graphiziation of Steel on Stress-Rupture Properties.* Welding Research Council Bulletin, 1957. **32**: p. 1-48.
48. He, K., et al., *An Electron Microscopic Study of Spheroidal Graphite Nodules formed in a Medium-Carbon Steel by Annealing.* Acta Materialia, 2007. **55**(9): p. 2919-2927.
49. Harry, E. D., *Subcritical Decomposition of Carbide Phase in Some Low-Carbon Silicon Steels.* Journal of the Iron and Steel Institute, 1954. **171**(1).
50. Dennis, W. E., *Heterogeneous Nucleation of Graphite in Hypo-Eutectoid Steels* Journal of the Iron and Steel Institute, 1952. **171**(1).
51. Smith, G. V., MacMillan, J. A., and Dults, E. J. *Some Aspects of Graphitization in Steel*. in *American Society for Metals -- Meeting, Oct 23-27 1950*. 1950. Cleveland, OH, United States: American Society for Metals.
52. American Institute of Mining Metallurgical and Petroleum Engineers. Iron and Steel Division. Committee on Physical Chemistry of Steelmaking., Alloys of iron research., and Washburn, T. S., *Basic Open Hearth Steelmaking*. Seeley W Mudd series. 1944, New York,: American Institute of Mining and Metallurgical Engineers. xvii, 632 p.
53. Elliott, J. F. and Gleiser, M., *Thermochemistry for Steelmaking*. Addison-Wesley series in the engineering sciences: metallurgy and materials. 1960, Reading, Mass.,: Addison-Wesley Pub. Co.
54. Bain, E. C. and Paxton, H. W., *Alloying Elements in Steel*. 2nd ed. 1961, Metals Park, Ohio: American Society for Metals. x, 254 p.
55. Smith, G. V., Miller, R. F., and Tarr, C. O. *Precipitation and Reversion of Graphite in Low-Carbon Low-Alloy Steel in Temperature Range 900 to 1300°F*. in *American Institute of Mining and Metallurgical Engineers -- Meeting, Feb*

1944. 1944. New York, NY, United States: American Institute of Mining and Metallurgical Engineers.
56. Wilson, J. G., *Graphitization of Steel in Petroleum Refining Equipment.* American Petroleum Institute -- Proceedings, 1955. **35**(Sec 3): p. 209-248.
57. Journal, W., *Graphitization and Failure of Steel in Service.* Welding Journal, 1948.
58. Thielsch, H., *Interpreting Graphitization: A Report for Power Plant Engineers* Combustion, 1954. **26**(4): p. 49-55.
59. Easterling, K. E., *Introduction to the Physical Metallurgy of Welding*. Butterworths Monographs in Materials. 1983, London ; Boston: Butterworths. 231 p.
60. Eberle, F., *Influence of Heat Treatment Upon the Susceptibility to Graphitization of High Aluminum Deoxidized Carbon Molybdenum Steel.* Welding Journal, 1946(May).
61. Foulds, J. R. and Viswanathan, R., *Graphitization of Steels in Elevated-Temperature Service.* First International Conference on Microstructures and Mechanical Properties of Aging Materials, 1993: p. 61-69.
62. Moss, C. J. and Davidson, J. L., *Graphitization in Type A201 Carbon Steel in Petro-Chemical Plant After Long Term Service.* Metals forum, 1993. **17**(4): p. 351-359.
63. Foulds, J. R. and Viswanathan, R., *Graphitization of Steels in Elevated-Temperature Service.* Journal of Materials Engineering and Performance, 2001. **10**(4): p. 484-492.
64. Foulds, J. R. and Shingledecker, J. P., *An Updated Assessment of Graphitization of Steels in Elevated Temperature Service.* Journal of Materials Engineering and Performance, 2015. **24**(2): p. 586-597.
65. Callister, W. D., *Materials Science and Engineering : An Introduction*. 2002. xviii, 602 pages.
66. Samuels, L. E., *Light Microscopy of Carbon Steels*. 1999, Materials Park, Ohio,: ASM International. 502 p.
67. Weisberg, H., *Report on High-Temperature Pipe Weld Investigation.* American Society of Mechanical Engineers -- Transactions, 1944.
68. Hughes, M. A. and Cutton, J. G., *Graphitization in Hypo-Eutectoid Steels.* Iron and Coal Trades Review, 1946. **153**(4090): p. 92.
69. Conant, W. G. and Reich, W. A. *Graphitization Studies of Materials for High Temperature Service in Steam Plants*. in *American Society of Mechanical*

Engineers -- Meeting A-78, Dec 2-6 1946. 1946. New York, NY, United States: American Society of Mechanical Engineers (ASME).

70. Hoyt, S. L., Williams, R. D., and Hall, A. M., *Summary Report on Joint E.E.I.-A.E.I.C. Investigation of Graphitization of Piping.* American Society of Mechanical Engineers -- Transactions, 1946. **68**(6): p. 571-577.
71. Smith, G. V., Brambir, S. H., and Benz, W. G., *Comparative Graphitization of Some Low-Carbon Steels With and Without Molybdenum and Chromium.* American Society of Mechanical Engineers -- Transactions, 1946. **68**(6): p. 589-595.
72. Boetcher, H. N., *Investigation of Graphitization of Piping.* American Society of Testing Materials Bulletin, 1944. **130**(12): p. 37-40.
73. Campbell, F. C., *Elements of Metallurgy and Engineering Alloys*. 2008, Materials Park, Ohio 44073: ASM International. xiii, 656 p.
74. Brown, F., *Nucleation and Growth of Graphite in Steel.* Welding Journal, 1954. **33**(June).
75. Hardigree, R. S., *Graphitization of High-Temperature Steam Mains.* Electric Light and Power, 1956. **34**(17): p. 98-103.
76. Pavlichko, W. R. and Solomon, A., *Graphitization Studies at Fossil Fuel Power Plants.* Microstructural Science, 1980. **8**: p. 231-245.
77. Hattingh, D. G., et al., *Process Parameter Influence on Performance of Friction Taper Stud Welds in AISI 4140 Steel.* Materials & Design, 2011. **32**(6): p. 3421-3430.
78. Wedderburn, I. N., et al., *Condition Monitoring of High Temperature, High Stress Components by Means of Core Sampling and Friction Weld Repair*, in *18th World Conference on Nondestructive Testing*, 2012: Durban, South Africa.
79. Bulbring, D. L. H., et al., *Friction Hydro Pillar Process as an Alternative Repair Technology for Creep Evaluation Sites on Thick-Walled 10CrMo910 Creep-Resistant Steel Structures.* Journal of the Southern African Institute of Mining and Metallurgy, 2013. **113**(2): p. 131-138.
80. Nicholas, E. D. *Friction Hydro Pillar Processing* in *Advances in Welding Technologies*. 1995. Annual North American Welding Research Conference.
81. Meyer, A., *Friction Hydro Pillar Processing : Bonding Mechanism and Properties*. 2003.
82. Nicholas, E. D., *Friction Processing Technologies.* Welding in the World, 2003. **47**(11-12): p. 2-9.

83. Hattingh, D. G., et al. *Friction Taper Stud Welding of Creep Resistant 10CrMo910*. in *Friction Stir Welding and Processing V, 15-19 February*. 2009. Warrendale, PA, USA: Metals & Materials Society (TMS).
84. Hattingh, D. G., Von Wielligh, L. G., and Pentz, W. G., *Feasibility of Utilising Friction Hydro Pillar Processing as a Repair Technique for Incorrectly Drilled Holes.* International Institute of Welding, 2012.
85. Hattingh, D. G. and Zyl, v. C., *Temperature Distribution for a Friction Taper Stud Weld in Thick Walled 10CrMo910 Steel.* R &D Journal of the South African Institution of Mechanical Engineering, 2012. **28**: p. 37-45.
86. Zyl van C., *Analysis and Modelling of the Temperature Distribution during the Friction Taper Stud Welding of 10CrMo910*, in *Nelson Mandela Metropolitan University, Faculty of Engineering, the Built Environment and Information Technology,* 2008, Nelson Mandela Metropolitan University. p. 205.
87. Hankinson, L. E., Purcell, T. E., and Bailey, A. D., *Fundamental Investigation of Graphitization of Piping - Progress Report 5.* Edison Electric Institute -- Bulletin, 1946. **14**(2): p. 48-52.
88. Nippes, E. F. and Nelson, E. C., *Prediction of Weld Heat-Affected Zone Microstructures from Continuous Cooling Transformation Data.* Welding Journal, 1958. **37**: p. 289s-294s.
89. Lundin, C. D. and Liu, P., *Studies Of Local Differences In Material Creep Properties On Weldments: Determination of Creep Behavior of Singular HAZ Regions to Model the Behavior of the Entire HAZ of Cr-Mo Steels in Elevated Temp Service.* Welding Research Council Bulletin, 2002. **475**.
90. Bhadeshia, H. K. D. H. *Interpretation of the Microstructures of Steels*. 2012 [cited 2016 10/12/2016]; Available from: http://www.msm.cam.ac.uk/phase-trans/2008/Steel_Microstructure/SM.html.
91. Minkoff, I., *The Physical Metallurgy of Cast Iron*. 1983, Chichester West Sussex ; New York: Wiley. xii, 305 p.
92. Kubaschewski, O., *Iron-Binary Phase Diagrams*, ed. N.Y. Springer-Varlag Berlin Heidelberg. 1982. ix, 185 pages.
93. ASME BPVC IX, *Welding, Brazing, and Fusing Qualifications*, in *Qualification Standard for Welding, Brazing, and Fusing Procedures; Welders; Brazers; and Welding, Brazing, and Fusing Operators*2016, The American Society of Mechanical Engineers: Two Park Avenue, New York, NY 10016.

Appendix

Appendix-A - Tables for Thermodynamic Calculations

TABLE 16-1. THERMODYNAMIC FUNCTIONS FOR IRON*

°K	$-\frac{F^\circ - H_0^\circ\dagger}{T}$, cal/(gram atom)(°C)			$H^\circ - H_0^\circ$, cal/gram atom			C_P, cal/(gram atom) (°C)		
	$\alpha(\delta)$	γ	Liquid	$\alpha(\delta)$	γ	Liquid	$\alpha(\delta)$	γ	Liquid
0	0			0			0		
298.16	2.900	−1.410		1070	2932		5.98	6.39	
400	4.058	+1.347		1712	3593		6.55	6.59	
500	5.068	3.298		2388	4268		6.99	6.79	
600	5.976	4.826		3114	4952		7.54	6.99	
700	6.805	6.085		3902	5661		8.25	7.19	
800	7.575	7.167		4773	6389		9.23	7.39	
900	8.303	8.094		5765	7138		10.74	7.58	
1000	9.005	8.929		6970	7906		13.80	7.78	
1020	9.145	9.085		7262	8062		15.62	7.82	
C_P max. 1033				7481			18.00		
1040	9.285	9.238		7591	8219		13.58	7.86	
1060	9.424	9.389		7844	8377		11.92	7.90	
1080	9.563	9.537		8076	8535		11.30	7.94	
1100	9.701	9.682		8297	8695		10.83	7.98	
1120	9.836	9.824		8511	8855		10.49	8.02	
1140	9.972	9.964		8718	9015		10.23	8.06	
1160	10.106	10.102		8920	9177		10.01	8.10	
1180	10.237	10.237					9.85	8.12	
$\alpha \rightarrow \gamma$ 1183.16	10.2581	10.2581		9150	9365		9.83	8.15	
1200	10.3676	10.3698		9315	9503		9.72	8.17	
1250	10.6860	10.6934		9795	9914		9.51	8.28	
1300	10.9946	11.0049	10.257	10267	10330	13431	9.41	8.38	10.28
1308	11.0431	11.0536		10342	10397	13514	9.40	8.39	
1350	11.2937	11.3052	10.647	10736	10752	13946	9.36	8.48	10.29
1400	11.5838	11.5953	11.023	11203	11178	14461	9.33	8.58	10.32
1450	11.8653	11.8759	11.385	11670	11610	14978	9.32	8.68	10.35
1500	12.1389	12.1478	11.734	12136	12046	15496	9.33	8.77	10.37
1550	12.4048	12.4116	12.074	12602	12487	16015	9.34	8.87	10.40
1600	12.6634	12.6678	12.402	13071	12933	16536	9.37	8.97	10.42
1650	12.9154	12.9171	12.720	13541	13384	17057	9.43	9.07	10.44
$\gamma \rightarrow \delta$ 1673.16	13.0301	13.0301	12.864	13760	13595	17299	9.45	9.12	10.45
1700	13.161	13.160	13.029	14014	13841	17580	9.48	9.17	10.46
1750	13.400	13.396	13.328	14489	14302	18103	9.54	9.27	10.48
$\delta \rightarrow l$ 1812	13.689	13.681	13.689	15083	14880	18753	9.60	9.39	10.50
1873	13.966	13 954	14.031	15671	15457	19394	9.68	9.51	10.53
1900	14.086	14.072	14.179	15932	15715	19678	9.72	9.57	10.54
2000	14.517	14.498	14.711	16911	16681	20734	9.86	9.77	10.58

* L. S. Darken and R. P. Smith, *Ind. Eng. Chem.*, **43**, 1815 (1951).
† H_0° refers to $\alpha(\delta)$-iron in all cases.

Figure A- 1 Thermodynamic functions for iron[29, 30]

TABLE 16-2. ENTHALPY AND FREE-ENERGY FUNCTIONS FOR CEMENTITE AND GRAPHITE

°K	Cementite*		Graphite†	
	$H^\circ - H_0^\circ$, cal/gram mole	$-\frac{F^\circ - H_0^\circ}{T}$, cal/(gram mole) (°C)	$H^\circ - H_0^\circ$, cal/gram atom	$-\frac{F^\circ - H_0^\circ}{T}$, cal/(gram atom) (°C)
0	0	0	0	0
298.16	4,329	10.405	251.56	0.517
300	4,376	10.493	255.31	0.523
400	7,023	15.128	502.6	0.825
500	9,952	19.304	820.8	1.146
600	12,746	23.069	1198.1	1.477
700	15,452	26.410	1622.0	1.810
800	18,248	29.408	2081.7	2.138
900	21,073	32.131	2569.4	2.459
1000	23,951	34.627	3074.6	2.771
1100	26,939	36.934	3596.	3.073
1200	30,042	39.089	4130.	3.365
1300	33,165	41.113	4680.	3.647
1400	36,315	43.020	5242.	3.919
1500	39,508	44.824	5814.	4.181
1600	42,744	46.536	6400.	4.43
1700	45,970	48.165	6987.	4.68
1800	49,211	49.718	7578.	4.92
1900	52,499	51.204	8170.	5.15
2000	55,798	52.627	8780.	5.37

* From L. S. Darken and R. W. Gurry, *Trans. AIME*, **191**, 1015 (1951).
† From Rossini, Wagman, Evans, Levine, and Jaffe, *Natl. Bur. Standards, Circ.* 500 (1952).

TABLE 16-3. SOLUBILITY OF CEMENTITE IN α-IRON AND OTHER FUNCTIONS LEADING TO THE SOLUBILITY OF GRAPHITE IN α-IRON

°K	ΔF°_3,* cal	Solubility of cem. in α-Fe, wt. % C	Ratio of gr. to cem. solubility in α-Fe	Solubility of gr. in α-Fe, wt. % C
298	4760	2×10^{-7}	0.00032	6×10^{-11}
400	4262	1.4×10^{-5}	0.0047	6×10^{-8}
500	3637	0.00015	0.026	4×10^{-6}
600	2915	0.00076	0.087	7×10^{-5}
700	2185	0.0024	0.207	0.0005
800	1478	0.0057	0.394	0.0022
900	827	0.0113	0.630	0.0071
1000	273	0.0195	0.870	0.0170

* For the reaction $3Fe(\alpha) + C(gr.) = Fe_3C(cem.)$.

Figure A- 2 Enthalpy and free-energy functions for cementite and graphite[29, 30].

Appendix B - Metallographic Examination

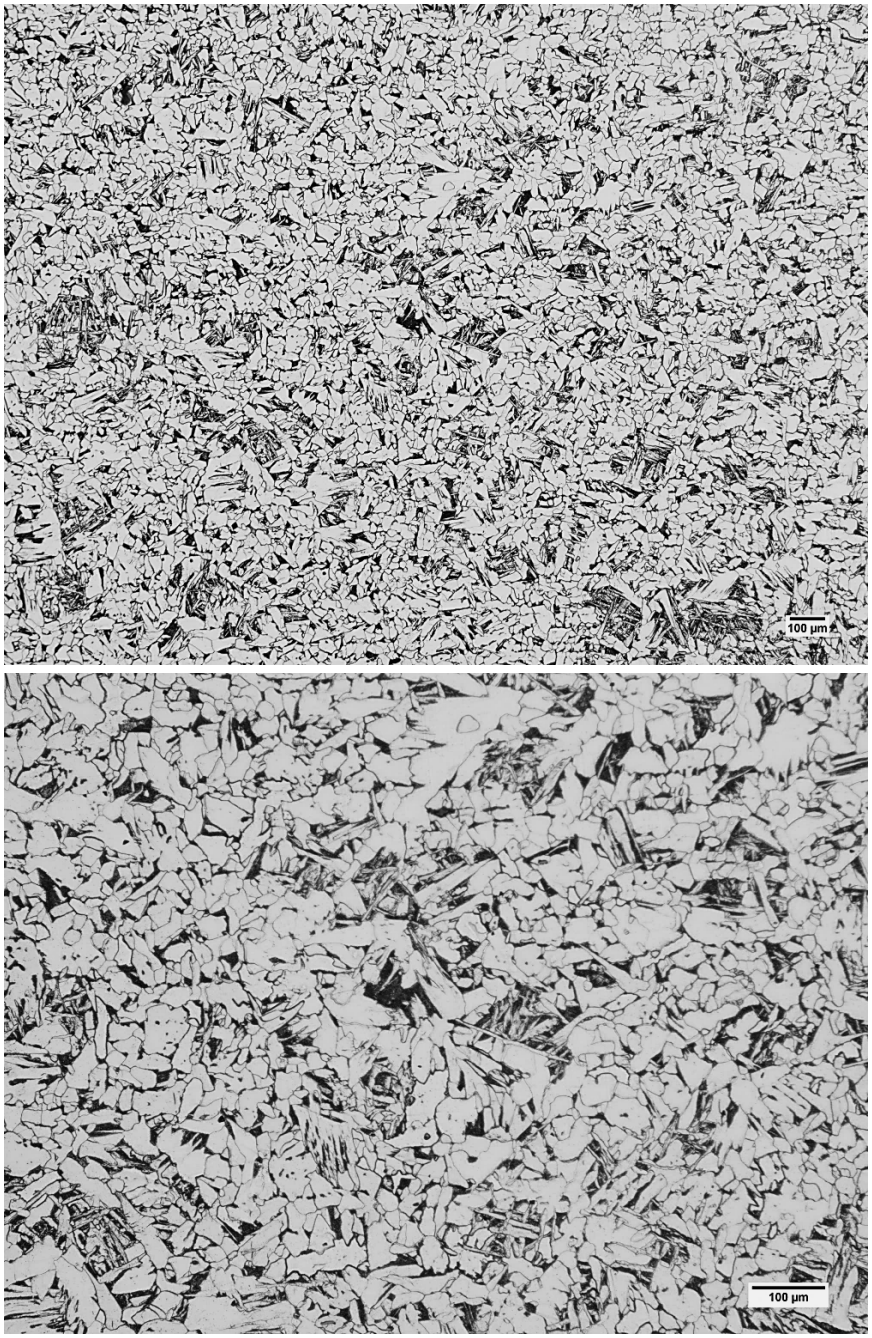


Figure B-1.Optical micrographs, A) 50X, and B) 100X in base metal C1 showing no graphitization. Microstructure consists of ferrite and bainite, 2% Nital etch.

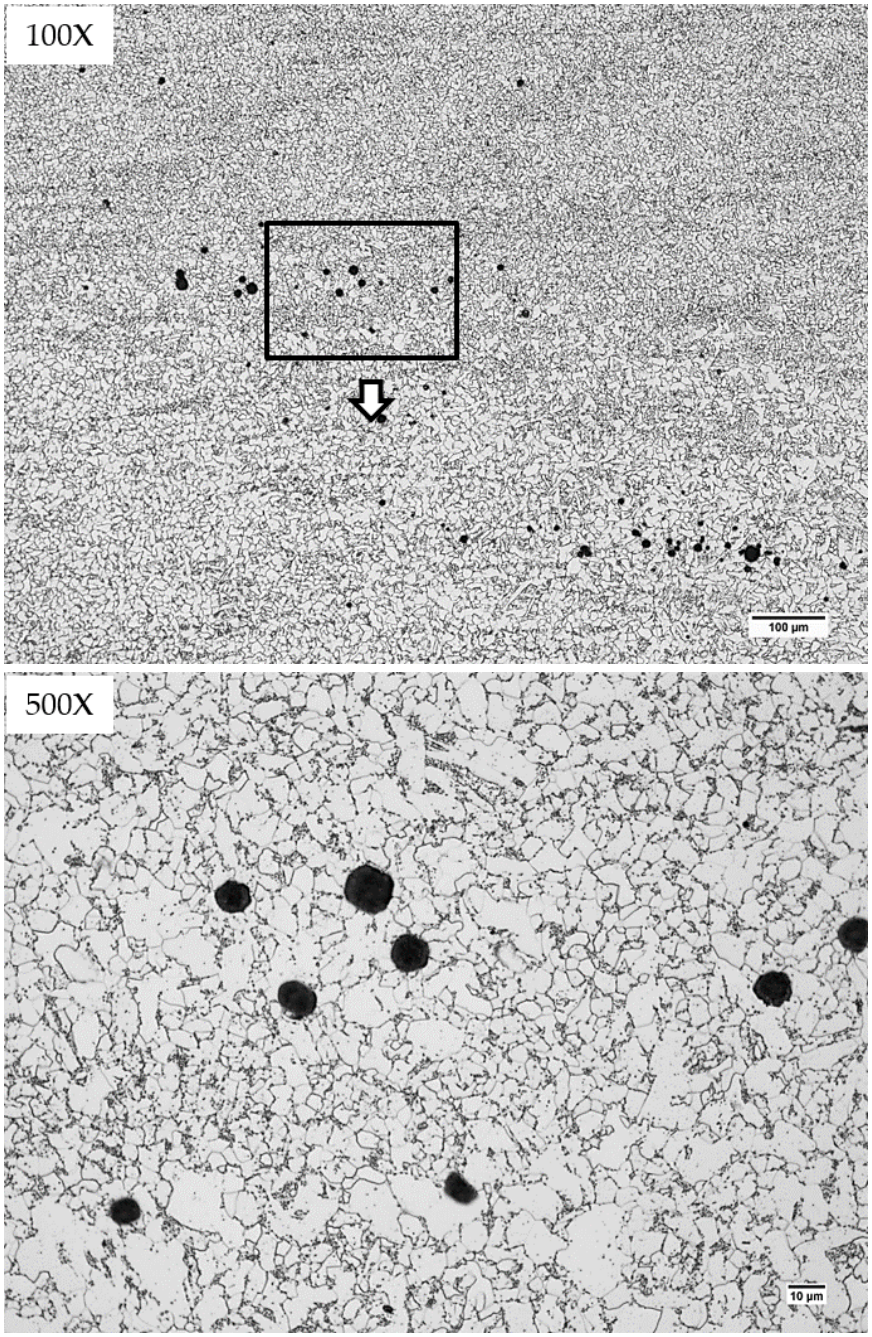


Figure B-2. Optical micrographs, in LSW-D showing evidence of graphitization the FGHAZ, 2% Nital etch.

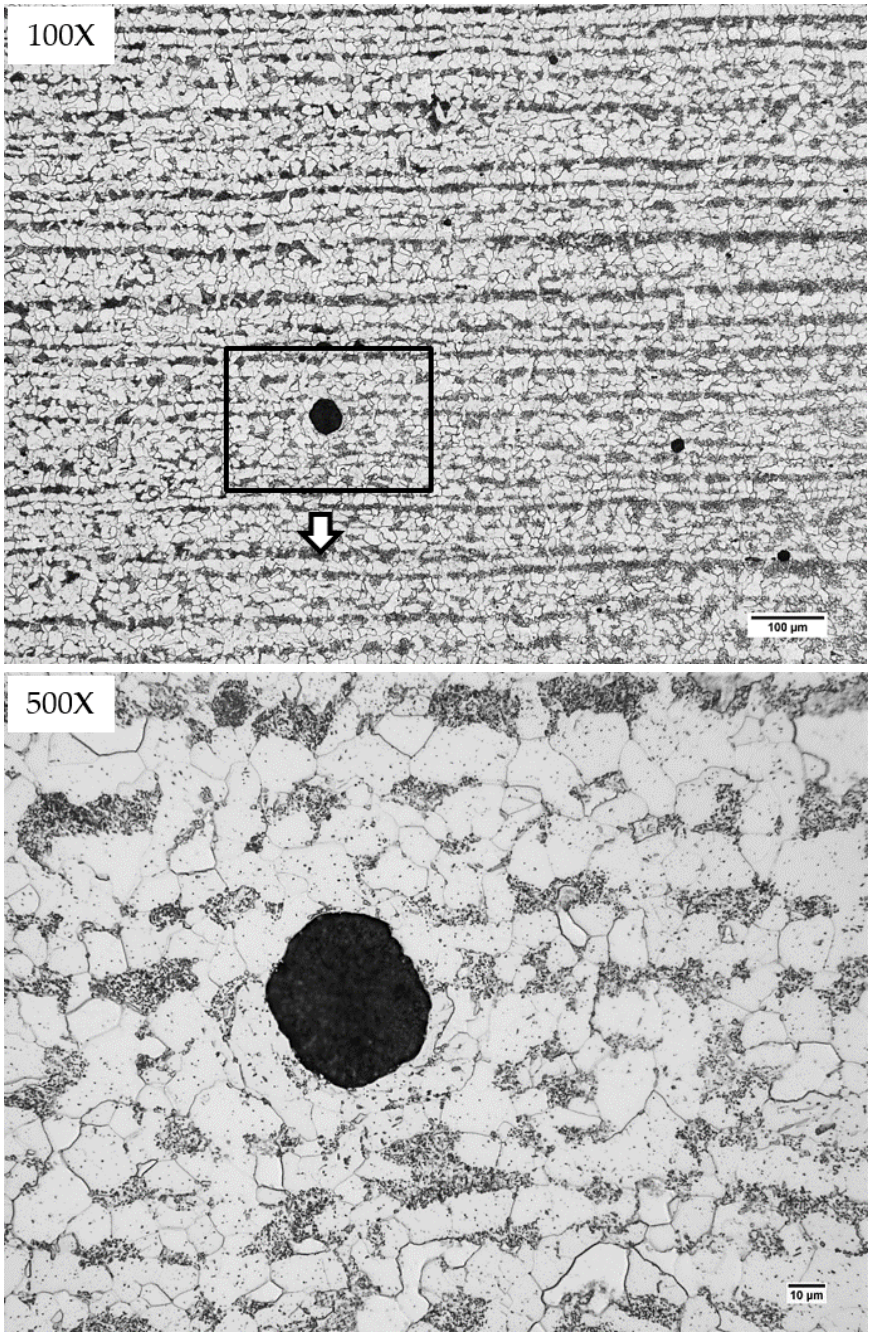


Figure B-3. Optical micrographs, in LSW-E showing evidence of graphitization in the base metal, 2% Nital etch.

Appendix C - Creep Data

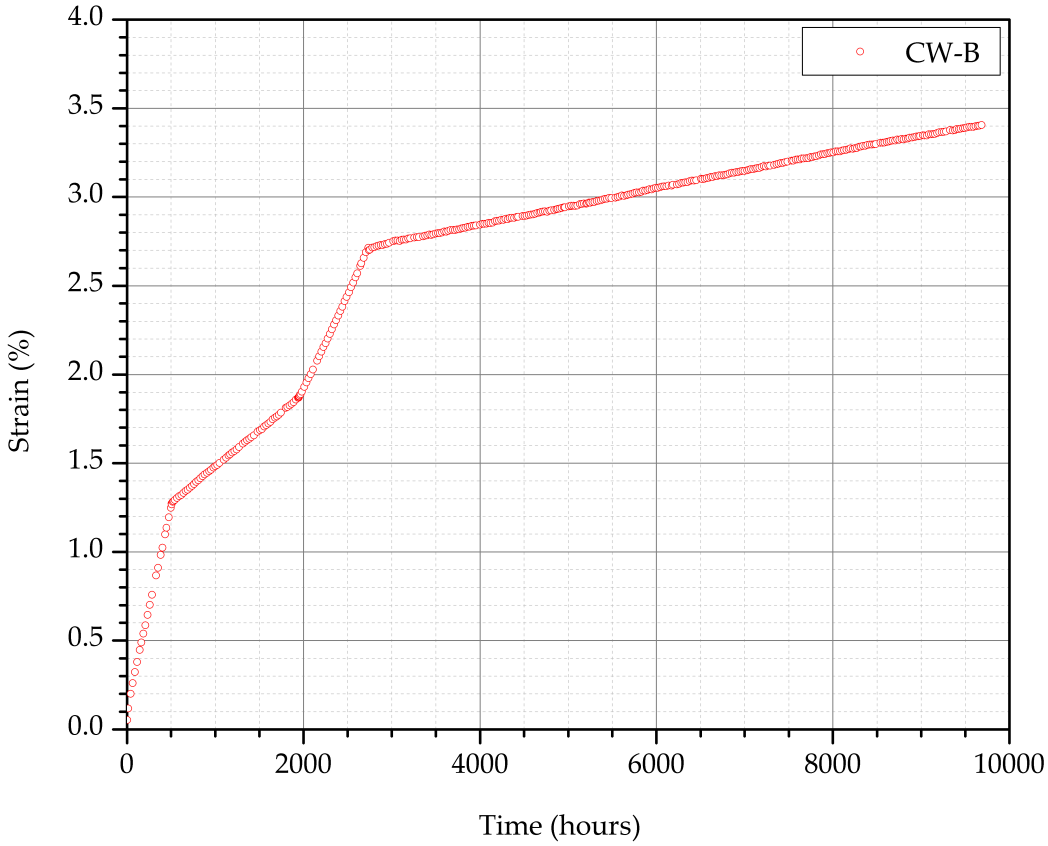


Figure C- 1. Creep curve for CW-B circumferential weld. Creep testing conditions and steady state creep rate provided in Table below.

Test Time (hours)	Temperature (°F)	Stress (ksi)	Steady State Creep Rate (%/hr x 10^{-4})
504	950	10	23.0
1442	900	10	4.1
789	925	10	10.8
6951	850	10	1.0

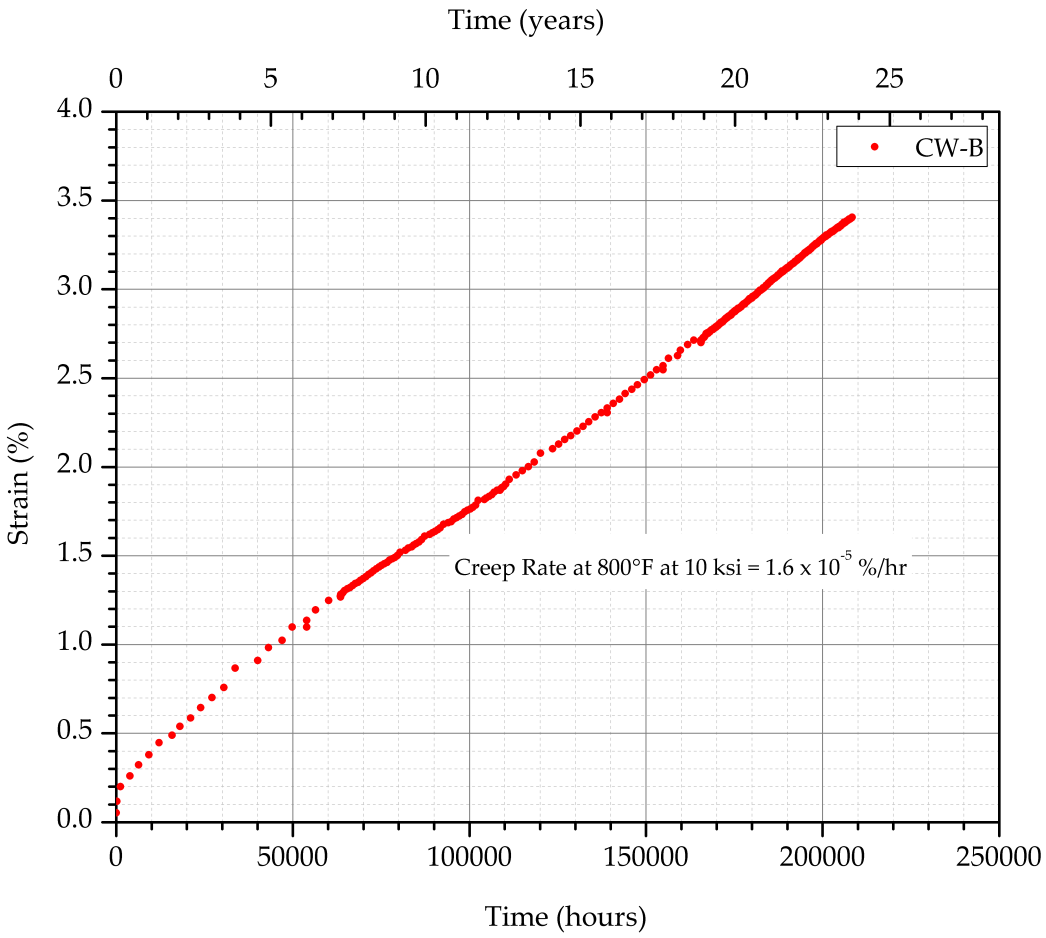


Figure C- 2. Normalized creep curve for CW-B (Creep data presented in Figure C-1).

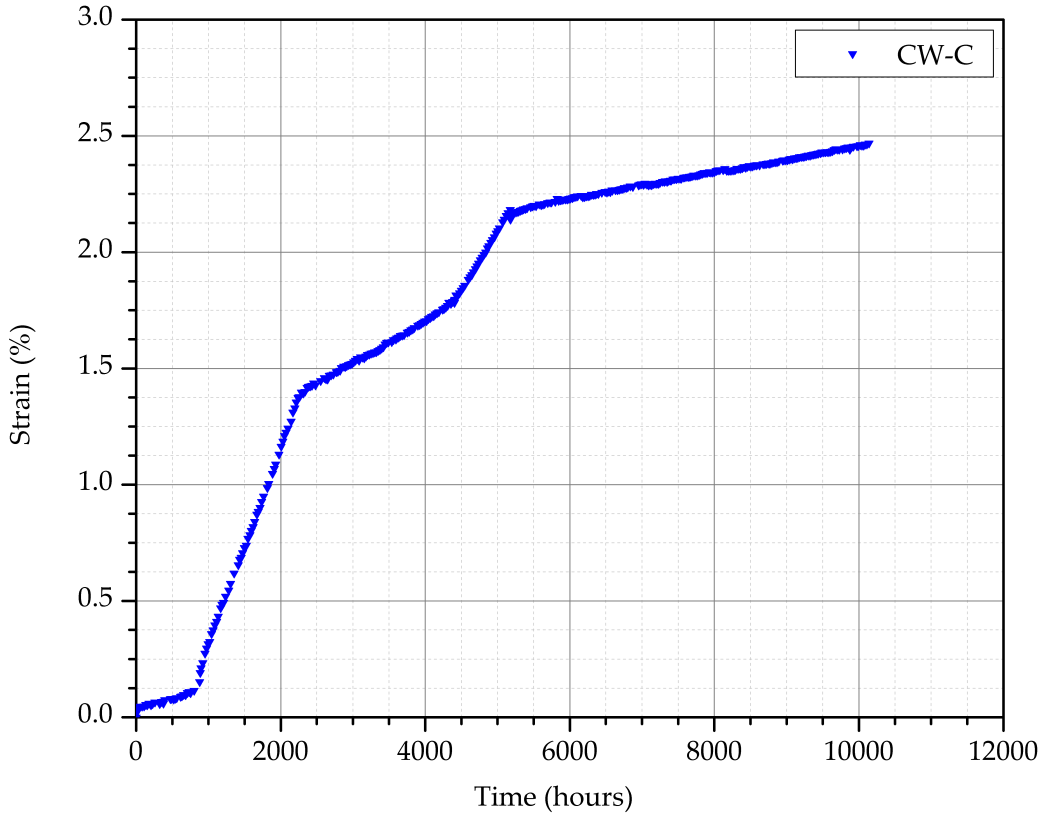


Figure C- 3. Creep curve for CW-C circumferential weld.

Creep testing conditions and steady state creep rate provided in Table below.

Test Time (hours)	**Temperature (°F)**	**Stress (ksi)**	**Steady State Creep Rate (%/hr x 10^{-4})**
376	900	4.4	0.4
503	950	4.4	1.2
1371	950	10	8.5
2155	900	10	1.8
772	925	10	4.8
4961	850	10	0.6

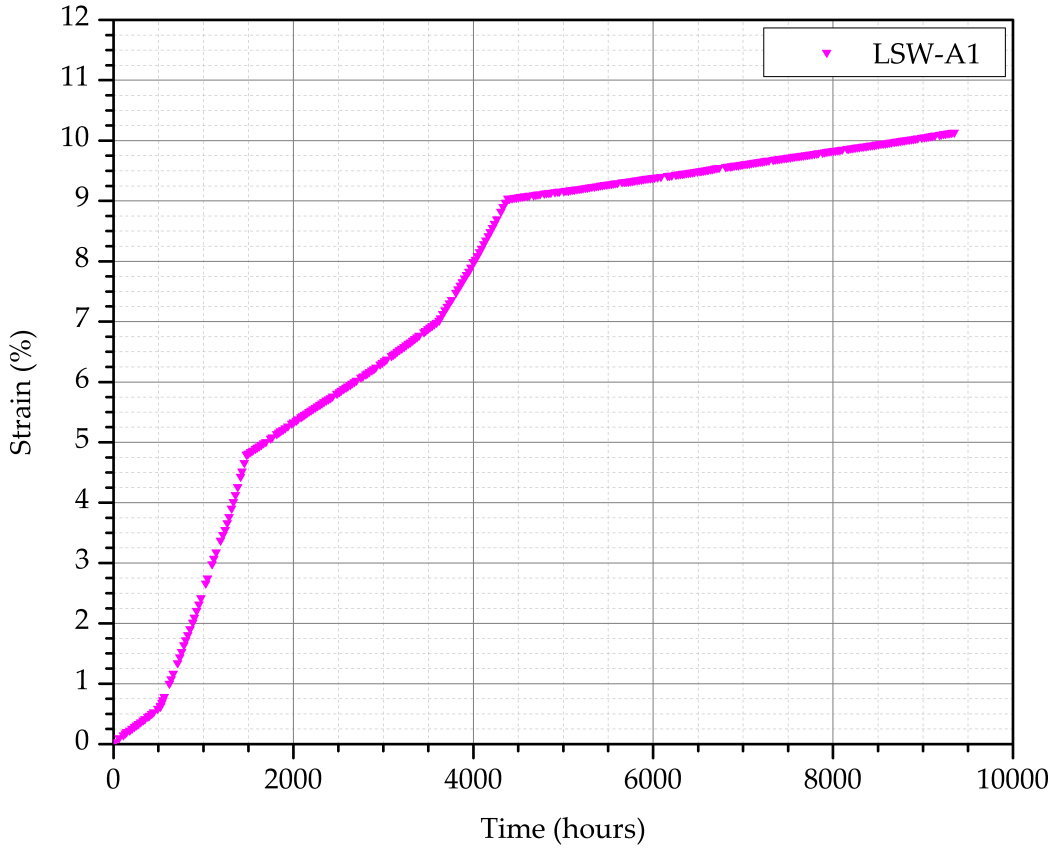


Figure C- 4. Creep curve for LSW-A1 longitudinal seam weld.

Creep testing conditions and steady state creep rate provided in Table below.

Test Time (hours)	Temperature (°F)	Stress (ksi)	Steady State Creep Rate (%/hr x 10^{-4})
524	950	8	11.4
953	950	10	43.5
2143	900	10	10.3
767	925	10	26.1
4963	850	10	2.2

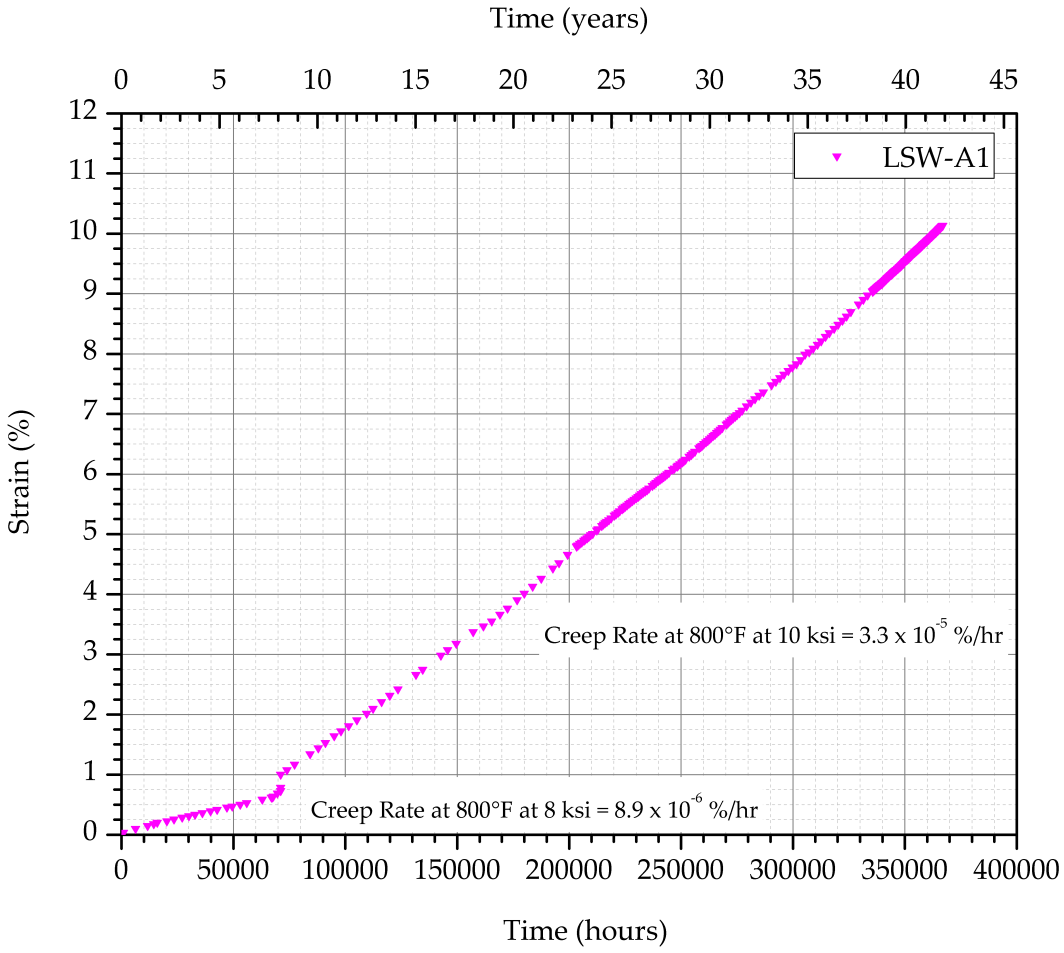


Figure C- 5. Normalized creep curve for LSW-A1.

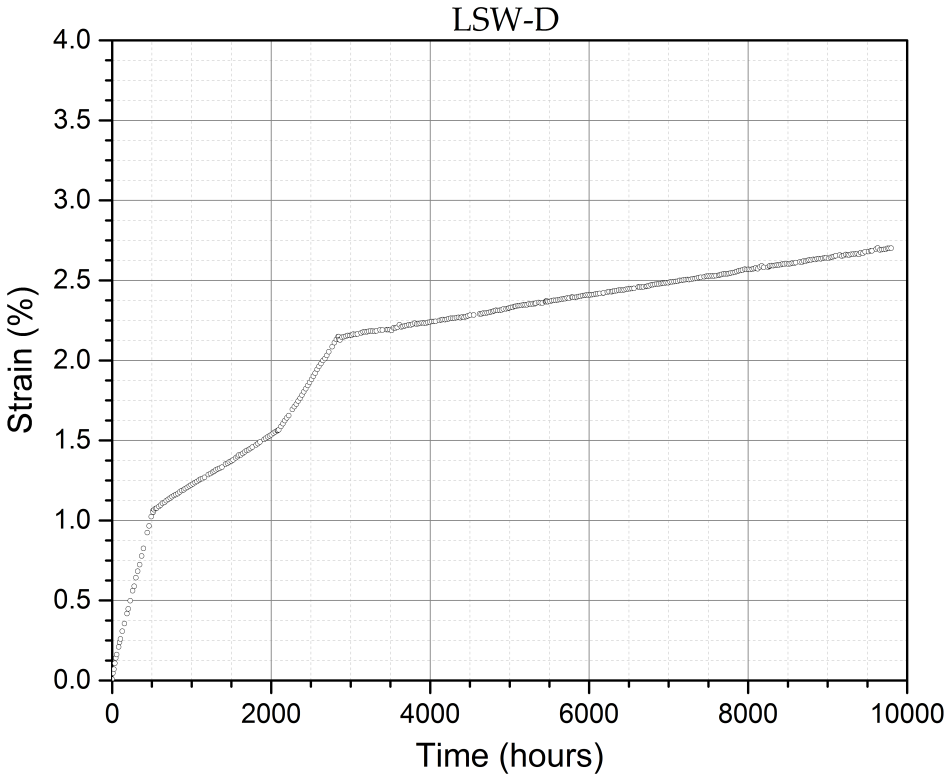


Figure C- 6. Creep Curve for LSW-D Circumferential Weld. Creep testing conditions and steady state creep rate provided in Table below.

Test Time (hours)	**Temperature (°F)**	**Stress (ksi)**	**Steady State Creep Rate (%/hr x 10^{-4})**
493	950	10	20.2
1585	900	10	3.1
771	925	10	7.9
6951	850	10	0.8

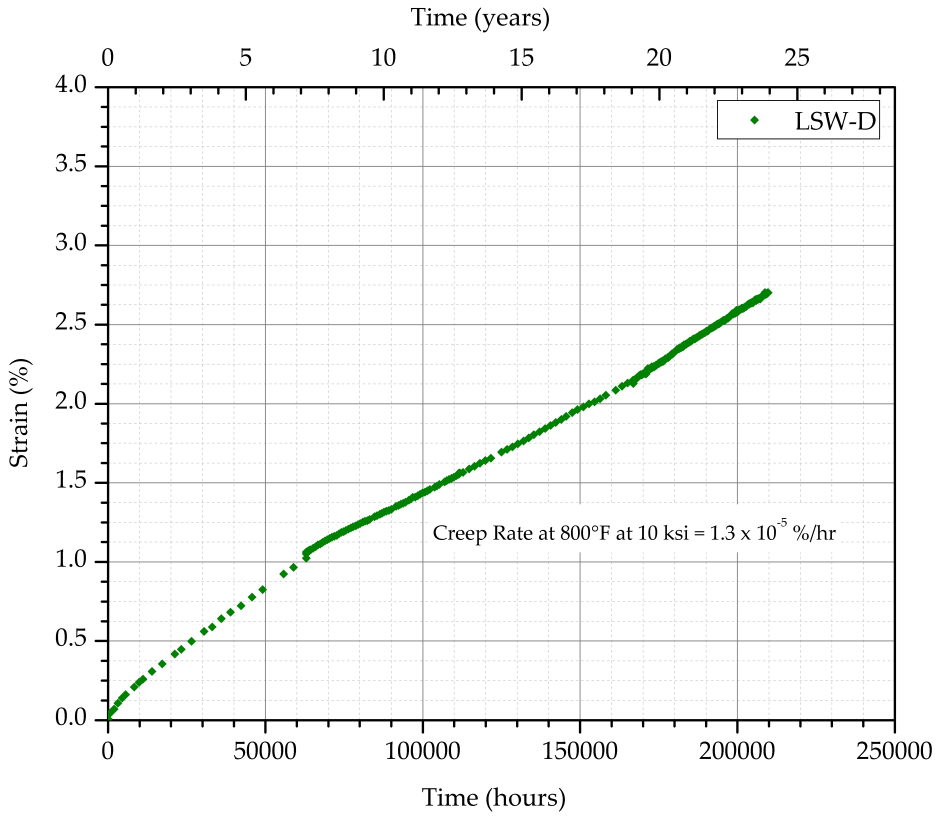


Figure C- 7. Normalized creep data for LSW-D.

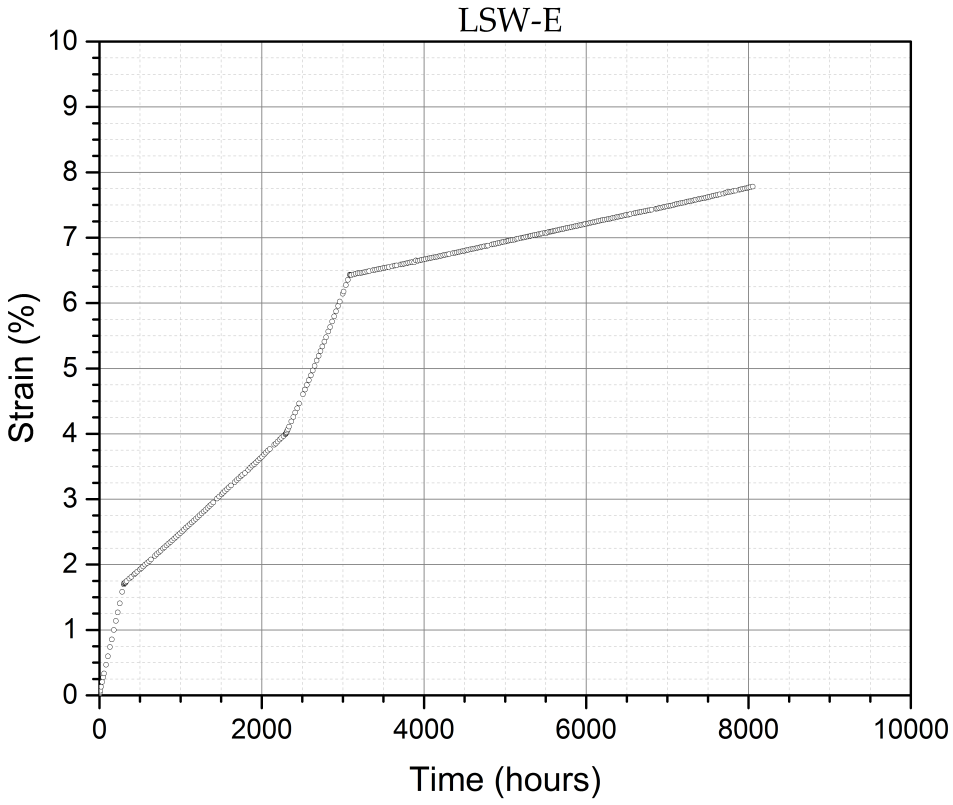


Figure C- 8. Creep curve for LSW-E circumferential weld. Creep testing conditions and steady state creep rate provided in Table below.

Test Time (hours)	**Temperature (°F)**	**Stress (ksi)**	**Steady State Creep Rate (%/hr x 10^{-4})**
303	950	10	55.9
1996	900	10	11.5
786	925	10	30.8
4967	850	10	2.7

Appendix D – Relevant ASTM Standards

ASTM A516

Designation: A516/A516M – 10 (Reapproved 2015)

Used in USDOE-NE Standards

Standard Specification for Pressure Vessel Plates, Carbon Steel, for Moderate- and Lower-Temperature Service[1]

This standard is issued under the fixed designation A516/A516M; the number immediately following the designation indicates the year of original adoption or, in the case of revision, the year of last revision. A number in parentheses indicates the year of last reapproval. A superscript epsilon (ε) indicates an editorial change since the last revision or reapproval.

This standard has been approved for use by agencies of the U.S. Department of Defense.

1. Scope

1.1 This specification[2] covers carbon steel plates intended primarily for service in welded pressure vessels where improved notch toughness is important.

1.2 Plates under this specification are available in four grades having different strength levels as follows:

Grade U.S. [SI]	Tensile Strength, ksi [MPa]
55 [380]	55–75 [380–515]
60 [415]	60–80 [415–550]
65 [450]	65–85 [450–585]
70 [485]	70–90 [485–620]

1.3 The maximum thickness of plates is limited only by the capacity of the composition to meet the specified mechanical property requirements; however, current practice normally limits the maximum thickness of plates furnished under this specification as follows:

Grade U.S. [SI]	Maximum Thickness, in. [mm]
55 [380]	12 [305]
60 [415]	8 [205]
65 [450]	8 [205]
70 [485]	8 [205]

1.4 For plates produced from coil and furnished without heat treatment or with stress relieving only, the additional requirements, including additional testing requirements and the reporting of additional test results of Specification A20/A20M apply.

1.5 The values stated in either inch-pound units or SI units are to be regarded separately as standard. Within the text, the SI units are shown in brackets. The values stated in each system are not exact equivalents; therefore, each system must be used independently of the other. Combining values from the two systems may result in nonconformance with the specification.

[1] This specification is under the jurisdiction of ASTM Committee A01 on Steel, Stainless Steel and Related Alloys and is the direct responsibility of Subcommittee A01.11 on Steel Plates for Boilers and Pressure Vessels.

Current edition approved Sept. 1, 2015. Published September 2015. Originally approved in 1964. Last previous edition approved in 2010 as A516/A516M – 10. DOI: 10.1520/A0516_A0516M-10R15.

[2] For ASME Boiler and Pressure Vessel Code applications, see related Specification SA-516/SA-516M in Section II of that Code.

2. Referenced Documents

2.1 *ASTM Standards:*[3]

A20/A20M Specification for General Requirements for Steel Plates for Pressure Vessels

A435/A435M Specification for Straight-Beam Ultrasonic Examination of Steel Plates

A577/A577M Specification for Ultrasonic Angle-Beam Examination of Steel Plates

A578/A578M Specification for Straight-Beam Ultrasonic Examination of Rolled Steel Plates for Special Applications

3. General Requirements and Ordering Information

3.1 Material supplied to this product specification shall conform to Specification A20/A20M, which outlines the testing and retesting methods and procedures, permissible variations in dimensions and mass, quality and repair of defects, marking, loading, and ordering information.

3.2 In addition to the basic requirements of this specification, certain supplementary requirements are available where additional control, testing, or examination is required to meet end use requirements. The purchaser is referred to the listed supplementary requirements in this specification and to the detailed requirements in Specification A20/A20M.

3.3 If the requirements of this specification are in conflict with the requirements of Specification A20/A20M, the requirements of this specification shall prevail.

3.4 Coils are excluded from qualification to this specification until they are processed into finished plates. Plates produced from coil means plates that have been cut to individual lengths from coil. The processor directly controls, or is responsible for, the operations involved in the processing of coils into finished plates. Such operations include decoiling, leveling, cutting to length, testing, inspection, conditioning, heat treatment (if applicable), packaging, marking, loading for shipment, and certification.

[3] For referenced ASTM standards, visit the ASTM website, www.astm.org, or contact ASTM Customer Service at service@astm.org. For *Annual Book of ASTM Standards* volume information, refer to the standard's Document Summary page on the ASTM website.

Copyright © ASTM International, 100 Barr Harbor Drive, PO Box C700, West Conshohocken, PA 19428-2959. United States

Copyright ASTM International
Provided by IHS under license with ASTM
No reproduction or networking permitted without license from IHS

Licensee=University of Tennessee/5622000001, User=Bharadwaj, Maneel
Not for Resale, 11/13/2016 12:12:42 MST

NOTE 1—For plates produced from coil and furnished without heat treatment or with stress relieving only, three test results are reported for each qualifying coil. Additional requirements regarding plate produced from coil are described in Specification A20/A20M.

3.5 If the requirements of this specification are in conflict with the requirements of Specification A20/A20M, the requirements of this specification shall prevail.

4. Materials and Manufacture

4.1 *Steelmaking Practice*—The steel shall be killed and shall conform to the fine austenitic grain size requirement of Specification A20/A20M.

5. Heat Treatment

5.1 Plates 1.50 in. [40 mm] and under in thickness are normally supplied in the as-rolled condition. The plates may be ordered normalized or stress relieved, or both.

5.2 Plates over 1.50 in. [40 mm] in thickness shall be normalized.

5.3 When notch-toughness tests are required on plates 1½ in. [40 mm] and under in thickness, the plates shall be normalized unless otherwise specified by the purchaser.

5.4 If approved by the purchaser, cooling rates faster than those obtained by cooling in air are permissible for improvement of the toughness, provided the plates are subsequently tempered in the temperature range 1100 to 1300°F [595 to 705°C].

6. Chemical Composition

6.1 The steel shall conform to the chemical requirements given in Table 1 unless otherwise modified in accordance with Supplementary Requirement S17, Vacuum Carbon-Deoxidized Steel, in Specification A20/A20M.

7. Mechanical Properties

7.1 *Tension Test*—The plates, as represented by the tension test specimens, shall conform to the requirements given in Table 2.

8. Keywords

8.1 carbon steel; carbon steel plate; pressure containing parts; pressure vessel steels; steel plates for pressure vessels

TABLE 1 Chemical Requirements

Elements	Composition, %			
	Grade 55 [Grade 380]	Grade 60 [Grade 415]	Grade 65 [Grade 450]	Grade 70 [Grade 485]
Carbon, max:[A,B]				
½ in. [12.5 mm] and under	0.18	0.21	0.24	0.27
Over ½ in. to 2 in. [12.5 to 50 mm], incl	0.20	0.23	0.26	0.28
Over 2 in. to 4 in. [50 to 100 mm], incl	0.22	0.25	0.28	0.30
Over 4 to 8 in. [100 to 200 mm], incl	0.24	0.27	0.29	0.31
Over 8 in. [200 mm]	0.26	0.27	0.29	0.31
Manganese:[B]				
½ in. [12.5 mm] and under:				
Heat analysis	0.60–0.90	0.60–0.90[C]	0.85–1.20	0.85–1.20
Product analysis	0.55–0.98	0.55–0.98[C]	0.79–1.30	0.79–1.30
Over ½ in. [12.5 mm]:				
Heat analysis	0.60–1.20	0.85–1.20	0.85–1.20	0.85–1.20
Product analysis	0.55–1.30	0.79–1.30	0.79–1.30	0.79–1.30
Phosphorus, max[A]	0.025	0.025	0.025	0.025
Sulfur, max[A]	0.025	0.025	0.025	0.025
Silicon:				
Heat analysis	0.15–0.40	0.15–0.40	0.15–0.40	0.15–0.40
Product analysis	0.13–0.45	0.13–0.45	0.13–0.45	0.13–0.45

[A] Applies to both heat and product analyses.
[B] For each reduction of 0.01 percentage point below the specified maximum for carbon, an increase of 0.06 percentage point above the specified maximum for manganese is permitted, up to a maximum of 1.50 % by heat analysis and 1.60 % by product analysis.
[C] Grade 60 plates ½ in. [12.5 mm] and under in thickness may have 0.85–1.20 % manganese on heat analysis, and 0.79–1.30 % manganese on product analysis.

Copyright ASTM International
Provided by IHS under license with ASTM
No reproduction or networking permitted without license from IHS

Licensee=University of Tennessee/5622000001, User=Bharadwaj, Maneel
Not for Resale, 11/13/2016 12:12:42 MST

TABLE 2 Tensile Requirements

	Grade			
	55 [380]	60 [415]	65 [450]	70 [485]
Tensile strength, ksi [MPa]	55–75 [380–515]	60–80 [415–550]	65–85 [450–585]	70–90 [485–620]
Yield strength, min,[A] ksi [MPa]	30 [205]	32 [220]	35 [240]	38 [260]
Elongation in 8 in. [200 mm], min, %[B]	23	21	19	17
Elongation in 2 in. [50 mm], min, %[B]	27	25	23	21

[A] Determined by either the 0.2 % offset method or the 0.5 % extension-under-load method.
[B] See Specification A20/A20M for elongation adjustment.

SUPPLEMENTARY REQUIREMENTS

Supplementary requirements shall not apply unless specified in the purchase order.

A list of standardized supplementary requirements for use at the option of the purchaser is included in ASTM Specification A20/A20M. Those that are considered suitable for use with this specification are listed below by title.

S1. Vacuum Treatment,

S2. Product Analysis,

S3. Simulated Post-Weld Heat Treatment of Mechanical Test Coupons,

S4.1 Additional Tension Test,

S5. Charpy V-Notch Impact Test,

S6. Drop Weight Test (for Material 0.625 in. [16 mm] and over in Thickness),

S7. High-Temperature Tension Test,

S8. Ultrasonic Examination in accordance with Specification A435/A435M,

S9. Magnetic Particle Examination,

S11. Ultrasonic Examination in accordance with Specification A577/A577M,

S12. Ultrasonic Examination in accordance with Specification A578/A578M, and

S17. Vacuum Carbon-Deoxidized Steel.

ADDITIONAL SUPPLEMENTARY REQUIREMENTS

In addition, the following supplementary requirement is suitable for this application.

S54. Requirements for Carbon Steel Plate for Hydrofluoric Acid Alkylation Service

S54.1 Plates shall be provided in the normalized heat-treated condition.

S54.2 The maximum carbon equivalent shall be as follows:

Plate thickness less than or equal to 1 in. [25 mm]: CE maximum = 0.43

Plate thickness greater than 1 in. [25 mm]: CE maximum = 0.45

S54.3 Determine the carbon equivalent (CE) as follows:

$$CE = C + Mn/6 + (Cr + Mo + V)/5 + (Ni + Cu)/15$$

S54.4 Vanadium and niobium maximum content based on heat analysis shall be:

Maximum vanadium = 0.02 %

Maximum niobium = 0.02 %

Maximum vanadium plus niobium = 0.03 %

(Note: niobium = columbium)

S54.5 The maximum composition based on heat analysis of Ni + Cu shall be 0.15 %.

S54.6 The minimum C content based on heat analysis shall be 0.18 %. The maximum C content shall be as specified for the ordered grade.

S54.7 Welding consumables for repair welds shall be of the low-hydrogen type. E60XX electrodes shall not be used and the resulting weld chemistry shall meet the same chemistry requirements as the base metal.

S54.8 In addition to the requirements for product marking in the specification, an "HF-N" stamp or marking shall be provided on each plate to identify that the plate complies with this supplementary requirement.

Copyright ASTM International
Provided by IHS under license with ASTM
No reproduction or networking permitted without license from IHS

Licensee=University of Tennessee/5622000001, User=Bharadwaj, Maneel
Not for Resale, 11/13/2016 12:12:42 MST

ASTM International takes no position respecting the validity of any patent rights asserted in connection with any item mentioned in this standard. Users of this standard are expressly advised that determination of the validity of any such patent rights, and the risk of infringement of such rights, are entirely their own responsibility.

This standard is subject to revision at any time by the responsible technical committee and must be reviewed every five years and if not revised, either reapproved or withdrawn. Your comments are invited either for revision of this standard or for additional standards and should be addressed to ASTM International Headquarters. Your comments will receive careful consideration at a meeting of the responsible technical committee, which you may attend. If you feel that your comments have not received a fair hearing you should make your views known to the ASTM Committee on Standards, at the address shown below.

This standard is copyrighted by ASTM International, 100 Barr Harbor Drive, PO Box C700, West Conshohocken, PA 19428-2959, United States. Individual reprints (single or multiple copies) of this standard may be obtained by contacting ASTM at the above address or at 610-832-9585 (phone), 610-832-9555 (fax), or service@astm.org (e-mail); or through the ASTM website (www.astm.org). Permission rights to photocopy the standard may also be secured from the Copyright Clearance Center, 222 Rosewood Drive, Danvers, MA 01923, Tel: (978) 646-2600; http://www.copyright.com/

Copyright ASTM International
Provided by IHS under license with ASTM
No reproduction or networking permitted without license from IHS

Licensee=University of Tennessee/5622000001, User=Bharadwaj, Maneel
Not for Resale, 11/13/2016 12:12:42 MST

Hardness Conversion Tables

Designation: A370 – 12

Standard Test Methods and Definitions for Mechanical Testing of Steel Products[1]

This standard is issued under the fixed designation A370; the number immediately following the designation indicates the year of original adoption or, in the case of revision, the year of last revision. A number in parentheses indicates the year of last reapproval. A superscript epsilon (ε) indicates an editorial change since the last revision or reapproval.

This standard has been approved for use by agencies of the Department of Defense.

1. Scope*

1.1 These test methods[2] cover procedures and definitions for the mechanical testing of steels, stainless steels, and related alloys. The various mechanical tests herein described are used to determine properties required in the product specifications. Variations in testing methods are to be avoided, and standard methods of testing are to be followed to obtain reproducible and comparable results. In those cases in which the testing requirements for certain products are unique or at variance with these general procedures, the product specification testing requirements shall control.

1.2 The following mechanical tests are described:

	Sections
Tension	5 to 13
Bend	14
Hardness	15
Brinell	16
Rockwell	17
Portable	18
Impact	19 to 28
Keywords	29

1.3 Annexes covering details peculiar to certain products are appended to these test methods as follows:

	Annex
Bar Products	A1.1
Tubular Products	Annex A2
Fasteners	Annex A3
Round Wire Products	Annex A4
Significance of Notched-Bar Impact Testing	Annex A5
Converting Percentage Elongation of Round Specimens to Equivalents for Flat Specimens	Annex A6
Testing Multi-Wire Strand	Annex A7
Rounding of Test Data	Annex A8
Methods for Testing Steel Reinforcing Bars	Annex A9
Procedure for Use and Control of Heat-Cycle Simulation	Annex A10

1.4 The values stated in inch-pound units are to be regarded as the standard.

1.5 When this document is referenced in a metric product specification, the yield and tensile values may be determined in inch-pound (ksi) units then converted into SI (MPa) units. The elongation determined in inch-pound gauge lengths of 2 or 8 in. may be reported in SI unit gauge lengths of 50 or 200 mm, respectively, as applicable. Conversely, when this document is referenced in an inch-pound product specification, the yield and tensile values may be determined in SI units then converted into inch-pound units. The elongation determined in SI unit gauge lengths of 50 or 200 mm may be reported in inch-pound gauge lengths of 2 or 8 in., respectively, as applicable.

1.6 Attention is directed to ISO/IEC 17025 when there may be a need for information on criteria for evaluation of testing laboratories.

1.7 *This standard does not purport to address all of the safety concerns, if any, associated with its use. It is the responsibility of the user of this standard to establish appropriate safety and health practices and determine the applicability of regulatory limitations prior to use.*

2. Referenced Documents

2.1 *ASTM Standards:*[3]

A623 Specification for Tin Mill Products, General Requirements

A623M Specification for Tin Mill Products, General Requirements [Metric]

A703/A703M Specification for Steel Castings, General Requirements, for Pressure-Containing Parts

A781/A781M Specification for Castings, Steel and Alloy, Common Requirements, for General Industrial Use

A833 Practice for Indentation Hardness of Metallic Materials by Comparison Hardness Testers

E4 Practices for Force Verification of Testing Machines

E6 Terminology Relating to Methods of Mechanical Testing

E8/E8M Test Methods for Tension Testing of Metallic Materials

[1] These test methods and definitions are under the jurisdiction of ASTM Committee A01 on Steel, Stainless Steel and Related Alloys and are the direct responsibility of Subcommittee A01.13 on Mechanical and Chemical Testing and Processing Methods of Steel Products and Processes.

Current edition approved March 15, 2012. Published March 2012. Originally approved in 1953. Last previous edition approved in 2011 as A370 – 11a. DOI: 10.1520/A0370-12.

[2] For *ASME Boiler and Pressure Vessel Code* applications see related Specification SA-370 in Section II of that Code.

[3] For referenced ASTM standards, visit the ASTM website, www.astm.org, or contact ASTM Customer Service at service@astm.org. For *Annual Book of ASTM Standards* volume information, refer to the standard's Document Summary page on the ASTM website.

***A Summary of Changes section appears at the end of this standard.**

Copyright © ASTM International, 100 Barr Harbor Drive, PO Box C700, West Conshohocken, PA 19428-2959, United States.

Copyright ASTM International
Provided by IHS under license with ASTM
No reproduction or networking permitted without license from IHS

Licensee=University of Tennessee/5622000001
Not for Resale, 08/21/2012 14:58:07 MDT

TABLE 2 Approximate Hardness Conversion Numbers for Nonaustenitic Steels[A] (Rockwell C to Other Hardness Numbers)

Rockwell C Scale, 150-kgf Load, Diamond Penetrator	Vickers Hardness Number	Brinell Hardness, 3000-kgf Load, 10-mm Ball	Knoop Hardness, 500-gf Load and Over	Rockwell A Scale, 60-kgf Load, Diamond Penetrator	Rockwell Superficial Hardness			
					15N Scale, 15-kgf Load, Diamond Penetrator	30N Scale 30-kgf Load, Diamond Penetrator	45N Scale, 45-kgf Load, Diamond Penetrator	Approximate Tensile Strength, ksi (MPa)
68	940	. . .	920	85.6	93.2	84.4	75.4	. . .
67	900	. . .	895	85.0	92.9	83.6	74.2	. . .
66	865	. . .	870	84.5	92.5	82.8	73.3	. . .
65	832	739	846	83.9	92.2	81.9	72.0	. . .
64	800	722	822	83.4	91.8	81.1	71.0	. . .
63	772	706	799	82.8	91.4	80.1	69.9	. . .
62	746	688	776	82.3	91.1	79.3	68.8	. . .
61	720	670	754	81.8	90.7	78.4	67.7	. . .
60	697	654	732	81.2	90.2	77.5	66.6	. . .
59	674	634	710	80.7	89.8	76.6	65.5	351 (2420)
58	653	615	690	80.1	89.3	75.7	64.3	338 (2330)
57	633	595	670	79.6	88.9	74.8	63.2	325 (2240)
56	613	577	650	79.0	88.3	73.9	62.0	313 (2160)
55	595	560	630	78.5	87.9	73.0	60.9	301 (2070)
54	577	543	612	78.0	87.4	72.0	59.8	292 (2010)
53	560	525	594	77.4	86.9	71.2	58.6	283 (1950)
52	544	512	576	76.8	86.4	70.2	57.4	273 (1880)
51	528	496	558	76.3	85.9	69.4	56.1	264 (1820)
50	513	482	542	75.9	85.5	68.5	55.0	255 (1760)
49	498	468	526	75.2	85.0	67.6	53.8	246 (1700)
48	484	455	510	74.7	84.5	66.7	52.5	238 (1640)
47	471	442	495	74.1	83.9	65.8	51.4	229 (1580)
46	458	432	480	73.6	83.5	64.8	50.3	221 (1520)
45	446	421	466	73.1	83.0	64.0	49.0	215 (1480)
44	434	409	452	72.5	82.5	63.1	47.8	208 (1430)
43	423	400	438	72.0	82.0	62.2	46.7	201 (1390)
42	412	390	426	71.5	81.5	61.3	45.5	194 (1340)
41	402	381	414	70.9	80.9	60.4	44.3	188 (1300)
40	392	371	402	70.4	80.4	59.5	43.1	182 (1250)
39	382	362	391	69.9	79.9	58.6	41.9	177 (1220)
38	372	353	380	69.4	79.4	57.7	40.8	171 (1180)
37	363	344	370	68.9	78.8	56.8	39.6	166 (1140)
36	354	336	360	68.4	78.3	55.9	38.4	161 (1110)
35	345	327	351	67.9	77.7	55.0	37.2	156 (1080)
34	336	319	342	67.4	77.2	54.2	36.1	152 (1050)
33	327	311	334	66.8	76.6	53.3	34.9	149 (1030)
32	318	301	326	66.3	76.1	52.1	33.7	146 (1010)
31	310	294	318	65.8	75.6	51.3	32.5	141 (970)
30	302	286	311	65.3	75.0	50.4	31.3	138 (950)
29	294	279	304	64.6	74.5	49.5	30.1	135 (930)
28	286	271	297	64.3	73.9	48.6	28.9	131 (900)
27	279	264	290	63.8	73.3	47.7	27.8	128 (880)
26	272	258	284	63.3	72.8	46.8	26.7	125 (860)
25	266	253	278	62.8	72.2	45.9	25.5	123 (850)
24	260	247	272	62.4	71.6	45.0	24.3	119 (820)
23	254	243	266	62.0	71.0	44.0	23.1	117 (810)
22	248	237	261	61.5	70.5	43.2	22.0	115 (790)
21	243	231	256	61.0	69.9	42.3	20.7	112 (770)
20	238	226	251	60.5	69.4	41.5	19.6	110 (760)

[A] This table gives the approximate interrelationships of hardness values and approximate tensile strength of steels. It is possible that steels of various compositions and processing histories will deviate in hardness-tensile strength relationship from the data presented in this table. The data in this table should not be used for austenitic stainless steels, but have been shown to be applicable for ferritic and martensitic stainless steels. The data in this table should not be used to establish a relationship between hardness values and tensile strength of hard drawn wire. Where more precise conversions are required, they should be developed specially for each steel composition, heat treatment, and part. Caution should be exercised if conversions from this table are used for the acceptance or rejection of product. The approximate interrelationships may affect acceptance or rejection.

Copyright ASTM International
Provided by IHS under license with ASTM
No reproduction or networking permitted without license from IHS

]]
Licensee=University of Tennessee/5622000001
Not for Resale, 08/21/2012 14:58:07 MDT

TABLE 3 Approximate Hardness Conversion Numbers for Nonaustenitic Steels[A] (Rockwell B to Other Hardness Numbers)

Rockwell B Scale, 100-kgf Load 1/16-in. (1.588-mm) Ball	Vickers Hardness Number	Brinell Hardness, 3000-kgf Load, 10-mm Ball	Knoop Hardness, 500-gf Load and Over	Rockwell A Scale, 60-kgf Load, Diamond Penetrator	Rockwell F Scale, 60-kgf Load, 1/16-in. (1.588-mm) Ball	Rockwell Superficial Hardness			Approximate Tensile Strength ksi (MPa)
						15T Scale, 15-kgf Load, 1/16 -in. (1.588-mm) Ball	30T Scale, 30-kgf Load, 1/16-in. (1.588-mm) Ball	45T Scale, 45-kgf Load, 1/16-in. (1.588-mm) Ball	
100	240	240	251	61.5	...	93.1	83.1	72.9	116 (800)
99	234	234	246	60.9	...	92.8	82.5	71.9	114 (785)
98	228	228	241	60.2	...	92.5	81.8	70.9	109 (750)
97	222	222	236	59.5	...	92.1	81.1	69.9	104 (715)
96	216	216	231	58.9	...	91.8	80.4	68.9	102 (705)
95	210	210	226	58.3	...	91.5	79.8	67.9	100 (690)
94	205	205	221	57.6	...	91.2	79.1	66.9	98 (675)
93	200	200	216	57.0	...	90.8	78.4	65.9	94 (650)
92	195	195	211	56.4	...	90.5	77.8	64.8	92 (635)
91	190	190	206	55.8	...	90.2	77.1	63.8	90 (620)
90	185	185	201	55.2	...	89.9	76.4	62.8	89 (615)
89	180	180	196	54.6	...	89.5	75.8	61.8	88 (605)
88	176	176	192	54.0	...	89.2	75.1	60.8	86 (590)
87	172	172	188	53.4	...	88.9	74.4	59.8	84 (580)
86	169	169	184	52.8	...	88.6	73.8	58.8	83 (570)
85	165	165	180	52.3	...	88.2	73.1	57.8	82 (565)
84	162	162	176	51.7	...	87.9	72.4	56.8	81 (560)
83	159	159	173	51.1	...	87.6	71.8	55.8	80 (550)
82	156	156	170	50.6	...	87.3	71.1	54.8	77 (530)
81	153	153	167	50.0	...	86.9	70.4	53.8	73 (505)
80	150	150	164	49.5	...	86.6	69.7	52.8	72 (495)
79	147	147	161	48.9	...	86.3	69.1	51.8	70 (485)
78	144	144	158	48.4	...	86.0	68.4	50.8	69 (475)
77	141	141	155	47.9	...	85.6	67.7	49.8	68 (470)
76	139	139	152	47.3	...	85.3	67.1	48.8	67 (460)
75	137	137	150	46.8	99.6	85.0	66.4	47.8	66 (455)
74	135	135	147	46.3	99.1	84.7	65.7	46.8	65 (450)
73	132	132	145	45.8	98.5	84.3	65.1	45.8	64 (440)
72	130	130	143	45.3	98.0	84.0	64.4	44.8	63 (435)
71	127	127	141	44.8	97.4	83.7	63.7	43.8	62 (425)
70	125	125	139	44.3	96.8	83.4	63.1	42.8	61 (420)
69	123	123	137	43.8	96.2	83.0	62.4	41.8	60 (415)
68	121	121	135	43.3	95.6	82.7	61.7	40.8	59 (405)
67	119	119	133	42.8	95.1	82.4	61.0	39.8	58 (400)
66	117	117	131	42.3	94.5	82.1	60.4	38.7	57 (395)
65	116	116	129	41.8	93.9	81.8	59.7	37.7	56 (385)
64	114	114	127	41.4	93.4	81.4	59.0	36.7	...
63	112	112	125	40.9	92.8	81.1	58.4	35.7	...
62	110	110	124	40.4	92.2	80.8	57.7	34.7	...
61	108	108	122	40.0	91.7	80.5	57.0	33.7	...
60	107	107	120	39.5	91.1	80.1	56.4	32.7	...
59	106	106	118	39.0	90.5	79.8	55.7	31.7	...
58	104	104	117	38.6	90.0	79.5	55.0	30.7	...
57	103	103	115	38.1	89.4	79.2	54.4	29.7	...
56	101	101	114	37.7	88.8	78.8	53.7	28.7	...
55	100	100	112	37.2	88.2	78.5	53.0	27.7	...
54	...	...	111	36.8	87.7	78.2	52.4	26.7	...
53	...	...	110	36.3	87.1	77.9	51.7	25.7	...
52	...	...	109	35.9	86.5	77.5	51.0	24.7	...
51	...	...	108	35.5	86.0	77.2	50.3	23.7	...
50	...	...	107	35.0	85.4	76.9	49.7	22.7	...
49	...	...	106	34.6	84.8	76.6	49.0	21.7	...
48	...	...	105	34.1	84.3	76.2	48.3	20.7	...
47	...	...	104	33.7	83.7	75.9	47.7	19.7	...
46	...	...	103	33.3	83.1	75.6	47.0	18.7	...
45	...	...	102	32.9	82.6	75.3	46.3	17.7	...
44	...	...	101	32.4	82.0	74.9	45.7	16.7	...
43	...	...	100	32.0	81.4	74.6	45.0	15.7	...
42	...	...	99	31.6	80.8	74.3	44.3	14.7	...
41	...	...	98	31.2	80.3	74.0	43.7	13.6	...
40	...	...	97	30.7	79.7	73.6	43.0	12.6	...
39	...	...	96	30.3	79.1	73.3	42.3	11.6	...
38	...	...	95	29.9	78.6	73.0	41.6	10.6	...
37	...	...	94	29.5	78.0	72.7	41.0	9.6	...
36	...	...	93	29.1	77.4	72.3	40.3	8.6	...
35	...	...	92	28.7	76.9	72.0	39.6	7.6	...
34	...	...	91	28.2	76.3	71.7	39.0	6.6	...
33	...	...	90	27.8	75.7	71.4	38.3	5.6	...

Copyright ASTM International
Provided by IHS under license with ASTM
No reproduction or networking permitted without license from IHS

Licensee=University of Tennessee/5622000001
Not for Resale, 08/21/2012 14:58:07 MDT

Vita

Maneel Bharadwaj was born in Palpa, Nepal to his parents Mr. Madhav Raj Sharma and Mrs. Kamala Devi Sharma. He has an older brother Mr. Maneesh Bharadwaj. After finishing his high school at Saints Xavier's School in Nepal, Maneel moved to the United States to pursue higher education. After receiving his B.S. in Extractive Metallurgy from the University of Idaho Moscow, Idaho in 2008, Maneel moved to Atlanta, Georgia to work as a Research Intern He worked on estimation of the dihedral angle on W-Fe-Ni liquid phase sintered alloys, where his desire for further education fortified. He joined the University of Tennessee, Knoxville for his doctoral degree under the guidance of world renowned Professor Carl D. Lundin in the field of welding and physical metallurgy. Maneel worked on multiple projects which involved metallurgical studies on both ferrous and non-ferrous alloys. He studied high temperature hydrogen attack (HTHA) on carbon steel and C-½ Mo steels, a common problem in petrochemical industry to assist American Petroleum Institute (API). Maneel presented his HTHA work on multiple conferences and also published his C-½ Mo study work in WRC-548 and WRC-568. For his PhD, Maneel worked on

graphitization problems in carbon steel weldments operating at elevated temperature.

Apart from his research, Maneel has worked as a teaching assistant for various MSE departmental courses including MSE-201 (Introduction to materials science and engineering), MSE 300 (Principles of materials laboratories -I&II), MSE-370 (Materials processing), MSE-480 (Material selection and design) and MSE-489 (Failure analysis). MSE-480 and MSE-489 are the capstone courses for undergraduates at the department of material science and engineering. Maneel received a departmental study for excellence in teaching award in 2016. Maneel has also been involved with annual ASM materials camp assisting students with failure analysis projects. Maneel has also been actively involved in local American Welding Society (AWS) local chapter. He was also presented a section award for his contribution to the local chapter in 2016. Upon completion of his doctoral degree, he plans to continue to assist local industries in US with problems related to welding/metallurgy and inspire new generation to pursue careers in science and engineering.